Microstructural Studies of High Dose Oxygen Implanted Silicon

Thesis for the degree of Doctor of Philosophy

at the

University of Oxford

Chris Marsh

Department of Materials and Wolfson College

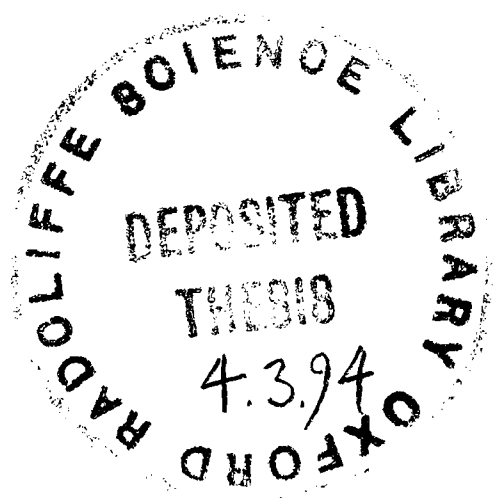

Trinity Term 1993

Abstract

Microstructural Studies of High Dose Oxygen Implanted Silicon

Chris Marsh
Wolfson College

Doctor of Philosophy
Trinity Term 1993

This work describes results obtained from detailed TEM, TED, HREM and SIMS analysis of the as-implanted and annealed microstructures of high dose ($0.1x10^{17}/cm^2$ to $1.7x10^{18}/cm^2$) oxygen implanted silicon (Si). Molecular oxygen (O_2^+) has been implanted into Si wafers at equivalent energies of 200keV/O^+, 90keV/O^+, 70keV/O^+ and 50keV/O^+ to form, after annealing in flowing N_2 or Ar + ½ % O_2, buried SiO_2 layers below single crystal surface Si layers. This process is called Separation by the IMplantation of OXygen (SIMOX). The energies and doses investigated are potentially suitable for the fabrication of two types of "thin-film" SIMOX substrates, which have major potential benefits for high-performance CMOS devices. This work is concerned with investigating the as-implanted and annealed microstructures, understanding the basic processes and mechanisms taking place during implantation and annealing, and establishing optimum fabrication parameters.

Similar microstructures and changes in microstructure as a function of the dose are observed for the different implant energies investigated. For all the different energies and doses investigated, SiO_2 precipitates are present after implantation. Five different precipitate morphologies are observed. The precipitate morphology depends on the oxygen concentration and the depth below the surface. The local and long range strain also play a role in determining the precipitate morphology. For doses of $0.5x10^{18}O/cm^2$ to $0.7x10^{18}O/cm^2$ at 200keV defects at the wafer surface are non-uniformly distributed across the implanted area. The regions of defects are in plan-view rectangular in shape with edges parallel to <100> directions. The percentage of the implanted surface that is covered by these rectangular regions depends on both the dose and the time-averaged beam current density. This is the first known report of such non-uniform distribution across the implanted area of defects at the wafer surface and their occurrence in regions with precise rectangular shapes. Previously unreported "line" defects below the peak of the as-implanted oxygen distribution for these energies are investigated. They are considered to be platelets on {100} planes and edge dislocation loops on {110} planes.

After annealing, two major types of defects are present, threading dislocations in the surface Si layer and Si islands within the buried SiO_2 layer. Correlation of as-implanted and annealed microstructure suggests that the threading dislocations originate in the defects present at the wafer surface after implantation and grow down during annealing. The Si islands originate from Si isolated from the surface Si layer and the substrate during implantation or annealing. The optimum dose for forming a SIMOX structure at a particular energy with both a low threading dislocation density and a low Si island density is just greater than the minimum dose for forming a continuous buried SiO_2 layer after annealing. In order to try and reduce the density of Si islands within the buried SiO_2 layer, graded low energy implants and interim rapid thermal anneals are investigated. Their influence on the microstructure is reported. The experimental results enable, for the implantation and anneal conditions used, the likely threading dislocation and Si island density after annealing to be estimated for a particular dose and energy.

Simple models have been proposed for calculating typical oxygen diffusion lengths during implantation, the thicknesses of the buried SiO_2 and surface Si layers after annealing and conversely the implant dose and energy required to fabricate a SIMOX substrate with a certain thickness of buried SiO_2 and a certain thickness of surface Si layer after annealing.

Thin-film SIMOX substrates consisting of a thin surface Si layer above a thin buried oxide layer suitable for high-performance "fully depleted" CMOS devices have been successfully fabricated by implanting doses of ≥ 0.35 and $\geq 0.33x10^{18}O/cm^2$ at energies of 90keV and 70keV, repectively. Thin-film SIMOX substrates with a thin buried oxide layer below a standard thickness surface Si layer suitable for radiation hard circuits with reduced circuit self-heating have been successfully fabricated by implanting doses of $\geq 0.56x10^{18}O/cm^2$ at an energy of 200keV.

Preface

This thesis is an account of original work carried out by the author in the Department of Materials, University of Oxford between January and September 1988 and January 1990 and May 1993. Where the work of others is reported their contribution has been acknowledged. No part of this thesis has been submitted for any other degree at this or any other University. The work performed during the later period was part of an SERC funded academic collaboration entitled "Materials Processing for Advanced SOI Substrates" involving the University of Oxford, the University of Surrey, Imperial College and the University of Liverpool. Parts of the work presented in this thesis have been published as follows,

The role of implantation temperature and dose in the control of the microstructure of SIMOX.
K J Reeson, A K Robinson, P L F Hemment, C D Marsh, K N Christensen, G R Booker, R J Chater, J A Kilner, G Harbeke, E F Seigmeir & G K Celler.
Microelectronic Engineering 8 p163, 1988.

Formation of thin silicon films using low energy oxygen ion implantation.
A K Robinson, C D Marsh, U Bussmann, J A Kliner, Y Li, J Vanhellemont, K J Reeson, P L F Hemment & G R Booker.
Presented at the Eighth Int' Ion Implantation Tech. Conf. (Guildford, UK), 1990 & published in Nucl. Inst. & Meths. B55 p555, 1991.

Low energy oxygen dose optimisation for thin film SIMOX.
A K Robinson, Y Li, C D Marsh, R J Chater, P L F Hemment, J A Kilner, & G R Booker.
Presented at the Spring Euro. Mats. Res. Soc. Conf. (Strasbourg, France), 1991 & published in Mat. Sci. & Eng. B12 p41, 1992.

SIMS, RBS, ion channeling and TEM studies of low energy SIMOX structures.
Y Li, J A Kilner, P L F Hemment, A K Robinson, J Zhang, K J Reeson, C D Marsh & G R Booker.
Presented at Ion Beam Analysis 10 Conf. (Eindhoven, The Netherlands), 1991 & published in Nucl. Inst. & Meths. B64 p750, 1992.

Analysis of thin film silicon-on-insulator structures formed by low-energy oxygen implantation.
Y Li, J A Kilner, A K Robinson, P L F Hemment & C D Marsh.
J. of Appl. Phys. 70 No7 p3605, 1991.

Study of the microstructure of low energy (70keV) oxygen implanted silicon.
Y Li, J A Kilner, P L Hemment, A K Robinson, J Zhang, K Reeson, C D Marsh & G R Booker.
Appl. Phys. Lett. 59 No24 p3130, 1991.

Identification of optimal doses for device quality thin-film and standard SIMOX structures formed by low or high energy oxygen implantation.
C D Marsh, G R Booker, A Nejim, L F Giles, P L F Hemment, Y Li, R J Chater, J A Kilner, S Wainwright & S Hall.
Proc. of the 1992 IEEE Int'l SOI Conf. (Ponte Vedra, USA) p8, 1992.

The effects of dose and target temperature on low energy SIMOX layers.
Y Li, J A Kilner, R J Chater, P L F Hemment, A Nejim, A K Robinson, K J Reeson, C D Marsh & G R Booker.
Presented at the Fifth Int'l Symp. on Silicon-on-Insulator Technology and Devices (St Louis, USA), 1992 & published in J. Electrochem. Soc. 140 No6 p1780, 1993.

Direct formation of device worthy thin film structures by low energy implantation.
A Nejim, Y Li, C D Marsh, P L F Hemment, J A Kilner & G R Booker.
Presented at the Eighth Int'l Ion Beam Modifications of Materials Conf. (Heidelberg, Germany), 1992 & published in Nucl. Inst. & Meths. B80/81 p822, 1993.

Process optimisation for direct formation of device worthy thin film SIMOX structure using 90keV oxygen implantation.
A Nejim, Y Li, C D Marsh, P L F Hemment, R J Chater, J A Kilner & G R Booker.
Presented at the Ninth Int'l Ion Implantation Tech. Conf. (Gainesville, USA), 1992 & published in Nucl. Inst. & Meths. B74 p170, 1993.

Control of the buried oxide thickness and Si defect density in SIMOX substrates - structural investigation and process optimisation.
C D Marsh, A Nejim, Y Li, G R Booker, P L F Hemment, R J Chater & J A Kilner.
Presented at the Ninth Int'l Ion Implantation Tech. Conf. (Gainesville, USA), 1992 & published in Nucl. Inst. & Meths. B74 p197, 1993.

An investigation of the role of time averaged ion beam current density upon defect densities in thin film SIMOX.
A Nejim, C D Marsh, L F Giles, P L F Hemment, Y Li, R J Chater & J A Kilner
Presented at the Spring Euro. Mats. Res. Soc. Conf. (Strasbourg, France), 1993 & to be published in Nucl. Inst. & Meths. in 1993.

Crystallographic defect studies in SIMOX material thinned by sacrifical oxidation.
L F Giles, C D Marsh, A Nejim, P L F Hemment & G R Booker.
Presented at the Spring Euro. Mats. Res. Soc. Conf. (Strasbourg, France), 1993 & to be published in Nucl. Inst. & Meths. in 1993.

TEM and HREM studies of as-implanted high-dose oxygen implanted silicon at doses and energies suitable for thin-film silicon-on-insulator substrates.
C D Marsh, Y Li, A Nejim, J A Kilner, P L F Hemment & G R Booker.
Presented at the Eighth Oxford Conf. on the Microscopy of Semiconducting Materials, 1993 & published in Inst. Phys. Conf. Ser. 134, p129, 1993.

Oxygen isotopic exchange during the annealing of low energy SIMOX layers.
Y Li, J A Kilner, R J Chater, A Nejim, P L F Hemment, C D Marsh & G R Booker.
Presented at Ion Beam Analysis 11 Conf. (Budapest, Hungary), 1993 & to be published in Nucl. Inst. & Meths. in 1993.

Oxygen isotopic exchange and diffusion between a $^{18}O^{+}$ implanted silicon layer and a natural SiO_2 capping layer during high temperature annealing.
Y Li, J A Kilner, R J Chater, A Nejim, P L F Hemment, C D Marsh & G R Booker.
To be published in Appl. Phys. Lett. in 1993.

Acknowledgements

I am indebted to the many people who have helped with this work. I should like to thank,

Professor Sir Peter Hirsch FRS and Professor R J Brook for the provision of laboratory facilities,
Dr G R Booker for being my supervisor,
SERC and AERE Harwell for financial support,
Dr P L F Hemment, at the Dept. of Electronic and Electrical Engineering, University of Surrey, for the provision of material,
Dr A Nejim, Dr A K Robinson at the Dept. of Electronic and Electrical Engineering, University of Surrey, and the staff at the D R Chick Laboratory, University of Surrey, for carrying out the implants, the RBS analysis, and running the computer program IRIS,
Dr Y Li and Dr J A Kilner, at the Dept. of Materials, Imperial College, University of London for performing the SIMS analysis and supplying sputtering data from the computer program Profile Code,
Mr R J Chater at the Dept. of Materials, Imperial College, for performing the nitrogen anneals,
Dr T G Tate at the Dept. of Electronic Engineering, Imperial College, for the RTA anneals,
the staff at the Microelectronics Centre, University of Southampton, for performing the argon plus ½ % oxygen anneals,
Dr P L F Hemment, Dr A Nejim, Dr K J Reeson, Dr A K Robinson, Mr L-P Giles, at the Dept. of Electronic and Electrical Engineering, University of Surrey, Dr Y Li, Dr J A Kilner, Mr R J Chater at the Dept. of Materials, Imperial College, University of London and Dr S Hall, at the Dept. of Electrical Engineering and Electronics, University of Liverpool, for many useful discussions,
Dr M L Jenkins and Dr J L Hutchinson for teaching me how to use the microscopes,
Mr G Dixon-Brown, Mr R Doole and Mr P Hambridge for maintaining the microscopes,
Mr M Taheri and Mr A McKnight for photographic work,
members of the Semiconductor Group, past and present, for discussions and coffee time conversations, in particular Dr M C Roberts for first teaching me how to prepare TEM specimens, Dr R E Mallard for help with the HREM microscopy, the interpretation of the HREM images and many discussions on materials problems and Dr Z Laczik for his help with various aspects of computing,
and finally friends at Wolfson College, in particular Jennifer and those I had the privilege to row with, for their friendship and support.

Symbols

The symbols used to represent parameters in this thesis are listed below. They are also defined at the first point they appear in each chapter.

Symbol	Units	Definition
α	Si_i/s	generation rate of interstitials
ß	Si_i/O	No. of Si interstitials generated per incident oxygen atom
γ	Si_V/O	No. of Si vacancies absorbed per oxygen atom
ε	Si/O	No. of Si atoms incorporated in oxide per incident oxygen atom
Φ	O/cm^2	dose
${}^{I}\Phi_c$	O/cm^2	critical dose for forming a continuous SiO_2 layer during implantation
${}^{A}\Phi_c$	O/cm^2	critical dose for forming a continuous SiO_2 layer after annealing
${}^{A}\Phi_{dc}$	O/cm^2	largest dose observed to form a discontinuous SiO_2 layer after anneal
$\Phi_{OS=0}$	O/cm^2	critical dose for which the original surface is consumed after annealing
$\Phi_{Si=0}$	O/cm^2	critical dose for which the surface Si is consumed after annealing
ϕ	degrees	angle of rotation of TEM specimen about the eucentric axis
ρ	g/cm^3	density
σ	J/cm^2	interface energy
A	cm	thickness of Si layer equal to the No. of Si atoms incorporated in oxide
B	cm	thickness of Si layer equal to the No. of excess Si_i generated
c_o	$atoms/cm^3$	concentration of oxygen
c_i	Si_i/cm^3	concentration of silicon interstitials
c_v	Si_v/cm^3	concentration of silicon vacancies
C_o	$atoms/cm^3$	thermal equilibrium concentration of oxygen
C_i	Si_i/cm^3	thermal equilibrium concentration of silicon interstitials
C_v	Si_v/cm^3	thermal equilibrium concentration of silicon vacancies
D	cm^2/s	diffusion coefficient
E	eV	implantation energy
F	J	strain energy
G	cm	depth of the centre of the oxygen distribution after implantation
H	cm	shift in the depth of the centre of the oxygen distribution for doses $>{}^{I}\Phi c$
I	µA	beam current
I'	$\mu A/cm^2$	beam current density
k	J/K	Boltzmann constant
N	$atoms/cm^3$	atomic density
N_p	$atoms/cm^3$	atomic density at peak of implant distribution
N_{avo}	atoms/mol	avogadro's constant

Symbols (cont.)

Symbol	Units	Definition
O'	O/ s cm^2	rate of arrival of oxygen atoms
q	C	elementary charge
r_c	cm	critical radius for precipitate stability
$\hat{R}_p$	cm	depth of the peak in the oxygen distribution
$\bar{R}_p$	cm	mean projected range
ΔR_p	cm	straggle
S	cm	surface growth
S'	cm/s	rate of surface growth
Si_{Si}		silicon atom on lattice site
Si_v		silicon vacancy
Si_i		silicon interstitial
T	K	temperature
T_i	°C	implant temperature
$^{A}T_{Si}$	cm	thickness of surface Si layer after annealing
$^{A}T_{SiO_2}$	cm	thickness of buried SiO_2 layer after annealing
t	s	time
V(a)	cm^3	volume of atom or molecule "a"
$\delta V(O)$	cm^3	accommodation volume required per oxygen atom to form
$\delta V(SiO_2)$	cm^3	accommodation volume required to form one molecule of SiO_2
w	cm	width of thickness fringes
x	cm	diffusion length
Y	atoms/O	sputtering yield per incident oxygen atom
z	cm	thickness of TEM specimen
Z		atomic weight

Abbreviations

The acronyms and abbreviations used in the text of this thesis are defined below. They are also defined at the first point they appear in each chapter.

Ar	- Argon
CMOS	- Complementary Metal-Oxide-Semiconductor
c.s.	- cross-section(s)
CVD	- Chemical Vapour Deposition
Cz	- Czochralski
Eq	- Equation
EDX	- Energy Dispersive X-ray
Fig(s)	- Figure(s)
Fz	- Float zone
HF	- HydroFlouric acid
HREM	- High Resolution Electron Microscopy
hr(s)	- hour(s)
IC	- Integrated Circuit(s)
MFD	- Multiple Faulted Defect(s)
N_2	- Nitrogen
p.v.	- plan-view(s)
RBS	- Rutherford Backscattering Spectroscopy
ref(s)	- reference(s)
RTA	- Rapid Thermal Anneal(s)
SADP	- Selected Area Diffraction Pattern
SF	- Stacking Fault(s)
SFP	- Stacking Fault Pyramid(s)
SFT	- Stacking Fault Tetrahedra
Si	- Silicon
SIA	- Sequential Implant and Anneal
SIMOX	- Separation by the IMplantation of OXygen
SIMS	- Secondary Ion Mass Spectroscopy
SiO_2	- silicon dioxide
SOI	- Silicon-On-Insulator
TEM	- Transmission Electron Microscopy
TRIM	- TRansport of Ions in Matter
VLSI	- Very Large Scale Integration

Contents

Chapter 1
Introduction

1.1 Introduction

With the increasing use of digital electronics for information processing there is a large interest in improving the performance of integrated circuits (IC), e.g. microprocessors and memories. A key approach to improving circuit performance for digital electronics is very large scale integration (VLSI). This is because a reduction in the dimensions of devices and signal lines leads to greater packing densities, faster device switching speeds, reductions in signal transit times and lower power consumption. Of the present device fabrication technologies, complementary metal oxide semiconductor (CMOS) technology is best able to fabricate circuits with both a high packing density and a low power consumption. This makes CMOS technology very important for VLSI. Improvements can be made to CMOS VLSI circuits if the devices are fabricated in a layer of silicon (Si) thinner than the thickness of a bulk Si wafer. For such device fabrication the Si layer requires mechanical strength and hence needs to be supported by an electrically insulated substrate, referred to as a silicon-on-insulator (SOI) wafer/substrate. SOI substrates also have potential advantages for other device technologies, such as bipolar[1], BiCMOS[2] high voltage MOS[3] and 3-D integration[4] but it is the suitability for CMOS VLSI that is the major driving force for the interest in SOI substrates[5].

There are four major advantages of SOI substrates over bulk wafers for fabricating CMOS VLSI circuits:

1) The key device structure in CMOS circuits is an inverter, comprising a "n" channel and a "p" channel MOS transistor (fig. 1.1a). A major problem with CMOS circuits fabricated on bulk wafers is the vulnerability of the inverter to a condition known as latch-up. Unwanted parasitic bipolar transistors are inherent in a CMOS inverter on bulk Si wafers (fig. 1.1a) and under certain conditions, such as input voltage transients or exposure to ionising radiation, they can be biased on. These parasitic bipolar transistors are both n-p-n and p-n-p types and occur in such a way that the collectors of one type feeds the base of the other type (fig. 1.1a & 1.1b).

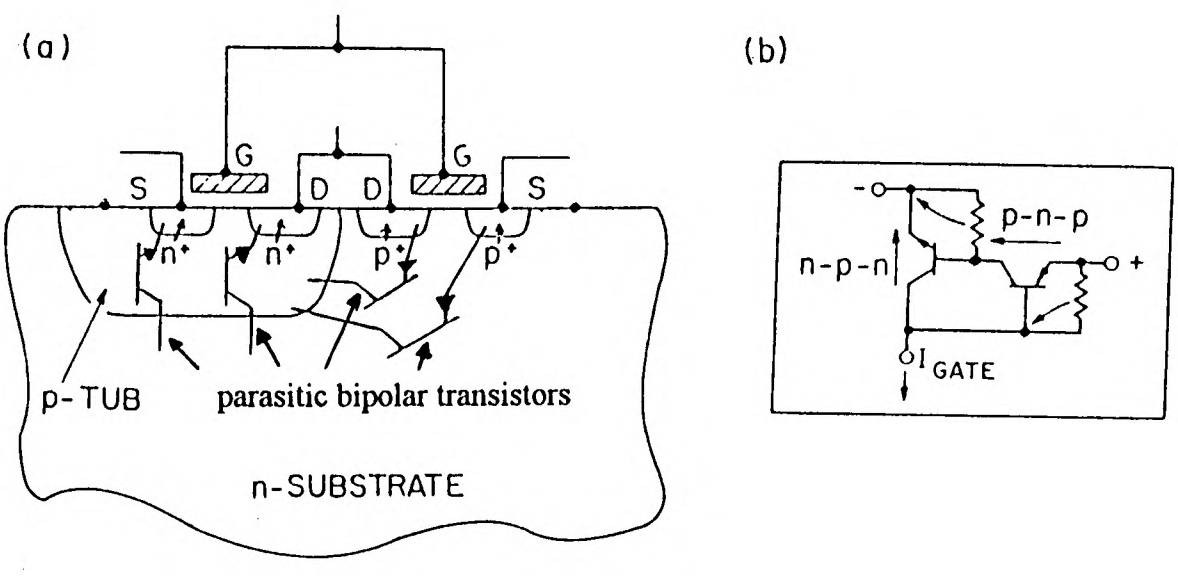

Figure 1.1 a) cross-section of a CMOS inverter in a bulk silicon wafer showing where parasitic bipolar transistors occur (S = source, D = drain, G = gate, modified from ref. 6) b) equivalent circuit diagram of the parasitic bipolars showing that when in a "latch-up" state they form a silicon controlled rectifier allowing large currents to flow.

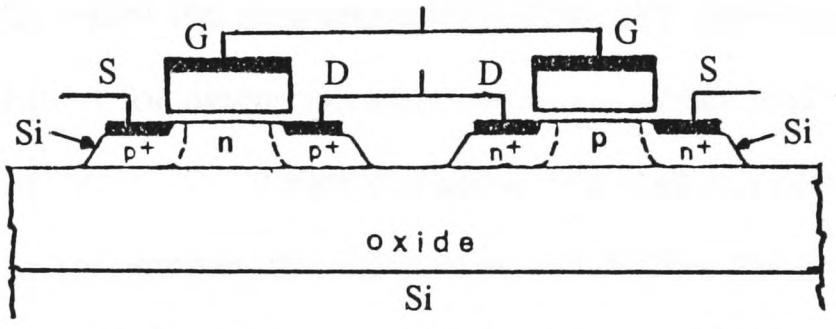

Figure 1.2 Cross-section of a CMOS inverter fabricated on a SIMOX substrate. The presence of the buried oxide layer enables the two transistors of the inverter to be fabricated in isolated Si eliminating the parasitic bipolars and preventing latch-up (S = source, D = drain, G = gate).

	BULK	THICK SOI E>0,3um	THIN SOI 0,1um<E<0,3um	ULTRA THIN SOI E<0,1um
DEVICES :				
SHORT CHANNEL EFFECTS	-	- =BULK	++	++
SUBTHRESHOLD SLOPE	+	+	++	++
FLOATING BODY EFFECTS	++	-	+	++
BREAKDOWN VOLTAGE	++	-	+	++
RADIATION HARDENING	-	- TRANSIENT DOSE	+	- CUMULATIVE DOSE
COMPLEX CIRCUIT :				HIGH SPEED CASE
PACKING DENSITY	+	+	++	++
PARASITIC ELEMENTS	-	+	++	++
PROCESS FACILITY	-	+	++	+
LATERAL ISOLATION	-	+	++	++
JUNCTION METALLISATION	-	+	++	?
MATERIAL	++	-	+	-
++ VERY GOOD + GOOD - LESS GOOD				

Table 1.1 Comparison of the influence of silicon surface layer thickness (E in this table) in SOI substrates with bulk wafers for device and circuit performance (taken from ref. 5).

This forms a positive feedback arrangement (fig 1.1b), effectively a Si controlled rectifier, so once the bipolars are biased on, a large sustained current will flow (latch-up). This current can be sufficiently large to corrupt a logic operation (a soft error) or destroy a device. The problem of latch-up can be overcome if CMOS circuits are fabricated using an SOI substrate. This is because the buried insulator enables the two transistors of a CMOS inverter to be fabricated in isolated Si (fig. 1.2) which eliminates the parasitic bipolar transistors and latch-up can not occur.

2) SOI substrates also enable VLSI circuits to be fabricated with a higher packing density, leading to an increase in the signal processing speed and a decrease in the fabrication cost per IC. For CMOS circuits the increase in packing density arises because the buried insulator means that there is no need for either the area-consuming deep field oxides and biased p-n junctions (channel stop regions) used for device isolation, or the substrate and well contacts used with bulk Si wafers. The absence of the isolation regions and contacts means the circuits are also easier to fabricate, and the simpler the fabrication the higher the yields and the lower the fabrication cost.

3) The buried insulator in a SOI substrate also reduces many of the parasitic capacitances associated with devices and interconnects, e.g. source and drain p-n junction capacitances and interconnect-substrate capacitances. The reduction in source and drain junction capacitances arises because junctions can be fabricated with a reduced area. Reducing these parasitic capacitances leads to higher operating speeds and to lower dynamic power consumption.

4) Circuits fabricated on SOI substrates are less sensitive to ionising radiation. In bulk wafers ionising radiation can generate enough electron-hole pairs to change the logic state of a gate (soft error) or to cause latch-up. The SOI structure prevents latch-up, as discussed previously, and reduces the probability of soft errors because the volume of Si acting as a potential source of electron-hole pairs is reduced by the presence of the insulating layer.

Standard SOI substrates have a surface Si layer thickness between 250nm and 500nm depending on the fabrication technology[1,7-15]. If the surface Si layer has a thickness of 100nm or less it has been shown that devices operate with the Si layer in a fully depleted mode[5,16-20]. This

leads to an increase in device speed, an increase in transconductance, an improvement in the subthreshold slope, a higher drain current saturation voltage and a reduction in hot carrier degradation, compared to devices fabricated in standard SOI substrates and the elimination of the kink in the I-V curves that is characteristic of devices fabricated in standard SOI substrates[5,16,17,18,19,20]. Hence SOI substrates with thin ($\leq$100nm) surface Si layers have potential advantages for device performance, especially for sub-micron CMOS devices, over standard SOI substrates. A comparison of device and circuit performance in bulk wafers and SOI substrates with different thicknesses of surface Si layer is summarised in Table 1.1[5]. It should be pointed out that if the optimum thickness for the surface Si layer for device performance is say 100nm then because some of the surface Si is lost during device fabrication, e.g. during the formation of the gate oxide, the optimum thickness of the surface Si prior to device fabrication is greater than 100nm by typically a few tens of nanometers, exactly how much larger depends on the device design and fabrication procedure used.

Devices fabricated in such a thin surface Si layer SOI substrate described above have one disadvantage. As the transistor drain current is modulated by the back-Si/SiO_2-interface states, fully depleted transistors are not suitable for total dose radiation-hardness[18]. For transistors fabricated in "standard" SOI substrates the surface Si layer under the gate of the transistors is only partially depleted and this is not a problem. In device applications where total radiation hardness is important, i.e. telecommunication satellites in space, the minimisation of circuit self-heating is also important. The effects of circuit self-heating can be reduced if the structure of the insulator is modified to improve the thermal conductivity[21]. If the insulator is a buried silicon dioxide (SiO_2) layer within a Si substrate the thermal conductivity can be improved by reducing the thickness of the buried SiO_2 layer. Hence SOI substrates with thin ($<$300nm) buried SiO_2 layers, below standard thickness Si layers (250nm to 500nm) have potential advantages over standard SOI substrates for device performance in applications where the combination of radiation hardness and the minimisation of circuit self-heating are important. The two types of SOI substrates described in this and the previous paragraph are collectively referred to as "thin-film" SOI substrates.

1.2 SOI Technologies

There are currently five different groups of technologies for fabricating SOI substrates; a) ion implantation based methods such as Separation by IMplantation of OXygen (SIMOX)[9] or Separation by IMplantation of NItrogen (SIMNI)[10], b) wafer bonding[11], c) oxidation based methods such as Dielectric Isolation (DI)[12] and Full Isolation by Porous Silicon (FIPOS)[13], d) crystallisation methods such as Zone Melt Recrystallisation (ZMR)[14] and e) solid state epitaxy[15] and epitaxy based methods such as Epitaxial Lateral Overgrowth (ELO)[8], Silicon-On-Diamond (SOD)[22], silicon-on-spinel ($MgAl_2O_4$)[23] or Silicon-On-Sapphire (SOS)[7].

As SIMOX is based on ion implantation, uses SiO_2 for the insulator and is fully compatible with bulk Si wafer processing, these give it potential advantages over the other SOI technologies. Ion implantation potentially enables good uniformity, controllability and reproducibility, and because it is carried out in a vacuum, it is a dry and relatively clean process. Using SiO_2 for the insulator has the advantages of an already existing large volume of knowledge based on thermally deposited SiO_2 and it does not introduce into the processing an element which may produce contamination. Further it also has a lower interface charge state density than silicon nitride and a greater mechanical stability when both are formed by ion implantation. A consequence of these advantages is that increasingly the majority of SOI research is concerned with SIMOX substrates (fig. 1.3) and as a result SIMOX is currently the most mature SOI technology[24]. For the advantages discussed previously there is considerable interest in fabricating thin-film SOI substrates, especially for fully depleted, sub-micron CMOS devices. Due to the potential uniformity, controllability and reproducibility, SIMOX is expected to be the only technology capable of fabricating thin-film SOI substrates with the required materials specification[24,25]. More information on the state of development of the different SOI technologies is given in refs. [24,26-29].

1.3 The SIMOX process

The SIMOX process consists of implanting a high dose (10^{17}-$10^{18}O/cm^2$) of oxygen at a high energy large enough (usually 150-200keV) to synthesise a buried layer of SiO_2 beneath a

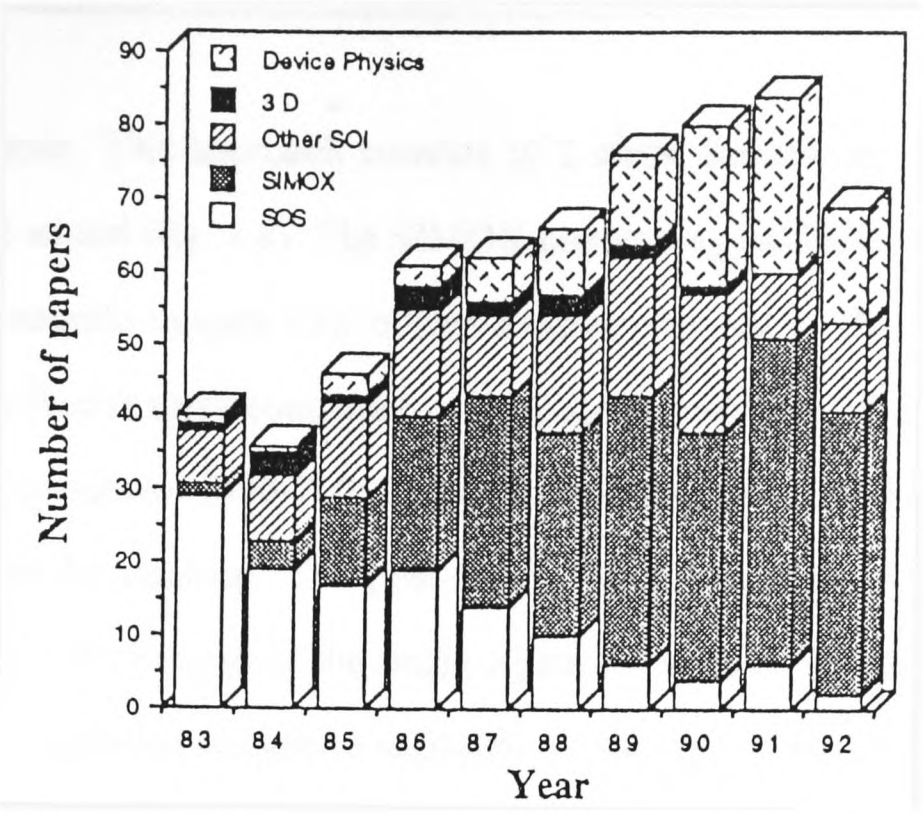

Figure 1.3 Papers presented at the SOS/SOI Technology Workshop/International Conferences 1983-92 showing the SOI topics of the papers and the increasing research interest in SIMOX[28].

	1990	Future
Layer Thickness		
Silicon Film Uniformity (Å)	<±100	<±25
Buried Oxide Thickness (μ)	0.3-0.5	0.05-0.5
Buried Oxide Uniformity (6mm edge exclusion)	±3%	±1%
Buried Oxide Reproducibility	±5%	±1%
Defect Uniformity Average (cm^{-2})	10^5-10^4	10^3-10^2
Particulates		
Added As Implanted (cm^{-2}) (particle size, 6mm edge exclusion)	<0.75(>1μ)	<0.016
Added After Anneal(cm^{-2}) (particle size)	<0.016 (>0.35μ)	<0.016 (>0.1μ)
Contamination		
Metallic Contamination (SPV diffusion length) • As Implanted (μ)	≥150	≥275
•After Anneal (μ)	≥60	≥275
Carbon Contamination (cm^{-3})	<$2x10^{18}$	<$5x10^{17}$

Table 1.2 Comparison, in terms of the materials specifications, of the capabilities in 1990 for fabricating "standard" SIMOX substrates (for implants using the Eaton Nova NV200 dedicated oxygen implanter, energy 200keV, implant temperature 600°C, doses >$1.4x10^{18}O/cm^2$, anneal 1300°C for 6hrs) and future needs in terms of the specifications for thin-film SIMOX substrates (table taken from ref. 25).

thin surface Si layer. This approach consists of 2 steps, implanting the oxygen followed by a high temperature anneal (fig. 1.4). The SIMOX process is possible because most of the damage caused by the energetic oxygen ions occurs towards the end of the range, i.e. the amount of damage at the surface is small compared to the damage near the end of range. Consequently by implanting at temperatures (500-700°C) above room temperature the single crystal nature of the surface Si can be retained. The post-implant high temperature (1150-1300°C) anneal is important to reduce the damage in the single crystal Si (surface Si layer) above the buried oxide and to enable the implanted oxygen to segregate to the peak of the oxygen distribution, forming a buried SiO_2 layer and reducing the oxygen content in the surface Si layer. To protect the wafer surface during annealing the wafers are usually capped with SiO_2. The requirement that the peak of the implanted oxygen distribution needs to be sufficiently below the wafer surface for the surface to be free from oxide precipitates after annealing initially led to the use of implantation energies of 150-200keV. This in turn led to the generally accepted specification of energy (150-200keV) and dose ($1.4\text{-}2\text{x}10^{18}O/cm^2$) followed by an anneal at 1150°C for 2hrs, for the formation of "standard" SIMOX substrates (surface Si layer 250-300nm and buried SiO_2 layer 300-400nm, fig. 1.5a). After the annealing an epitaxial Si layer had to be grown on top of the wafer surface in order to fabricate devices. With the use of very high temperature anneals (e.g. 1300°C for 6hrs) it became possible to fabricate "standard" SIMOX substrates in which oxide precipitates were eliminated from the surface Si layer and the growth of the epitaxial layer for device fabrication became unnecessary.

The disadvantages of "standard" SIMOX are the long implantation times, which increases the cost per substrate, and the high cost of the implanter. To date a dedicated high current oxygen implanter (100 mA) has been developed and sold commercially (Eaton Nova NV200)[30,31]. This machine can simultaneously implant up to 25 Si wafers each of 3 inch diameter (fewer at larger diameters) reducing the cost per SIMOX substrate and at the same time increasing the supply. Six of these machines are now operating in different locations around the world. A second generation (beam current 200mA) commercial dedicated oxygen implanter has also been designed and is in the process of development[32]. Both these machines are currently designed to implant O^+ at energies of 125-200keV.

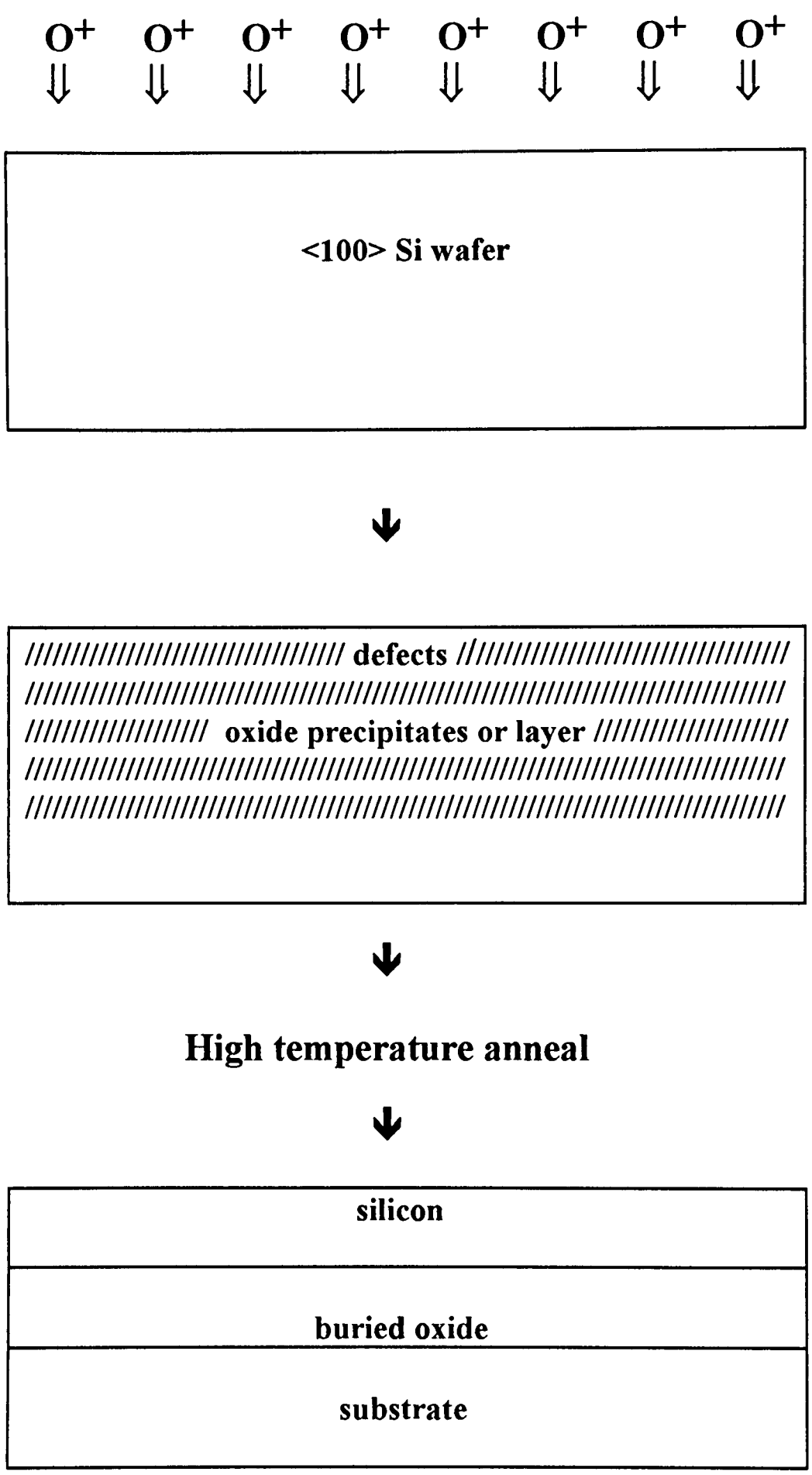

Figure 1.4 Schematic diagram of the fabrication of a SIMOX substrate.

a) Standard SIMOX

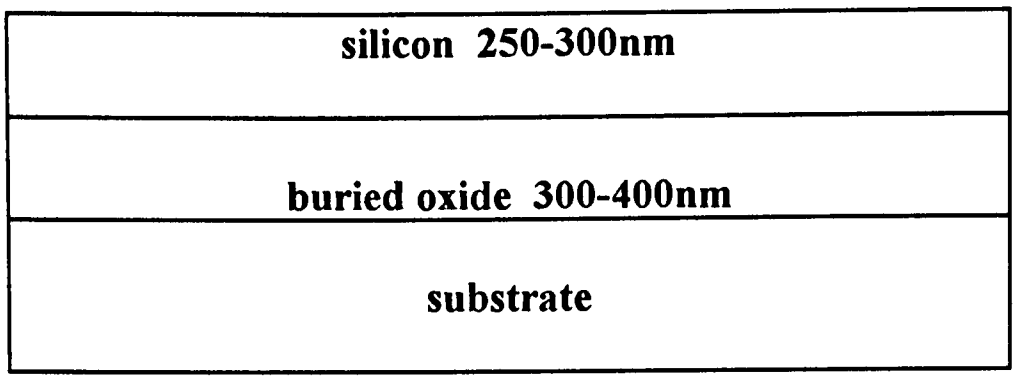

b) Thin-film SIMOX - thin silicon and buried oxide layers

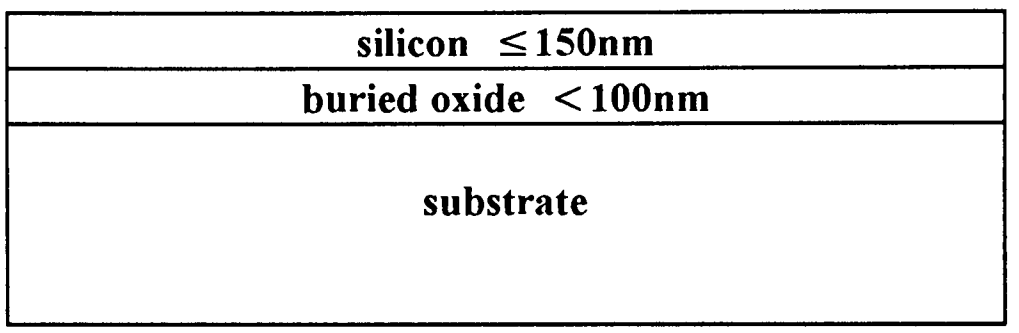

c) Thin-film SIMOX - thin buried oxide layer in standard SIMOX

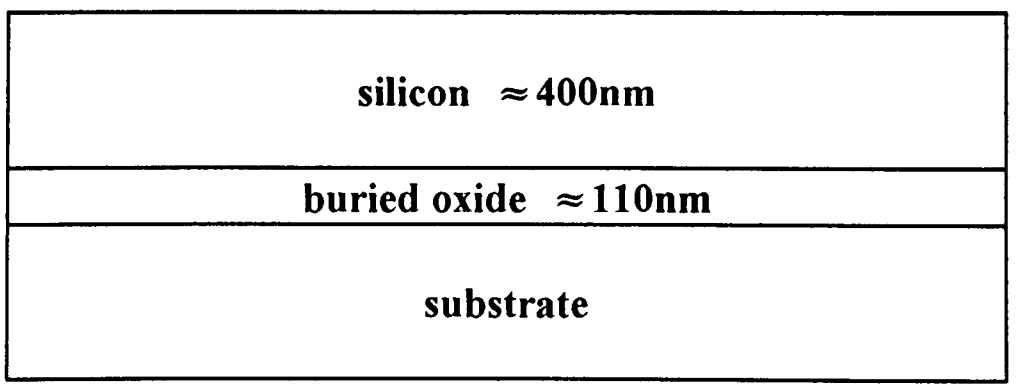

Figure 1.5 Schematic diagrams comparing a) a "standard" SIMOX substrate, b) a thin-film SIMOX substrate consisting of a thin Si surface layer above a thin buried oxide layer, suitable for fully-depleted CMOS VLSI, and c) a thin-film SIMOX substrate consisting of a thin buried oxide layer below a standard thickness surface Si layer, suitable for reducing circuit self-heating in radiation environments.

With the use of high temperature anneals (e.g. 1300°C for 6hrs) to eliminate the oxide precipitates from the surface Si layer the fabrication of SIMOX substrates with thinner (<250nm) surface Si layers became a possibility. Thin-film SIMOX substrates consisting of a thin ($\leq$150nm) surface Si layer can be fabricated by two methods; implanting a standard high dose (1.4-2x10^{18}O/cm^2) at a high energy (150-200keV) to form a "standard" SIMOX substrate (fig. 1.5a) and then sacrificially oxidising the surface to reduce the thickness of the surface Si layer, or by implanting a lower dose (typically 10^{17}O/cm^2) at a lower energy (<100keV) and directly synthesising a buried SiO_2 layer closer to the wafer surface (fig.1.5b).

The high-energy, high-dose, sacrificial oxidation approach is of interest because it is derived from the fabrication of "standard" SIMOX substrates, and is therefore based on an accumulation of SIMOX knowledge, and sacrificial oxidation is considered a well known technique[122]. Further because of the development of the dedicated Eaton Nova NV200 oxygen implanters, which are not designed to operate at energies <125keV, the majority of the supply of SIMOX wafers can only be produced, at the present, using high energy implants. The materials specifications that are required for thin-film SIMOX substrates are more stringent for devices than those met by producing "standard" SIMOX substrates using the Eaton Nova NV200 implanter and high temperature annealing (table 1.2). Hence to meet these material specifications for thin-film SIMOX substrates by this approach either the fabrication of the SIMOX substrate prior to sacrificial oxidation has to be improved or alternative means of fabricating thin-film SIMOX substrates are required.

To date the direct synthesis of a buried SiO_2 layer by implanting a lower dose (typically 10^{17}O/cm^2) at a lower energy (50-90keV) has not received as much attention as the high-energy, high-dose, sacrificial oxidation approach. The main advantage of directly synthesising a buried SiO_2 layer at a lower energy (50-90keV) over the high-energy, high-dose, sacrificial oxidation approach is that a thin ($\leq$150nm) Si layer can potentially be formed by implanting a lower dose and hence reducing the implantation time and the fabrication cost. The possibility of forming a SIMOX substrate with a lower dose is due to the reduction in the straggle of the implanted oxygen ions with decreasing energy. This technique also involves one less processing step which reduces the processing complexity and further reduces the cost. Further, implanting

at lower energies may be a way to achieve the more stringent materials specifications required for thin Si layer SIMOX substrates (table 1.2). For applications where it is required this technique can also potentially fabricate thin Si layer SIMOX substrates with buried oxides as thick as the previous approach, and therefore enabling circuits to benefit from the reduction in parasitic capacitances between the circuit components and the substrate due to the thick buried SiO_2, but again this approach uses one fewer processing step and hence reduces the cost .

Thin-film SIMOX substrates consisting of a thin ($\approx$110nm) buried SiO_2 layer (fig. 1.5c), i.e. SIMOX substrates with improved thermal conductivity over "standard" SIMOX substrates (fig. 1.5a) for radiation hard environments, can be fabricated by implanting a dose lower than the standard dose (1.4-2x10^{18}O/cm^2) at a high energy (150-200keV). As described in the previous paragraph implanting a lower dose reduces the implantation time and hence the fabrication cost of this type of thin-film SIMOX substrate compared to "standard" SIMOX substrates.

1.4 Development of SIMOX

1.4.1 Historical perspective

The idea that the surface of an element could be converted to its oxide by implantation was first suggested by Smith[33] in 1956, although the first implantations of oxygen into Si were not reported until 1966 by Watanabe and Tooi[34], and 1967 by Pavlov and Shitova[35]. In the period 1967-1977 several authors[36-39] reported using low energy implants to produce surface layers of SiO_2 and Brack and Schwutte[40] reported work on high energy (1 MeV) oxygen implants, but at doses lower than required to form a buried SiO_2 layer. The first buried SiO_2 layer was reported by Badawi and Anand[41] in 1977. The implanted doses were not given (they quoted estimated peak oxygen concentrations instead) but they used an energy of 80keV and annealed at 900°C for 1hr. They were also the first to suggest that buried SiO_2 layers could be used for dielectric isolation on ICs, but did not demonstrate it themselves. The first demonstration was carried out by Izumi *et al*[42] in 1978. They implanted a dose of 1.2x10^{18}O/cm^2 at an energy of 150keV and annealed at 1150°C for 2 hours. They considered

that the resulting surface Si would not support device action directly and so grew a thin Si epilayer after annealing and then fabricated a 19 stage CMOS ring oscillator. This operated at twice the speed of the same circuit fabricated on a bulk Si wafer. They also coined the acronym SIMOX (Separation by the IMplantation of OXygen). This report initiated considerable interest in SIMOX because it demonstrated its potential for high-performance VLSI circuits. In 1981 Ohwada *et al*[43] reported the first devices on SIMOX with 1μm channel lengths. In 1987/8 J C Sturm[16] and J P Colinge[17] reported that very thin Si films ($\leq$150nm) further substantially improved device performance. These two reports initiated considerable interest in the fabrication of thin-film ($\leq$150nm) SIMOX substrates because it was then and is still presently regarded[24] as the only SOI technology with the potential capability to fabricate thin-film SOI substrates suitable for fully depleted devices.

1.4.2 Evolution of implantation conditions used in this work

In order to form a buried SiO_2 layer the oxygen ions are implanted with an energy large enough that the peak of the gaussian profile is well below the wafer surface. In the early work surface SiO_2 layers were reported for low energy ($\leq$60keV) implants due to the combination of the low implant energy, and the low implant and low anneal temperatures (300°C[34] to 550°C[38,39] and 550°C to <800°C[38,39] respectively). Although the first buried SiO_2 layer reported by Badawi and Anand[41] was successfully formed using an energy of 80keV, Izumi *et al*[42] considered, because of the increase in the mean projected range with energy, that an energy of 150keV would be more effective for forming a buried SiO_2 layer. When a CMOS ring oscillator was successfully fabricated in a chemical vapour deposited (CVD) Si epitaxial layer grown on a SIMOX substrate formed using an energy of 150keV and annealed at 1150°C for 2hrs[42], subsequent transmission electron microscopy (TEM) showed at the wafer surface only a thin region of Si free from oxide precipitates (e.g. ref 44). Conversely, 150keV/O became regarded as the minimum energy to form a SIMOX substrate suitable for the growth of an epitaxial Si layer. This led to the commercial development of Eaton Nova NV200 high current (100mA) dedicated oxygen ion implanter for implanting at energies in the range 150-200keV[30,31]. With the use of high temperature and longer anneals (see following section) the oxide precipitates

within the surface Si layer are eliminated and thus the formation of a device quality surface Si layer without the epitaxial Si layer becomes a possibility. Such "standard" SIMOX substrates with thick buried oxide layers (fig. 1.5a) have been studied by many research groups[45-50], but standard SIMOX substrates with thin buried SiO_2 layers (fig. 1.5c) have not been studied in detail. A detailed investigation of the microstructure formed at 200keV with doses suitable for forming a thin buried oxide layer and a thick surface Si layer (fig. 1.5c) and the associated process optimisation is the basis of some of the work in this thesis. The elimination of the oxide precipitates from the surface Si layer after annealing also makes it possible to form SIMOX substrates at lower than the standard "high" energies. The synthesis after annealing of a SIMOX substrate at energies <100keV has been demonstrated[51,52] but not studied in detail. A detailed investigation of the microstructure formed at these lower energies (fig. 1.5b) and the optimisation of the process parameters is the basis of the majority of the work in this thesis.

For doses less than that required to form SiO_2 at the peak of the as-implanted oxygen distribution (<$1.2x10^{18}O/cm^2$ at 200keV), the oxygen depth profile follows a skewed gaussian shape[53,54,55]. Gill and Wilson[55] and Hayashi *et al*[56] reported that for doses greater than that required to form SiO_2 at the peak of the oxygen distribution, the resulting oxygen follows a flat topped gaussian distribution[53,54,55] with the maximum oxygen concentration equal to that in SiO_2 ($4.48x10^{22}/cm^3$). Prior to this work, the evolution of the as-implanted and annealed microstructure as a function of dose for high energy (150-200keV) implants and doses lower than standard doses (<$1.4x10^{18}O/cm^2$) has been reported, but not in detail, by the author of this thesis using different implantation and anneal conditions[49,57]. A detailed study using new implantation and anneal conditions is the subject of part of the work in this thesis. The evolution of the as-implanted and annealed microstructure as a function of dose for low energy (<100keV) implants has not been previously reported and detailed study of this forms the subject of part of this thesis.

Morehead *et al*[58] first reported that the surface of an implanted Si wafer would remain crystalline if the substrate temperature was allowed to rise during implantation. For the fabrication of SIMOX this is vital in order to retain the single crystal nature of the surface Si. For implantation temperatures between 350°C and 500°C (dose $1.8x10^{18}O/cm^2$, energy

200keV) Tuppen *et al*[44] reported the surface Si layer consists of a surface region of highly damaged single crystal Si and an amorphous Si layer next to the buried SiO_2. Further they reported that in order to retain the single crystal nature of all the surface Si layer an implant temperature >500°C has to be used[44]. Subsequently the effect of the implantation temperature on the microstructure has been studied by several authors[49,59,60,61]. Hemment *et al*[62] and Hatzopoulos *et al*[59] have reported that over the temperature range 200°C to 700°C (energy 200keV, doses $2.4x10^{18}O/cm^2$ and $2.5x10^{17}O/cm^2$, respectively,) the as-implanted oxygen distribution is independent of the implant temperature. In all these reports the heating of the wafers was achieved by thermally isolating the wafers and allowing the beam to raise the wafer temperature. It should be noted that in many reports the details of how the temperature was varied or the values of instantaneous and time-averaged beam current densities used are often not given.

In order to preheat the wafer and increase the implantation temperature the use of external heating during implantation was used by Wilson *et al*[63], Holland *et al*[64] and Bruel *et al*[65] in 1984/5. These reports suggested that the structures implanted using external heating were superior to those implanted using beam heating only. This was considered to be because of the ability to preheat the wafer prior to implantation[64] and to further increase the implant temperature to $\geq 600°C$[65]. These external heaters all relied on the implanted wafer being in thermal contact with the heater which meant the wafers were prone to contamination. To avoid this problem Maillet *et al*[66] used a tungsten-halogen lamp to heat the wafers during implantation. This group also reported that while using external heating the as-implanted oxygen distribution was independent of the implant temperature (dose $1.4x10^{18}O/cm^2$, energy 150keV). Halogen lamps are now used by the majority of research groups to provide external heating during implantation[67,68,69] and a halogen lamp heater[70] was used during implantation for the work in this thesis.

1.4.3 Evolution of anneal conditions used in this work

Badawi and Anand[41] formed the first buried SiO_2 layer by annealing at 900°C for 1 hour. In 1981 Lam *et al*[71] showed for temperatures up to 1150°C (anneal time 2hrs) the

crystalline quality of the surface Si layer improved with increasing temperature. In the same year Izumi *et al*[42] used an anneal temperature of 1150°C to form the SIMOX structure in which they first demonstrated the benefits of SIMOX substrates for circuits. In the following years the influence of high temperature anneals and anneal time were investigated by many authors[47,48,57,60,72,73,74]. These reports showed that annealing at temperatures $\leq$1250°C for two hours resulted in a surface Si layer divided into two regions. At the wafer surface was a thin region of Si that was free from oxide precipitates. This was acceptable as a seed for the growth of a CVD epitaxial Si layer for subsequent device fabrication. Below this was a broad defective region containing a high density of oxide precipitates. Annealing at 1250°C for 24 hours[73], 1300°C for 6 hours[74] or 1405°C for 30 minutes[57,72] eliminated all the SiO_2 precipitates and resulted in almost atomically abrupt interfaces between the Si and the buried SiO_2 layer. As mentioned previously the elimination of the oxide precipitates made the growing of an epitaxial Si layer unnecessary for device fabrication[75] and made possible the idea of directly synthesising a SIMOX substrate by implanting at a lower (<100keV) energy. The 1300°C anneals were made possible by replacing silica tubes in conventional furnaces with either polysilicon or silicon carbide tubes[48,73,74,75] and the 1405°C anneals by using radiant heating in a cold wall chamber[57,72]. No difference in the microstructure after the 6 hour anneal at 1300°C and the 30 minute anneal at 1405°C was reported, and as conventional furnaces capable of annealing at temperatures $\geq$1300°C were available, a 6 hour anneal at $\geq$1300°C was chosen as the standard anneal for the work in this thesis.

1.4.4 Previous structural investigations

In this section previous structural investigations in the literature and the experimental parameters used are described. The experimental parameters used in these structural investigations are listed. Where experimental parameters are not given, i.e. where it is not indicated whether the atomic (O^+) or the molecular (O_2^+) ion was implanted or whether the beam current or time-averaged beam current density used are not quoted, it is because the parameter was not reported. The convention in the literature on SIMOX for quoting energy and

dose, for both atomic and molecular implanted oxygen ions, is to quote the energy per oxygen atom and the dose in terms of the number of oxygen atoms per square cm.

Badawi and Anand[41] after implanting doses of $\approx 10^{17}O/cm^2$, O_2^+, at an energy of 80keV, beam currents of 1-15μA and annealing at 900°C for 1 hour, used ellipsometry and infra-red spectroscopy to confirm the presence of the oxide. Izumi *et al*[42], after implanting a dose of $1.2x10^{18}O/cm^2$, O^+, at an energy of 150keV, beam current density of 24$\mu A/cm^2$ and annealing at 1150°C for 2 hours, used sputter Auger electron spectroscopy to directly prove that a buried layer was formed. In 1980-2 Hayashi *et al*[56,76,77,78] using the same implant and anneal conditions as Izumi *et al*[42], reported the first detailed post-anneal analysis of the buried oxide layer, using sputter Auger electron spectroscopy, and of the surface Si and epitaxial layer, using p.v. TEM. They reported the presence of dislocations in the epitaxial Si layer and a high density of oxide precipitates below a thin precipitate denuded zone in the surface Si layer prior to growth of the epitaxial layer. They also reported that during implantation the oxygen concentration in the buried oxide layer does not exceed that of stochiometric SiO_2, the thickness of the as-implanted and annealed buried SiO_2 layers depended on dose and after annealing abrupt buried SiO_2/Si interfaces are possible.

Pinizotto *et al*[79] in 1982, first described the rapid diffusion of oxygen in SiO_2 as the mechanism for the formation of abrupt Si/SiO_2 interfaces. Kilner *et al*[53] demonstrated that SIMS analysis could be used to analyse SIMOX structures and showed that for a dose of $1.8x10^{18}O/cm^2$, O_2^+, implanted at 200keV/O between temperatures of 325-600°C, the post-anneal (1150°C, 2hrs) oxygen distribution depended on the implantation temperature. By implanting $^{18}O^+$ at 200keV into buried SiO_2 layers formed by implanting $^{16}O_2^+$ at a dose $1.2x10^{18}O/cm^2$ at 200keV/O and an implant temperature between 400 and 600°C, Kilner *et al*[80] confirmed the model of rapidly diffusing oxygen to the edges of the buried SiO_2 layer as proposed by Pinizotto *et al*[79]. Kilner *et al*[80] also showed that once a buried SiO_2 layer formed during implantation any subsequent oxidation took place at the upper SiO_2/Si interface. Using the same oxygen implantation conditions this was further confirmed by Reeson[81] and Hemment *et al*[82] using a buried silicon nitride marker layer below the buried oxide.

Fathy *et al*[83] in 1983 implanted a dose of $2.0x10^{18}O/cm^2$, O_2^+, implanted at 200keV/O at two dose rates of $18\mu A/cm^2$ and $25\mu A/cm^2$ and using c.s TEM and high resolution electron microscopy (HREM) to analyse, for the first time, the as-implanted microstructure. They showed that the microstructure of the buried oxide layer depended on the dose rate/implant temperature. Fathy *et al*[83] did not investigate the morphology of the oxide precipitates or the defects in the surface Si layer.

Holland *et al*[64] in 1984 after implanting doses of $1.9\text{-}2.1x10^{18}O/cm^2$, O^+, at 180keV with a beam current density of $37\mu A/cm^2$, Wilson *et al*[63] in 1984 using the same implantation conditions as Holland *et al*, and Bruel *et al*[65] in 1985 after implanting a dose of $1.7x10^{18}O/cm^2$, O^+, at 200keV with a beam current density of $50\mu A/cm^2$ and an implant temperature of 600°C reported, used RBS and showed that the crystallinity of the surface Si layer after implantation is improved by external heating of the wafer during implantation. This was attributed to greater thermal annealing during implantation. Using heated implants and analysising the as-implanted microstructure by TEM, Holland *et al*[84] using the same implantation conditions as above, and T P Sjoreen *et al*[85] using the same implantation conditions as Holland *et al*[84], reported linear arrays of spherical oxide precipitates. Stoemenos *et al*[74] after implanting a dose of $1.9x10^{18}O/cm^2$ at 200keV and 650°C reported an array of spherical "micro-precipitates" with a short range periodicity of 5nm. These reports were the first to show high magnification TEM micrographs of individual oxide precipitates in the surface Si layer, although the precipitates were not studied in any detail or reasons proposed for their presence in arrays. Prior to these reports the emphasis of the structural research had been on the annealed microstructure and any as-implanted micrographs reported were at magnifications too low to identify the individual precipitates. At the same time as these reports of ordered arrays Jaussaud *et al*[86], after implanting a dose of $3x10^{18}O/cm^2$ at 200keV and 500°C, reported a random speckle contrast in the surface Si layer which they attributed to oxide precipitates.

In 1986/7 Van Ommen *et al*[87,88], after implanting a dose of $2.5x10^{18}O/cm^2$, O_2^+, at 300keV/O with a beam current density of $1.5\mu A/cm^2$ and an implant temperature of 550°C, also using external heating during implantation, reported a detailed TEM study of spherical oxide precipitates, diameters 2nm and distance apart 5nm, present in a cubic array in the surface

Si layer after implantation. Using Raman measurements[88] they reported lower stress in the surface Si layer of a sample containing the ordered precipitates compared to a sample in which the precipitates were randomly distributed. The ordering was only observed when the oxygen beam current was uniform during the implantation. Minimisation of the long range elastic strain was proposed as the mechanism for the ordering. In all these reports the ordered precipitates were present below a narrow precipitate denuded zone and Van Ommen[88] suggested that the width of this denuded zone was determined by the out-diffusion of oxygen during the implantation.

Stoemenos *et al*[89] after implanting a dose of $1.9x10^{18}O/cm^2$ at 200keV and 650°C reported a detailed TEM investigation of ordered precipitates. They proposed that because a large number of Si_i are created during implantation the migration of the Si_i is determined by the low migration energy (0.3eV) rather than the formation energy (5eV). Hence the Si_i could diffuse rapidly towards the surface which acts as a sink. They suggested that because at the implantation temperature (700°C) the diffusion of Si_i in SiO_2 is negligible ($D=10^{-29}cm^2/s$) the ordering of the precipitates results because such a distribution could accommodate the flux of interstitials towards the surface.

In the reports of Holland *et al*[84], Van Ommen *et al*[87,88] and Stoemenos *et al*[89] they all reported that with increasing depth the oxide precipitates become larger and randomly distributed. After implanting a dose of $1.0x10^{18}O/cm^2$ at 200keV and 600°C, Stoemenos *et al*[89] reported the presence of [001] columnar oxide precipitates near the Si/SiO_2 interface.

Fathy *et al*[83], after implanting a dose of $2.0x10^{18}O/cm^2$, O_2^+, at 200keV/O and two dose rates of $18\mu A/cm^2$ and $25\mu A/cm^2$, showed micrographs containing rod-like defects in the as-implanted surface Si layer, although they did not comment upon them or investigate their microstructure. Stoemenos *et al*[89], after implanting a dose of $1.8x10^{18}O/cm^2$ at 200keV and 500°C, reported rod-like defects lying on {111} planes in the surface Si layer close to the interface with the buried SiO_2 layer. They suggested that these were Frank type dipoles. More recently in work performed at the same time as the work in this thesis Visitserngtrakul *et al*[67,90,91], after implanting doses in the range $0.3\text{-}1.8x10^{18}O/cm^2$, O^+, at 200keV and 600°C and using a beam current densities of 1 and $10mA/cm^2$, observed similar rod-like defects. They

investigated these defects using HREM and suggested that they were multiply faulted defects (MFD), consisting of several parallel discontinuous stacking faults (SF) within 2-8 {111} lattice planes of each other. Using HREM they identified one MFD as consisting of an intrinsic and extrinsic SF pair. They attributed the presence of the MFD to stresses generated by the volume change at the boundary of precipitates. In all the reports of these defects by these three research groups the defects disappeared after annealing for all temperatures reported ($\geq$1150°C). Rod-like defects have also been reported very recently by Nakashima and Izumi[92] but the microstructure was not investigated.

In 1981 Das *et al*[93], after implanting a dose of 1.4x10^{18}O/cm^2, O_2^+, at 200keV/O and 550°C with a beam current density of 15-17μA/cm^2, annealing at 1100°C for 5 minutes in hydrogen and growing an epitaxial Si layer at 1100°C, published the first c.s. TEM micrographs of SIMOX structures after annealing and the growth of epitaxial Si layers on the surface. They directly revealed the buried oxide, the damage structures at the different depths and identified the source of the dislocations in the epitaxial Si as the damage zone immediately above the buried oxide. Tuppen *et al*[44,94], after implanting doses between 1.4-2.4x10^{18}O/cm^2, O_2^+, at 200keV/O and temperatures between 350-550°C and annealing at 1150°C for 2hrs reported, using both sputter Auger electron spectroscopy and c.s. TEM, a detailed analysis of the effect of implantation temperature on the as-implanted and post-anneal microstructure and oxygen distribution. They showed that for a dose of 1.8x10^{18}O/cm^2, low implant temperatures (350-500°C) resulted in amorphous Si regions next to the buried oxide layer and that after annealing these resulted in a polycrystalline Si region. For higher implant temperatures (500-550°C) the annealed surface Si layer consisted of a narrow precipitate denuded zone at the surface and a wider region containing a high density of oxide precipitates next to the buried oxide layer, confirming the previous reports of Hayashi *et al*[56,76,77,78]. They also demonstrated that the post-anneal oxygen distribution depended strongly on the post-anneal microstructure and hence on the implantation temperature. This explained the earlier observations of variations in the post-anneal oxygen distribution with variation in the implantation temperature by Kilner *et al*[53] and was confirmed again in a later study by Maillet *et al*[66].

Stoemenos *et al*[74], after implanting a dose of $1.5x10^{18}O/cm^2$ at 200keV and 700°C, reported that annealing at 1300°C for 6hrs eliminated the oxide precipitates from the surface Si layer and resulted in very sharp Si/SiO_2 interfaces. This was explained in terms of an Ostwald ripening process in which at the anneal temperature (1300°C) the critical radius for a precipitate to be stable is so large that the only stable precipitates are the buried oxide layer and the anneal cap. A similar mechanism was proposed by Jaussaud *et al*[86] after implanting a dose of $3x10^{18}O/cm^2$ at 200keV and 500°C and annealing at 1210°C for 6hrs, by Jaussaud *et al*[95] after implanting a dose of $1.6x10^{18}O/cm^2$, O^+, at 200keV and 700°C and annealing at 1300°C for 6hrs, by Mao *et al*[48] after implanting a dose of $2.25x10^{18}O/cm^2$, O^+, at 150keV and 500°C and annealing at 1300°C for 2hrs, and by Celler *et al*[72] after implanting a dose of $1.8x10^{18}O/cm^2$, O_2^+, at 200keV/O and 500°C and annealing at 1405°C for 30 minutes. Krause *et al*[60,96], after implanting a dose of $2.4x10^{18}O/cm^2$, O_2^+, at 200keV/O and 550°C and annealing at temperatures in the range 1150-1250°C for 2, 4 or 8 hrs, reported that the size of the oxide precipitates observed in the surface Si layer was determined by the thermodynamics of stable precipitate size rather than the kinetics of oxygen diffusion. They described a qualitative model to explain the removal of the precipitates during annealing involving the growth and dissolution of the precipitates, the out-diffusion of oxygen to the surface and the consuming of precipitates as the buried oxide layer grows towards the surface.

Employing a high temperature anneal (1405°C, 30 minutes) Marsh *et al*[57], and Reeson *et al*[49] in collaboration with the author of this thesis, after implanting doses in the range 0.1-$1.4x10^{18}O/cm^2$, O_2^+, at 200keV/O, an implantation temperature of 550°C and using beam only heating during implantation, were the first to study both the as-implanted and annealed microstructure as a function of dose, for doses smaller than the standard dose of 1.4-$2.0x10^{18}O/cm^2$. Marsh *et al*[57] reported that the minimum dose for forming a continuous buried SiO_2 layer after annealing was $0.6x10^{18}O/cm^2$. More recently, at the same time that the work presented in this thesis was being carried out, Guerra[25] after implanting O^+ at 200keV and at 600°C, using background heating during implantation and annealing at 1300°C for 6hrs reported that the minimum dose for forming a continuous buried SiO_2 layer after annealing was as low as $0.5x10^{18}O/cm^2$. Also at the same time that the work presented in this thesis was being

carried out, Nakashima & Izumi[46] after implanting doses in the range 0.2-2.0x10^{18}O/cm^2, O^+, at 180keV and 550°C using background heating during implantation and annealing at 1300°C for 4hrs reported that the minimum dose for forming a continuous buried SiO_2 layer after annealing was 0.4x10^{18}O/cm^2. Reeson *et al*[49], using the same conditions as described above, reported for doses of 0.75x10^{18}O/cm^2 and 1.4x10^{18}O/cm^2 that Si islands faceted by {111} and {100} planes occurred throughout the buried oxide layer. Steomenos *et al*[97], after implanting a dose of 1.3x10^{18}O/cm^2, O^+, at 200keV and at 600°C using background heating during implantation and annealing at 1300°C for 6hrs, reported similar faceted Si islands throughout the buried oxide layer. Steomenos *et al*[97] suggested that the facets are determined by the different oxidation rates of the different Si planes, the large {100} facets being due to the slower growth rate of the {100} planes.

Stoemenos *et al*[74], after implanting a dose of 1.5x10^{18}O/cm^2 at 200keV, O^+, and 700°C using background heating during implantation, reported that after annealing at 1300°C for 6hrs threading dislocations were present at a density of 10^7/cm^2. This was two orders of magnitude lower than the densities previously reported by other groups implanting doses of 1.8x10^{18}O/cm^2, O_2^+, at 200keV/O and 500°C using beam heating only and annealing at 1150°C for 2hrs[54,93,98]. The lower dislocation density of Stoemenos *et al*[74] was attributed to the combination of using external heating to preheat the wafer prior to implantation and to raise the temperature during implantation to 700°C, and to the high anneal temperature (1300°C). Mogro-Campero *et al*[47], after implanting a dose of 2.0x10^{18}O/cm^2 at 150keV and 600°C, and annealing at temperatures between 1150-1295°C for 6hrs, reported that the threading dislocation density (10^8/cm^2 for their samples) was insensitive to the anneal temperature, while Mao *et al*[48], after implanting a dose of 2.25x10^{18}O/cm^2, O^+, at 150keV and 500°C, and annealing at temperatures between 1150-1300°C for 2hrs, reported that the threading dislocation density decreased with increasing anneal temperature, but did not quote reliable density values. At the same time Krause *et al*[99], after implanting a dose of 2.4x10^{18}O/cm^2, O_2^+, at 200keV/O and temperatures between 300-500°C, annealing at 1150°C for 3hrs and growing an epitaxial Si layer, reported that the threading dislocation density in the epitaxial layer was independent of the implantation temperature.

Jaussaud *et al*[95] and Stoemenos *et al*[89], and Reeson *et al*[49] in collaboration with the author of this thesis, proposed that the accommodation volume for oxide precipitates during implantation is provided by the generation of an excess of Si_i. Jaussaud *et al*[95] and Stoemenos *et al*[89] suggested that the excess Si_i migrate to the surface which acts as a sink leading to the growth of the surface. Van Ommen[88,100] and Stoemenos *et al*[89] suggested that the threading dislocations after annealing originate from the Si_i generated during implantation. Van Ommen[88,100] by considering the two sources of the Si_i during implantation, Frenkel pairs and the ejection from the Si matrix to provide the accommodation volume for internal oxidation, and because the peak in both processes occurs at depths close to the peak of the oxygen distribution, suggested that the threading dislocations start to form at this depth and grow up to the wafer surface during annealing. Reeson *et al*[49] in collaboration with the author of this thesis, after implanting doses of 0.25-1.8x10^{18}O/cm^2, O_2^+, at 200keV/O and 550°C, observed after implantation defects at the wafer surface and suggested that if during implantation the surface growth rate was slower than the arrival rate of Si_i at the surface, the Si_i are likely to coalesce to form defects. De Vireman *et al*[101] suggested that these defects at the wafer surface may be the source of the threading dislocations, which then grow down to the buried oxide during annealing. Steomenos *et al*[102], after implanting doses of 0.15x10^{18}O/cm^2 at energies in the range 140-207keV at 520°C, also observed defects at the wafer surface after implantation and also suggested that these may be the source of the threading dislocations Similarly Visitserngtrakul *et al*[91] suggested that the threading dislocation density after annealing may be reduced if defects at the surface do not form during implantation.

Van Ommen[100], after implanting a dose of 2.5x10^{18}O/cm^2, O_2^+, at 300keV/O and 570°C, in a channelled direction with a constant, low beam current density (1.5μA/cm^2) and annealing at 1300°C for 6hrs, reported that the threading dislocation density was <10^5/cm^2. Van Ommen attributed the low dislocation density to the presence of ordered oxide precipitates and associated low stress measured by Raman spectroscopy[100] after implantation, which in turn was attributed to a combination of the channelled implant, the low beam current density and the uniformity of the beam current during the implantation. It was proposed that the very low beam current density allowed the material to equilibriate during implantation and therefore a

concentration of Si_i or stress did not build up. Further it was suggested that non-uniform beam current densities could result in the formation of heterogenous nucleation sites for threading dislocations and in his work these were eliminated by the very uniform beam current density used. Implanting in a channelled direction, where displacement damage is reduced, may also have helped reduce the threading dislocation density.

Homma *et al*[78], after implanting doses of 0.1-2.4x10^{18}O/cm^2, O^+, at 150keV and 500°C, and annealing at 1150°C for 2 hours, reported that a dose threshold (0.6x10^{18}O/cm^2) exists for the formation of dislocations in subsequently grown epitaxial layers. Reeson *et al*[49] in collaboration with the author of this thesis, after implanting doses of 0.1-1.8x10^{18}O/cm^2, O_2^+, at 200keV and 550°C, and annealing at 1405°C for 30 minutes, reported a dose threshold (0.6x10^{18}O/cm^2) for the formation of high (>10^8/cm^2) threading dislocation densities in the surface Si layer. In the work of Reeson *et al*[49] the threshold dose coincided with the minimum dose for forming a continuous SiO_2 layer after annealing. As for doses greater than the threshold dose, the Si_i can not escape to the substrate, or to the surface because of the anneal cap, this suggests that the trapping of Si_i in the surface Si layer during annealing may be leading to the formation of threading dislocations. Hill *et al*[103,104] and Margail *et al*[45] after annealing, reported threading dislocation densities <10^5/cm^2 by performing sequential implantation and anneals (SIA). In the reports of Hill *et al*[103,104] three implants of 0.4x10^{18}O/cm^2, O^+, at 150keV and 475°C with an anneal of 1250°C for 17hrs following each implant were performed. In the report of Margail *et al*[45] two implants of 0.8x10^{18}O/cm^2, at 200keV and 600°C, with an anneal of 1300°C for 6hrs after each implant were performed. Hill *et al*[103,104] attributed the low threading dislocation density to the implants of less than the critical threshold dose. Margail *et al*[45] proposed the low threading dislocation density was due to the intermediate anneal dissolving the oxide precipitates in the as-implanted surface Si layer so that during the second implant they did not form a barrier to the diffusion of Si_i to the wafer surface. Hence after the second implant the Si surface layer contained a lower concentration of Si_i compared to a single implant of the same dose and therefore after the second anneal a lower threading dislocation density resulted.

El-Ghor *et al*[105,106,107], after implanting doses in the range 1.6-2.0x10^{18}O/cm^2, O^+, at 180keV, and temperatures between 600°C and 675°C, and using a beam current density of 34μA/cm^2, reported the presence of spherical and spheroidal voids in the surface Si layer. The voids were distinguished from oxide precipitates using electron energy loss spectroscopy. The voids were randomly distributed and it was speculated that they were stabilised by the presence of oxygen gas. The presence of the voids for such a narrow temperature range was explained in terms of classical nucleation theory and the analogous case of radiation induced voids in metals. Maszara *et al*[108] after implanting doses in the range 1.6-2.0x10^{18}O/cm^2 at 150keV and temperatures between 530°C and 615°C with a beam current density of 1mA/cm^2, Visitserngtrakul *et al*[91,109] after implanting doses in the range 0.5-1.8x10^{18}O/cm^2, O^+, at 200keV and 600°C with a beam current density of 1mA/cm^2, Nakashima and Izumi[68] after implanting doses in the range 1.0-2.0x10^{18}O/cm^2, O^+, at 180keV and temperatures between 550°C and 700°C with beam currents of 40-80mA, and Jaussaud *et al*[101], after implanting a dose of 1.8x10^{18}O/cm^2, O^+, at 200keV and 600-675°C, also observed spherical and spheroidal voids but in these reports the voids were aligned along the beam direction. It should be pointed out that all reports of aligned voids were implanted using the Eaton Nova NV200 high current (100mA) dedicated oxygen implanter. The formation of the voids along the beam direction has been attributed to the overlapping of thermal spikes caused by electronic interactions (ionizations) of the oxygen ions and the host atoms[108]. The aligned voids are also thought to be stabilised by oxygen gas. Maszara *et al*[108] speculated that the slower arrival rate of oxygen ions in the work of El-Ghor *et al*[105,106,107] would not stabilise columns of voids and only a random distribution of voids would result. Visitserngtrakul *et al*[91,109] after annealing at 1325°C for 2hrs, Jaussaud *et al*[69] after annealing at 1300°C for 6hrs and El-Ghor *et al*[107] after annealing at 1300°C for 6hrs, reported that the voids disappeared and the threading dislocation densities where <10^5/cm^2. These low dislocation densities were attributed to the voids acting as sinks for Si_i during the annealing. These reports suggest that the presence of voids is very sensitive to the implantation conditions (implantation temperature, instantaneous and time-averaged beam current densities) and that the implant conditions which determine the presence of voids are not fully understood. Despite this the voids can be obtained using the Eaton Nova NV200 high

current (100mA) dedicated oxygen implanter[69,101] and hence this is the technique being used to produce the majority of low threading dislocation density ($<10^5/cm^2$) "standard" SIMOX substrates presently being produced. It is such SIMOX substrates which are used for research into the fabrication of thin ($\leq$150nm) Si SIMOX substrates using sacrificial oxidation to reduce the post-anneal thickness of the surface Si layer.

Das *et al*[110], after implanting a dose of $1.4x10^{18}O/cm^2$, O_2^+, at 200keV and 550°C with a beam current density of 15-17$\mu A/cm^2$ and annealing at 1100°C reported that hydrogen was an inappropriate ambient for annealing SIMOX because after long anneals the oxygen content at the depth of the oxide layer decreases. This was attributed to the hydrogen reacting with the implanted oxygen to form water, which diffuses out of the material. Hamdi *et al*[111,112] in 1982/3, after implanting a dose of $2.1x10^{18}O/cm^2$, O^+, at 150keV and a temperature between 300°C and 600°C, and annealing at 1150°C for times between 10 and 240 minutes, used RBS to make the first comparison between Ar and N_2 anneal ambients. Their results suggested that annealing in a Ar ambient produced slightly better results, although in the absence of detailed TEM analysis this was not conclusive. More recently at the same time that the work in this thesis was being carried out, Serapin *et al*[113] in 1991, after implanting a dose of $1.8x10^{18}O/cm^2$ at 200keV and 600°C and annealing at 1320°C for 2hrs or 6hrs, used TEM and secondary ion mass spectroscopy (SIMS) to compare the influence of nitrogen + ½ % oxygen and argon + ½ % oxygen ambients. After annealing for 2hrs they observed oxide precipitates in the surface Si layer for both ambients. The precipitate density was $3x10^4/cm^2$ for the sample annealed in argon + ½ % oxygen and $2x10^5/cm^2$ for the sample annealed in nitrogen + ½ % oxygen. After annealing for 6hrs no oxide precipitates were observed for either ambient but the sample annealed in nitrogen contained a more wavy interface than the sample annealed in argon. SIMS analysis showed a build up of nitrogen at the Si/buried SiO_2 interfaces during the nitrogen anneals and the higher density of oxide precipitates in the surface Si layer after the 2hr nitrogen anneal and the more wavy Si/buried SiO_2 interfaces after the 6hr nitrogen anneal were attributed to the presence of oxynitride complexes at the Si/SiO_2 interfaces inhibiting the diffusion of oxygen across the interfaces.

At the same time as the work in this thesis was being carried out Krause *et al*[114], after implanting a dose of $1.8x10^{18}O/cm^2$ at 200keV and 620°C, tried to reduce the threading dislocation density after annealing by using a rapid thermal anneal (RTA) at 1320°C for 1 minute prior to a 1300°C 5hr conventional anneal. They reported that such samples contained a higher threading dislocation density ($10^9/cm^2$) compared with conventionally annealed samples ($10^6/cm^2$), and fewer Si islands in the buried oxide layer close to the interface with the substrate. The higher threading dislocation density was attributed to the very high ramp rate (50°C/s) of the RTA.

1.4.5 Modelling

Several authors have developed models to calculate the oxygen profiles and layer thicknesses after high dose oxygen implantation into Si. Maydell-Ondrusz *et al*[115] calculated as-implanted profiles by taking into account the changes of target composition after successive implantations of small incremental doses and Jäger *et al*[116] solved the partial differential equations describing the mass transport during implantation. Both these models included fitting parameters and therefore could not be applied in the absence of experimental data. More recently, at the same time as the work presented in this thesis was being carried out and developed in collaboration with the author of this thesis, a set of semi-empirical formulas have been reported for estimating the critical dose for forming a buried SiO_2 layer after implantation, the critical dose for forming a buried SiO_2 layer after annealing and the thicknesses of the surface Si and the buried SiO_2 layers after annealing[117,118]. Further, at the same time as the work presented in this thesis was being carried out, a computer model titled Implantation of Reactive Ions in Solids (IRIS), which takes into account the physical processes of surface growth, diffusion, thermal segregation and sputtering has been developed[119,120,121]. This model, applied to the case of high-dose oxygen implantation into Si, calculates using incremental doses the as-implanted oxygen distribution and the redistribution of the oxygen during annealing and also the thickness of the surface Si and buried SiO_2 layers.

1.5 Work in this Thesis

The aim of the work in this thesis is to investigate the as-implanted and annealed microstructure of thin-film SIMOX substrates directly synthesised by oxygen ion implantation, to understand the basic processes and mechanisms taking place during implantation and annealing and establish the optimum fabrication parameters. The microstructure of two types of thin-film SIMOX substrates are investigated; a thin-film SIMOX substrate consisting of a thin surface Si layer ($\leq$150nm) above a thin ($<$100nm) buried SiO_2 layer (fig. 1.5b) formed at low energies (90keV, 70keV & 50keV) and a thin-film SIMOX substrate consisting of a thin buried SiO_2 layer (110nm) below a standard thickness ($\approx$400nm) surface Si layer (fig. 1.5c), formed at a high energy (200keV). In addition the microstructures of thin-film SIMOX substrates consisting of a thin surface Si layer ($\leq$150nm) above a thick ($\leq$340nm) buried SiO_2 layer formed at low energies (90keV, 70keV & 50keV) are investigated.

The main new work of this thesis is summarised as follows. The first detailed TEM investigation reported on SIMOX structures;

a) as-implanted and annealed (1320-1360°C, 6hrs) formed at energies of 90keV, 70keV and 50keV,

b) as-implanted and annealed (1320-1360°C, 6hrs) at these low energies as a function of the dose,

c) as-implanted and annealed (1320-1360°C, 6hrs) resulting from implanting lower than standard doses ($<1.4x10^{18}O/cm^2$) at 200keV,

d) the as-implanted oxide precipitate morphology is correlated with the as-implanted oxygen distribution (from SIMS analysis) over a range of energies (200keV, 90keV, 70keV & 50keV) and a range of doses ($0.1\text{-}1.6x10^{18}O/cm^2$) and hence as a function of the depth below the surface and the oxygen concentration ($\approx 10^{18}\text{-}4.48x10^{22}/cm^3$),

e) as-implanted, a previously unreported defect observed below the peak of the oxygen distribution (200keV, 90keV, 70keV & 50keV),

f) annealed, a comparison of the influence of nitrogen and argon anneal ambients at both high (200keV) and low energies (90keV & 70keV) after implanting doses just greater than the

minimum for forming a continuous buried SiO_2 layer after annealing at each energy, and annealing at 1300°C or 1320/60°C for 6hrs,

g) as-implanted and annealed, the influence of time-averaged beam current densities, between 2.5μA/cm^2 and 6.25μA/cm^2 for a constant implantation temperature of 680°C, a dose of 0.7x10^{18}O/cm^2 and an energy of 200keV,

h) annealed, the influence of graded energy implants at low energies (65keV, 70keV & 75keV, anneal 1320-1360°C, 6hrs), in particular on the morphology of the Si islands present within the thin (<100nm) buried SiO_2 layer,

i) annealed, the use of rapid thermal anneals (1300°C, 1minute), at doses just above the minimum dose to form a continuous buried SiO_2 layer after annealing, at both low (70keV) and high (200keV) energies, to redistribute the oxygen distribution prior to the conventional anneal (1320-1360°C, 6hrs) and hence try to reduce the density of Si islands within the buried SiO_2 layer.

In addition simple models are proposed for;

a) the typical oxygen diffusion length during implantation as a function of the implantation parameters,

b) estimating, prior to implantation, the thickness of the buried SiO_2 and surface Si layer after high temperature annealing from the dose and energy or conversely the required dose and energy to form a structure with a certain buried SiO_2 thickness and a certain surface Si layer thickness.

The likely mechanisms for the following are described;

a) the roles of the oxygen concentration, Si_i, Si_v, stress and thermal contraction in determining the as-implanted precipitate morphologies and defect microstructure,

b) the formation of the buried oxide layer during annealing, including the role of the as-implanted microstructure,

c) the origin of threading dislocations present after annealing, including the role of the as-implanted microstructure,

The optimal doses for forming at energies of 90-70keV thin-film SIMOX substrates, consisting of a thin (<160nm) surface Si layer above a thin (<100nm) buired SiO_2 layer, suitable for the subsequent fabrication of "fully depleted" high performance CMOS devices, and for forming at energies of 200keV thin-film SIMOX substrates, consisting of a thin (110nm) buried SiO_2 layer below a standard thickness (400nm) surface Si layer, suitable for the subsequent fabrication of radiation hard devices and circuits with reduced circuit self-heating, are established. In addition thin-film SIMOX substrates, consisting of a thin (<150nm) surface Si layer a thick ($\leq$340nm) buried SiO_2 layer, also suitable for the subsequent fabrication of "fully depleted" high performance CMOS devices, are formed. The results enable, for the implantation conditions used, the likely threading dislocation and Si island density to be estimated for a particular dose and energy.

This work has been carried out as part of a collaborative project with the Department of Electronic & Electrical Engineering, University of Surrey, the Department of Materials, Imperial College, University of London and the Department of Electrical Engineering and Electronics, University of Liverpool.

In Chapter 2 the experimental methods used in this work are described. In Chapter 3 the as-implanted precipitate morphology and the defect microstructures are described, the precipitate morphology is correlated to the local oxygen concentration, the mechanisms taking place during implantation are discussed and a simple model for a typical oxygen diffusion length during implantation is presented. In Chapter 4 the annealed microstructures are described, the as-implanted and annealed microstructure are correlated, the formation of the buried SiO_2 layer and the threading dislocations during annealing are discussed. In Chapter 5 simple models are described which can be used prior to implantation to estimate the thickness of the buried SiO_2 layer and the surface Si layer after annealing and conversely also to calculate the required dose and energy to fabricate a structure with a certain buried oxide layer and a certain surface Si layer thickness. The values obtained are compared to the experimental results and to values

obtained from a semi-empirical equation and a computer model reported in the literature. In Chapter 6 the conclusions from this work and suggestions for further work are presented.

1.6 References

[1] K Yallup, Proc. Electrochem. Soc. 92-13, p43 (1992).

[2] F. Vogt, B Mutterlin & H Vogt, Proc. Electrochem. Soc. 92-13, p77 (1992).

[3] B Tillack, R Banisch, F Januschewski, A Chovet, K Hoppner & H H Richter, Proc. Electrochem. Soc. 92-13, p185 (1992).

[4] T Nishimura & Y Akasaka, Proc. Electrochem. Soc. 90-6, p389 (1990).

[5] A J Auberton-Herve, Proc. Electrochem. Soc. 90-6, p455 (1990).

[6] S M Sze, *VLSI Technology*, (McGraw Hill International, Singapore, 1988).

[7] H M Manasevit & W I Simpson, J. Appl. Phys. 35, p1349 (1964).

[8] A Ogura, A Furuya & R Koh, Proc. Electrochem. Soc. 92-13, p425 (1992).

[9] see the majority of references in this work

[10] C D Meekison, G R Booker, K J Reesson, P L F Hemment, R F Peart, R J Chater, J A Kilner & J R Davis, J. Appl. Phys. 69, p3503 (1991).

[11] K Auborn, Proc. Proc. 1992 IEEE Int. SOI Conf., p154 (1992).

[12] K E Bean & W R Runyan, J. Electrochem. Soc. 124, p5 (1977).

[13] S S Tsao, IEEE Circuits & Devices Magazine 6, p3 (1987).

[14] I T P Allen, Proc. SPIE Advanced Processing of Semicond. Dev. II 945, p126 (1988).

[15] H Isiwara, Proc. Electrochem. Soc. 90-6, p72 (1990).

[16] J C Sturm, Proc. Mats. Res. Soc. 107, p295 (1988).

[17] J P Colinge, IEDM Tech. Dig. p817 (1989).

[18] J Gautier & G Riembold, Proc. Electrochem. Soc. 92-13, p135 (1992).

[19] R Sundaresan & C Chen, Proc. Electrochem. Soc. 90-6, p437 (1990).

[20] J P Colinge, Hewlet Packard Journal Feb., p87 (1988).

[21] S Hall, Dept. Electronic Engineering, University of Liverpool, private communication.

[22] P C Karulkar, Proc. 1992 IEEE Int. SOI Conf., p108 (Ponte Vedra, USA, 1992)

[23] M Ihara, T Kimura, H Yamawaki & O Ueda, Proc. Electrochem. Soc. 90-6, p399 (1990).

[24] H Ryssel, R Schork & N X Chen, Proc. INFOS'93 (Delft, Netherlands,1993).

[25] M A Guerra, Proc. Electrochem. Soc. 90-6, p21 (1990).

[26] Proc. IVth Int. Symp. SOI Tech. & Dev., Electrochem. Soc. 90-6, (Montreal, Canada, 1990).

[27] Proc. Vth Int. Symp. SOI Tech. & Dev., Electrochem. Soc. 92-13, (St Louis, USA, 1992).

[28] Proc. 1992 IEEE Int. SOI Conf. (Ponte Vedra, USA, 1992).

[29] Proc. 1993 IEEE Int. SOI Conf. (Palm Springs, USA, 1993).

[30] J P Ruffel, D H Douglas-Hamilton, R E Kaim & K Izumi, Nucl. Inst. & Meths, B21, p229 (1987).

[31] D H Douglas-Hamilton, J P Ruffel, R E Kaim & K Izumi, Nucl. Inst. & Meths, B21, p324 (1987).

[32] M A Guerra, Mats. Sci. & Eng. B12, p145 (1992).

[33] M L Smith, *Electromagnetically Enriched Isotopes and Mass Spectroscopy*, (Butterworth Sci. Pub., London, 1956).

[34] M Watanabe & A Tooi, Jap. J. Appl. Phys. 5, p737 (1966).

[35] P V Pavlov & E V Shitova, Sov. Phys. 12, p11 (1967).

[36] J H Freeman, G A Gard, D J Mazey, J H Stephen & F B Whiting, Proc. of Euro. Conf. on Ion Implantation, (Reading, England) p74 (1970).

[37] V M Gusev, M I Gusev, V I Kurinnvy, V V Titov, V S Tsyplenkov, E K Baranova & L P Streltsov, Radio Eng. & Elec. Phys. 16, p1357 (1971).

[38] J Dyleswki & M C Joshi, Thin Solid Films 35, p241 (1976).

[39] J Dyleswki & M C Joshi, Thin Solid Films 42, p227 (1977).

[40] K Brack & G H Schwuttke, Inst. Phys. Conf. Ser. 23, p440 (1975).

[41] M H Badawi & K V Anand, J. Phys. D : Appl. Phys. 10, p1931 (1977).

[42] K Izumi, M Doken & H Ariyoshi, Elec. Letts. 14, p593 (1978).

[43] K Ohwada, Y Omura & E Sano, IEEE Trans. Elec. Dev. 28, p1084 (1981).

[44] C G Tuppen, M R Taylor, P L F Hemment & R P Arrowsmith, Appl. Phys. Lett. 45, p57 (1984).

[45] J Margail, J Stoemenos, C Jaussaud & M Bruel, Appl. Phys. Lett. 54, p526 (1989).

[46] S Nakashima & K Izumi, Nucl. Inst. & Meths. B55, p847 (1991).

[47] A Mogro-Campero, R P Love, N Lewis, E L Hall & M D McConnel, J. Appl. Phys. 60, p2103 (1986).

[48] B-Y Mao, P H Chang, H W Lam, B W Shen & J A Keenan. Appl. Phys. Lett. 48, p794 (1986).

[49] K J Reeson, A K Robinson, P L F Hemment, C D Marsh, K N Christensen, G R Booker, R J Chater, K J Kilner, G Harbeke, E F Steigmeir & G K Celler, Microelectron. Eng. 8, p163 (1988).

[50] S J Krause, C O Jung, T S Ravi, S R Wilson & D E Burke, Proc. Mats. Res. Soc. 107, p93 (1988).

[51] F Namavar, E Cortesi, B L Buchanan & P Sioshansi, Proc. 1989 IEEE SOS/SOI Tech. Conf., p117 (Stateline, USA, 1989).

[52] F Namavar, E Cortesi, N M Kalkhoran, J M Manke & B L Buchanan, Proc. 1990 IEEE SOS/SOI Tech. Conf. (Key West, USA, 1990).

[53] J A Kilner, S D Littlewood, P L F Hemment, E Maydell-Ondrusz & K G Stevens, Nucl. Inst. & Meths. 218, p573 (1983).

[54] P L F Hemment, E Maydell-Ondrusz, K G Stevens, J A Kilner & J Butcher, Vacuum 34, p203 (1984).

[55] S S Gill & I H Wilson, Thin Solid Films 55, p435 (1978).

[56] T Hayashi, H Okamoto & Y Homma, Inst. Phys. Conf. Ser. 59, p533 (1980).

[57] C D Marsh, G R Booker, K J Reeson, P L F Hemment, R J Chater, J A Kilner, J Alderman & G Celler, Proc. Euro. Mats. Res. Soc. P137 (1986).

[58] F F Morehead, B L Crowder & R S Title, J. Appl. Phys. 43, p1112 (1972).

[59] N Hatzopoulos, R Chater, U Bussman, P L F Hemment & J A Kilner, Mats. Sci. & Eng. B12, p37 (1992).

[60] S J Krause, C O Jung, T S Ravi, S R Wilson & D E Burke, Proc. Mats. Res. Soc. 107, p93 (1988).

[61] A E White, K T Short, L N Peiffer, K W West & J L Bapstone, Proc. Mats. Res. Soc. 74, p585 (1987).

[62] P L Hemment, E Maydell-Ondrusz, K G Stevens, J Butcher, D Ioannou & J Alderman, Nucl. Inst. Meths. 209, p157 (1983).

[63] S R Wilson & D Fathy, J. Elec. Mats. 13, p127 (1984).

[64] O W Holland, T P Soreen, D Fathy & J Narayan, Appl. Phys. Lett. 45, p1081 (1984).

[65] M Bruel, J Margail, J Stoemenos, P Martin & C Jaussaud, Vacuum 35, p589 (1985).

[66] S Maillet, R Stuck, J J Grob, A Golanski, R Pantel & A Perio, Nucl. Inst. & Meths. B19, p294 (1987).

[67] S Visitserngtrakul, S J Krause & B F Cordts, J. Appl. Phys. 69, p1784 (1991).

[68] S Nakashima & K Izumi, J. Mat. Res. 5, p1918 (1990).

[69] C Jaussaud, J Stoemenos, J Margail, A M Papon & M Bruel, Vacuum 42, p341 (1991).

[70] A K Robinson, C D Marsh, U Bussmann, J A Kliner, Y Li, J Vanhellemont, K J Reeson, P L F Hemment & G R Booker, Nucl. Inst. & Meths. B55, p555 (1991).

[71] H W Lam, R F Pinizotto, H T Yuan & D W Bellevance, Elec. Letts. 14, p358 (1981).

[72] G K Celler, P L F Hemment, K W West & J M Gibson, Appl. Phys. Lett. 48, p532 (1986).

[73] C D Marsh, J L Hutchison, G R Booker, K J Reeson, P L F Hemment & G K Celler, Inst. Phys. Conf. Ser. 87, p409 (1987).

[74] J Stoemenos, C Jausaud, M Bruel & J Margail, J. Crys. Growth 73, p 546 (1985).

[75] J R Davis, K J Reeson, P L F Hemment & C D Marsh, Elec. Dev. Lett. 8, p291 (1987).

[76] T Hayashi, H Okamoto & Y Homma, Jap. J. Appl. Phys. 19, p1005 (1980).

[77] T Hayashi, S Maeyama & S Yoshi, Jap. J. Appl. Phys. 19, p1111 (1980).

[78] Y Homma, M Oshima & T hayahsi, Jap. J. Appl. Phys. 21, p890 (1982).

[79] R F Pinizotto, B L Vaandrager & H W Lam, Proc. Mats. Res. Soc. 7, p401 (1982).

[80] J A Kilner, R J Chater, P L F Hemment, R F Peart, E A Maydell-Ondrusz, M R Taylor & P R Arrowsmith, Nucl. Inst. Meths. B7, p293 (1985).

[81] K J Reeson, Nucl. Inst. & Meths. B19/20, p269 (1987).

[82] P L F Hemment, K J Reeson, J A Kilner, R J Chater, C D Marsh, G R Booker, J R Davis & G K Celler, Nucl. Inst. & Meths. B21, p129 (1987).

[83] D Fathy, O L Krivanek, R W Carpenter & S R Wilson, Inst. Phys. Conf. Ser. 67, p (1983).

[84] O W Holland, D Fathy, J Narayan, T P Sjoreen & S R Wilson, J. Non-Crystline Solids 71, p

163 (1985).

[85] T P Sjoreen, O W Holland, D Fathy, K More & R F Davis, Nucl. Inst. & Meths. B10, p754 (1985).

[86] C Jaussaud, J Stoemenos, J Margail, N Dupuy, B Blanchard & M Bruel, Appl. Phys. Lett. 46, p1064 (1985).

[87] A H Van Ommen, B H Koek & P A Viegers, Appl. Phys. Lett. 49, p162 (1986).

[88] A H Van Ommen & P A Viegers, Inst. Phys. Conf. Ser. 87, p (1987).

[89] J Stoemenos, J Margail, M Dupuy & C Jausaud, Physica Scripta 35, p42 (1987).

[90] S Visitserngtrakul, C O Jung, S J Krause & B F Cordts, Proc. Electrochem. Soc. 90-6, p106 (1990).

[91] S Visitserngtrakul, S J Krause, B F Cordts & P Roitman, Vacuum 42, p353 (1991).

[92] S Nakashima & K Izumi, J. Mat. Res. 8, p523 (1993).

[93] K Das, J B Butcher, M C Wilson, G R Booker, D W Welby, P L F Hemment & K V Anand, Inst. Phys. Conf. Ser. 60, p307 (1981).

[94] C G Tuppen, M R Taylor, P L F Hemment & R P Arrowsmith, Thin Solid Films 131, p233 (1985).

[95] C Jaussaud, J Margail, J Stoemenos & M Bruel, Proc. Mats. Res. Soc. 107, p17 (1988).

[96] S J Krause, C O Jung, M E Burnham & S R Wilson, Inst. Phys. Conf. Ser. 87, p391 (1987).

[97] J Stoemenos, J Margail, C Jausaud, M Dupuy & M Bruel, Appl. Phys. Lett. 48, p1470 (1986).

[98] I H Wilson, Nucl. Inst. & Meths. B1, p331 (1984).

[99] S J Krause, C O Jung, S R Wilson, R P Lorigan & M E Burnham, Proc. Mat. Res. Soc. 53, p257 (1986).

[100] A H Van Ommen, Proc. Mat. Res. Soc. 107, p79 (1988).

[101] A De Vireman, J Van Landuyt, J Vanhellemont, H E Maes & K Yallup, Vacuum 42, p367 (1991).

[102] J Stoemenos, K J Reeson, A K Robinson & P L Hemment, J Appl. Phys. 69, p793 (1991).

[103] D Hill, P Fraundorf & G Traundorf, Proc. 1987 IEEE SOS/SOI Tech. Workshop (Durango,

USA, 1987).

[104] D Hill, P Fraundorf & G Traundorf, J. Appl. Phys. 63, p4933 (1988).

[105] M K El-Ghor, S J Pennycock, F Namavar & N Karam, Appl. Phys. Lett. 57, p156 (1990).

[106] M K El-Ghor, S J Pennycock, T P Sjoreen C W White & J Narayan, Mats. Res. Soc. Proc. 107, p235 (1988).

[107] M K El-Ghor, S J Pennycock & J Narayan, Proc. Mats. Res. Soc. 74, p591 (1987).

[108] W P Maszara, J. Appl. Phys. 64, p123 (1988).

[109] S Visitserngtrakul, C O Jung, T S Ravi, B Cordts, D E Burke & S J Krause, Inst. Phys. Conf. Ser. 100, p557 (1989).

[110] K Das, J B Butcher & K V Anand, Proc. Electrochem. Soc. 81-7, p427 (1981).

[111] A H Hamdi, F D McDaniel, R F Pinizotto, S matteson, H W Lam & S D S Malhi, Appl. Phys. Lett. 41, p1143 (1982).

[112] R F Pinizotto, B L Vaandrager, S Matheson, H W Lam, S D S Malhi, A H Hamdi & F D Mcdaniel, IEEE Trans. Nucl. Sci. NS-30, p1718 (1983).

[113] S Serapin, S J Krause, P Roitman, D S Simons & B F Cordts, Appl. Phys. Lett. 59, p3003 (1991).

[114] S J Krause, J D Lee, J C Park, P Roitman & M El-Ghor, Proc. Electrochem. Soc. 92-13, p221 (1992).

[115] E A Maydell-Ondrusz & I H Wilson, Thin Solid Films 114, p357 (1984).

[116] H U Jäger, J A Kilner, R J Chater, P L F Hemment, R F Peart & K J Reeson, Thin Solid Films 161, p333 (1988).

[117] Y Li, J A Kilner, A K Robinson, P L F Hemment & C D Marsh, J. Appl. Phys. 70, p3605 (1991).

[118] Y Li & J A Kilner, Mats. Sci. & Eng. B12, p77 (1992).

[119] U Bussman & P L F Hemment, Nucl. Inst. & Meths. B47, p22 (1990).

[120] U Bussman & P L F Hemment, Appl. Phys. Lett. 57, p1200 (1990).

[121] U Bussman, A K Robinson & P L F Hemment, Nucl. Inst. & Meths. B55, p852 (1991).

[122] J Margail, J M Lamure, A M Papon, & J Steomenos, Proc. Electrocem. Soc. 92-13, p207 (1992).

Chapter 2

Experimental Methods

2.1 Introduction

This chapter describes the experimental conditions under which the silicon (Si) wafers were implanted and annealed, and the analytical techniques used to gain microstructural information, before and after the anneal treatments. Transmission electron microscopy (TEM) was the primary research tool because structures within specimens can be examined at a high spatial resolution and diffraction contrast affects can be used to identify defects, e.g. by determining their displacement vectors. The techniques used for preparing samples for TEM examination are described.

2.2 Ion Implantation

The oxygen was implanted into 3 inch diameter [001] n-type and p-type float zone (Fz) and Czochralski (Cz) Si wafers using the 500keV Heavy Ion Research Implanter at the University of Surrey. The implanter had a RF type ion source[1] which produced beams of either O^+ atomic ions or O_2^+ molecular ions. However, the molecular ion current was typically three times the atomic ion current. It has been shown theoretically by Badawi and Anand[2] that implanting the molecular ion results in the same oxygen distribution in the Si as implanting the atomic ion at half the molecular ion energy. Consequently, in the present work the molecular O_2^+ ion was implanted at the higher energy so as to obtain the required high doses more rapidly. The implanted doses in this thesis, as is the normal convention in the reports on SIMOX in the literature, are quoted in terms of the number of oxygen atoms per cm. All samples were implanted with ^{16}O, except two which were implanted with ^{18}O. The vacuum in the implanter was $\approx 10^{-7}$ torr.

For implantation the wafers were mounted in front of a bank of halogen lamps[3] which preheated the wafers to either $650\pm10°C$, $680\pm10°C$ or $700\pm10°C$ for 10 minutes prior to implantation and maintained that temperature during implantation. All the wafers were

implanted at an angle of 7° from the [001] wafer normal in order to minimise channelling effects. The area implanted was an $8cm^2$ square in the centre of the wafers. The wafers were rotated so that the edges of the square were offset by 10° from the <110> crystallographic directions. The implanted area was defined using a Si aperture in the beam line. Doses in the range $0.1x10^{18}O/cm^2$ to $1.7x10^{18}O/cm^2$ were implanted. The nominal implanted dose was measured using a charge integrator connected to the sample to count the total charge arriving at the sample during implantation. An electrostatic suppression plate (not exposed to the beam) between the aperture and the sample was used to suppress secondary electrons and improve the accuracy of the dose measurement. Uniformity of dose was achieved by electrostatic beam scanning in both the x and y directions using a "saw tooth" waveform at frequencies of 66Hz in the x direction and 625Hz in the y direction. The beam was scanned over an area larger than the aperture. The molecular oxygen ions were implanted at energies of 100keV, 140keV, 180keV and 400keV, equivalent to energies per oxygen atom of 50keV, 70keV, 90keV and 200keV, respectively. In the rest of this thesis, as is the convention in the reports on SIMOX in the literature, the implant energies quoted are the equivalent energies per oxygen atom. Typical oxygen currents in the beam line of 40μA, 45μA, 60μA and 85μA at 50keV/O, 70keV/O, 90keV/O and 200keV/O, respectively, were used. Due to the scanned beam striking the area defining aperture for $\approx 50\%$ of the time, the time-averaged beam currents arriving at the samples (column 1, table 2.1) were approximately half of these values. In the rest of this thesis when the beam currents are mentioned it is the time-averaged beam currents arriving at the samples that are being referred to. Beam spot sizes of $0.72cm^2$ and $\geq 1cm^2$, depending on energy, were used (table 2.1). The instantaneous beam current densities were between $\approx 40\mu A/cm^2$ and $118\mu A/cm^2$ and the time-averaged beam current densities between $2.5\mu A/cm^2$ and $6.25\mu A/cm^2$ (table 2.1). The beam currents and beam current densities quoted in this work refer to the O_2^+ current. Due to an increase in the extraction efficiency of the ion source with increasing energy, the available beam current increased with increasing implantation energy (table 2.1). The implantations took between 40 minutes and 7 hours and 45 minutes.

The implant conditions for the samples investigated in this work are shown in Table 2.2.

Energy/ oxygen atom (keV)	Beam current O_2^+ (±10%) (μA)	Molecular ion (O_2^+) beam current densities used		Equivalent atomic ion (O^+) beam current densities	
		Time-averaged* (μA/cm^2)	Instantaneous# (μA/cm^2)	Time-averaged* (μA/cm^2)	Instantaneous# (μA/cm^2)
200	20	2.5	45	5	90
"	30	3.75	75	7.5	150
"	40	5	85	10	170
"	45	5.625	118	11.25	236
"	50	6.25	§	12.5	§
90	30	3.75	<60	7.5	<120
70	25	3.125	<45	6.25	<90
50	20	2.5	§	5	§

Table 2.1 The time-averaged O_2^+ molecular ion beam currents arriving at the sample (column 1) and the beam current densities used at the different implant energies in this work, and the equivalent beam current densities for the O^+ atomic ion. The standard time-averaged beam current used for 200keV implants was 45μA. *The implanted area was 8cm^2. #The area of the beam spot was 0.72cm^2 at 200keV and $\geq$1cm^2 at 90keV and 70keV, and not meausred at 50keV. § = not measured.

Sample number	Implantation conditions					Anneal conditions		
	Energy (keV/O)	Φ (10^{18}O/cm^2) Nom.	Ret.	Temp. (±10°C)	O_2^+ Current (μA±10%)	Temp. (°C)	Time (hrs)	Ambient
Ho3a$_i$	50	0.2	-	680	20	-	-	-
Ho3a$_a$	"	"	-	"	"	1320	2	N_2
Ho3c$_i$	"	0.5	-	680	20	-	-	-
Ho3c$_a$	"	"	-	"	"	1320	2	N_2
Ho3b$_i$	"	0.7	-	680	20	-	-	-
Ho3b$_a$	"	"	-	"	"	1320	2	N_2
H36a$_i$	70	0.1	-	680	25	-	-	-
H36a$_a$	"	"	-	"	"	1320	6	N_2
H151$_i$$^{\#}$	"	0.1	-	680	25	-	-	-
H151$_a$$^{\#}$	"	"	-	"	"	1360	6	N_2
H56a	"	0.17	0.25	680	25	1300	6	Ar + ½ % O_2
K339a	"	0.3	-	680	25	-	-	-
H11$_i$	"	0.33	-	680	25	-	-	-
H11$_a$	"	"	-	"	"	1320	6	N_2
H57	"	0.33	0.35	680	25	1300	6	Ar + ½ % O_2
H114	"	0.33	0.35	650	25	1300	6	Ar + ½ % O_2
H36c$_i$	"	0.4	-	680	25	-	-	-
H36c$_a$	"	"	-	"	"	1320	6	N_2
H89	"	0.4	0.45	680	25	1300	6	Ar + ½ % O_2
H90	"	0.5	0.53	680	25	1300	6	Ar + ½ % O_2
H36b$_i$	"	0.5	-	680	25	-	-	-
H36b$_a$	"	0.5	-	"	"	1320	6	N_2
K339c$_i$	"	0.7	-	680	25	-	-	-
K339c$_a$	"	"	-	"	"	1320	6	N_2
K339b$_i$	"	1.0	-	680	25	-	-	-
K339b$_a$	"	"	-	"	"	1320	6	N_2
H127	65,70,75	3 x 0.1	-	680	25	1320	6	N_2
H131$_i$	75,70,65	3 x 0.1	-	680	25	-	-	-
H131$_a$	"	"	-	"	"	1320	6	N_2
H124	90	0.3	0.22	680	30	1320	6	N_2
H123	"	0.4	0.29	680	30	1320	6	N_2
H100	"	0.3	0.35	680	30	1300	6	Ar + ½ % O_2
H99	"	0.4	-	680	30	1300	6	Ar + ½ % O_2
H122	"	0.5	0.4	680	30	1320	6	N_2
H142$_i$	"	0.43	-	700	35	-	-	-
H142$_a$	"	"	-	"	"	1360	6	N_2
H143a$^{\#}$	"	0.43	-	680	25	-	-	-
H143b$^{\#}$	"	"	-	"	"	1360	6	N_2
H143c$^{\#}$	"	"	-	"	"	RTA	1min	1300°C N_2
H143d$^{\#}$	"	"	-	"	"	3xRTA	1min	1300°C N_2
H143e$^{\#}$	"	"	-	"	"	RTA + CA	1min 6hrs	1300°C N_2 1360°C N_2

Table 2.2 (part 1) Implantation and anneal conditions, Φ = dose (Nom. = nominal dose, Ret. = retained dose), $^{\#}$implanted with ^{18}O, RTA = rapid thermal anneal and CA = conventional anneal.

Sample number	Implantation conditions					Anneal conditions		
	Energy (keV/O)	Φ (10^{18}O/cm^2) Nom.	Φ (10^{18}O/cm^2) Ret.	Temp. (±10°C)	O_2^+ Current (μA±10%)	Temp. (°C)	Time (hrs)	Ambient
H97	90	0.5	0.5	680	30	1300	6	Ar + ½ % O_2
H106	"	0.5	0.52	680	30	1300	6	Ar + ½ % O_2
H113	"	0.5	0.56	650	30	1300	6	Ar + ½ % O_2
H42a*i*	"	0.6	0.6	680	30	-	-	-
H42a*a*	"	"	-	"	"	1320	6	N_2
H42b*i*	"	0.8	0.7	680	30	-	-	-
H42b*a*	"	"	-	"	"	1320	6	N_2
H42c*i*	"	1.0	0.9	680	30	-	-	-
H42c*a*	"	"	-	"	"	1320	6	N_2
H42d*i*	"	1.2	1.0	680	30	-	-	-
H42d*a*	"	"	-	"	"	1320	6	N_2
H41	"	1.0	-	680	30	1300	6	Ar + ½ % O_2
H103	"	1.0	-	680	30	1300	6	Ar + ½ % O_2
H42e*i*	"	1.8	1.5	680	30	-	-	-
H42e*a*	"	"	-	"	"	1320	6	N_2
H135*i*	200	0.4	-	700	45	-	-	-
H135*a*	"	"	-	"	"	1360	6	N_2
H133*i*	"	0.5	0.46	700	45	-	-	-
H133*a*	"	"	-	"	"	1360	6	N_2
H35*i*	"	0.6	0.56	680	45	-	-	-
H35*a*	"	"	-	"	"	1320	6	N_2
H93	"	0.43	0.56	650	45	1300	6	Ar + ½ % O_2
H136a	"	0.6	0.6	680	45	-	-	-
H136b	"	"	"	"	"	1360	6	N_2
H136c	"	"	"	"	"	RTA	1min	1300°C N_2
H136d	"	"	"	"	"	3xRTA	1min	1300°C N_2
H136e	"	"	"	"	"	RTA + CA	1min 6hrs	1300°C N_2 1360°C N_2
H104	"	0.6	0.65	700	45	1300	6	Ar + ½ % O_2
H132*i*	"	0.7	-	680	20	-	-	-
H132*a*	"	"	-	"	"	1360	6	N_2
H134*i*	"	0.7	0.69	680	30	-	-	-
H134*a*	"	"	"	"	"	1360	6	N_2
H130*i*	"	0.7	0.72	680	40	-	-	-
H130*a*	"	"	"	"	"	1320	6	N_2
H174	"	0.7	-	"	50	-	-	-
H121*i*	"	1.6	1.2	700	45	-	-	-
H121*a*	"	"	"	"	"	1310	6	N_2
H128*i*	"	1.8	1.6	700	45	-	-	-
H128*a*	"	"	"	"	"	1320	6	N_2
H43	"	1.8	1.6	680	50	1300	6	Ar + ½ % O_2
H88	"	1.8	1.7	680	50	1300	6	Ar + ½ % O_2

Table 2.2 (part 2) Implantation and anneal conditions, Φ = dose (Nom. = nominal dose, Ret. = retained dose), RTA = rapid thermal anneal and CA = conventional anneal.

2.3 Post-implant Anneals

After implantation the majority of the wafers were annealed. Annealing was carried out in a flowing N_2 or an Ar + ½ % O_2 ambient in resistively heated furnaces, or in a N_2 ambient in a lamp rapid thermal anneal (RTA) furnace. To prevent pitting of the wafer surface during annealing the wafers were capped with 0.5μm of low temperature (450°C) chemical vapour deposited (CVD) SiO_2. The standard anneal treatment was 6 hours in resistively heated furnaces at a constant temperature between 1300 and 1360°C. The RTA anneals were carried out at 1300°C for 1 minute.

For the Ar + ½ % O_2 ambient anneals the sample handling equipment for the furnace could only accomodate whole 3" wafers. Samples were loaded with the furnaces at 800°C and the temperature increased to 1300°C at 5°C/min. After annealing the furnaces were ramped down to 800°C at 5°C/min. The samples were then removed and left to cool. These anneals were performed at the Microelectronics Centre, University of Southampton.

For the N_2 anneals the furnace could only accommodate small pieces of silicon, of the order of a 1cm^2. The small pieces were loaded with the furnace at room temperature and the temperature was then increased to a temperature between 1310°C and 1360°C at 10°C/min. After annealing the furnaces were ramped down to room temperature at a rate of 10°C/min. These anneals were performed at the Department of Materials, Imperial College, University of London.

For the RTA anneals small (1cm^2) pieces of the samples were placed in the lamp annealer at room temperature and ramped up to the anneal temperature of 1300°C at a rate of 250°C/sec. Hence the samples took approximately 5 seconds to reach the anneal temperature. After the anneal the power was switched off and the samples were allowed to cool in the furnace for 1 minute. At the end of this minute the temperature of the samples is estimated as 200°C[4]. The samples are then removed from the furnace and allowed to cool down to room temperature. These anneals were performed at the Department of Electrical and Electronic Engineering, Imperial College, University of London.

A consequence of the different size pieces of Si required for the two different resistively heated anneal furnaces meant that if the as-implanted structure of a sample was examined by TEM other pieces of the same sample could not be annealed in the Ar + ½ % O_2 furnace and hence could only be annealed in a N_2 furnace. Conversely, for samples annealed in an Ar + ½ % O_2 furnace the as-implanted microstructure could not be examined by TEM. In theory this problem could be overcome by implanting two wafers with the same dose, one for analysis of the as-implanted structure and the structure after annealing in N_2 and the other for the analysis of the structure after annealing in Ar + ½ % O_2. In practice though due to difficulties with controlling the retained dose, this approach usually led to two wafers with two slightly different retained doses. Further, due to the furnaces sometimes breaking down and other reasons, there was at times limited access to the furnaces and the choice of anneal ambient was often determined by the availability of the furnace.

The anneal conditions for the samples investigated in this work are shown in Table 2.2.

2.4 Rutherford Backscattering Spectroscopy

After annealing the retained dose for many samples was checked with Rutherford backscattering spectroscopy (RBS) using 1.5 MeV $^4He^+$ beam and a backscattering angle of 160°. The values for the doses were obtained using random spectra and employing the surface energy approximation[5]. The nominal implanted dose and the retained dose where measured by RBS, for each sample are listed in Table 2.2. The discrepancy between the nominal and retained doses was typically within $\pm 15\%$ of the nominal dose, but sometimes it was as large as $\pm 30\%$ of the nominal dose. The discrepancy could be explained by either the implantation of an incorrect dose or the loss or addition of oxygen to the wafer after implantation. The retained dose was often larger than the nominal dose and as the addition of oxygen after implantation is unlikely, this suggests the discrepancy between the nominal and retained doses for these samples was due to the implantation of doses larger than the nominal doses. For samples with a retained dose lower than the nominal dose, the loss of oxygen during subsequent processing is a possibility but it is thought that this is also mainly due to the implantation of doses different

from the nominal doses. In the rest of this thesis the dose quoted for each sample is the retained dose where measured. For samples for which the retained dose was not measured by RBS the dose quoted in this thesis is the nominal dose.

RBS random and channelling measurements were also carried out on some of the as-implanted samples. The RBS measurements were performed in the Department of Electronic and Electrical Engineering, University of Surrey.

2.5 Transmission Electron Microscopy

2.5.1 Introduction

Transmission electron microscopy (TEM) concerns the formation of a highly magnified image by the use of high energy electrons that have been transmitted through a thin slice of a solid[6,7,8]. In crystalline materials the interaction between the electrons and the crystal planes scatters electrons in the form of one or more diffracted beams. One or more of these beams is then used to form an image. Contrast in the image arises from local variations in the electron scattering from lattice planes and the increase in scattering from atoms with increasing atomic number. Two methods, diffraction contrast or phase contrast, are used to produce the image contrast in TEM. In amorphous material the increase in scattering from atoms with increasing atomic number gives rise to contrast in the images.

In diffraction contrast an aperture in the back focal plane of the objective lens is used to select one electron beam which is then used to form the image[6,7]. This beam can either be the transmitted beam to form a bright field image, or a diffracted beam to form a dark field image. The intensities in the image are then proportional to the square of the amplitude of the waves in the single beam that passes through the aperture. The diffraction conditions normally used with this technique are a two-beam condition, where the sample has been tilted so that only one diffracted beam is strongly excited, i.e. only one set of crystal planes satisfying the Bragg condition, or, for forming bright field images, the many beam condition where the sample has been tilted so that electron beam is aligned along a major crystallographic direction (pole).

Using diffraction contrast the image width for dislocations is about a third of the effective extinction distance[6], hence by using diffraction conditions with a small effective extinction distance the image width of dislocations can be reduced. The effective extinction distance is related to the deviation from the exact Bragg condition and for large deviations the effective extinction distance is small. Hence using a **g**,3**g** diffraction condition, where the 3**g** spot is strongly excited and the weak **g** spot is used to form the image, low intensity images showing high contrast at highly strained local regions of the crystal can be formed. The dislocation image widths using this weak beam technique are substantially narrower than the image widths using two-beam diffraction conditions[6].

Using phase contrast (HREM) the sample is tilted so that the electron beam is aligned along a major crystallographic direction (pole) in the material. To form the image several diffracted beams are recombined with the transmitted beam in order that phase differences in the waves at the exit of the sample are converted into intensity differences in the image[8]. The intensities in the image are therefore a combination of phase changes (interference effects) and amplitude changes. The image contrast is also a function of the objective lens defocus and spherical aberration and the electron wavelength. It has been found[9] that at an optimum defocus the phase change introduced by the objective lens is roughly constant (out to a spatial frequency called the Scherzer resolution). This enables phase changes in the image to be directly related to structure in the sample. This defocus, called the Scherzer defocus, was used for the HREM images in this work.

2.5.2 Diffraction conditions

The implanted wafers were all examined by TEM in cross-section (c.s.) and for the majority of wafers also in plan-view (p.v.). The <110> pole c.s., because it is the easiest to prepare, was used to examine all samples and unless otherwise indicated all micrographs in this thesis are at the <110> pole. Some samples in Chapter 3 were also examined in c.s. at the <100>, <111>, <210> and <310> poles. The material was examined using the many beam

diffraction condition at the pole or close to the pole using two-beam diffraction conditions. Some material in Chapter 3 was also examined using **g**,3**g** weak beam diffraction conditions.

At the many beam diffraction condition at the poles information from all the low index planes is present in the bright field image. Further in bright field the extinction distance is less for the many beam diffraction condition at the pole than for the two-beam conditions near the pole. Hence the image width for dislocations is narrower using the many beam diffraction condition at the pole than for the possible two-beam conditions near the pole. Strain free precipitates are readily visible when $s=0$[6,7] but in this work, for the as-implanted material, the contrast from the SiO_2 precipitates was less than the contrast from the dislocations and therefore the precipitates were difficult to observe in regions of dislocation strain contrast. For the assessment of the microstructure it was desirable that the dislocations were visible. Hence minimising the bright field image width of the dislocations by using the many beam diffraction condition at the poles improves the conditions for observing the precipitates and enables both the precipitates and the dislocations to be observed in the same image. In bright field strain free precipitates are also readily visible when $s>>0$ but these are non-optimum conditions for observing dislocations[6,7]. Hence for observations where the imaging of both dislocations and precipitates was of interest, bright field images were formed using the many beam diffraction condition at the poles. Hence unless otherwise indicated the c.s. micrographs in this thesis are bright field images formed using the many beam condition at a <110> pole and the p.v. micrographs are bight field images formed using the many beam condition at the [001] pole.

In this work samples were examined using Philips CM12, Philips CM20 and JEOL 4000EX microscopes.

2.5.3 Sample Preparation

Examination of TEM samples in c.s. directly revealed the changes in microstructure with depth from the wafer surface. Plan-views provided microstructural information and a more accurate method for determining defect densities. Samples were prepared for TEM examination using Ar ion beam thinning and chemical etching. For the ion beam thinning in this work a

Gatan Dual Ion Mill was used with the Ar beam energy 5keV, beam current 40μA and angle of incidence 15°-17°, giving a sample thinning rate of ≈5μm per hour, per ion gun used.

Cross-section TEM samples were prepared using ion beam thinning by two preparation methods. In the first method, developed from the work of Roberts[10], a piece of scrap Si was glued, using Cryanoacrylate adhesive, to the sample to protect the implanted surface. The sample was mounted on a Pyrex disc with Crystal Bond wax and ground and polished with diamond paste to a thickness of 30-40μm. The final polish was with 1μm diamond paste. The sample was then dissolved from the disc in acetone. The piece of scrap Si was then removed from the sample and the sample cleaned by placing in hot (150°C) dimethylformamide. The sample was ion beam thinned from one side, using one ion gun and with no sample rotation for 4 hours[10]. The sample was then turned over and stuck down with Lacomit, to protect the side already ion beam thinned, and the second side was ion beam thinned using the same conditions until a hole was formed in the wafer surface. Typical total ion beam thinning time was 8hrs. The sample was then mounted on a grid and transferred to the microscope. In the second method, developed from the work of and Bravman *et al*[11], two samples were glued face to face, using either M-Bond 600 or epoxy adhesive. The two sample sandwich was ground and polished as described above. After polishing the sandwich was mounted on a 1.5mm diameter hole grid and then ion beam thinned from both sides simultaneously, using two ion guns and with the sample rotating, until a hole was formed in the wafer surface. A typical ion beam thinning time was 4hrs. The two samples, still glued surface to surface, were then transferred to the microscope. The first method had the advantage that it produced an electron transparent length of c.s. typically 75% longer (up to 100% longer) than the second method. This improved the accuracy of calculating the defect density from a c.s. when the defect density was low (see section 2.5.5). The second method had the advantages that it took about one third of the time to prepare a c.s. sample and c.s. from two different samples were prepared at the same time (so the effective time reduction per sample was a sixth). Due to these advantages the second method was used to prepare the majority of samples in this work. For both methods the Si all around the hole in the wafer surface was thin enough (<<0.5μm) to be electron transparent.

Where the hole reached the surface of the wafer the oxygen implanted region of the Si was thin enough to be examined in the microscope.

Plan-view samples were prepared using either ion beam thinning or chemical etching. Using ion beam thinning, the back surfaces of the samples were ground to a thickness of 40μm and polished and then the front surfaces were glued face down using Lacomit onto a piece of scrap Si so as to protect the surface. The samples were then thinned from the backside, using one ion gun and with the sample rotating, until a small hole perforated the sample. The Si around the edge of the hole was thin enough (<<0.5μm) for the sample to be examined in the electron microscope. The sample was then removed from the backing piece and cleaned by dissolving the Lacomit in hot (150°C) dimethylformamide, mounted on a grid and transferred to the microscope. This method could be used to prepare p.v. from all of the samples investigated and provided structural information about the surface Si layer and the buried SiO_2 layer.

The chemical etching technique was based on the etching away of the buried SiO_2 layer, using buffered hydroflouric acid (HF). Small pieces of sample, 2mm by 2mm, were dipped in HF until the buried oxide layer dissolved and the Si surface layer floated off. The latter was then carefully rinsed in water and floated onto a mesh grid. For examination in the microscope the thin surface Si layer was held between two mesh grids, i.e. no adhesive was used. This method could be used to prepare p.v. from samples in which the oxide layer was continuous and provided structural information about the surface silicon layer. It could not be used where the buried SiO_2 was non-continuous, i.e. for lower dose as-implanted or annealed samples, and was not practical where the defect density in the surface Si layer was high, i.e. for as-implanted high-dose implants. This was because unlike thinning by ion milling, the thickness of the p.v. sample is fixed by the thickness of the surface Si layer and so when the defect density is high the individual defects could not be resolved. It also did not provide any information about structure within the SiO_2 layer. This technique was quick compared to the time required for ion milling (typical etching times were from 5-30 minutes) and for the appropriate samples it produced flat TEM samples that were electron transparent over large areas ($\approx 1mm^2$). In the samples where the defect density in the surface Si was low the large electron transparent area

enabled an accurate determination of the defect density (see section 2.5.5). The etch rate of Si in HF, at room temperature, is $\approx$0.4nm per minute. Therefore during typical etch times, a Si thickness of 2nm to 12nm is also removed. This amount evenly removed from the surface would not affect the microstructure seen in the TEM. For samples left in the buffered HF for times of about two hours the Si did seem to undergo some localised etching. This artefact of the preparation technique can be seen as small circles or dots in the p.v. micrographs shown in Figs. 4.5g & 4.7g. This localised etching is not associated with the dislocations (Fig. 4.7g) and its origin is not understood.

2.5.4 Measuring Defect Densities in Annealed Material

The two major types of defect in the annealed material were dislocations that threaded through the surface Si layer, referred to as threading dislocations, and Si islands in the buried oxide layer. Using p.v. TEM, measuring the areal dislocation density (/cm^2) was straightforward. To estimate the densities from c.s., the area parallel to the wafer surface had to be measured. This was done by either measuring the thickness of the c.s. at either end of the piece of sample in which the defects were counted, or it was assumed that the thickness at the hole produced by ion beam thinning was zero and the thickness was measured at a measured distance from the hole. Both methods assume that the thickness varies linearly between the two points. The c.s. thickness was measured using the following method. The sample was aligned in the microscope sample holder with the wafer surface parallel to the eucentric tilt axis. After setting the eucentric height so that the samples remained at the same height during tilting, a g=220 two-beam condition close to a <110> pole was set up. The TEM c.s. was then tilted about the eucentric axis through an angle of 20°-30°. As the <220> direction is parallel to the eucentric axis then during tilting the diffraction conditions do not change (The alignment of the wafer surface and the eucentric axis could be checked by noting, after tilting, any deviation from the g=220 two-beam condition, using the Kikuchi lines.). After tilting several thickness fringes were present at the Si surface and by measuring the total width of the fringes, the thickness of the sample could be determined (fig. 2.1). The attraction of this technique was its

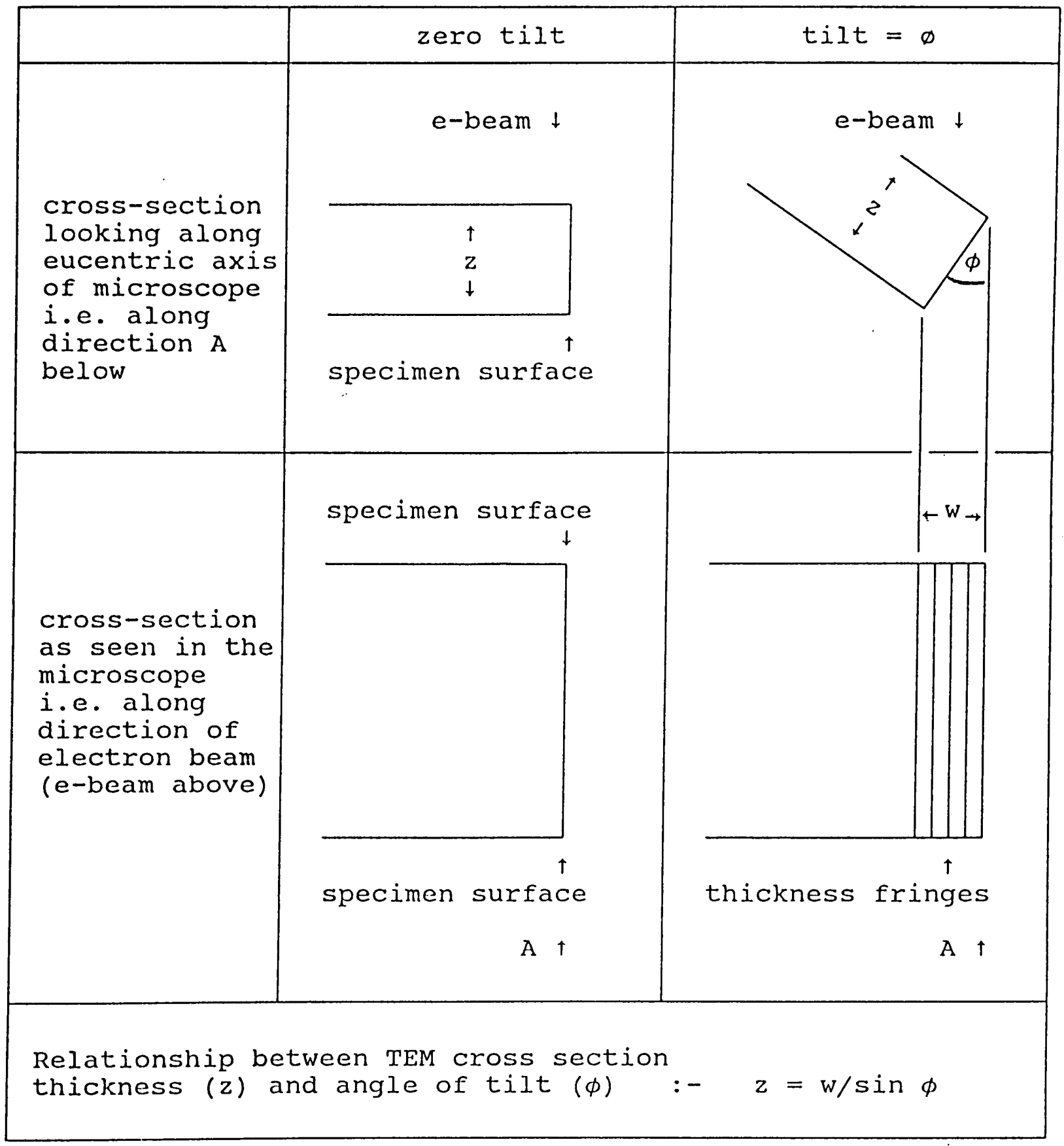

Figure 2.1 Schematic diagrams of a TEM cross-section specimen viewed along the eucentric axis of the microscope and the corresponding TEM cross-section image viewed in the direction of the electron beam, at both zero tilt and after tilting an angle ϕ about the eucentric axis. The origin of the thickness fringes and the relationship between the width of the region containing thickness fringes in the image (w), the angle of tilt (ϕ) and the cross-section specimen thickness (z) are shown.

simplicity, once the sample was correctly aligned in the holder. Misalignment of the sample surface with the eucentric axis of the holder contributed the largest error in this technique. The use of the Philips beryllium double-tilt holder with the locking washer prevented the aligned c.s from being rotated as the sample securing screw was tightened. It was estimated that this technique measured the thickness with an accuracy better than ± 10%, which was adequate for estimating the defect densities.

The minimum defect densities measurable using these techniques with c.s. samples depended on the area parallel to the wafer surface that was electron transparent. Using the first preparation method (the one side at a time thinning technique) the typical total length of electron transparent material (<0.5μm thick) on either side of the hole was 35μm (total length 70μm). This gives an area parallel to the wafer surface of $\approx 17.5\mu m^2$ ($1.75x10^{-7}cm^2$). Therefore the minimum measurable dislocation density is $6x10^6/cm^2$. Using the second preparation method (two sided thinning preparation technique), the typical total length of electron transparent material (<0.5μm thick) on either size of the hole was 20μm (total length 40μm). This gives an area parallel to the wafer surface of $\approx 10\mu m^2$ ($1x10^{-7}cm^2$). Therefore the minimum measurable dislocation density is $1x10^7/cm^2$.

Using the ion beam thinning preparation technique for p.v. samples produces a typical electron transparent area of $\approx 1000\mu m^2$ ($1x10^{-5}cm^2$). Therefore the minimum measurable defect density is $1x10^5/cm^2$. In practice to accurately determine the minimum defect density, the area covered and the minimum measurable defect density, are limited by the number of negatives it is practical to take and the high magnification at which each negative needs to be taken, which limits the area covered per negative, in order to resolve the defects being counted.

Using the chemical etching p.v. sample preparation technique, the electron transparent area is in theory only limited by the requirement to fit the thin sample onto a 3mm diameter grid and the area obscured by the two mesh grids used to hold the samples in the TEM. This means a typical maximum area of $\approx 1mm^2$ ($0.01cm^2$), which puts the minimum measurable defect density at $100/cm^2$. In practice though the thin surface Si layer is very fragile and the area of sample transferred onto the mesh grid is usually limited by the thin surface Si layer breaking

into smaller pieces during the washing in water and transferring onto the TEM grid. Further to accurately determine the minimum defect density, the area covered and the minimum measurable defect density are limited by the number of negatives it is practical to take and the high magnification at which each negative needs to be taken, which limits the area covered per negative, in order to resolve the defects being counted.

In this work when quoting minimum defect densities the use of the "<" symbol before a value, i.e. $<A/cm^2$, means that no defects were observed in an area equal to $1/A\ cm^2$.

2.5.5 Measuring layer thicknesses in annealed material

The interfaces of the buried oxide layer with the surface Si layer and the substrate under the conditions studied in this work were often wavy and Si protrusions into the oxide were sometimes present. In measuring the thickness of the buried oxide and surface Si layers the Si protrusions were ignored and to take into account the undulations in the interfaces the thickness was measured from the TEM c.s. in several places, usually three, and the average of these values taken as the value of the thickness. The maximum and minimum layer thicknesses measured for each layer were typically $\pm 5\%$ from the value determined in this way. Hence taking into account the other experimental errors the accuracy of the values of layer thickness are considered to be between 5% and 10%.

2.6 Secondary Ion Mass Spectroscopy

Secondary Ion Mass Spectroscopy (SIMS) was carried out on many samples to determine the oxygen distribution both after implantation and after annealing. A 10 keV xenon or cesium primary beam at normal incidence was used. The beam had a diameter of 100μm and was rastered over a square of dimensions 700μm. To avoid charging effects a 450-500eV electron flood gun was used during profiling. The analysis was performed on the negative, singularly charged secondary ions. In this configuration oxygen was detected whether it was present as an interstitial or in SiO_2. The ratio of oxygen to Si signals was measured to take account of fluctuations in the primary beam current and any residual surface charging effects.

For xenon and cesium primary beams the instrument background for oxygen is $10^{19}/cm^3$ and $10^{18}/cm^3$ respectively. Depth calibration was achieved by measuring the total crater depth after analysis. The intensity ratio can not be directly calibrated to an oxygen concentration because at concentrations greater than 10 atomic %, oxygen modifies both its own yield and that of Si and results in an enhancement of the intensity ratio[12]. The enhancement factor as a function of oxygen concentration has been determined by Griffin[13] and these results are used in this work to calibrate the SIMS ratio signal in terms of the oxygen concentration. The intensity ratio that corresponds to stoichiometric SiO_2 was calibrated using high purity quartz[12,13]. The SIMS analysis was carried out at the Department of Materials, Imperial College.

2.7 Computer Programs

A computer program called TRIM90[14] was used to predict the mean projected range, the depth of the maximum oxygen concentration and the depth of the vacancy production peak during implantation. The program calculates the penetration of energetic ions into solids taking into account target damage, ionization, phonon production and surface sputtering. The program is a Monte Carlo simulation, it calculates the range of each implanted ion and produces an ion distribution profile and a vacancy production profile. From the profiles the program calculates the mean projected range, the straggle, the depth of the maximum oxygen concentration, the depth of the damage peak and the average number of vacancies generated per incident ion. The program assumes the implanted material is amorphous. It is considered relevant to compare the predictions of TRIM90 with the experimental results because it is assumed that the amorphous target in the program is a reasonable approximation for the non-channelling implant direction used in this work. The predicted values of these parameters at energies used in this work are shown in Table 2.3 and an example, at 200keV, of the predicted depth distributions of the ion range and vacancy production are shown in Fig. 2.2.

The computer program PROFILE CODE[15] was used to generate the Si sputtering yields due to the implantation of $^{16}O^+$ into silicon at normal incidence. This program, based on empirical measurements[16], takes into account ion charge and mass, target charge and mass, ion

Parameter	Energy (keV)			
	50	70	90	200
Depth of peak in oxygen concentration $\hat{R}_p$(nm)	121	167	226	450
Mean projected range $\bar{R}_p$ (nm)	110	154	207	409
Straggle ΔR_p (nm)	37	47	55	89
Depth of maximum vacancy production (nm)	73	121	155	350
No of vacancies produced per incident ion	440	545	635	956

Table 2.3 The values of the implantation parameters predicted by the TRIM90[12] Monte Carlo program for oxygen atomic ions, energies 50keV, 70keV, 90keV and 200keV, into silicon.

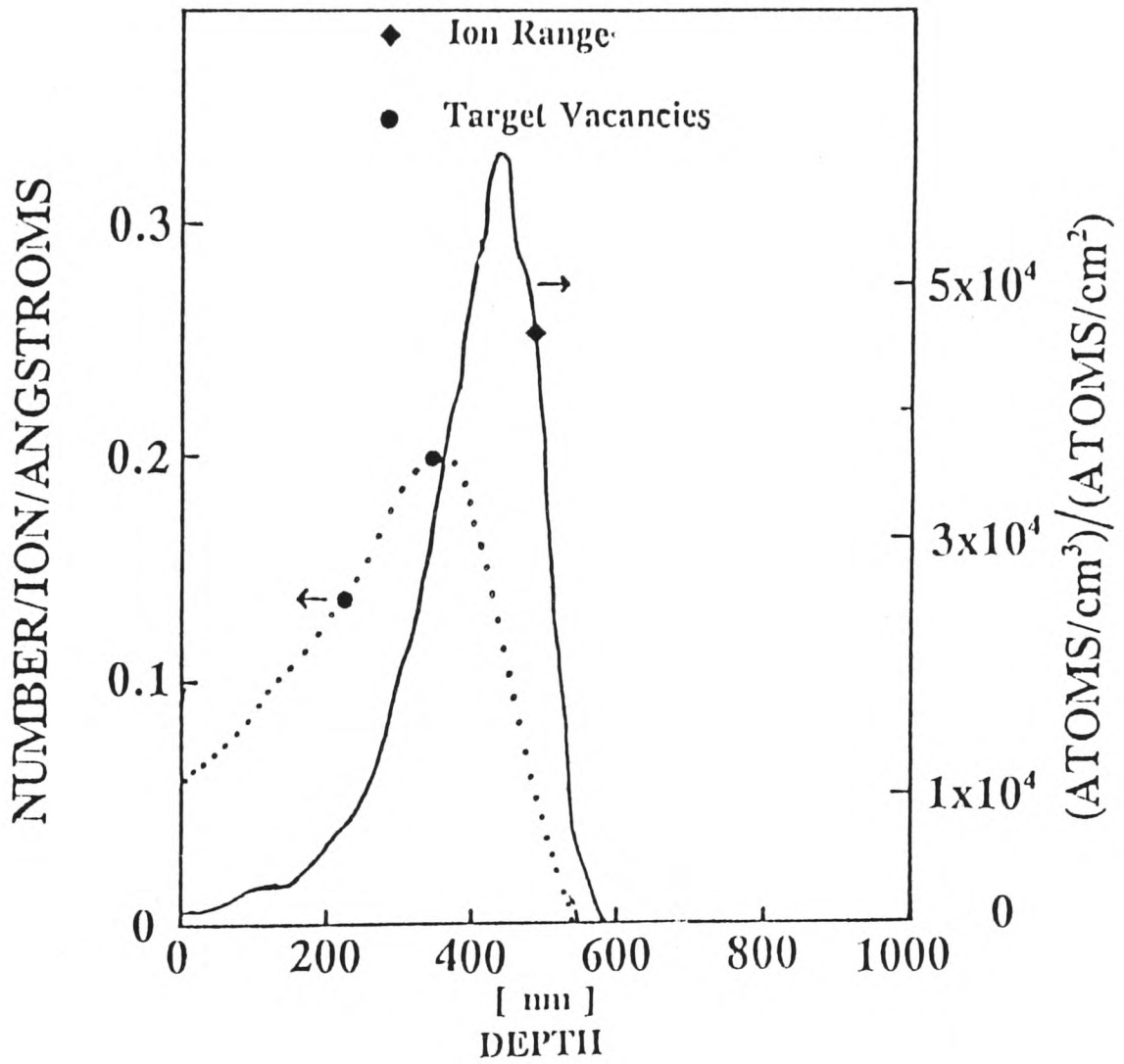

Figure 2.2 Ion range and vacancy production profiles predicted by the computer program TRIM90[12] for implanting 200keV oxygen ions into silicon. Prediction for approx. $2x10^4$ ions.

Energy (keV)	Sputtering yield (silicon atoms/incident oxygen ion)
200	0.15
90	0.25
70	0.3
50	0.35

Table 2.4 Sputtering yields of $^{16}O^+$ into Si from the computer program PROFILE CODE[13].

energy and angle of incidence. The calculated values of the sputtering yields for the energies used in this work are shown in Table 2.4.

2.8 References

[1] G Dearnley, J H Freeman, R S Nelson & J Stephens, *Ion Implantation,* Defects in Crystalline Solids vol 8, eds. S Amelinckx, R Gevers & J Nihoul (North Holland, Amsterdam, 1973).

[2] M H Badawi & K V Anand, J. Phys. D Appl. Phys. 10, p1931 (1977).

[3] A K Robinson, C D Marsh, U Bussmann, J A Kliner, Y Li, J Vanhellemont, K J Reeson, P L F Hemment & G R Booker, Nucl. Inst. & Meths. B55, p555 (1991).

[4] T G Tate, Department of Electronic Engineering, Imperial College, private communication.

[5] A Nejim, Department of Electronic Engineering, University of Surrey, private communication.

[6] P B Hirsch, A Howie, R B Nicholson, D W Pashley & M J Whelan, *Electron Microscopy of Thin Crystals* (Robert E Krieger, Florida, 1965).

[7] J W Edington, *Monographs in Practical Electron Microscopy in Materials Science* (Philips Technical Library, 1975).

[8] J L H Spence, *Experimental High Resolution Electron Microscopy* (Oxford University Press, 1980).

[9] O Scherzer, J. Appl. Phys. 20, p29 (1949).

[10] M C Roberts, D Phil Thesis, University of Oxford (1985).

[11] J C Bravman & R Sinclair, J. Elec. Micro. Tech. 1, p53 (1984).

[12] J A Kilner, S D Littlewood, P L F Hemment, E Maydell-Ondrusz & K G Stevens, Nucl.Inst. & Meths. 218, p573 (1983).

[13] C Griffin, Ph D Thesis, University of London (1989).

[14] J F Ziegler, J P Biersack & U Littmark, in *The Stopping and Ranges of Ions in Solids* vol 1, ed. J F Ziegler (Pergamon, New York, 1985).

[15] Profile Code, Implant Science Corp., Danvers MA, USA (1990).

[16] N Matsunami, Y Yamamura, Y Itikawa, N Itoh, Y Kazumata, S Miyagawa, K Morita, R Shimizu & H Tawara, At Data Nucl. Data Tables 31, p1 (1984).

Chapter 3

As-implanted Microstructure

3.1 Introduction

To help understand how the post-anneal microstructures arose, a detailed investigation was initially made of the corresponding as-implanted microstructure. Cross-section (c.s.) TEM micrographs of samples implanted at energies of 200keV, 90keV, 70keV and 50keV with doses (Φ) in the range of $0.1x10^{18}O/cm^2$ to $1.6x10^{18}O/cm^2$ are shown in Figs. 3.1, 3.14, 3.17 and 3.18 respectively. For all samples two distinct regions are present. These consist of a surface silicon (Si) layer and a buried damage/silicon dioxide (SiO_2) layer, labelled "X" and "Y", respectively, in Figs. 3.1, 3.14, 3.17 and 3.18. For all energies and doses the predicted depths of the mean projected range ($\bar{R}_p$) of the oxygen ions and the peak of the as-implanted oxygen distribution ($\hat{R}_p$), from TRIM90 (table 2.3), occur within the buried damage/SiO_2 layer. In this chapter, unless otherwise indicated, the c.s. micrographs are taken using the many beam diffraction condition at a <110> pole and the p.v. micrographs using the many beam diffraction condition at the [001] pole. Some samples are examined in c.s. at <100> and <111> poles, micrographs at these poles are also taken using the many beam diffraction condition unless otherwise indicated.

3.2 High Energy Implants at 200keV

Fig. 3.1 shows c.s. of samples after implanting doses (Φ) between $0.4x10^{18}O/cm^2$ and $1.6x10^{18}O/cm^2$, at an implantation temperature (T_i) of 680°C or 700°C with a time-averaged beam current density (I') of $5.6\mu A/cm^2$. For $\Phi = 0.4x10^{18}O/cm^2$ the surface Si and buried damage/SiO_2 layers are approximately 200nm and 550nm thick, respectively. With increasing Φ, over the range implanted, the thickness of the surface Si layer was approximately constant while the thickness of the buried damage/SiO_2 layer increased slightly. For $\Phi = 1.6x10^{18}O/cm^2$ the surface Si and buried damage/SiO_2 layers are approximately 200nm and 600nm thick, respectively. Hence the buried damage/SiO_2 layer is present approximately between the depths of 200nm and 800nm for all the doses. A large number of defects are present in the

Figure 3.1 Cross-section micrographs, at a <110> pole, of samples implanted at 200keV,
a) $\Phi = 0.4x10^{18}O/cm^2$ ($T_i = 700°C$, $I' = 5.6\mu A/cm^2$),
b) $\Phi = 0.46x10^{18}O/cm^2$ ($T_i = 700°C$, $I' = 5.6\mu A/cm^2$),
c) $\Phi = 0.6x10^{18}O/cm^2$ ($T_i = 680°C$, $I' = 5.6\mu A/cm^2$),
d) $\Phi = 0.7x10^{18}O/cm^2$ ($T_i = 680°C$, $I' = 5\mu A/cm^2$),
e) $\Phi = 1.2x10^{18}O/cm^2$ ($T_i = 700°C$, $I' = 5.6\mu A/cm^2$),
f) $\Phi = 1.6x10^{18}O/cm^2$ ($T_i = 700°C$, $I' = 5.6\mu A/cm^2$),
showing the surface silicon layer (X), the buried damage/oxide layer (Y), the substrate (Z) and the depth of the mean projected range ($\overline{R}_p$, from TRIM90[19]).

a)

b)

c)

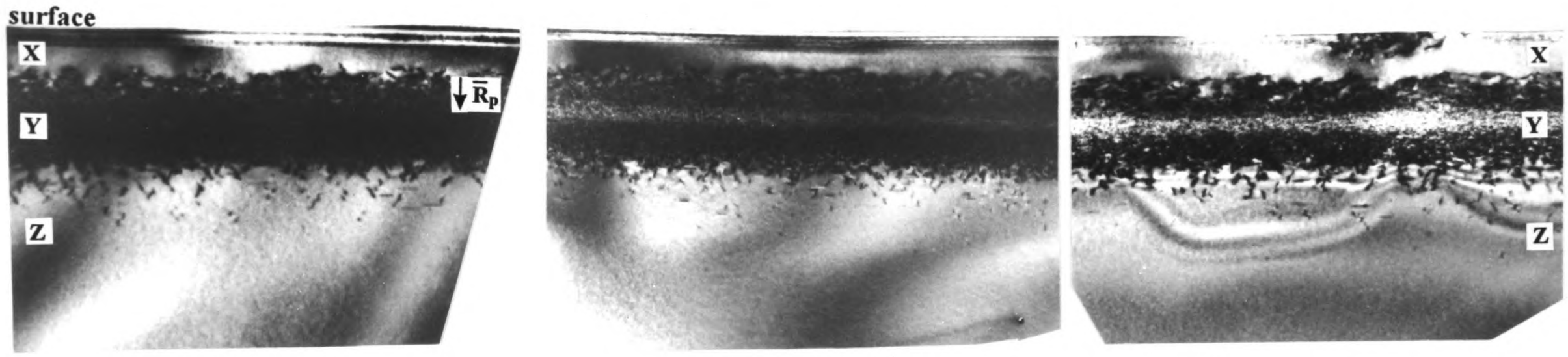

0.5μm

d)

e)

f)

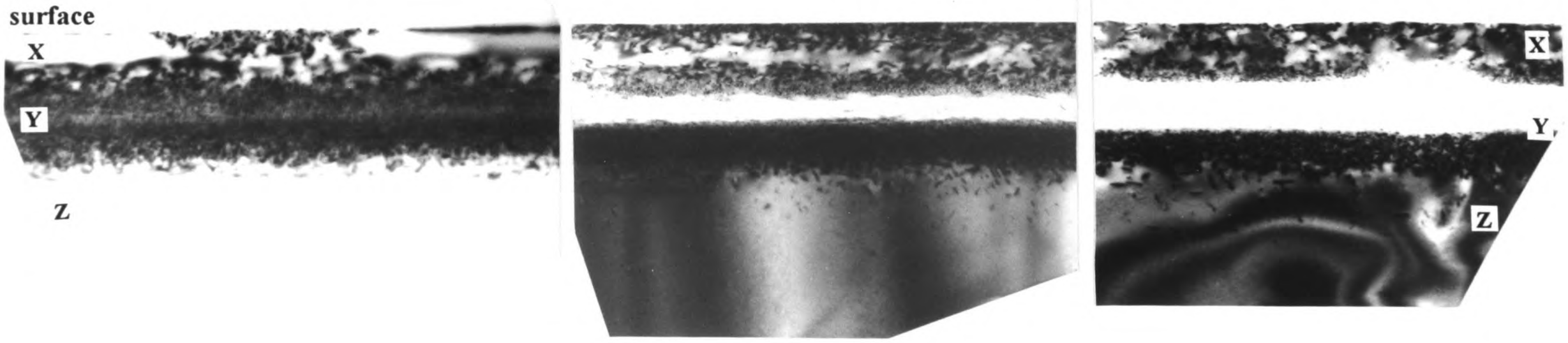

damage/SiO_2 layer but for the higher doses defects are also present in the surface Si layer at the wafer surface consisting of dislocations and small defects lying on {111} planes, shown later to be stacking faults (SF) (fig. 3.2). No defects are observed for a dose of $0.4x10^{18}O/cm^2$ but with increasing dose, the dislocations and SF first occur at the wafer surface and then the depth to which the dislocations are present increases with increasing dose, e.g. for a dose of $1.2x10^{18}O/cm^2$ the dislocations are present only at the wafer surface, while for a dose of $1.6x10^{18}O/cm^2$ the dislocations are present throughout the surface Si layer (fig. 3.1). For doses $0.46x10^{18}O/cm^2$ to $0.7x10^{18}O/cm^2$ the distribution of the dislocations and SF at the wafer surface is not uniform across the implanted area (fig. 3.1). In plan-view (p.v.) these regions of defects are rectangular in shape, with edges following approximately the Si <100> crystallographic directions (fig. 3.3) (the edges of the defected regions are not abrupt in p.v., as the dislocation segments themselves do not follow the <100> directions).

This is the first known observation of such non-uniform distribution across the implanted area of the defects at the wafer surface and hence also that these defect regions have, in p.v., an approximately geometric shape (rectangle). These rectangular regions of defects are randomly distributed across the implanted area. Some of the defect regions in the sample implanted with $0.7x10^{18}O/cm^2$ consist of adjacent rectangular regions that are merged together (fig. 3.3c). For doses of $0.4x10^{18}O/cm^2$, $0.46x10^{18}O/cm^2$ to $0.56x10^{18}O/cm^2$ and $0.6x10^{18}O/cm^2$ to $0.7x10^{18}O/cm^2$, the regions of defects are not observed in either c.s. or p.v., are observed only in p.v., and are observed in both p.v. and c.s., respectively. The density of the surface defect regions are $<10^5/cm^2$, $4\text{-}6x10^6/cm^2$ and $\geq 1x10^7/cm^2$, respectively, for these three dose ranges (table 3.1). The percentage of the implanted area that contains the defects at the surface increases with increasing dose for I' = $5.6\mu A/cm^2$ or $5\mu A/cm^2$ (fig. 3.4 & table 3.1) and decreases with increasing I' for a dose of $0.7x10^{18}O/cm^2$ (fig. 3.5 & table 3.2). The increase in the crystal disorder with increasing dose is also evident from Rutherford backscattering spectroscopy (RBS) results[1] where the average long range crystallographic order (χ_{min}) of the near surface region increases from 3.1% (equivalent to unimplanted Si) for the doses of $\leq 0.7x10^{18}O/cm^2$ to 34% for the dose of $1.6x10^{18}O/cm^2$.

Figure 3.2 Cross-section micrograph, at a <110> pole, of the sample implanted at 200keV, Φ = $0.6x10^{18}O/cm^2$, I' = $5.6\mu A/cm^2$, T_i = 680°C, showing that the defects at the surface consist of stacking faults (SF) and dislocations (D). Note the presence of spherical (P) and spheriodal (S) inclusions.

Figure 3.3 Plan-view micrographs, at the [001] pole, of the regions of defects in the samples implanted at 200keV,

a) $\Phi = 0.56x10^{18}O/cm^2$, I' = $5.6\mu A/cm^2$, T_i = 680°C,

b) $\Phi = 0.6x10^{18}O/cm^2$, I' = $5.6\mu A/cm^2$, T_i = 700°C,

showing that the regions are rectangular in shape with edges parallel with the <100> directions,

c) $\Phi = 0.7x10^{18}O/cm^2$, I' = $5\mu A/cm^2$, T_i = 680°C, showing that some of the regions of defects consist of adjacent rectangles which have merged together.

Figure 3.2

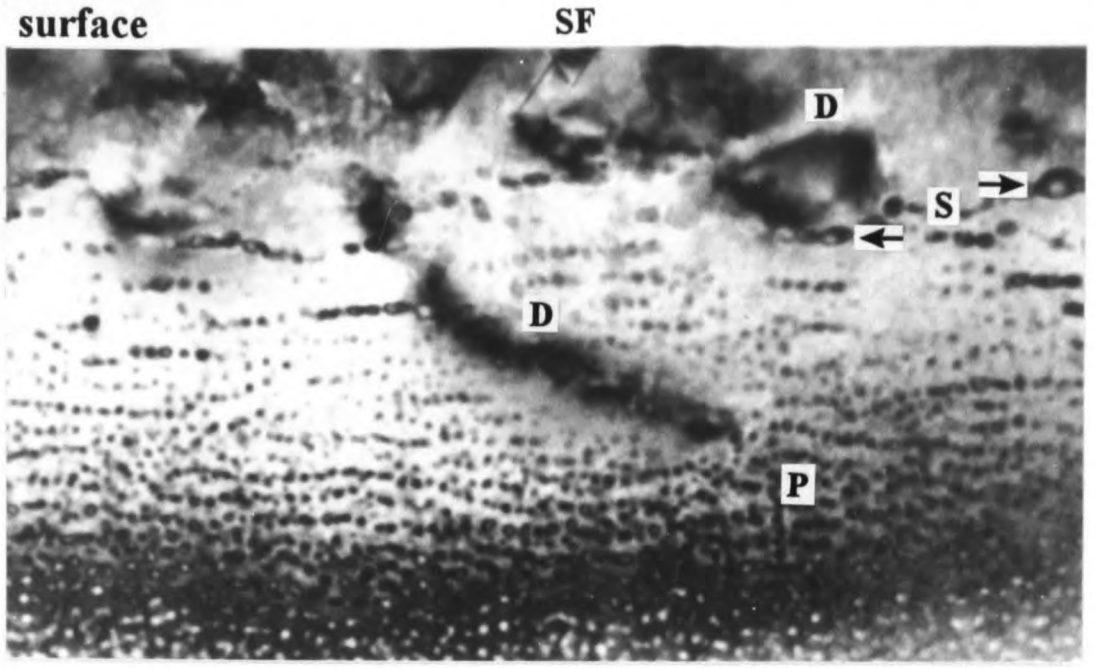

Figure 3.3

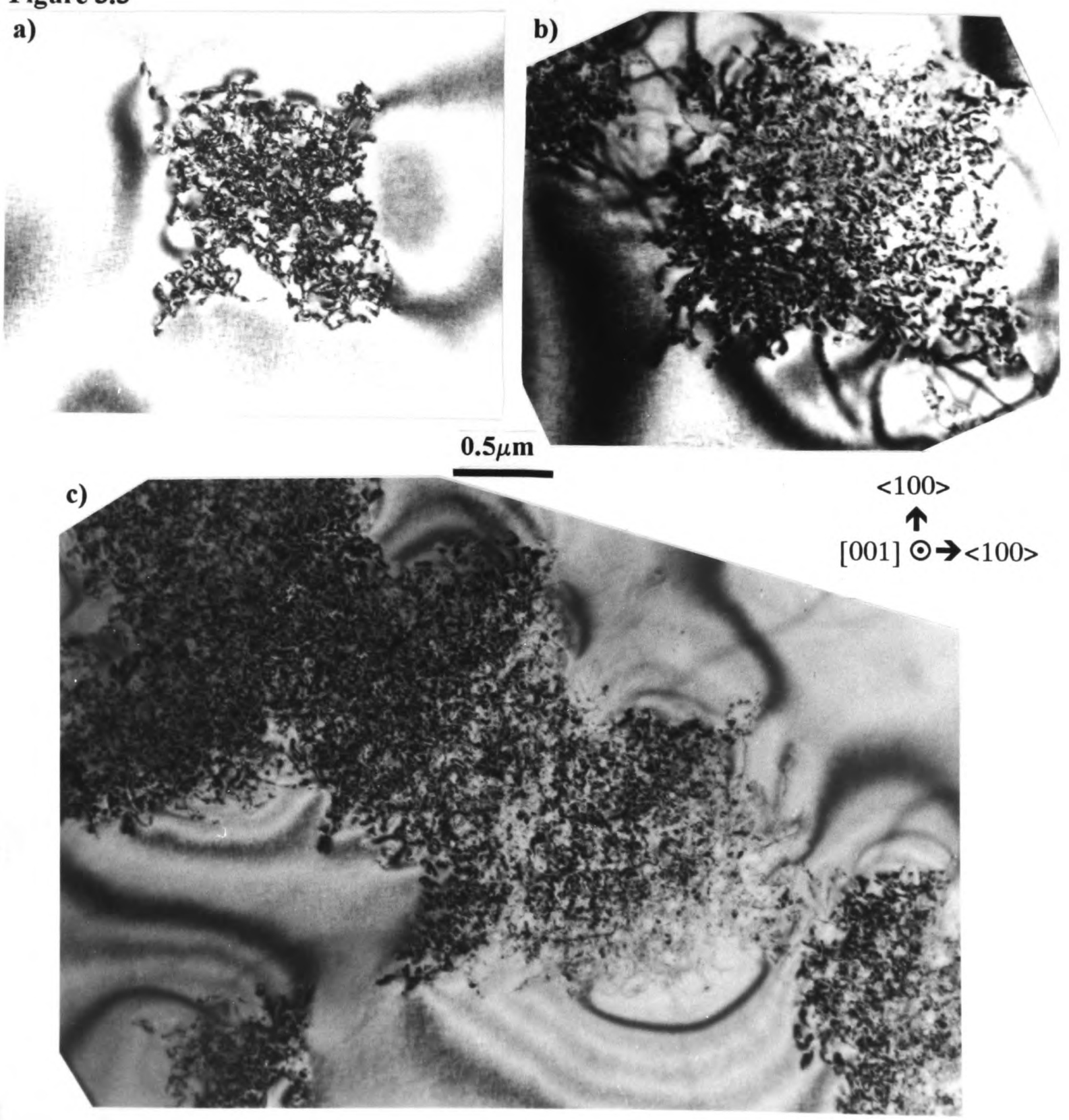

Figure 3.4 Plan-view micrographs, at the [001] pole, of the samples implanted at 200keV,
a) $\Phi = 0.46 \times 10^{18} O/cm^2$, $I' = 5.6 \mu A/cm^2$, $T_i = 700°C$,
b) $\Phi = 0.6 \times 10^{18} O/cm^2$, $I' = 5.6 \mu A/cm^2$, $T_i = 680°C$,
c) $\Phi = 0.72 \times 10^{18} O/cm^2$, $I' = 5 \mu A/cm^2$, $T_i = 680°C$,
showing regions of the defects at the wafer surface (A) and the increase in the fraction of the surface area that contains the defects with increasing dose. The directions shown in the top right hand corner of a) apply also to b) and c).

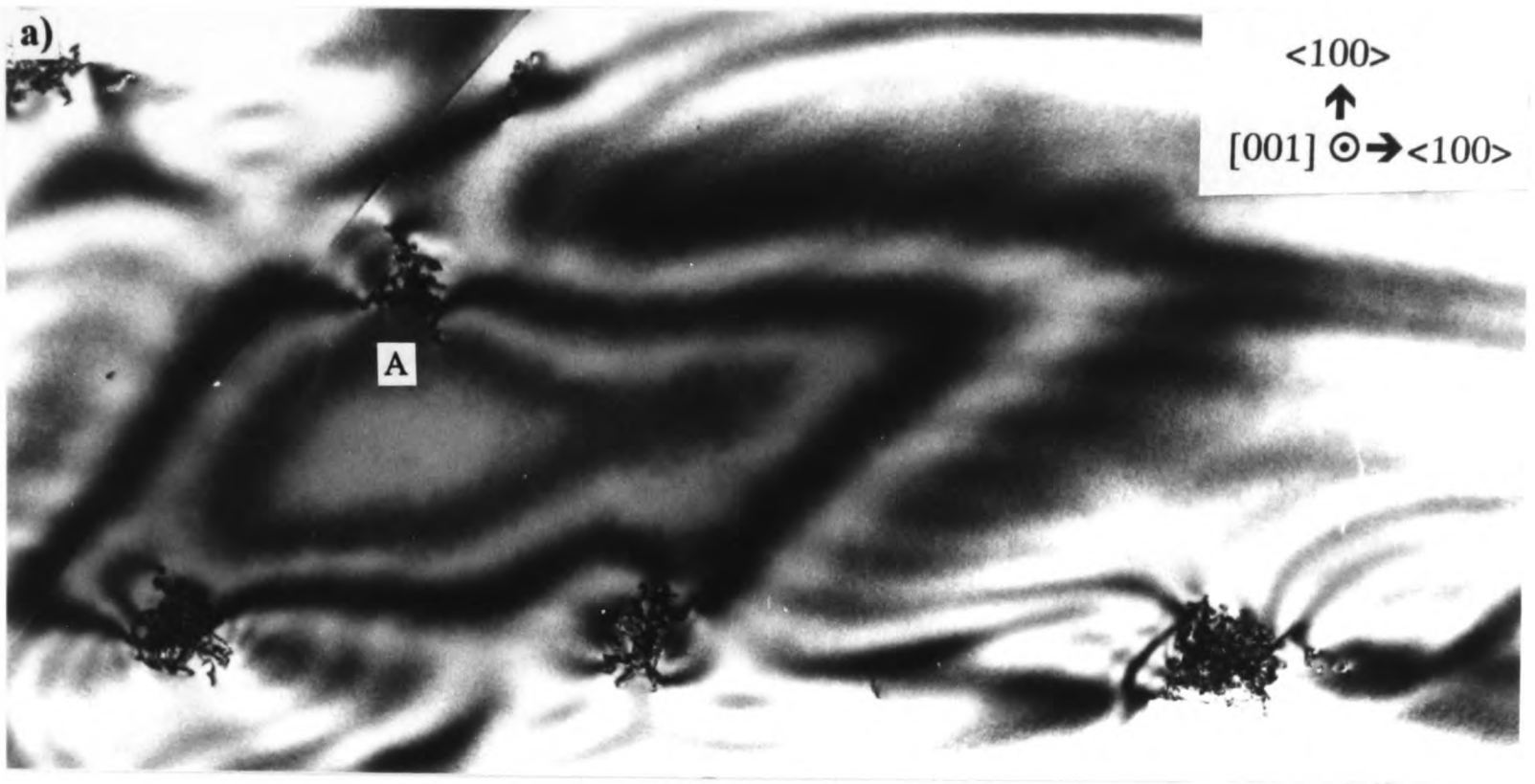
a)
<100>
[001] ⊙→<100>
A

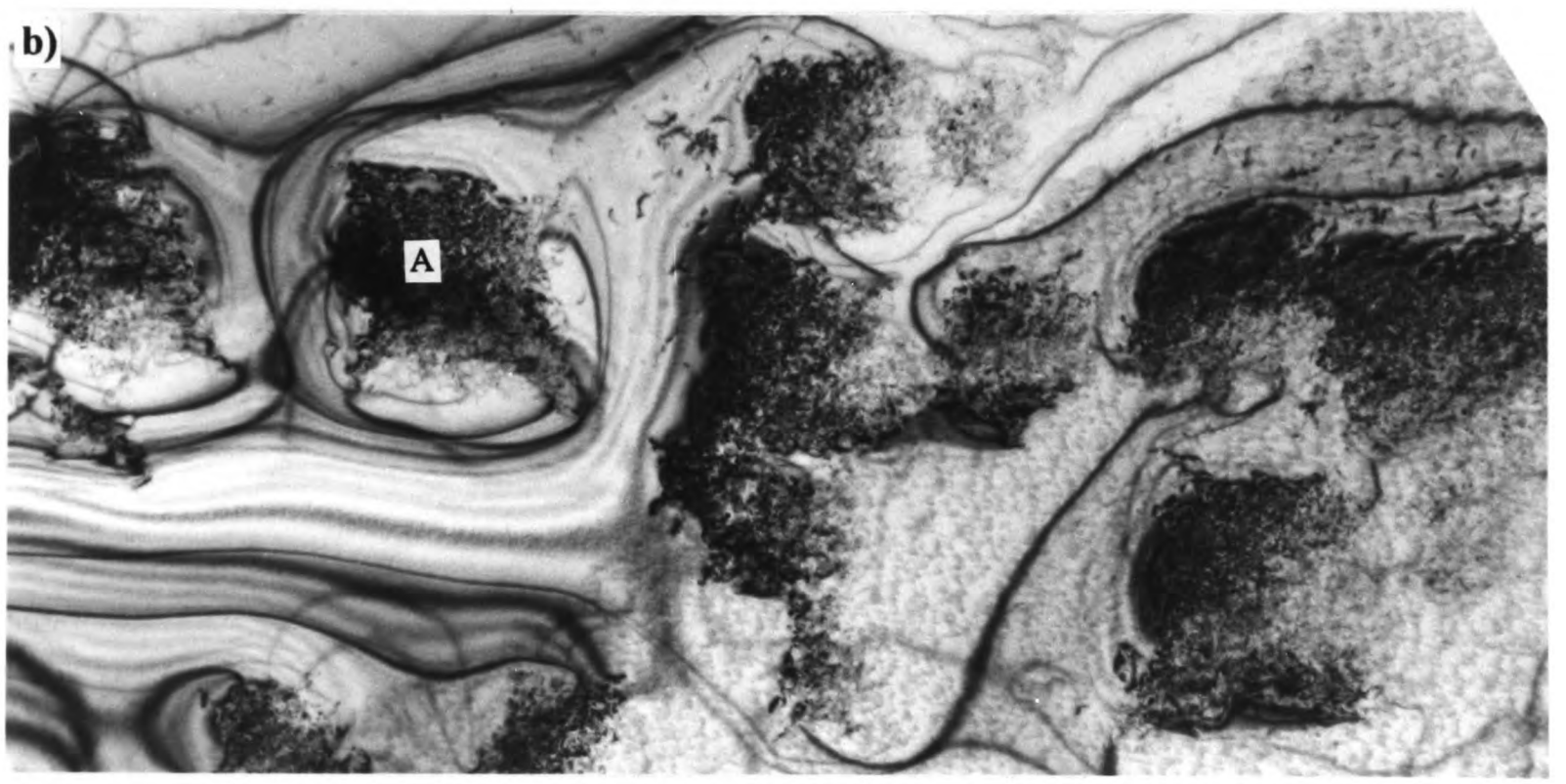
b)
A

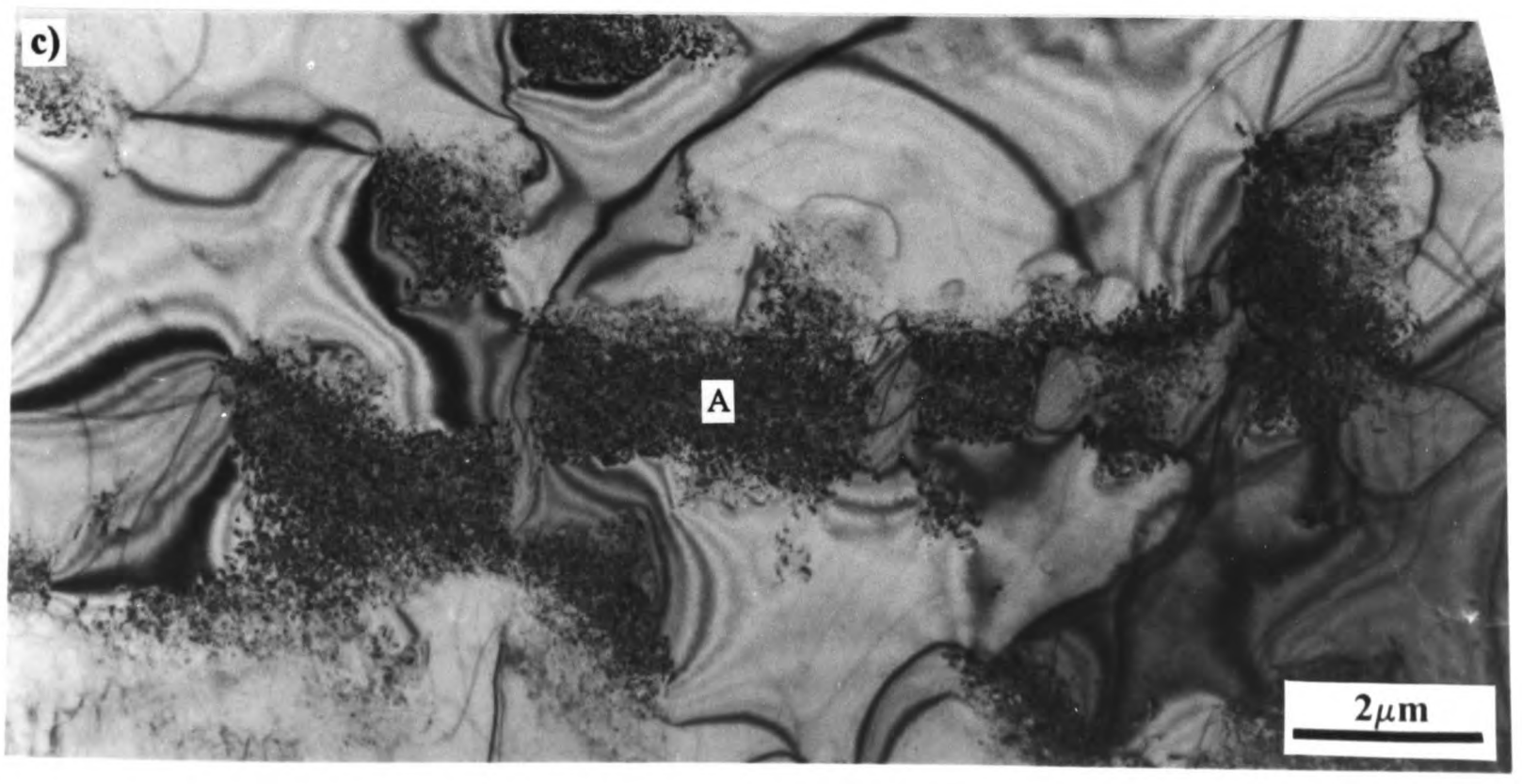
c)
A
2μm

Figure 3.5 Plan-view micrographs, at the [001] pole, of samples implanted at 200keV, T_i = 680°C,

a) I' = 2.5μA/cm^2 (Φ = 0.7x10^{18}O/cm^2),

b) I' = 3.75μA/cm^2 (Φ = 0.69x10^{18}O/cm^2),

c) I' = 5μA/cm^2 (Φ = 0.72x10^{18}O/cm^2),

showing regions of the defects at the wafer surface (A) and the decrease in the fraction of the surface area that contains the defects with increasing I'. The directions shown in the top right hand corner of a) apply also to b) and c).

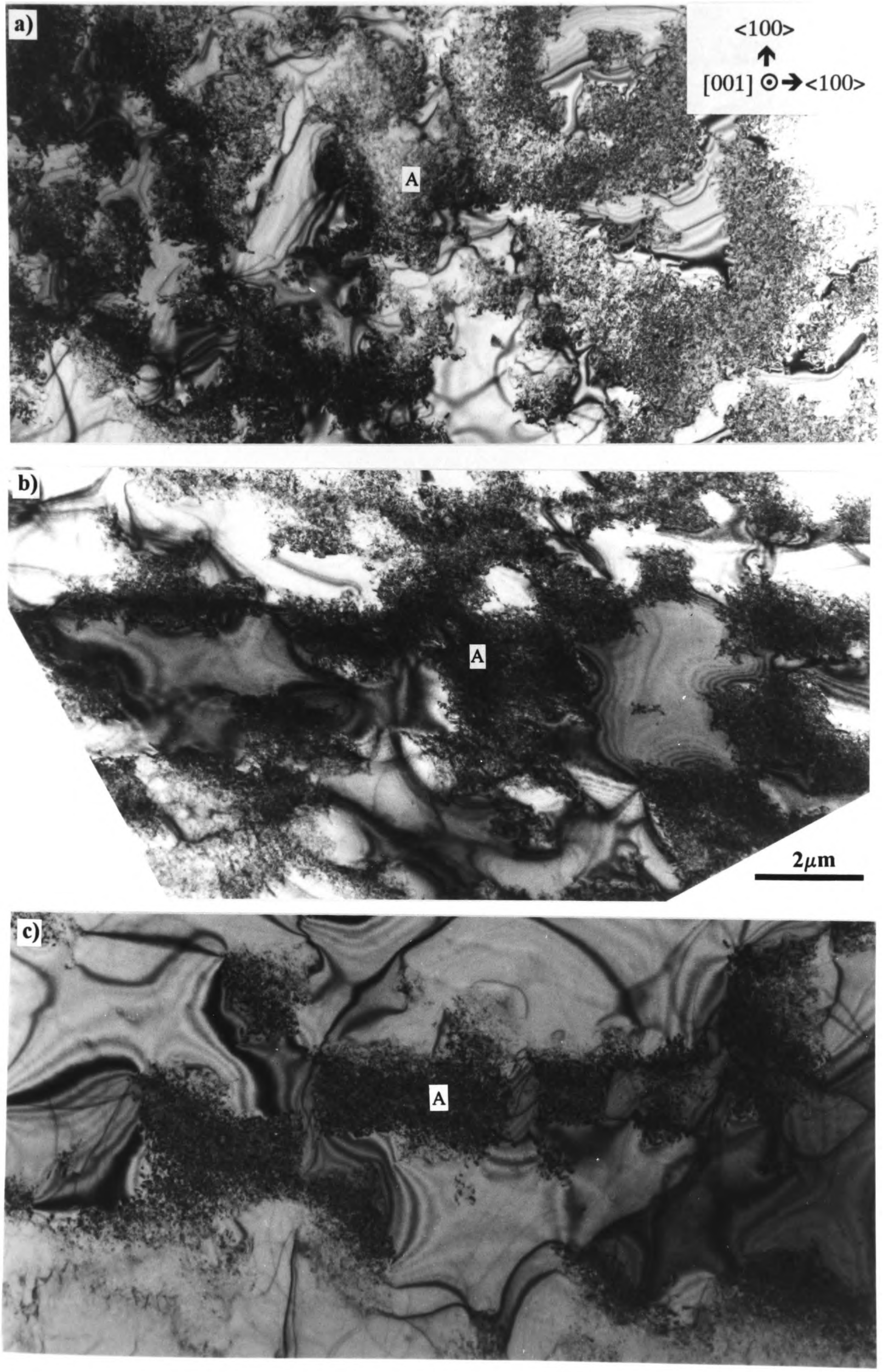
a)
<100>
[001] ⊙→<100>
A
b)
A
2μm
c)
A

	Dose ($x10^{18}O^+/cm^2$)					
	0.4	0.46	0.56	0.6	0.7	1.2
Density of the rectangular regions of defects at the wafer surface ($/cm^2$)	$<10^{5\#}$	$4x10^6$	$6x10^6$	$1x10^7$	$>10^{7*}$	-
Percentage of the implanted area containing defects at the surface (%)	-	3	2	25	33	100

Table 3.1 Density of the rectangular regions of defects at the wafer surface and the percentage of the implanted area containing these surface defects as a function of dose. #no defect regions observed in p.v. *a more accurate defect density was difficult to calculate due to the overlapping of many of the rectangular defect regions. The beam current density was $5.6\mu A/cm^2$ for all doses except for the dose of $0.7x10^{18}O^+/cm^2$ where it was $5\mu A/cm^2$. Energy = 200keV.

	Current density ($\mu A/cm^2$)		
	2.5	3.75	5
Percentage of the implanted area containing defects at the surface (%)	80	70	33

Table 3.2 Percentage of the implanted area containing surface defects as a function of beam current density (I') (Energy 200keV, at I' = $2.5\mu A/cm^2$, dose = $0.7x10^{18}O^+/cm^2$, at I' = $3.75\mu A/cm^2$, dose = $0.69x10^{18}O^+/cm^2$, at I' = $5\mu A/cm^2$, dose = $0.72x10^{18}O^+/cm^2$).

Dose ($x10^{18}O^+/cm^2$)	Denuded zone width (nm)
0.4	60
0.6	45
1.2	20
1.6	not observed

Table 3.3 The oxide precipitate denuded zone width as a function of the implanted dose, for 200keV implants (beam current density = $5.6\mu A/cm^2$).

The small defects lying on the {111} planes are present at the wafer surface for doses between $0.4x10^{18}O/cm^2$ and $0.7x10^{18}O/cm^2$. HREM images of the defects in which the structure could be interpreted were difficult to obtain, probably due to the presence of background strain from the nearby dislocations. HREM images of one defect showed it to be a SF (fig. 3.6). It was close to the thin edge of the c.s. sample and hence, because the sample is thin (confirmed below), the Si {111} lattice planes in this image are represented by lines of either black or white dots. Along the centre of the SF image lie black dots and their position is displaced relative to the lines of black dots inclined to the SF on either side. At the SF no white dots are displaced relative to the lines of white dots inclined to the SF on either side. By considering the symmetry in this projection of intrinsic and extrinsic SF and their possible images (black spots representing atoms or tunnels), this means the SF must be intrinsic (for an extrinsic fault two black dots and one white dot, or vice versa, depending on which represent atoms or tunnels, would be displaced relative to the inclined lines of the same type dots on either side of the fault)[2,3,4,5]. For an intrinsic fault the displaced dot at the SF represents the position of the atom columns and hence in this image the black dots represent the position of the atoms[2,3,4,5]. Comparison with simulated images generated by the computer program SHRLI[5] gave the best fit with the experimental image of the Si surrounding the SF with the back dots representing atoms (thickness and defocus values 7.5nm and -35nm, respectively), hence confirming the above conclusions. Finally drawing a Burgers circuit around the dislocation at the lower end of the SF shows that the inclined set of {111} planes are displaced by $^2/_3\ d_{111}$ (where d_{111} is the {111} lattice plane spacing) as they cross the fault, which is consistent with the defect being a SF.

Fig. 3.2 shows that spherical and spheroidal inclusions are present in the surface Si layer and at the wafer surface there is a zone denuded of inclusions. For doses $\leq 0.7x10^{18}O/cm^2$ the majority of the dislocations were present only in this denuded zone (fig. 3.7a). Where dislocations were observed at the same depth as the inclusions, the dislocation density was lower at the depth of the inclusions than in the denuded zone above (fig. 3.7b).

The contrast from the inclusions was sensitive to the inclusion density, TEM sample thickness, whether the inclusion is present all the way through the TEM sample, image focus, presence of Si thickness fringes and the depth within the TEM sample. In the as-implanted

Figure 3.6 Cross-section HREM micrograph, at a <110> pole, of a stacking fault at the wafer surface in the sample implanted at 200keV, $\Phi = 0.6 \times 10^{18} O/cm^2$, $T_i = 680°C$, $I' = 5.6 \mu A/cm^2$. Analysis of the stacking fault (see text) shows that it is intrinsic.

Figure 3.7 Cross-section micrographs, at a <100> pole, of the sample implanted at 200keV, $\Phi = 0.6 \times 10^{18} O/cm^2$, $T_i = 680°C$, $I' = 5.6 \mu A/cm^2$, showing,

a) the dislocations (D) are mainly confined to the zone (Z) denuded of inclusions,

b) when they are present at the same depth as the inclusions, the dislocations (D) occur at a lower density than in the denuded zone above.

Figure 3.6

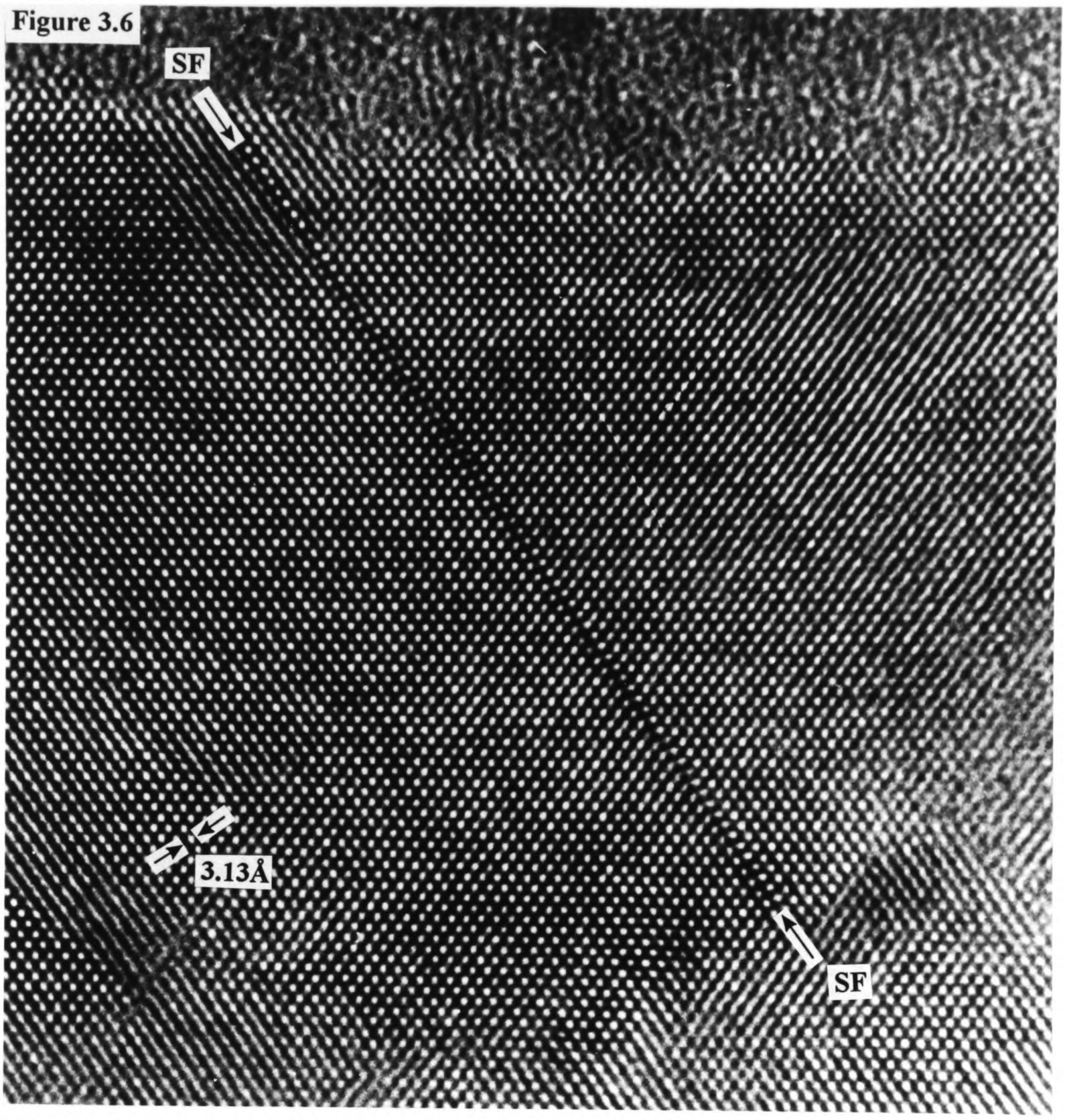

Figure 3.7

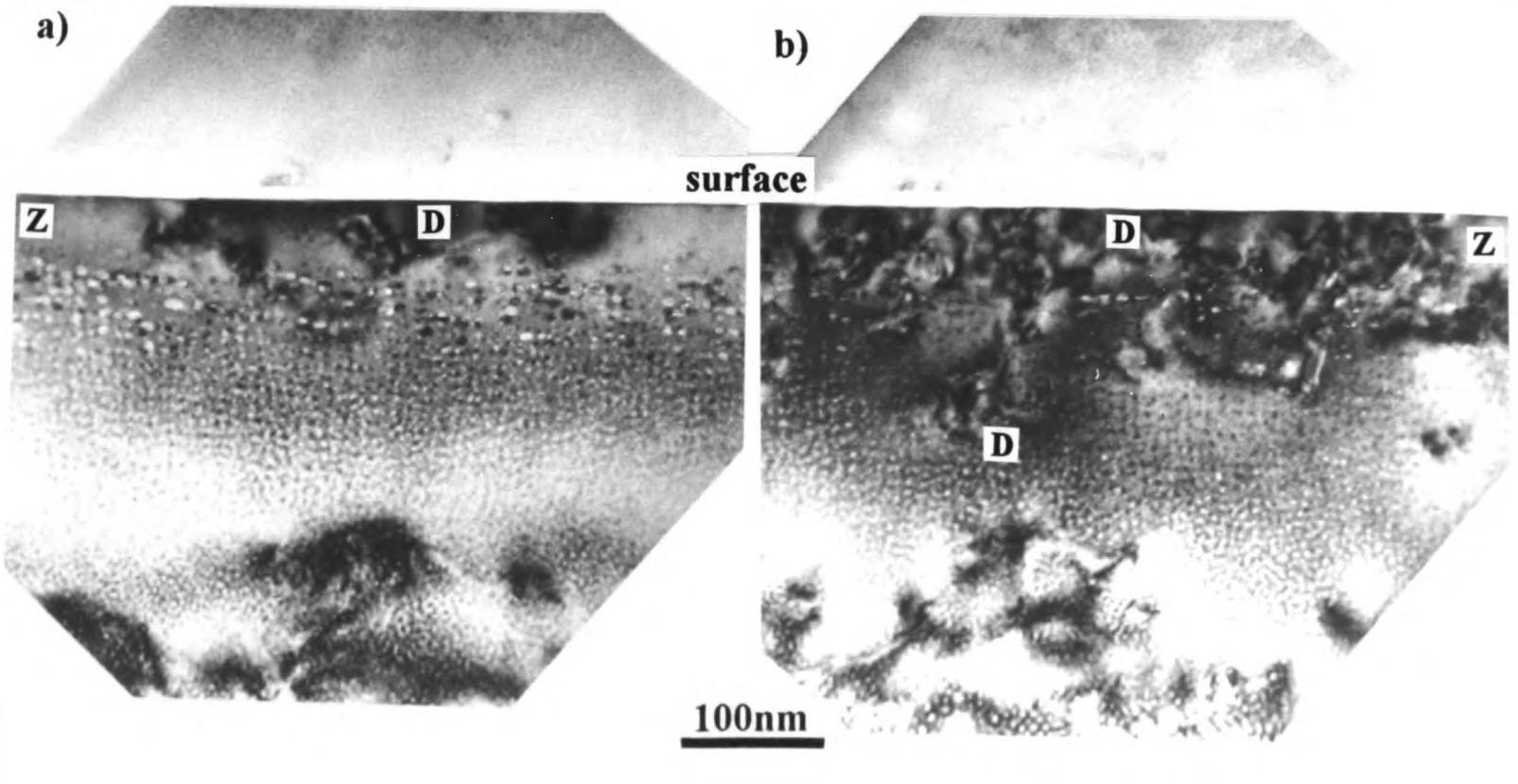

samples the inclusion density was high (e.g. fig. 3.2) but where the TEM sample was very thin (of the order of the nearest neighbour spacing $\approx$ 10nm) individual inclusions could be resolved. When the TEM c.s. sample was thicker or the inclusion density was higher a speckle/worm-like contrast, similar to that from amorphous SiO_2, originating from the overlapping oxide inclusions was present. In bright field at-focus images, using the many beam diffraction condition at the pole the buried SiO_2 layers (for high doses at the peak of the oxygen concentration) were lighter than the surrounding Si. For the latter the brighter intensity than the surrounding Si is due to the amorphous oxide scattering fewer electrons out of the transmitted beam than the crystalline Si. If the inclusions were SiO_2, or voids containing oxygen gas, the scattering of fewer electrons out of the transmitted beam might be expected to occur because of the lower atomic number of oxygen and the lower density of SiO_2 (2.2g/cm^3) and oxygen gas, compared to Si (2.3g/cm^3).

For over-focussed images the inclusions were darker than the surrounding Si and for under-focused images the inclusions were lighter than the surrounding Si. For areas of TEM samples <5 extinction distances (ε_g) thick, thickness fringes due to dynamical diffraction intensity oscillations in the transmitted and diffracted beams are present. The presence of inclusions in a column of Si effectively reduces the thickness of the Si in that column, and hence for the same sample thickness the intensity from the column of Si containing inclusions and a column containing only Si will be different, and as a function of sample thickness the intensities will oscillate out of phase. This qualitatively explains why, when thickness fringes are present, the inclusion contrast can be darker or lighter than the background Si intensity or very weak when the background Si intensity is dark or light and hence why the inclusion contrast can change with distance from the wafer surface in a c.s. sample. In this work because of the desire to resolve individual inclusions, areas of TEM samples of thickness $<5\varepsilon_g$ were often examined and hence the effect of sample thickness and dynamical diffraction plays an important role in determining the contrast observed from the inclusions in the micrographs presented in this work. These contrast effects are consistent with amorphous precipitates or voids[6,7,8].

HREM image contrast from the spherical inclusions suggest that they are amorphous and because oxygen is being implanted, Si oxide precipitates would be expected. Stochiometric SiO_2 is the commonest Si oxide and this is therefore considered the most probable composition of the

oxide precipitates. Hence in the rest of this thesis the spherical inclusions (fig. 3.2) are referred to as oxide precipitates. Although no HREM images were obtained from the spheroidal inclusions (fig. 3.2) they could also be oxide precipitates, but it is possible, based on reports in the literature, that these inclusions are voids. This is discussed in section 3.11. In the rest of this thesis because the spheroidal inclusions could be oxide precipitates or voids they will continue to be referred to as spheroidal inclusions.

The inclusion distribution in the surface Si layer after implanting a dose of $0.6x10^{18}O/cm^2$ consists of a denuded zone at the wafer surface to a depth of 45nm, spheroidal inclusions with diameters $\leq$7nm between depths of 45nm and 100nm, and a high density of oxide precipitates with diameters $\leq$4nm at depths greater than 100nm (fig. 3.8a). The width of the denuded zone decreases with increasing dose, for I' = $5.6\mu A/cm^2$ (fig. 3.9 & table 3.3) and increasing I', for a dose of $0.7x10^{18}O/cm^2$ (fig. 3.10). Plan-views and <100> c.s. show that the spheroidal inclusions at the edge of the denuded zone are aligned in <100> directions (fig. 3.8). In <110> c.s. they appear either randomly distributed or in linear arrays parallel to the wafer surface (fig. 3.10). The size of the largest of the spheroidal inclusions increases with increasing I', for a dose of $0.7x10^{18}O/cm^2$ (fig. 3.10). The spheroidal inclusions are present at lower densities in areas where dislocations are present at this depth (fig. 3.11). Cross-sections at a <100> pole indicate that the oxide precipitates, at depths immediately below the inclusions, are present in a square array, periodicity 4nm, and at depths further from the surface in a random distribution (figs. 3.8a, 3.9b & 3.9c). Long exposure SADPs from the depth of the square array showed extra diffraction spots in the <100> directions (fig. 3.8b) corresponding to the presence of an ordered structure with a periodicity of 4nm in the <100> directions. For doses of $1.2x10^{18}O/cm^2$ and $1.6x10^{18}O/cm^2$ [001] columnar and irregular precipitates are present in the surface Si layer (fig. 3.12b).

The buried damage/SiO_2 layer, for doses $<1.2x10^{18}O/cm^2$, consists of SiO_2 precipitates and damaged Si. For doses of $0.4x10^{18}O/cm^2$ to $0.7x10^{18}O/cm^2$ the precipitate morphology consists of [001] columnar SiO_2 precipitates (fig. 3.12a). For a dose of $1.2x10^{18}O/cm^2$ a continuous amorphous SiO_2 layer containing isolated Si "ribbons" is formed (fig. 3.1 & 3.12b). SADPs from this region show that the dark ribbons are Si at the same orientation as the

Figure 3.8,

a) cross-section micrograph, at a <100> pole, of the sample implanted at 200keV, Φ = $0.6x10^{18}O/cm^2$, T_i = 680°C, I' = $5.6\mu A/cm^2$, showing the denuded zone (Z), spheroidal inclusions (S) and oxide precipitates (P). The precipitates are aligned in a square pattern suggesting that they are ordered in a cubic array,

b) long exposure <100> SADP, using a selected area aperture corresponding to a $0.25\mu m$ diameter area, from the surface silicon layer of the sample in a), which shows extra spots in the <100> directions (examples arrowed) close to the main diffraction spots corresponding to an ordered structure with a periodicity of 4nm,

c) plan-view micrograph, at the [001] pole of the sample in a), showing the spheroidal inclusions are approximately aligned along the <100> directions.

a)

surface

Z

S

P

50nm

b)

(004)

{220}

{220}

transmitted spot

c)

50nm

<100>

[001] ⊙→<100>

Figure 3.9 Cross-section micrographs of samples implanted at 200keV,
a) $\Phi = 0.4x10^{18}O/cm^2$ ($T_i = 700°C$, $I' = 5.6\mu A/cm^2$), at a <110> pole,
b) $\Phi = 0.6x10^{18}O/cm^2$ ($T_i = 680°C$, $I' = 5.6\mu A/cm^2$), at a <100> pole,
c) $\Phi = 1.2x10^{18}O/cm^2$ ($T_i = 700°C$, $I' = 5.6\mu A/cm^2$), at a <100> pole,
showing that the width of the denuded zone (Z) decreases with increasing dose. b) and c) are at a <100> pole and the oxide precipitates (P) are in a square pattern suggesting they are ordered in a cubic array (also shown in fig. 3.8 and discussed in the text). S = spheroidal inclusions.

Figure 3.10 Cross-section micrographs, at a <110> pole, of samples implanted at 200keV, $\Phi = 0.7x10^{18}O/cm^2$, $T_i = 680°C$,
a) $I' = 2.5\mu A/cm^2$,
b) $I' = 6.25\mu A/cm^2$,
showing that the thickness of the denuded zone (Z) decreases with increasing I' and the size of the larger spheriodal inclusions (S) increases with increasing I' (P = oxide precipitates).

Figure 3.9

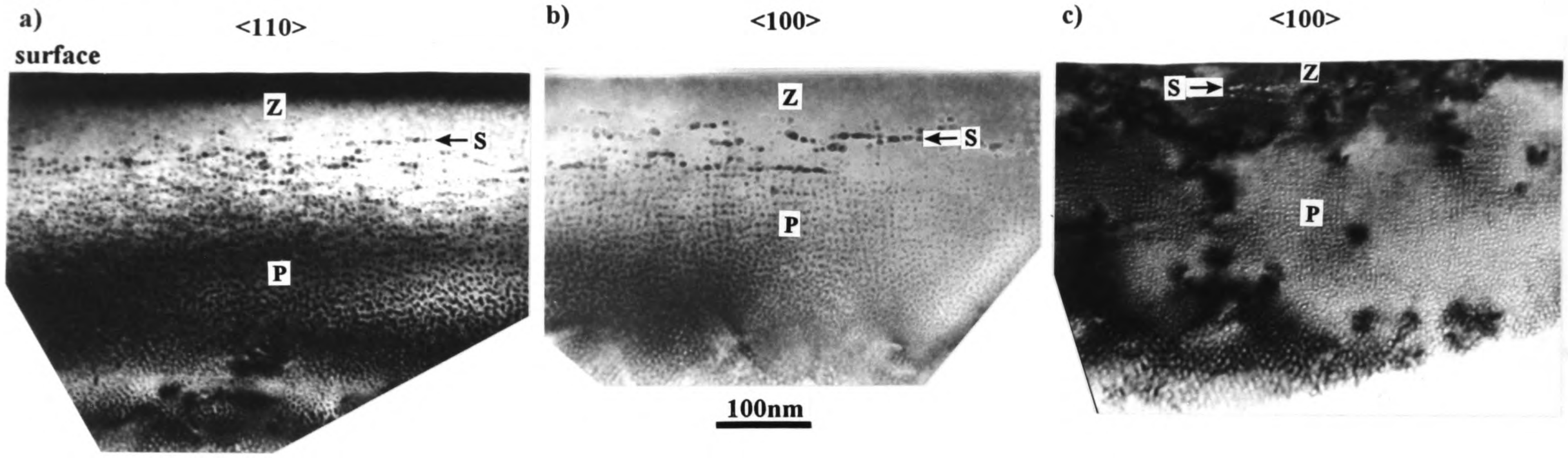

Figure 3.10

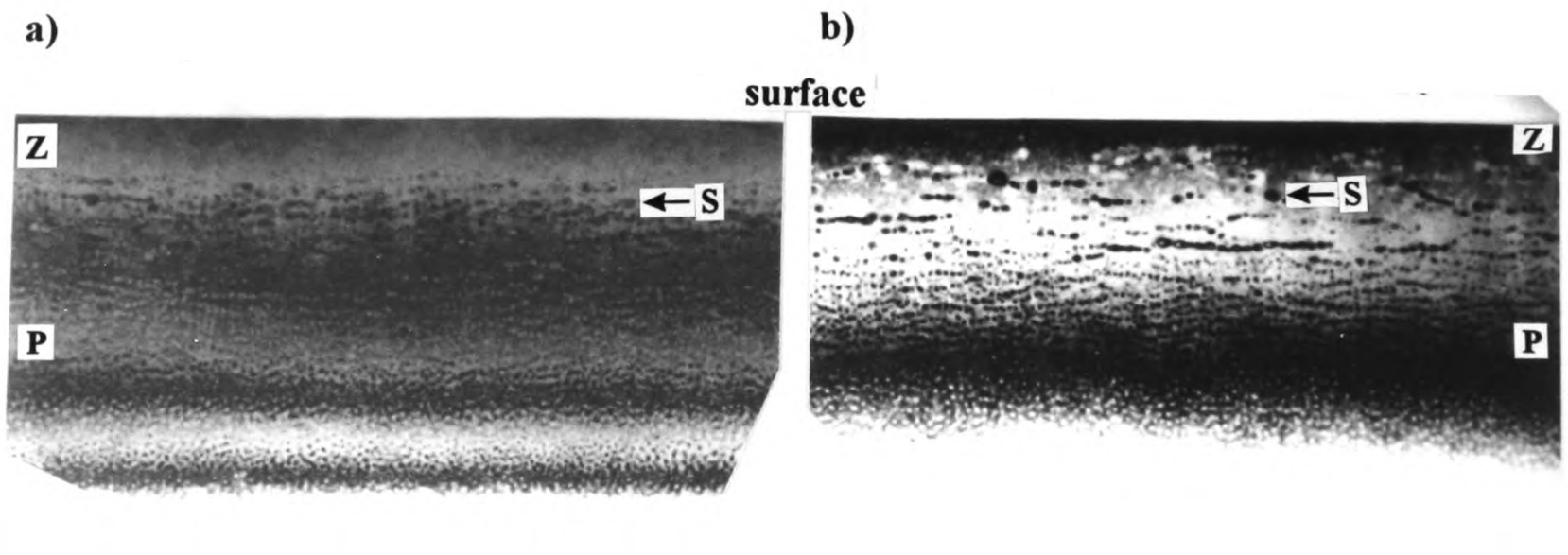

Figure 3.11 Cross-section micrographs, at <110> poles, of samples implanted at 200keV, T_i = 680°C,

a) I' = 5μA/cm^2 (Φ = 0.72x10^{18}O/cm^2),

b) I' = 6.25μA/cm^2 (Φ = 0.7x10^{18}O/cm^2),

showing different areas of the wafers containing either a high density of spheroidal inclusions and a low density of dislocations (A) or a high density of dislocations and a low density of inclusions (B). D = dislocations and S = spheroidal inclusions.

Figure 3.12 Cross-section micrographs, at a <110> pole, of samples implanted at 200keV, showing the microstructure near the depth of the oxygen mean projected range ($\overline{R}_p$, from TRIM90[19]),

a) Φ = 0.72x10^{18}O/cm^2 (T_i = 680°C, I' = 5μA/cm^2), [001] columnar oxide precipitates (C) are present,

b) Φ = 1.2x10^{18}O/cm^2 (T_i = 700°C, I' = 5.6μA/cm^2), ribbons (R) of silicon in a continuous oxide layer, and [001] columnar (C) and irregular (I) precipitates in the silicon near the interface with the buried oxide layer are present (for analysis of the defect labelled A, see fig. 3.20 and section 3.4.1),

c) long exposure <110> SADP, using a selected area aperture corresponding to a 0.25μm diameter area, centred on the buried oxide layer of the sample shown in b), showing arcing of the silicon diffraction spots in the directions of rings centered on the transmitted spot (T).

Figure 3.11

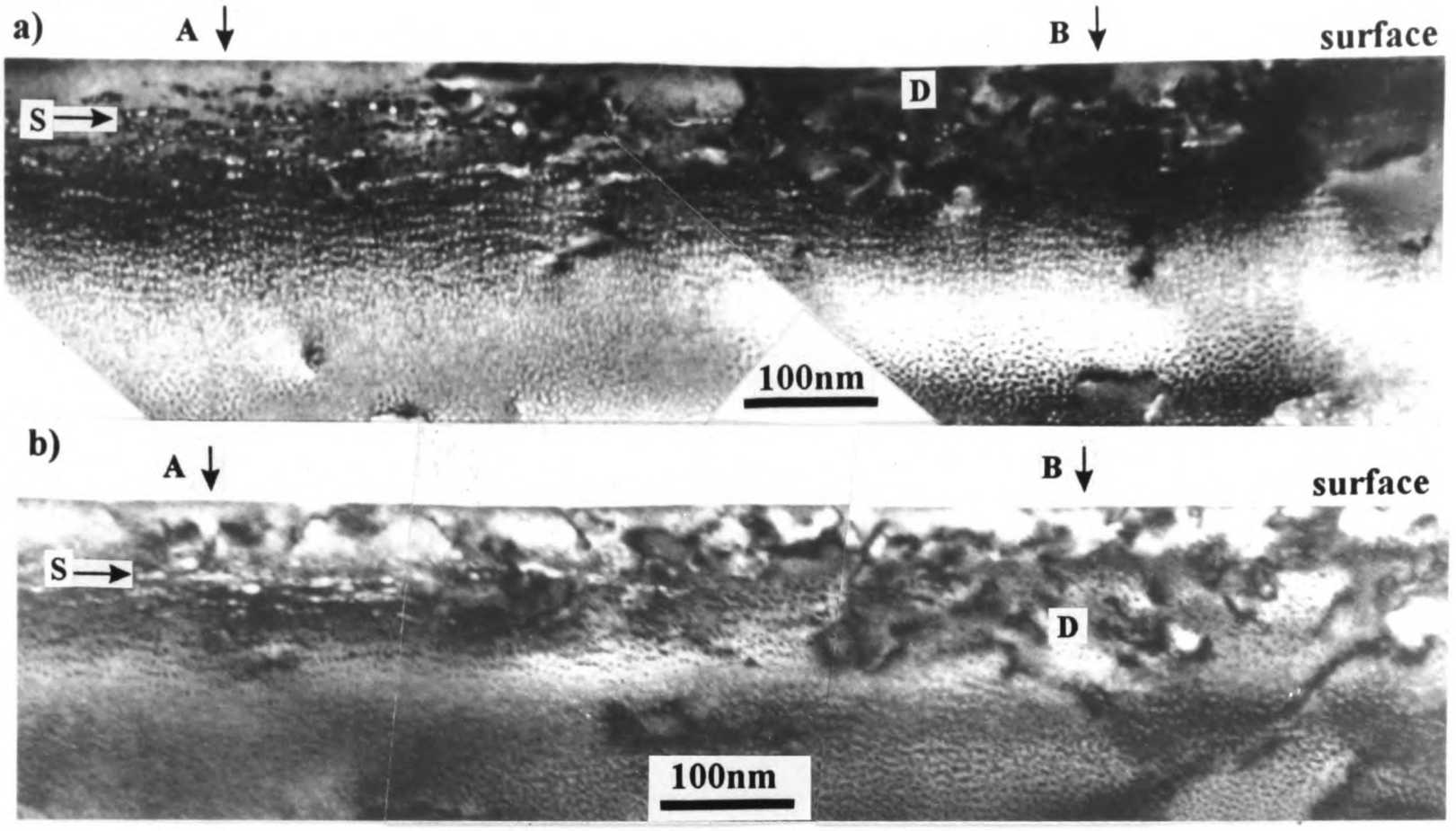

Figure 3.12

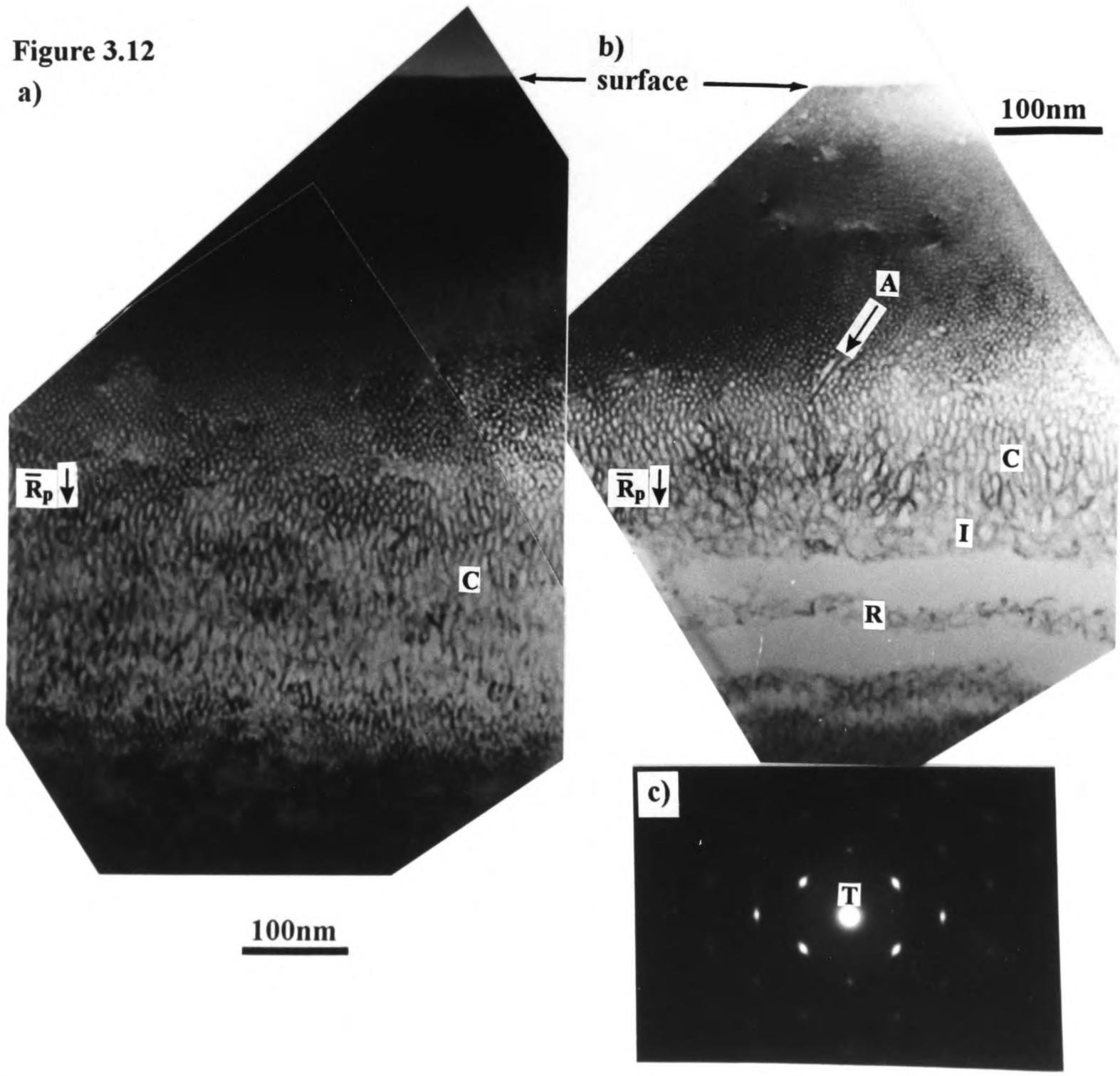

substrate but the diffraction spots are arced in the directions of rings centred on the transmitted spot (fig. 3.12). This arcing indicates that some of the Si has rotated a few degrees from the exact orientation of the substrate, probably because it is under strain from the surrounding SiO_2. The SiO_2 layer is only just continuous suggesting this dose is close to the minimum dose for forming a buried SiO_2 layer during implantation. For a dose of $1.6x10^{18}O/cm^2$ the buried damage/SiO_2 layer consists of a continuous SiO_2 layer with defects above and below (fig. 3.1). The thickness of the damage/SiO_2 layer is constant over the dose range investigated (fig. 3.1).

A schematic diagram of the oxide morphology in both the surface Si and the buried damage/SiO_2 layers as a function of depth and dose for these implants is shown in fig. 3.13.

3.3 Low Energy Implants

3.3.1 Implants at 90keV

Fig. 3.14 shows c.s. of samples implanted at 90keV, $\Phi = 0.43x10^{18}O/cm^2$ to $1.5x10^{18}O/cm^2$, $T_i = 680°C$ or 700°C and $I' = 3.75\mu A/cm^2$ or $3.1\mu A/cm^2$. The surface Si and buried damage/SiO_2 layers are approximately 150nm and 300nm thick, respectively, for $\Phi = 0.43x10^{18}O/cm^2$. With increasing Φ the thickness of the surface Si layer decreases and the buried damage/SiO_2 layer increases. For $\Phi = 1.5x10^{18}O/cm^2$ these layers are approximately 20nm and 450nm thick, respectively. Hence the buried damage/SiO_2 layer is present between the depths of 150nm and 450nm, for $\Phi = 0.43x10^{18}O/cm^2$, and between the depths of 20nm and 470nm for $\Phi = 1.5x10^{18}O/cm^2$. The decrease in the thickness of the surface Si layer, i.e. the presence of the buried damage/SiO_2 layer closer to the wafer surface, for 90keV implants compared to the 200keV implants, is because of the decrease in the mean projected range of the oxygen ions with decreasing energy (table 2.3). The width of the buried damage/SiO_2 layer is narrower for similar doses implanted at 90keV ($\Phi = 0.43x10^{18}O/cm^2$, width of damage/$SiO_2$ layer $\approx$ 300nm) compared to at 200keV (e.g. $\Phi = 0.4x10^{18}O/cm^2$, width of damage/SiO_2 layer $\approx$ 550nm) probably because of the decrease in the straggle of the oxygen ions with decreasing energy (table 2.3). In all these 90keV samples SiO_2 precipitates and dislocations are observed

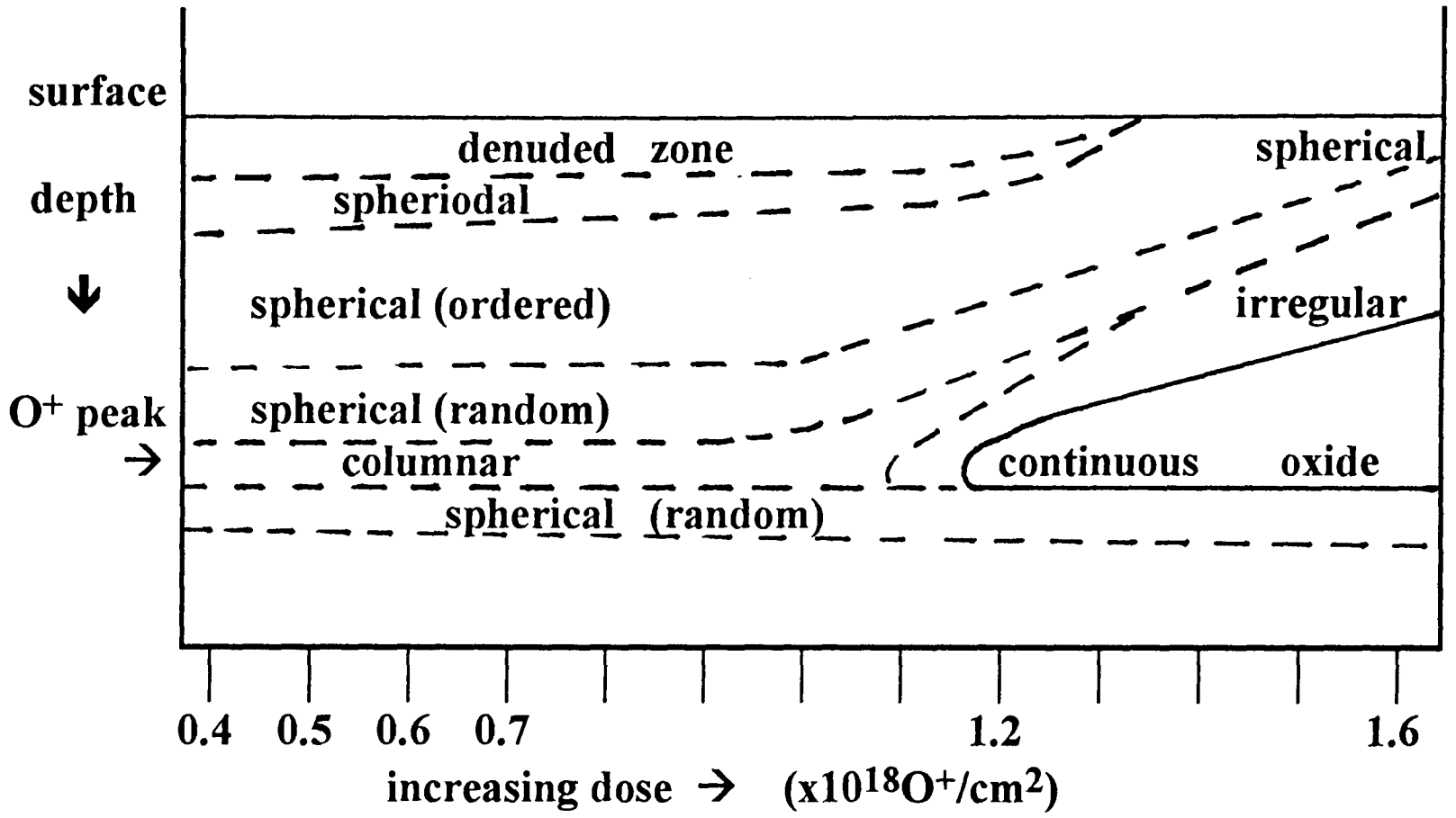

Figure 3.13 Schematic diagram of the precipitate morphology for 200keV implants of oxygen into Si at 680°C with a beam current density of 5.6μA/cm^2, as a function of depth and dose. The doses marked are the doses that were implanted (the depth axis is not to scale).

Figure 3.14 Cross-section micrographs, at a <110> pole, of samples implanted at 90keV, T_i = 680°C,

a) $\Phi = 0.43 \times 10^{18} O/cm^2$ ($I' = 4.4 \mu A/cm^2$),

b) $\Phi = 0.6 \times 10^{18} O/cm^2$ ($I' = 3.75 \mu A/cm^2$),

c) $\Phi = 0.7 \times 10^{18} O/cm^2$ ($I' = 3.75 \mu A/cm^2$),

d) $\Phi = 0.9 \times 10^{18} O/cm^2$ ($I' = 3.75 \mu A/cm^2$),

e) $\Phi = 1.0 \times 10^{18} O/cm^2$ ($I' = 3.75 \mu A/cm^2$),

f) $\Phi = 1.5 \times 10^{18} O/cm^2$ ($I' = 3.75 \mu A/cm^2$),

showing the surface silicon layer (X), the buried damage/oxide layer (Y) and the depth of the mean projected range ($\bar{R}_p$, from TRIM90[19]).

a) surface

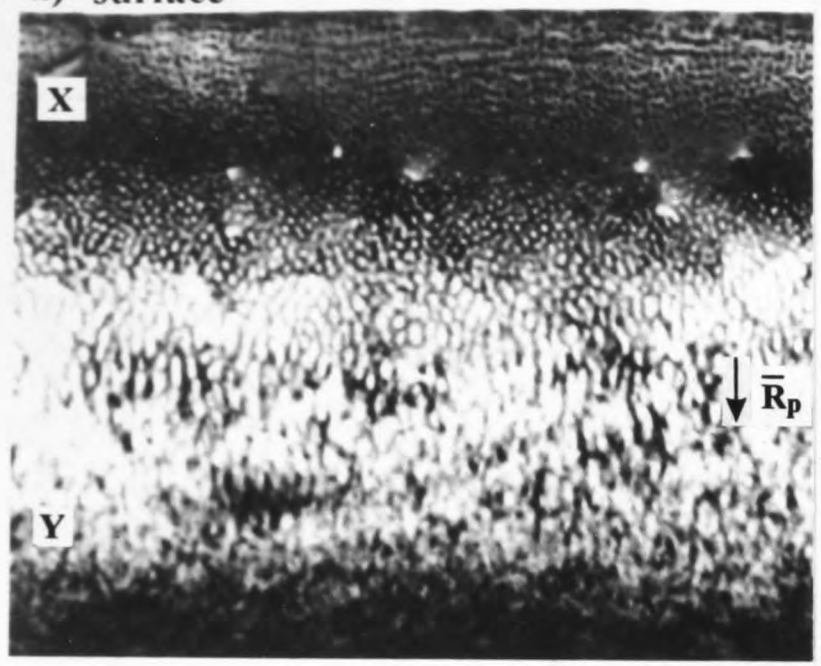

b)

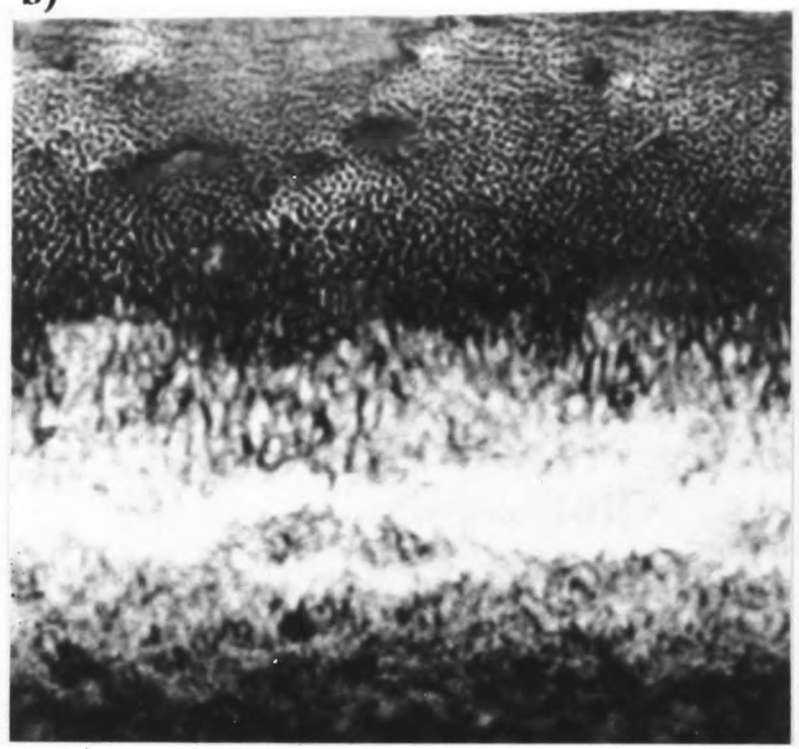

c)

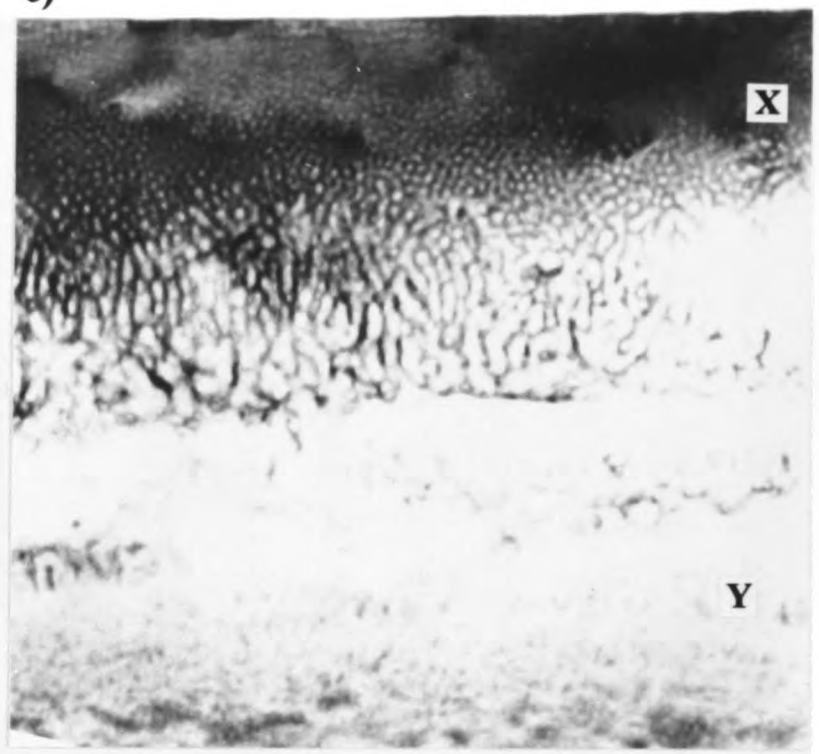

d)

surface

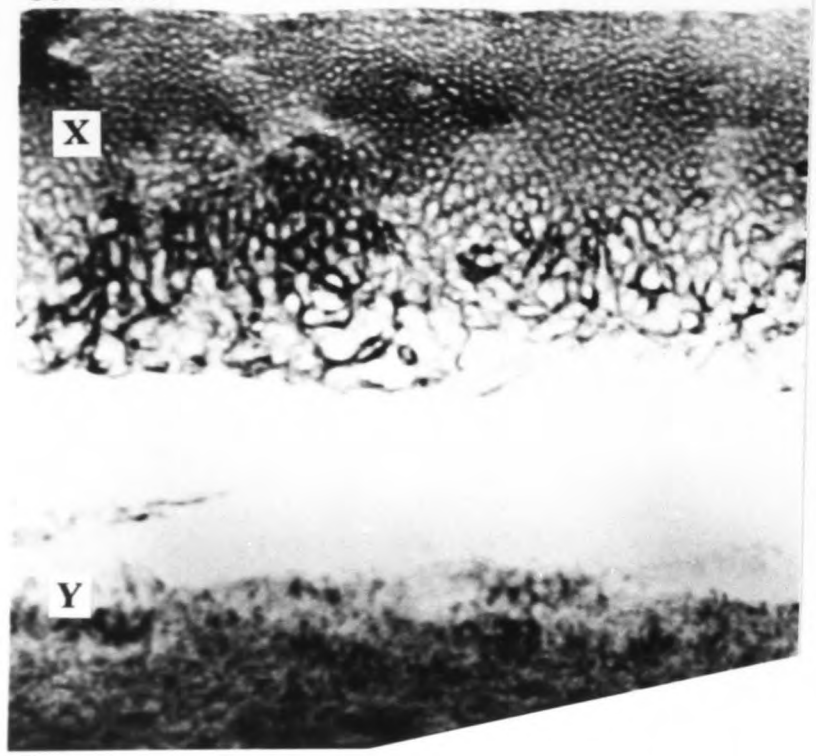

e)

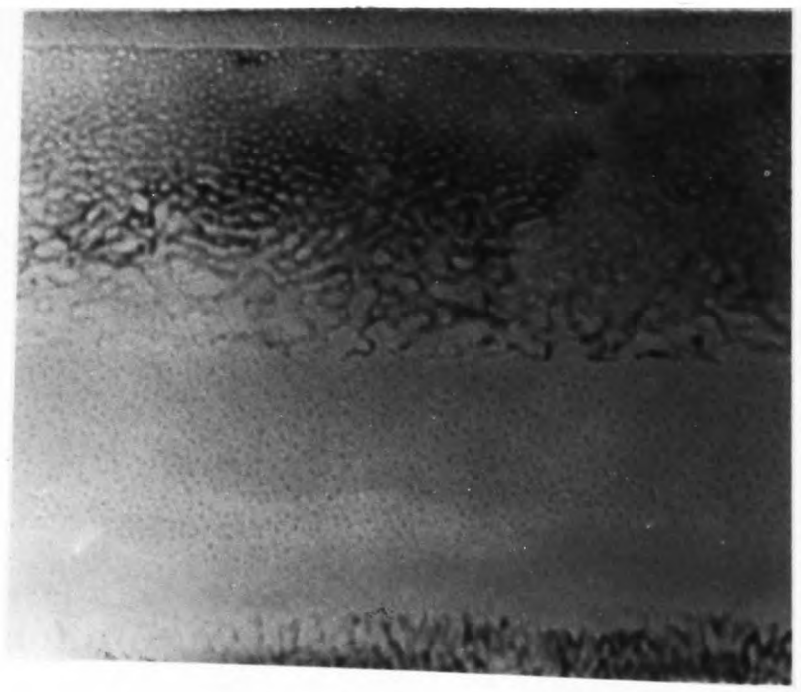

100nm

f)

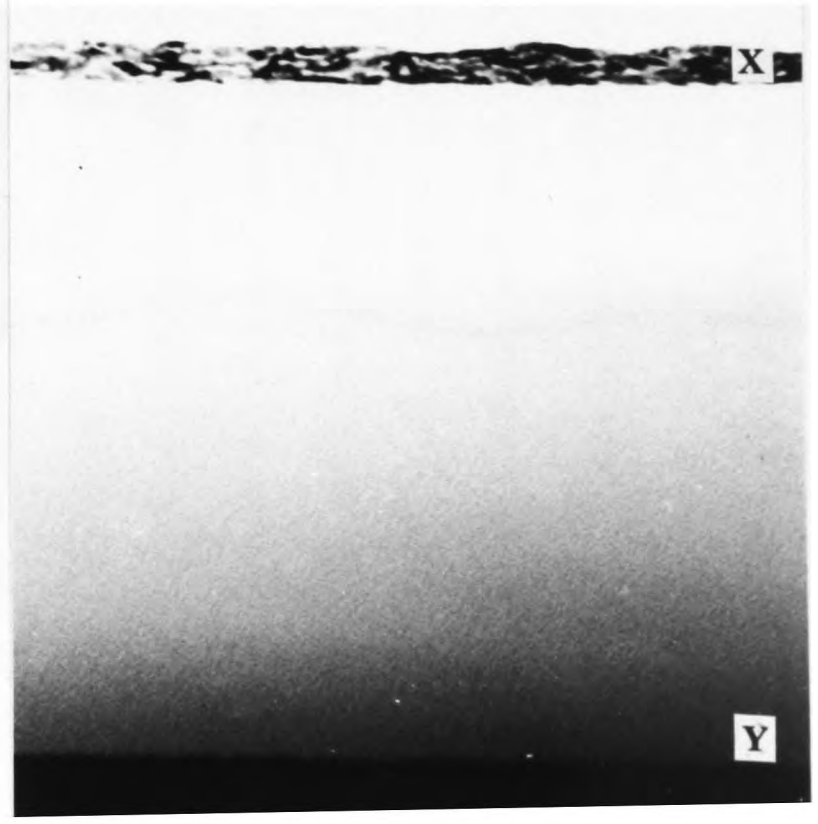

throughout the depth of the surface Si layer (for the dose of $1.5x10^{18}O/cm^2$ the layer is very thin (20-25nm) and defects are difficult to distinguish).

The surface Si layer of the three lowest dose samples ($0.43x10^{18}O/cm^2$, $0.6x10^{18}O/cm^2$ and $0.7x10^{18}O/cm^2$) contains spherical precipitates in a linear array in approximately the top 30nm of the surface and a random distribution of spherical precipitates below. A <100> c.s. of the lowest dose sample shows the precipitates in the top 30nm are of two types, regular in size <4nm in diameter and in an ordered approximately cubic array, and randomly distributed larger precipitates, up to 8nm in diameter (fig. 3.15). In the vicinity of the larger precipitates, small pits up to 8nm deep are also present in the wafer surface (fig. 3.15). A p.v. of the sample implanted with $0.6x10^{18}O/cm^2$ shows only randomly distributed precipitates with diameters 3nm to 7nm (fig. 3.16). The linear alignment of the precipitates in approximately the top 20nm of the <110> c.s. sample (fig. 3.14b) suggests, based on the observations of the lowest dose sample described above, that in the part of the sample that the c.s. sample was prepared from the precipitates at this depth are ordered approximately in a cubic array. The absence of ordering in the p.v. sample (fig. 3.16), prepared from an adjacent part of the sample, suggests that in this sample the morphology varies in different areas. For intermediate doses ($0.9x10^{18}O/cm^2$ & $1x10^{18}O/cm^2$) in the upper part of the surface Si layer, there are randomly distributed spherical precipitates below these large irregular SiO_2 precipitates (fig. 3.14). In the highest dose sample ($1.5x10^{18}O/cm^2$) the SiO_2 precipitates in the thin surface Si layer are elongated parallel to the wafer surface.

The microstructure at the centre of the buried damage/SiO_2 layer consists of [001] columnar precipitates for a dose of $0.43x10^{18}O/cm^2$, a continuous SiO_2 layer containing Si ribbons for doses of $0.6x10^{18}O/cm^2$ to $0.9x10^{18}O/cm^2$ and a continuous SiO_2 layer free from Si ribbons for doses of $1x10^{18}O/cm^2$ to $1.5x10^{18}O/cm^2$.

A schematic diagram of the precipitate morphology as a function of depth and dose for the 90keV implants is shown in Fig. 3:19.

3.3.2 Implants at 70keV

Fig. 3.17 shows c.s. of samples implanted at 70keV, $\Phi = 0.1x10^{18}O/cm^2$ to $1x10^{18}O/cm^2$, $T_i = 680°C$ and $I' = 3.1\mu A/cm^2$. The surface Si and buried damage/SiO_2 layers are

Figure 3.15 Cross-section micrographs, at a <100> pole, of a sample implanted at 90keV, Φ = $0.43x10^{18}O/cm^2$, T_i = 680°C, I' = $4.4\mu A/cm^2$,
a) an over-focused image of the precipitates near the surface showing they form a square pattern, suggesting that they are present in an ordered cubic array,
b) & c) at-focus images showing the presence of larger precipitates (A) at pits (B) near the wafer surface.
The precipitates are dark in a) and light in b) and c) due to the different foci used.

Figure 3.16 Plan-view micrograph, at the [001] pole, of the sample implanted at 90keV, Φ = $0.6x10^{18}O/cm^2$, T_i = 680°C, I' = $3.75\mu A/cm^2$, showing a random distribution of small and large oxide precipitates (P).

Figure 3.15

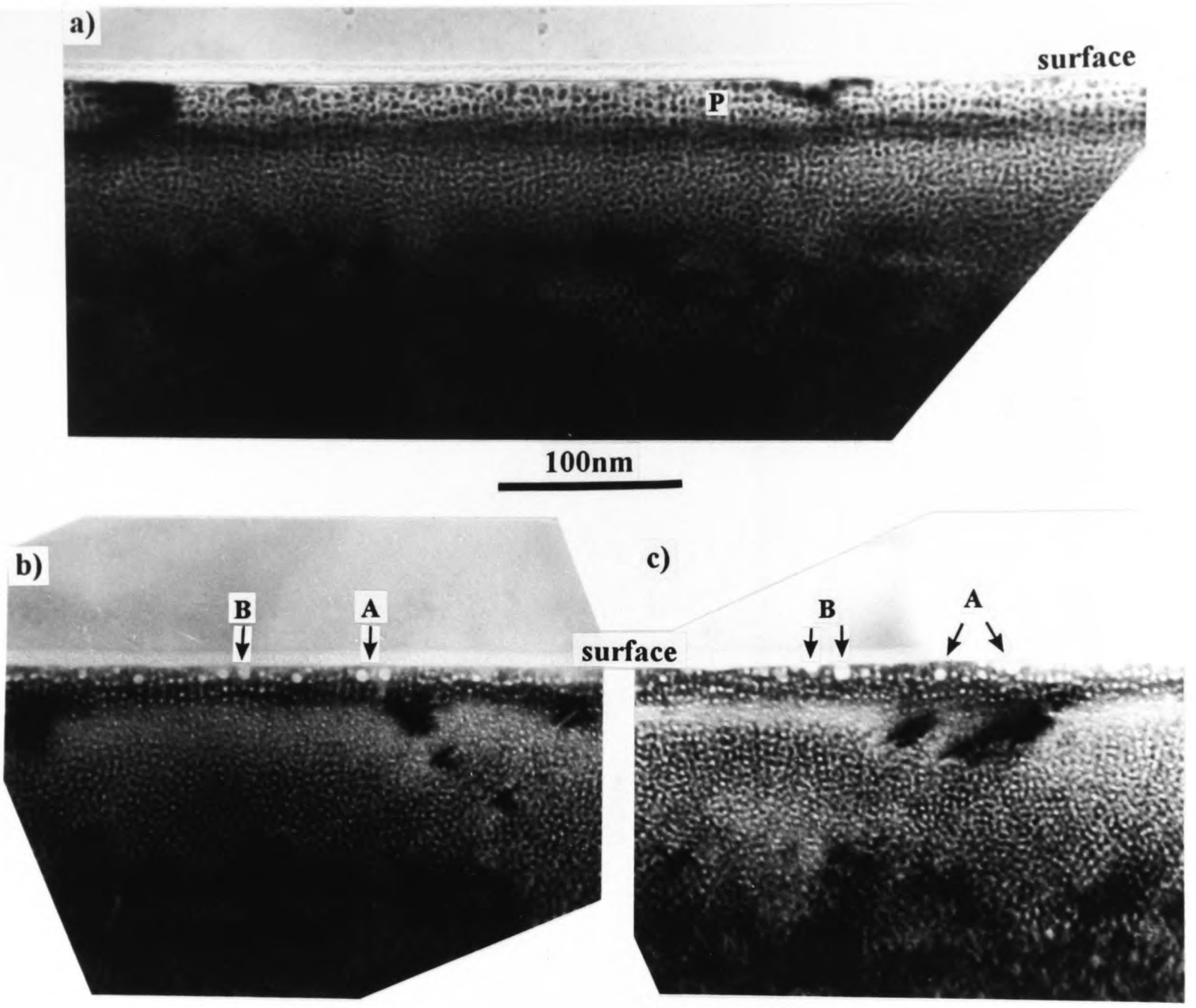

Figure 3.16

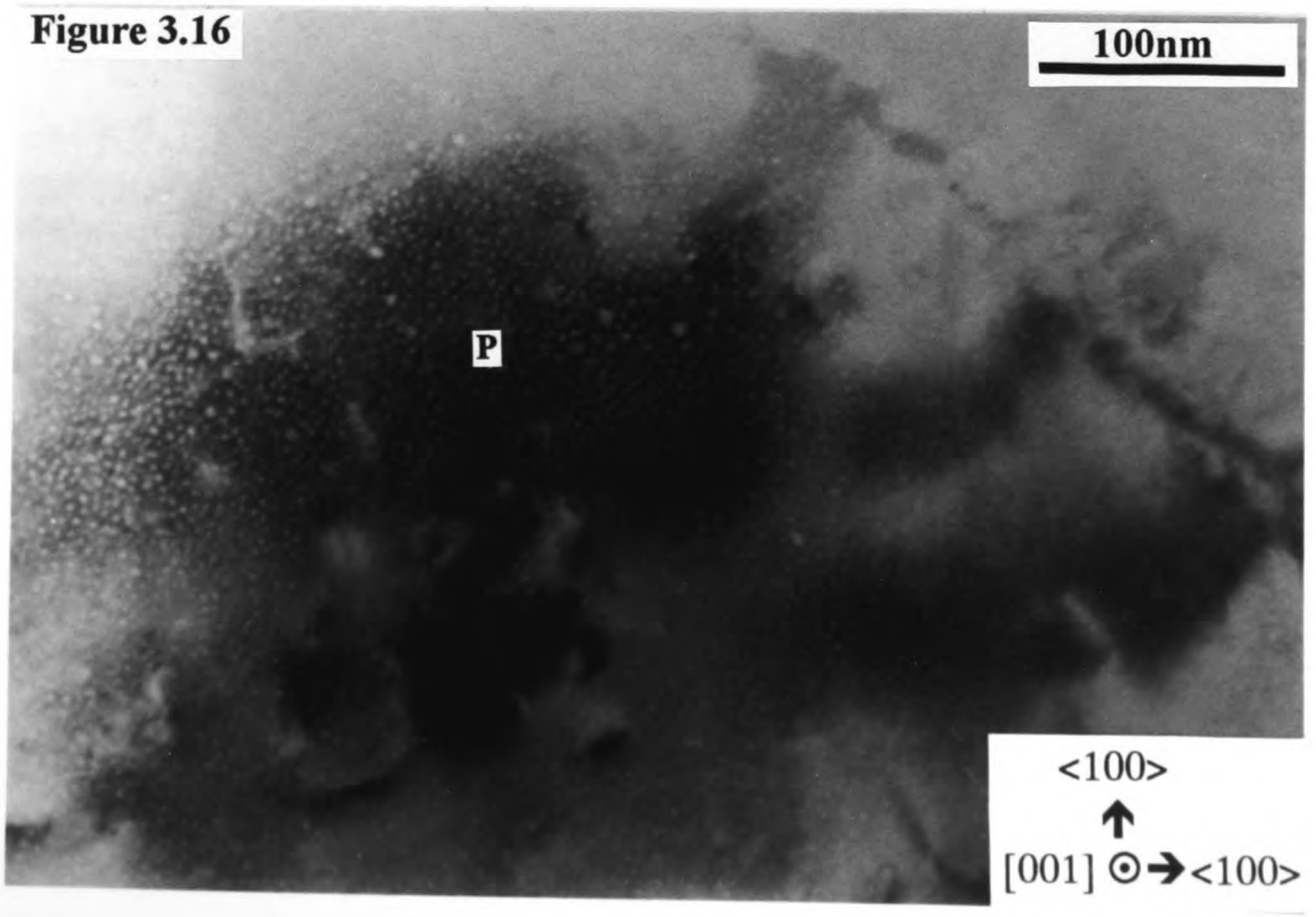

Figure 3.17 Cross-section micrographs, at a <110> pole, of samples implanted at 70keV, T_i = 680°C, I' = 3.1μA/cm^2,
a) $\Phi = 0.1 \times 10^{18}$O/cm^2,
b) $\Phi = 0.3 \times 10^{18}$O/cm^2,
c) $\Phi = 0.5 \times 10^{18}$O/cm^2,
d) $\Phi = 0.7 \times 10^{18}$O/cm^2,
e) $\Phi = 1.0 \times 10^{18}$O/cm^2,
showing the surface silicon layer (X), the buried damage/oxide layer (Y) and the depth of the mean projected range ($\bar{R}_p$, from TRIM90[19]).

a) surface

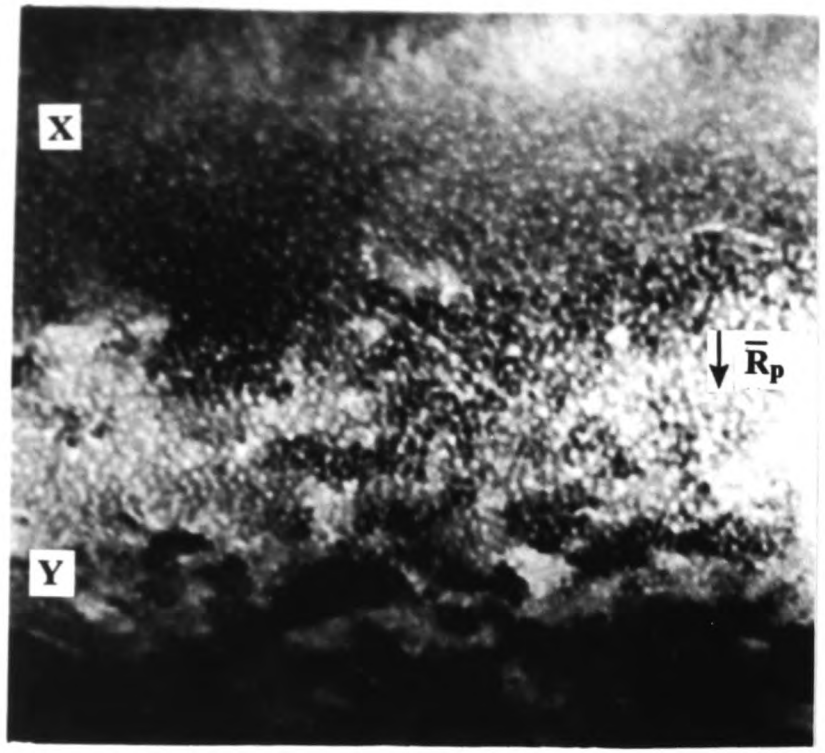

b)

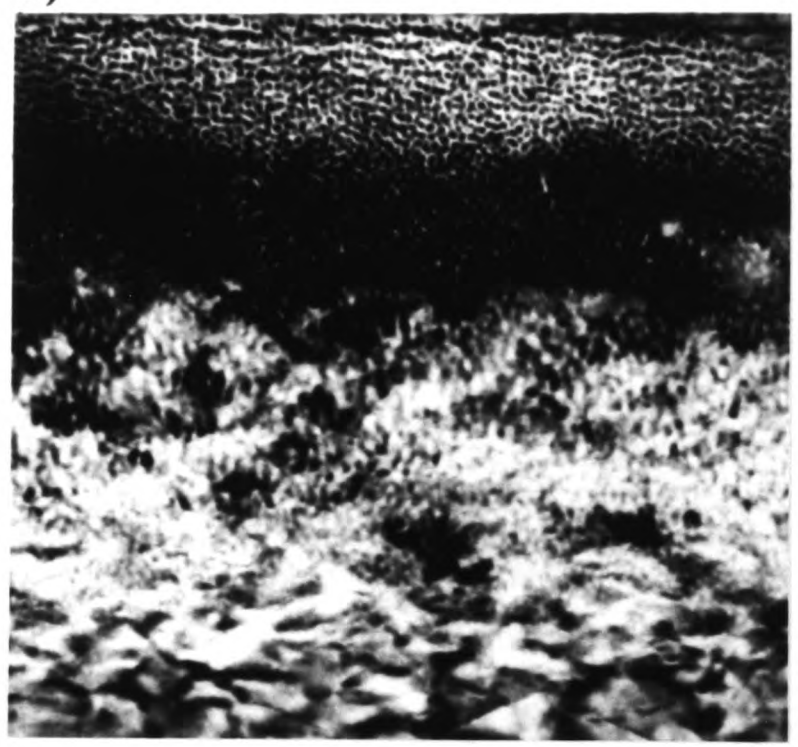

c)

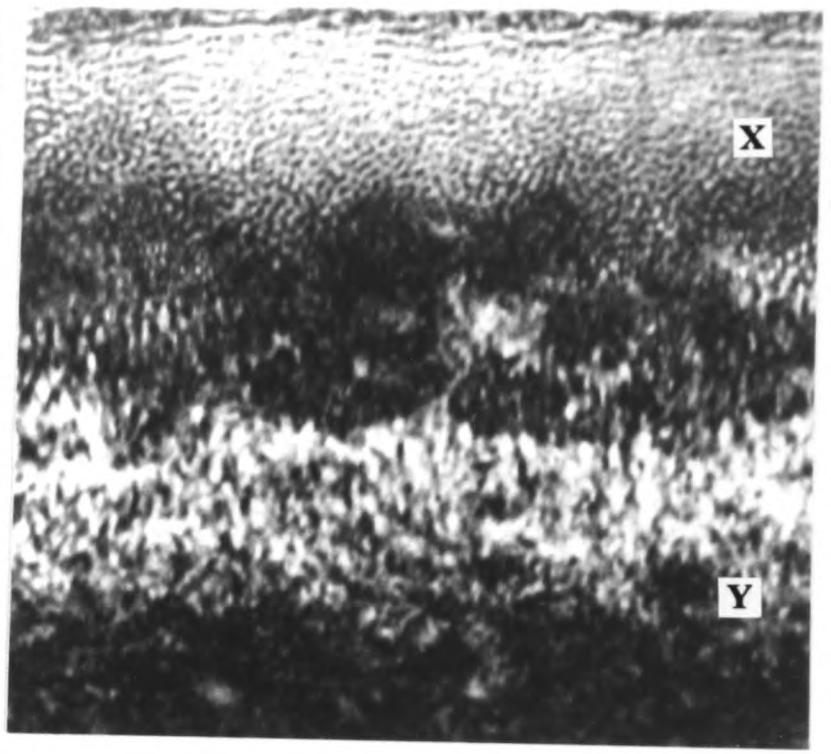

d)
surface

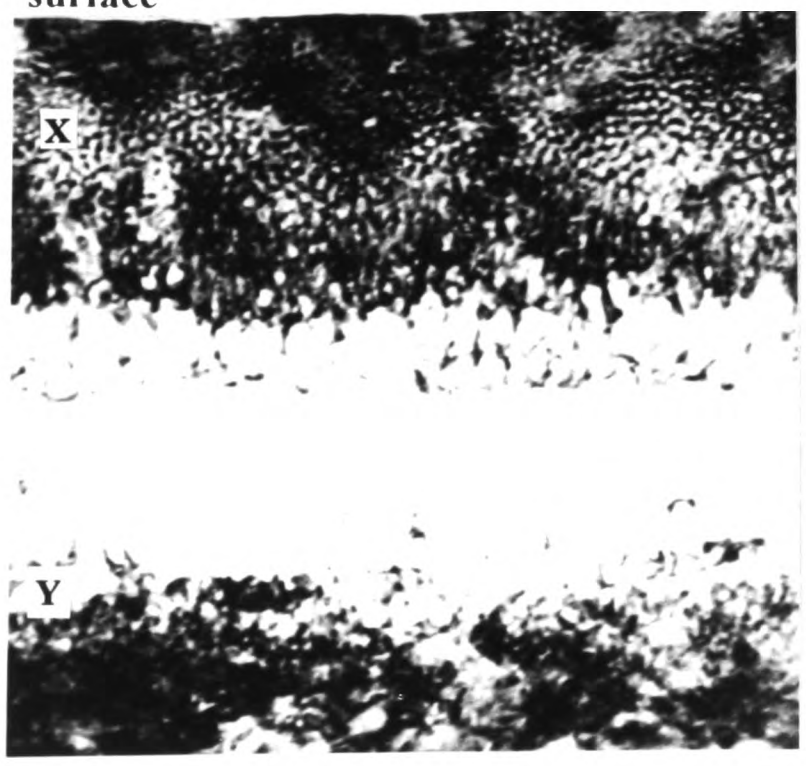

e)

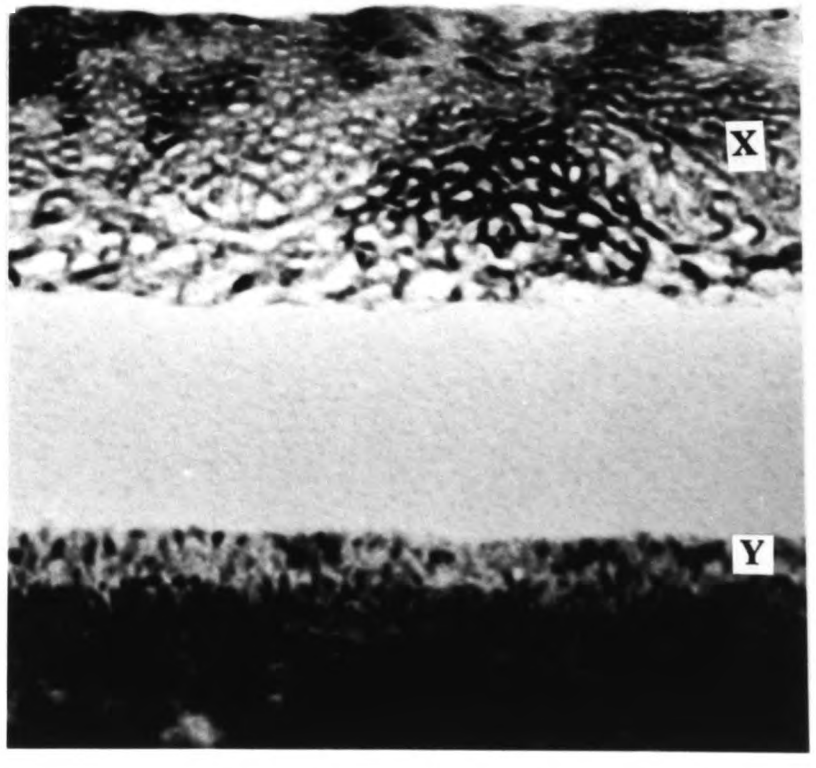

100nm

approximately 100nm and 300nm thick, respectively, for $\Phi = 0.1x10^{18}O/cm^2$. With increasing Φ the thickness of the surface Si layer remains approximately constant while the thickness of the buried damage/SiO_2 layer increases. For $\Phi = 1.0x10^{18}O/cm^2$ these layers are approximately 100nm and 400nm thick, respectively. Hence the buried damage/SiO_2 layer is present between the depths of 100nm and 400nm, for $\Phi = 0.1x10^{18}O/cm^2$, and between the depths of 100nm and 500nm for $\Phi = 1.0x10^{18}O/cm^2$. The reasons for the decrease in the thickness of the surface Si layer, i.e. the presence of the buried damage/SiO_2 layer closer to the wafer surface, and the decrease in the thickness of the buried damage/SiO_2 layer for an energy of 70keV compared to energies of 200keV and 90keV are the same as those discussed in the previous section (3.3.1) for implants at 90keV compared to at 200keV. For doses of $0.1x10^{18}O/cm^2$ to $0.3x10^{18}O/cm^2$, no dislocations are observed in the surface Si layer. For doses of $0.46x10^{18}O/cm^2$ and $0.7x10^{18}O/cm^2$, dislocations throughout the surface Si layer are present. For the dose of $1x10^{18}O/cm^2$ the surface Si layer contains a large number of SiO_2 precipitates and other defects were difficult to distinguish.

For a dose of $0.1x10^{18}O/cm^2$, a precipitate denuded zone is present at the wafer surface to a depth of 10nm and randomly distributed spherical precipitates with diameters <3nm are present throughout the rest of the layer. For intermediate doses ($0.3x10^{18}O/cm^2$ to $0.5x10^{18}O/cm^2$), there are spherical precipitates with diameters $\approx$3nm in a linear array and a lower density of larger precipitates with diameters up to 7nm, and also surface pits of typical depth 4nm similar to those present after 90keV implants (fig.3.15c). Randomly distributed spherical precipitates, diameter 3nm to 5nm, are present throughout the rest of the surface Si layer. For a dose of $0.7x10^{18}O/cm^2$ randomly distributed spherical precipitates are present through all of the surface Si layer. Close to the buried SiO_2 layer large irregular precipitates are present. For a dose of $1x10^{18}O/cm^2$, irregular precipitates, some of which are elongated parallel to wafer surface, are present in the upper half of the layer. Below the elongated precipitates larger irregular precipitates, typical diameter 50nm, are present.

The microstructure at the centre of the buried damage/SiO_2 layer consists of spherical precipitates after implanting a dose of $0.1x10^{18}O/cm^2$, [001] columnar precipitates after doses of

$0.3x10^{18}O/cm^2$ to $0.5x10^{18}O/cm^2$, a continuous SiO_2 layer containing Si ribbons after a dose of $0.7x10^{18}O/cm^2$ and a homogeneous SiO_2 layer after a dose of $1x10^{18}O/cm^2$.

A schematic diagram of the precipitate morphology as a function of depth and dose for the 70keV implants is shown in Fig. 3.19.

3.3.3 Implants at 50keV

Fig. 3.18 shows low and high magnification c.s. of samples implanted at 50keV, Φ = $0.2x10^{18}O/cm^2$, $0.5x10^{18}O/cm^2$ and $0.7x10^{18}O/cm^2$, $T_i = 680°C$ and $I' = 2.5\mu A/cm^2$. The surface Si and buried damage/SiO_2 layers are approximately 50nm and 190nm thick, respectively, for Φ = $0.2x10^{18}O/cm^2$. With increasing Φ the thickness of the surface Si layer remains approximately constant while the thickness of the buried damage/SiO_2 layer increases, for $\Phi = 0.7x10^{18}O/cm^2$ these layers are approximately 50nm and 220nm thick, respectively. Hence the buried damage/SiO_2 layer is present between the depths of 50nm and 240nm, for $\Phi = 0.2x10^{18}O/cm^2$, and between the depths of 50nm and 270nm for $\Phi = 0.7x10^{18}O/cm^2$. The reasons for the decrease in the thickness of the surface Si layer, i.e. the presence of the buried damage/SiO_2 layer closer to the wafer surface, and the decrease in the thickness of the buried damage/SiO_2 layer for an energy of 50keV compared to energies of 200keV, 90keV and 70keV are the same as those discussed in section 3.3.1 for implants at 90keV compared to at 200keV. For doses of $0.2x10^{18}O/cm^2$ and $0.5x10^{18}O/cm^2$, no dislocations are observed in the surface Si layer. However pronounced strain contrast and a large number of SiO_2 precipitates are present in the samples implanted with doses of $0.5x10^{18}O/cm^2$ and $0.7x10^{18}O/cm^2$, respectively, making other defects difficult to distinguish.

For a dose of $0.2x10^{18}O/cm^2$, spherical precipitates are present in a linear array in approximately the top 20nm and randomly distributed spherical precipitates are present below. The precipitates in the linear array are typically <3nm in diameter. A lower density of larger precipitates, diameter 3nm to 7nm, are also present. The sample implanted with $0.5x10^{18}O/cm^2$ contains randomly distributed spherical precipitates in the upper part of the surface Si layer and below these [001] columnar/large irregular precipitates with dimensions up to 13nm. The sample implanted with $0.7x10^{18}O/cm^2$ contains, in the upper half of the surface Si layer,

Figure 3.18 Cross-section micrographs, at a <110> pole, of samples implanted at 50keV, T_i = 680°C, I' = 2.5μA/cm^2,

a) $\Phi = 0.2 \times 10^{18}$O/cm^2, low magnification,

b) $\Phi = 0.5 \times 10^{18}$O/cm^2, low magnification,

c) $\Phi = 0.7 \times 10^{18}$O/cm^2, low magnification,

d) $\Phi = 0.2 \times 10^{18}$O/cm^2, high magnification,

e) $\Phi = 0.5 \times 10^{18}$O/cm^2, high magnification,

f) $\Phi = 0.7 \times 10^{18}$O/cm^2, high magnification,

showing the surface silicon layer (X), the buried damage/oxide layer (Y), the substrate (Z) and the depth of the mean projected range ($\bar{R}_p$, from TRIM90[19]).

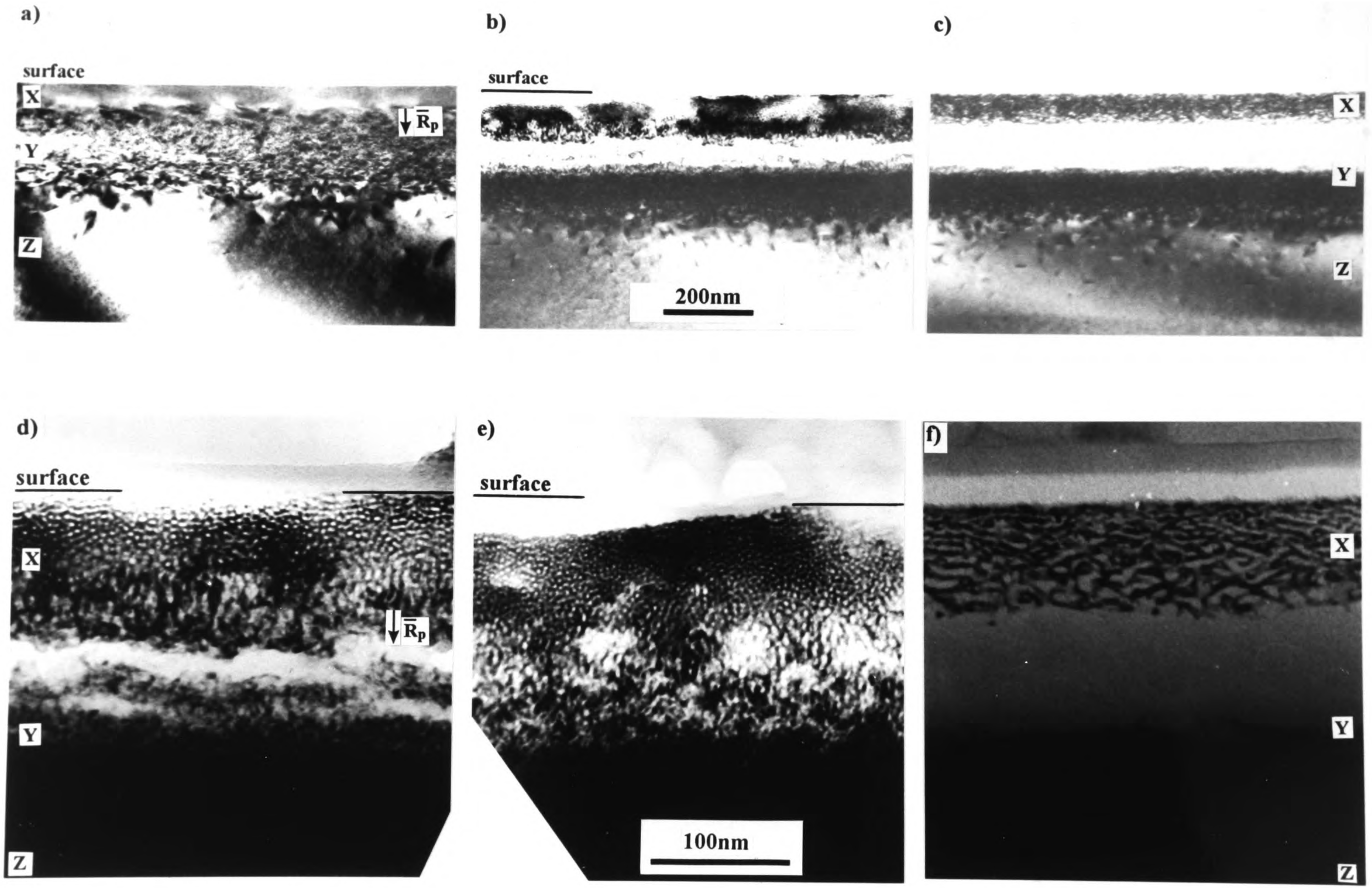
a)
surface
X
Y
Z
$\bar{R}_p$
b)
surface
200nm
c)
X
Y
Z
d)
surface
X
Y
Z
$\bar{R}_p$
e)
surface
100nm
f)
X
Y
Z

precipitates which tend to be elongated approximately parallel to the wafer surface and, next to the buried SiO_2 layer, larger more irregular precipitates. The precipitates in the upper half of the layer also appear elongated in a <100> c.s., suggesting these precipitates are platelets.

The microstructure at the centre of the buried damage/SiO_2 layer consists of [001] columnar precipitates after implanting a dose of $0.2x10^{18}O/cm^2$, a non-continuous SiO_2 layer containing Si ribbons after a dose of $0.5x10^{18}O/cm^2$ and a homogeneous SiO_2 layer after implanting a dose of $7x10^{18}O/cm^2$.

A schematic diagram of the precipitate morphology as a function of depth and dose for the 50keV implants is shown in Fig. 3.19.

3.4 Defects Above the Buried Damage/Oxide Layers

At the interface between the surface Si layer and the buried damage layer rod-like defects, 30-200nm long, lying on {111} planes are present for 90keV (fig. 3.20a) and 200keV (figs. 3.12b) implants for doses greater that the minimum dose to form a continuous SiO_2 layer after implantation ($^I\Phi c$). The defects tend to be longer for the 200keV implants. The defect densities are, based on c.s. observations, $\approx 10^7/cm^2$ in the 90keV implants and 10^7-$10^8/cm^2$ in the 200keV implants, referred to the sample surface. The microstructure of these defects was investigated using HREM. These defects are usually bordered on either side by an alignment of SiO_2 precipitates (fig. 3.20b). It was difficult, because of their low density, the background strain and the presence of SiO_2 precipitates, to form lattice images of these defects in which the microstructure could be determined. HREM lattice images, where the microstructure could be interpreted, were obtained from one of these defects (fig. 3.20). Using a similar argument to that discussed for the SF at the wafer surface in section 3.2[2-5], the defect is interpreted as consisting of two SF of opposite nature, i.e. one intrinsic and one extrinsic, lying on parallel {111} planes.

3.5 Defects Below the Buried Damage/Oxide Layers

At the interface between the buried damage/SiO_2 layer and the substrate, for all energies, a region of spherical randomly distributed SiO_2 precipitates and defects are present for all

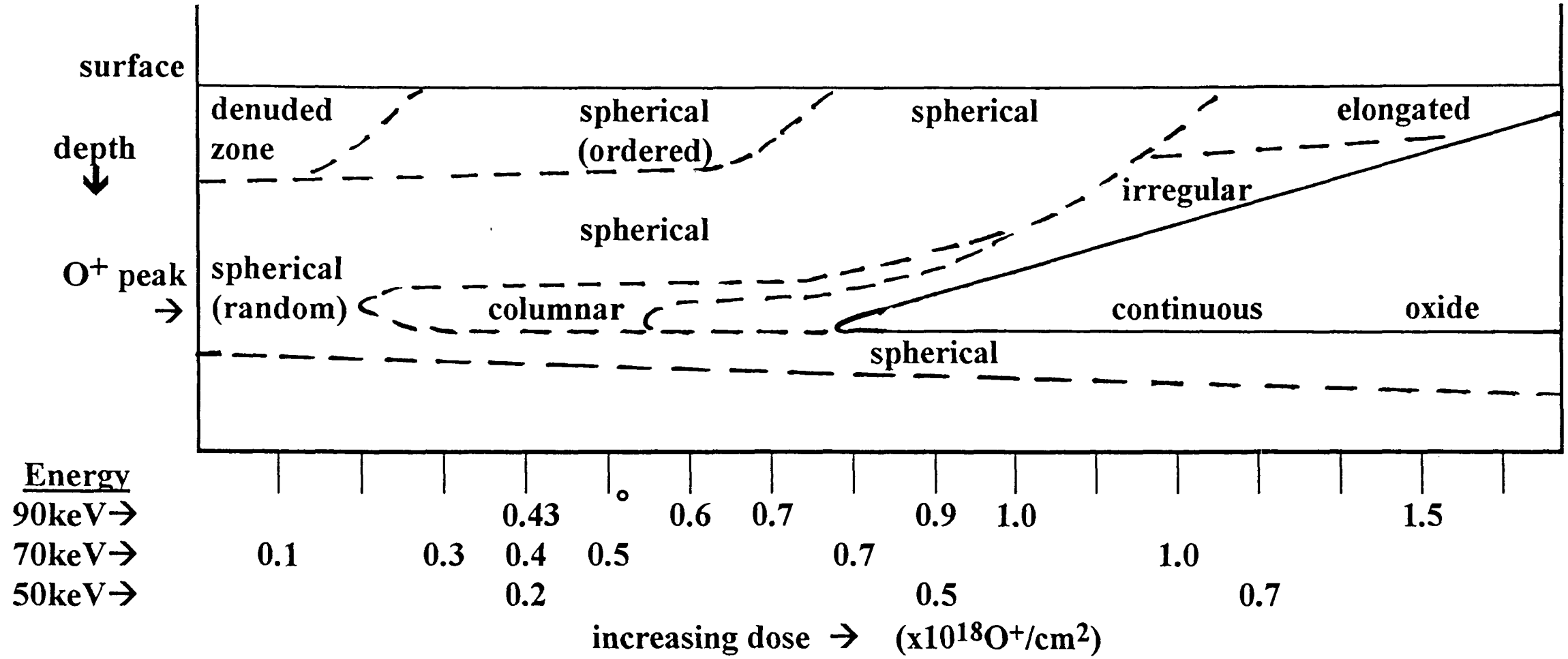

Figure 3.19 Schematic of the precipitate morphology for 90keV, 70keV and 50keV implants of oxygen into Si at 680°C with beam current densities of 3.75μA/cm², 3.1μA/cm² and 2.5μA/cm² respectively, as a function of depth and dose. The dose axis is labeled with three dose scales, one for each energy as is indicated in the bottom left hand corner of the figure. The doses marked are the doses that were implanted (The 90keV dose axis is labelled to scale, the 70keV and 50 keV dose axes are not to scale. The depth axis is also not to scale and is different for each energy, the higher the energy the deeper the oxygen peak).

Figure 3.20 Cross-section micrographs, at <110> poles, of rod-like (R) defects present in the surface silicon layer close to the buried oxide layer,
a) TEM image of a sample implanted at 90keV, Φ = 0.9x10^{18}O/cm^2, T_i = 680°C, I' = 3.75μA/cm^2 (see fig. 3.12 for a similar defect in a sample implanted at 200keV),
b) HREM image of a rod-like defect in a sample implanted at 200keV, Φ = 1.2x10^{18}O/cm^2, T_i = 700°C, I' = 5.6μA/cm^2, showing the silicon {111} planes and the alignment of the oxide precipitates (P) along either side of the rod-like defect,
c) HREM image of part of a rod-like defect different from that in b) but in the same sample, showing the silicon {111} planes and that this defect consists of two stacking faults (SF), one intrinsic (In) and one extrinsic (Ex), on parallel {111} planes.

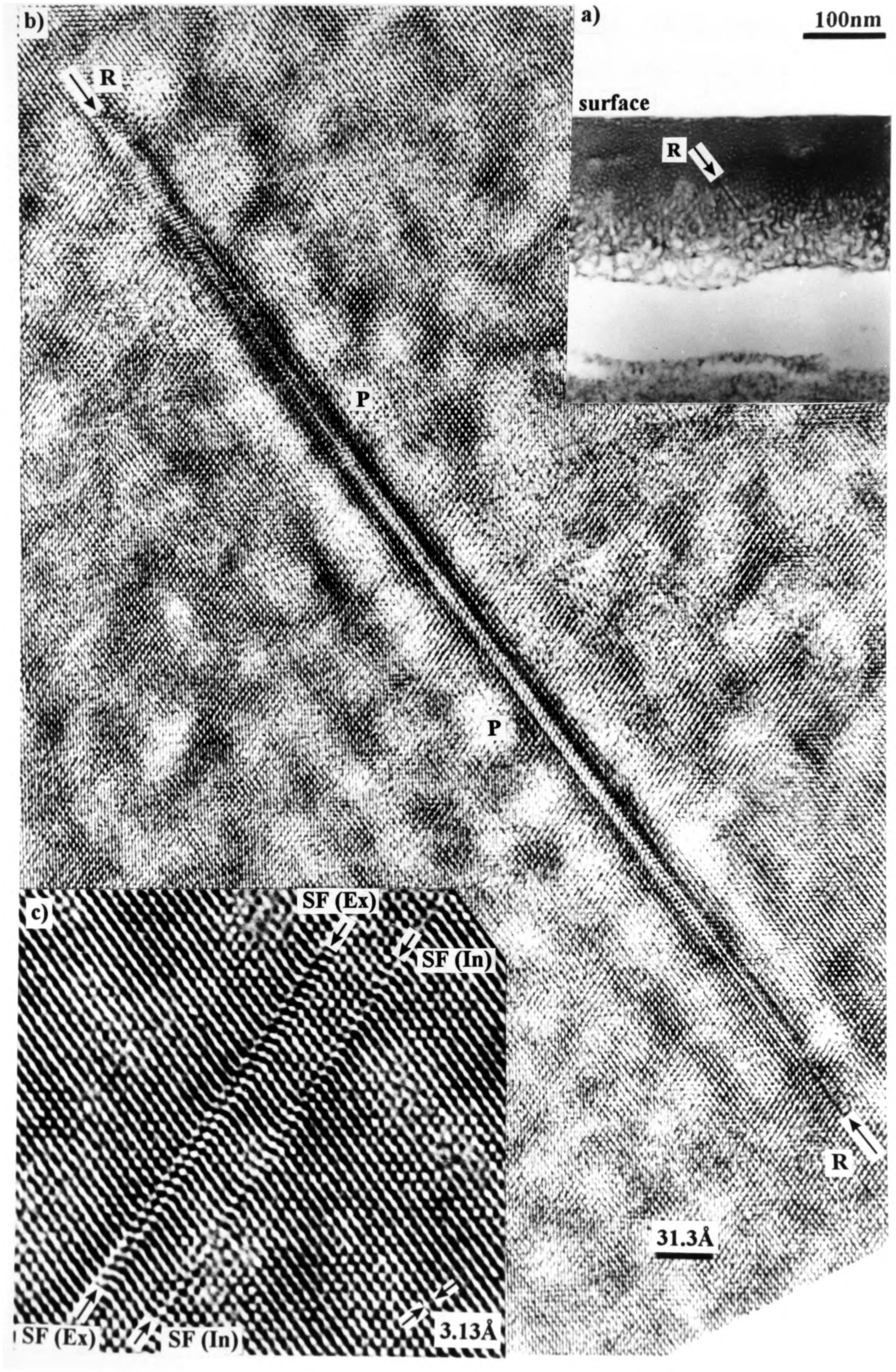
b)
a)
100nm
R
surface
R
P
P
c)
SF (Ex)
SF (In)
R
31.3Å
SF (Ex)
SF (In)
3.13Å

energies and doses. Three different types/orientations of defects, namely, zigzag defects on {311} planes, and "line" defects parallel and inclined to the wafer surface are present (fig. 3.21). The microstructure of the {311} defects was examined using HREM but the lattice images are difficult to interpret. Faint streaks present in the <311> directions in the [110] pole SADP (fig. 3.22), suggest that the {311} defects are platelets. Defects on {311} planes resulting from ion implantation have been studied by many authors[9,10,11] and their detailed microstructure is not pursued further in this work. The two types of "line" defect in the sample implanted with a dose of $1.2 \times 10^{18} O/cm^2$ at 200keV, $T_i = 700°C$ and $I' = 5.6 \mu A/cm^2$ are investigated using diffraction contrast. The observation of these defects has been reported only by one other research group[67] but there are no reports of the defect microstructure. Hence these defects are investigated in detail.

3.5.1 Morphology

Figs. 3.21 & 3.22 show images of these "line" defects at the [110] pole. The defects are either parallel to or inclined at 54° to the wafer surface. Faint streaks in the <001> directions in the [110] pole SADP (fig. 3.21c), suggest that the defects parallel to the wafer surface are platelets on the (001) plane. The inclined defects consist of elongated loops, oxide plates or rods and broad loops or oxide plates (fig. 3.22). Using diffraction conditions at the pole (fig. 3.21) or $\mathbf{g}(\bar{2}20),3\mathbf{g}$ weak beam (fig. 3.22), some of the defects near the thin edge of the TEM samples contain fringes inclined at $\approx 70°$ to the wafer surface. The inclination of the elongated defects/loops at 54° to the wafer surface and their elongated shape, suggests that these defects could lie either a) on edge on {111} planes or in the <110> directions inclined to the wafer surface on the {111} planes, b) in the <110> directions on the {110} planes inclined to the wafer surface or c) in the <110> directions on the (010) and (100) planes (fig. 3.26). As displacement fringes are always parallel to the intersection of the plane of the defect and the surface[6], then for a parallel faced (110) c.s., planar defects lying on the {100} planes would at this pole intersect the c.s. surface in lines at 90° to the wafer surface. However, the thin edge of the c.s. has a wedge shape resulting from the ion beam thinning. The wedge angle results in the {100} planes intersecting the c.s. surface in lines whose projected images at this pole make an

Figure 3.21,
a) cross-section micrograph, at a <110> pole, of defects below the buried damage/oxide layer, close to the buried oxide layer, in the sample implanted at 200keV, Φ = 0.4x10^{18}O/cm^2, T_i = 700°C, I' = 5.6μA/cm^2, showing inclined defects (A), defects parallel the wafer surface (B) and {311} defects (C) (Y = buried damage/oxide layer, Z = substrate),
b) cross-section micrograph, at a <110> pole, of defects below the buried damage/oxide layer, close to the buried oxide layer, in the sample implanted at 90keV, Φ = 0.4x10^{18}O/cm^2, T_i = 680°C, I' = 3.75μA/cm^2, showing inclined defects (A), defects parallel to the wafer surface (B) and {311} defects (C) (Y = buried damage/oxide layer, Z = substrate),
c) SADP, using an aperture corresponding to a 0.25μm diameter area centred on the region of silicon containing the defects in the sample implanted at 200keV, Φ = 1.2x10^{18}O/cm^2, T_i = 700°C, I' = 5.6μA/cm^2, showing spots with faint streaks in the <311> and <100> directions.

a)

100nm

Y

B

C

Z

A

b)

100nm

Y

C

A

B

Z

c)

{311}

(002)

{111}

{220}

transmitted spot

<311>

<001>

<311>

Figure 3.22 Cross-section micrographs, close to the [110] pole, showing the defects below the buried damage/oxide layer in the sample implanted at 200keV, $\Phi = 1.2x10^{18}O/cm^2$, $T_i = 700°C$, $I' = 5.6\mu A/cm^2$,

a) bright field g($\bar{2}$20) showing defects inclined to the (001) plane (A),

b) bright field g(004) showing defects parallel to the (001) plane (B),

c) weak beam **g**($\bar{2}$20),3**g**, showing inclined loops (or thin oxide platelets) (C),

d) weak beam **g**($\bar{2}$20),3**g**, showing broader defects containing weak fringes (D).

Figure 3.23,

a) cross-section micrograph, at the [100] pole, of the sample implanted at 200keV, $\Phi = 1.2x10^{18}O/cm^2$, $T_i = 700°C$, $I' = 5.6\mu A/cm^2$, showing the defects below the buried damage/oxide layer parallel (A), at 45°(B) and at 90°(C) to the (001) plane.

b) SADP from the specimen shown in a), using an aperture corresponding to an area of 0.25μm diameter centred on the region of silicon containing the defects shown in a), showing very faint streaks in the ±[001] direction. Fainter streaks are also present in the TEM negative in the ±[010] direction. Where the two streaks cross they give rise to faint spots in the (200) and (020) positions (T = transmitted spot).

Figure 3.22

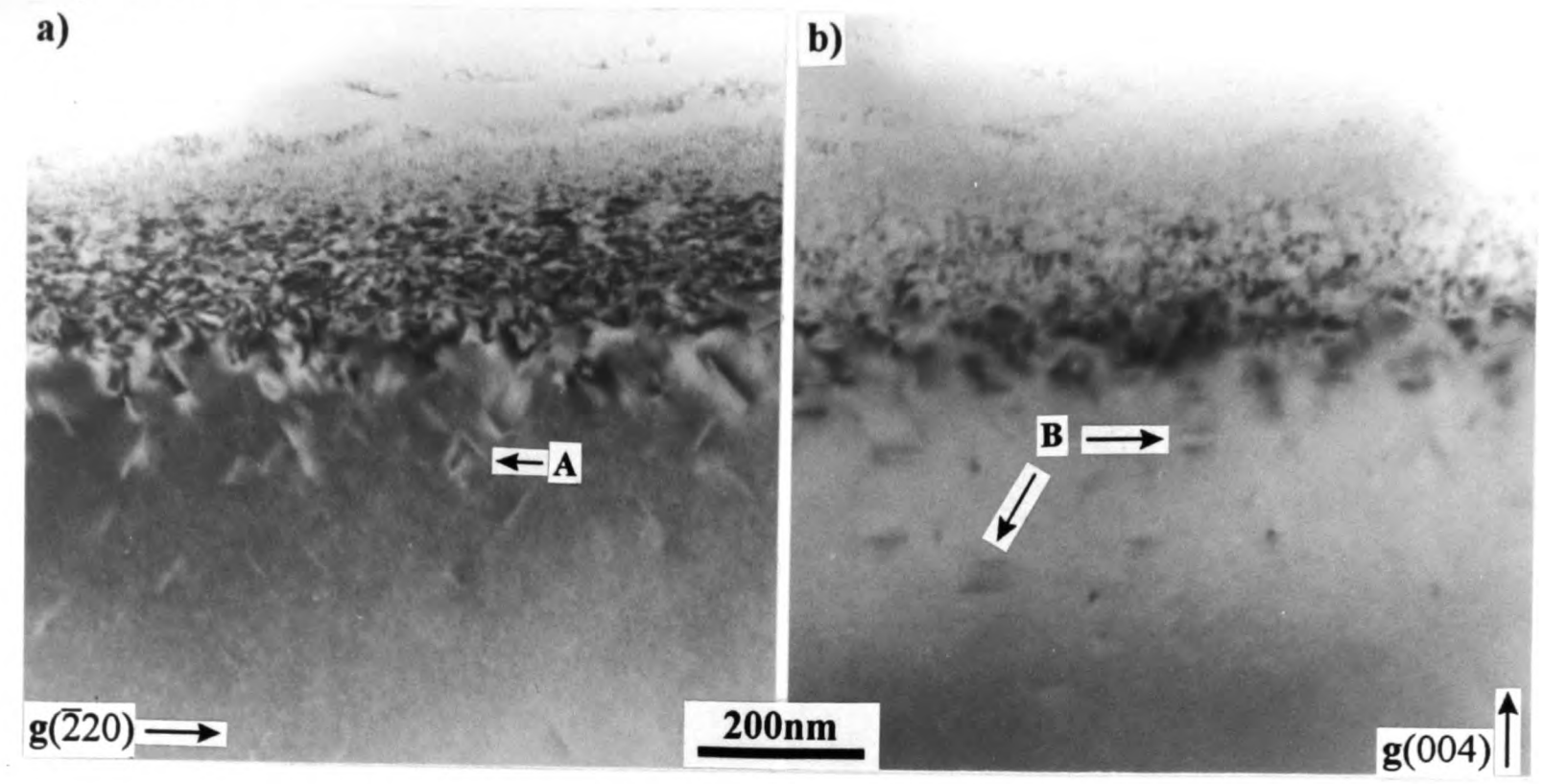

Figure 3.23

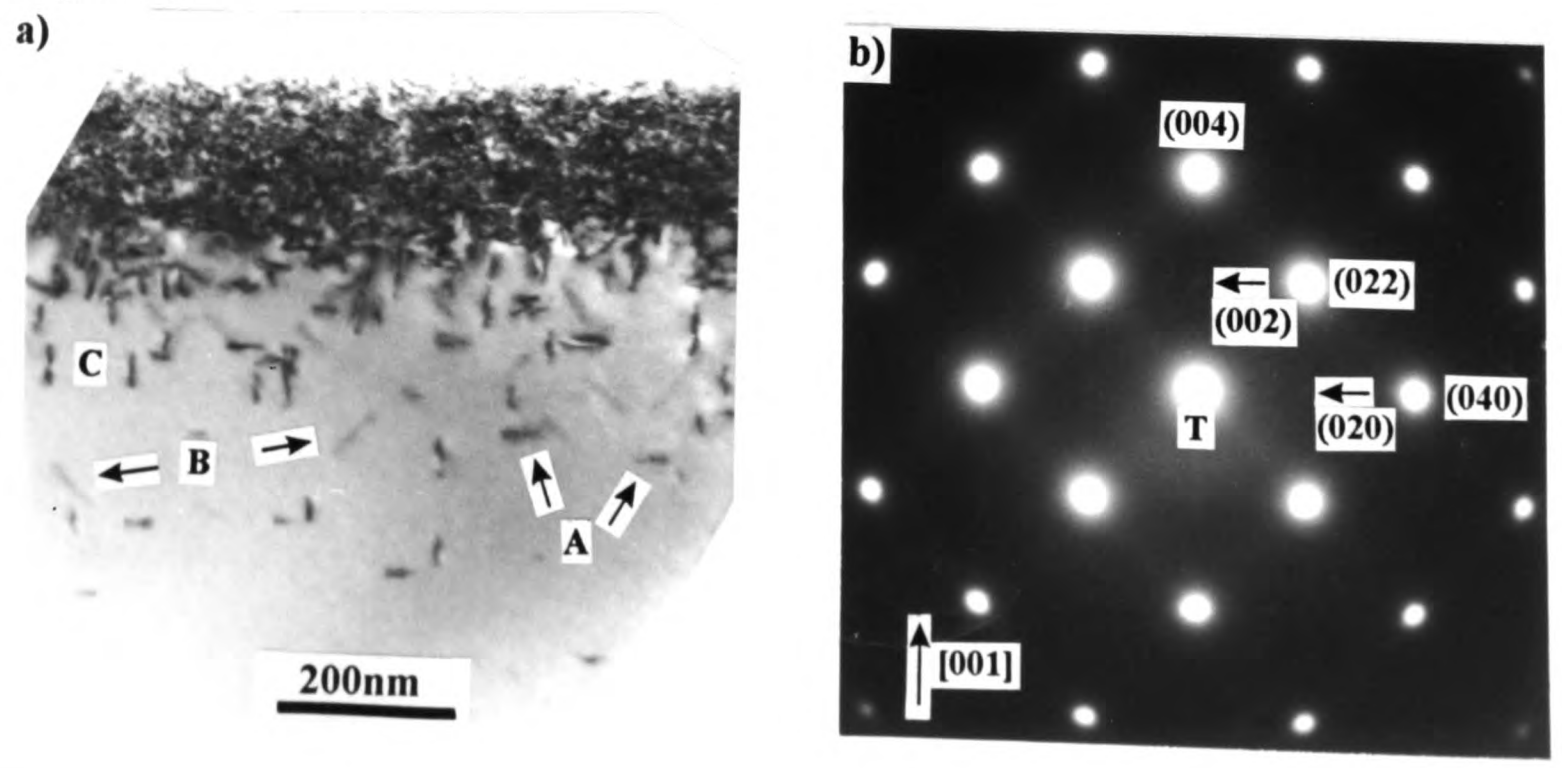

angle of <90° to the wafer surface. Hence the fringes observed experimentally could be from defects lying on the {100} planes.

At the [100] pole the "line" defects are either parallel, inclined at 45° or at right angles to the wafer surface (figs. 3.23 & 3.24). Faint streaks in the [001] and [010] directions in the [100] pole SADP (fig. 3.23), and the vertical and horizontal orientation of the defects in the images, suggests that these defects are platelets lying on the (001) and (010) planes. The angle of 45° between the inclined defects and the wafer surface suggests that these defects could either a) be elongated defects lying with their length in the <110> directions inclined to the wafer surface on the {111} planes, b) lie on edge on {011} planes or c) be elongated defects lying in the two orthogonal <110> directions on the (100) plane (fig. 3.26).

At the [111] pole elongated "line" defects parallel to the $[\bar{1}10]$, $[0\bar{1}1]$ and $\pm[\bar{1}01]$ directions (the defects parallel to the $\pm[0\bar{1}1]$ and $\pm[\bar{1}01]$ directions are therefore at an angle of 60° to the $\pm[\bar{1}10]$ direction) and shorter defects inclined at 30° to the $\pm[\bar{1}10]$ direction are present (fig. 3.25). Small defects in the $\pm[\bar{1}\bar{1}2]$ direction are also present (fig. 3.25). The defects parallel to the $\pm[\bar{1}10]$, $\pm[0\bar{1}1]$ and $\pm[\bar{1}01]$ directions could be either a) elongated defects lying with their length in the <110> directions inclined to the wafer surface on the (111) plane or nearly on edge on $(1\bar{1}1)$, $(11\bar{1})$ and $(\bar{1}11)$ planes, b) elongated defects in the <110> directions on the {110} planes inclined to the wafer surface or c) in the <110> directions on the (010) and (100) planes, where the <110> direction is parallel to a <110> direction in the (111) plane (fig. 3.26). At this pole the projected image of elongated defects lying on the (010) and (100) planes with line directions in the orthogonal <110> directions to those above, i.e. not parallel to a <110> direction in the [111] plane, make an angle of 30° with the $\pm[\bar{1}10]$ direction (fig. 3.26).

For defects of equal length, lying in the two orthogonal <110> directions on the (010) and (100) planes, the defects whose projected images at this [111] pole are inclined at 30° to the $\pm[\bar{1}10]$ direction, have a shorter projected length than the defects whose projected images are inclined at 60° to the $\pm[\bar{1}10]$ direction (fig. 3.26). Hence such defects are consistent with the experimental results. If these elongated defects are lying on the {110} planes then, as mentioned above, the defects inclined at 60° to the $\pm[\bar{1}10]$ direction have their length in the <110>

Figure 3.24 Cross-section micrographs, close to the [100] pole, of the same area showing the defects below the buried damage/oxide layer in the sample implanted at 200keV, Φ = $1.2x10^{18}O/cm^2$, $T_i = 700°C$, $I' = 5.6\mu A/cm^2$,

a) bright field **g**(004),

b) bright field **g**(040),

c) bright field **g**(022),

d) bright field **g**($0\bar{2}2$).

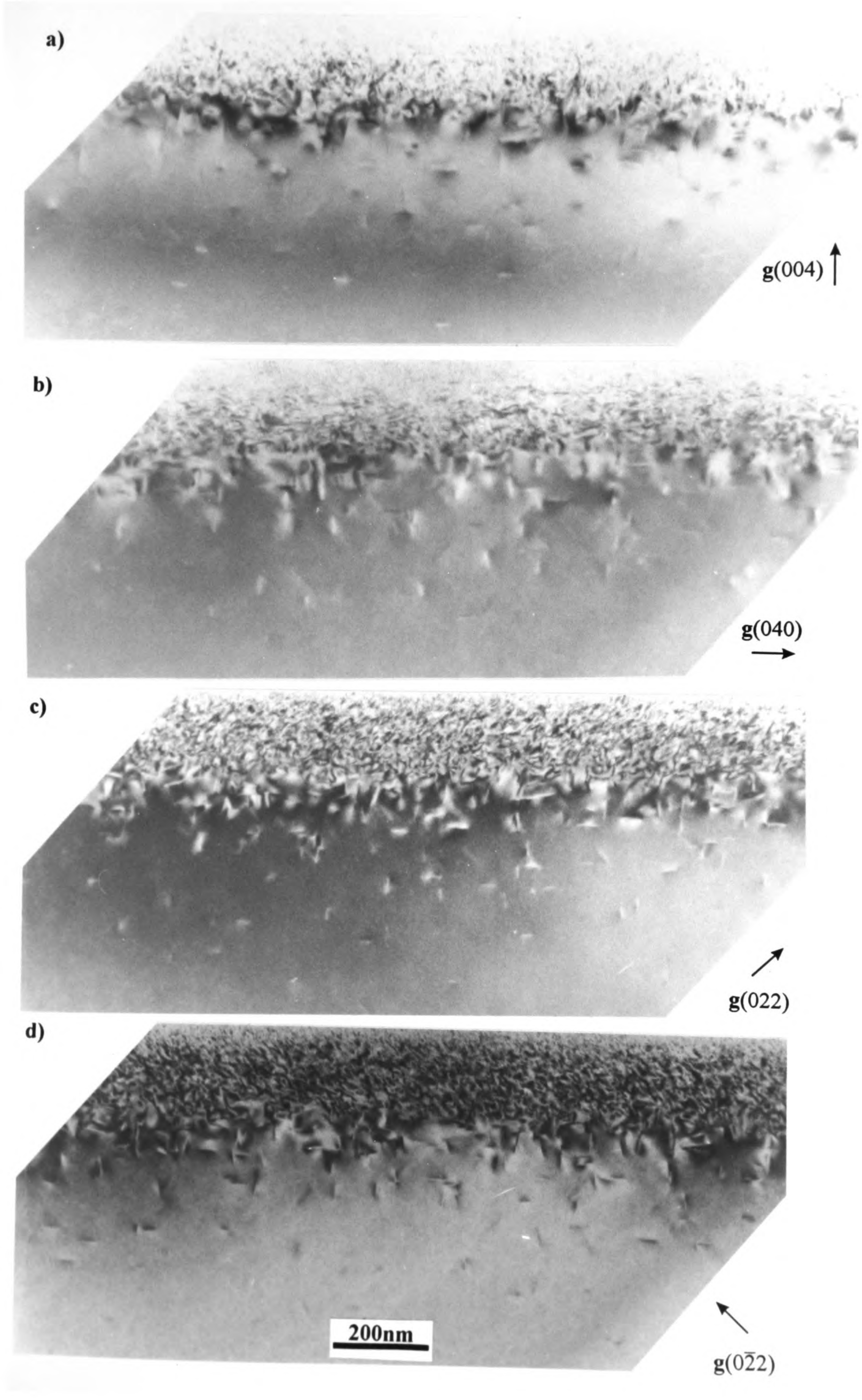
a)
g(004)
b)
g(040)
c)
g(022)
d)
200nm
g(0$\bar{2}$2)

Figure 3.25 Cross-section micrographs, close to the [111] pole, showing the defects below the buried damage/oxide layer in the sample implanted at 200keV, $\Phi = 1.2\text{x}10^{18}\text{O/cm}^2$, $T_i = 700°\text{C}$, $I' = 5.6\mu\text{A/cm}^2$,

a) bright field **g**$(0\bar{2}2)$, showing defects parallel (A) and at 90° (B) to the $[\bar{1}10]$ direction,

b) bright field **g**$(\bar{2}20)$, showing defects inclined at 60° (C) and 30° (D) to the $[\bar{1}10]$ direction,

c) weak beam **g**$(\bar{2}20)$,3**g** of the same area as in b), showing that the defects inclined at 30° consist of thin (E) and broad (F) defects and some of the latter contain weak fringes inclined at 40-50° to the $[\bar{1}10]$ direction,

d) bright field **g**$(\bar{2}20)$,

e) bright field **g**$(\bar{2}0\bar{2})$,

f) bright field **g**$(0\bar{2}2)$,

d) to f) show the defects are invisible when the **g** vector is parallel to the line direction of the defects.

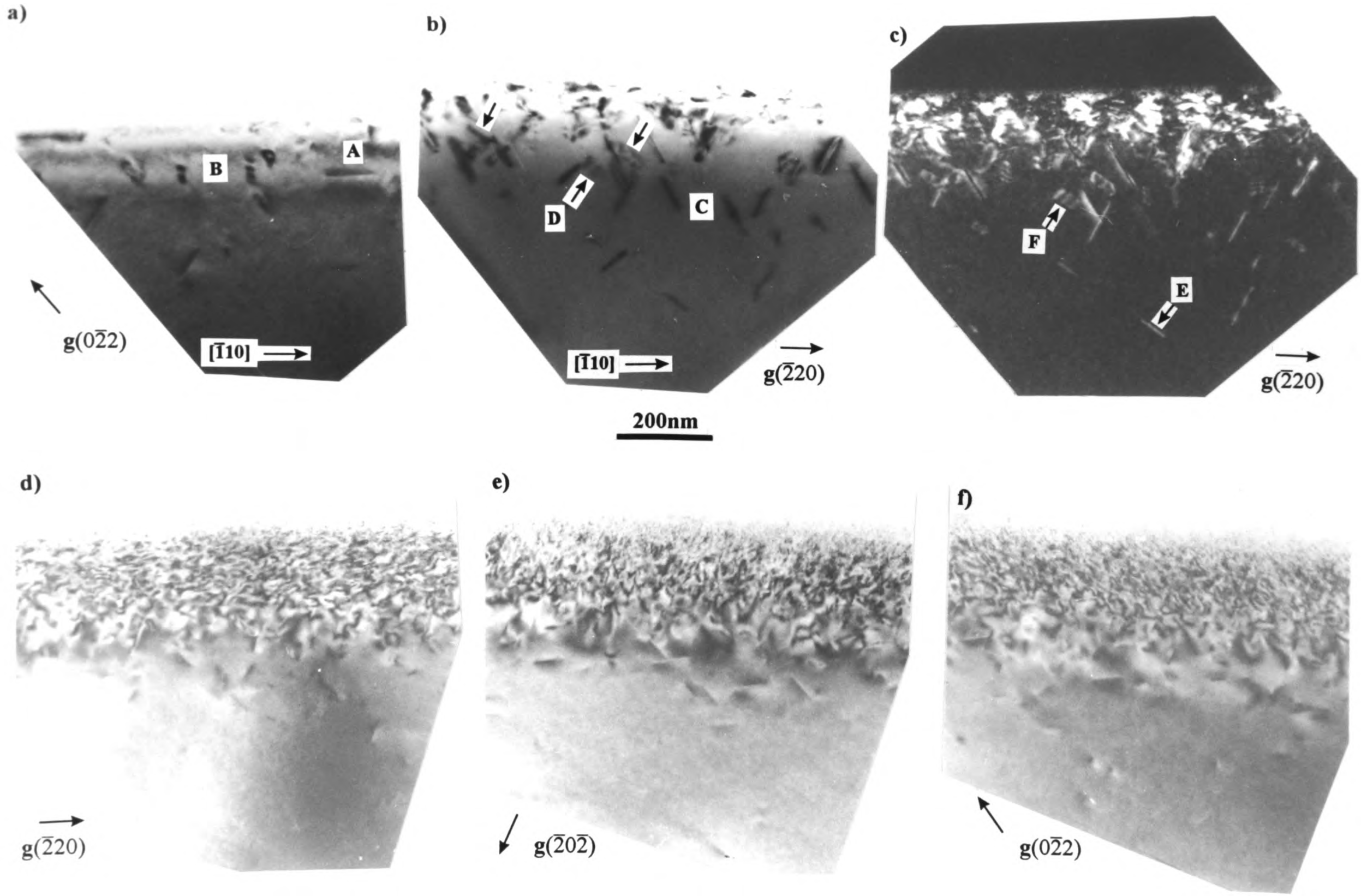
a)
b)
c)
A
B
C
D
E
F
g(0$\bar{2}$2)
[$\bar{1}$10]
[$\bar{1}$10]
g($\bar{2}$20)
g($\bar{2}$20)
200nm
d)
e)
f)
g($\bar{2}$20)
g($\bar{2}$0$\bar{2}$)
g(0$\bar{2}$2)

Figure 3.26 Projections of a rhombicuboctahedron, six {100}, twelve {110} and eight {111} faces, i) at the [110] pole, projected onto the (110) plane, ii) at the [100] pole, projected onto the (100) plane and iii) at the [111] pole, projected onto the {111} plane, showing the possible orientations of defects lying on the three lowest index planes, i.e. the {100}, {110} and {111} planes, that would be consistent with the TEM images of the defects inclined to the wafer surface (for angles other than 90°), a) defects lying in <110> directions on the {111} planes, b) defects lying in <110> or <100> directions on the <110> planes inclined to the wafer surface and c) defects lying in <110> directions on the vertical (100) and (010) planes. Note that in iii) the defects lying in the orthogonal <110> directions, on the (100) and (010) planes, make angles of 30° and 60° with the $[\bar{1}10]$ direction in this projection and for defects of equal length in the two orthogonal <110> directions, the <110> direction whose projected image makes an angle of 30° with the $[\bar{1}10]$ direction has a shorter projected length than the orthogonal <110> direction whose projected image makes an angle of 60° with the $[\bar{1}10]$ direction in this projection. The defects whose projected image make an angle of 30° with the $[\bar{1}10]$ direction in this projection are shaded darker for clarity. The directions indicated refer to directions in the plane of each projection.

i) [110] pole

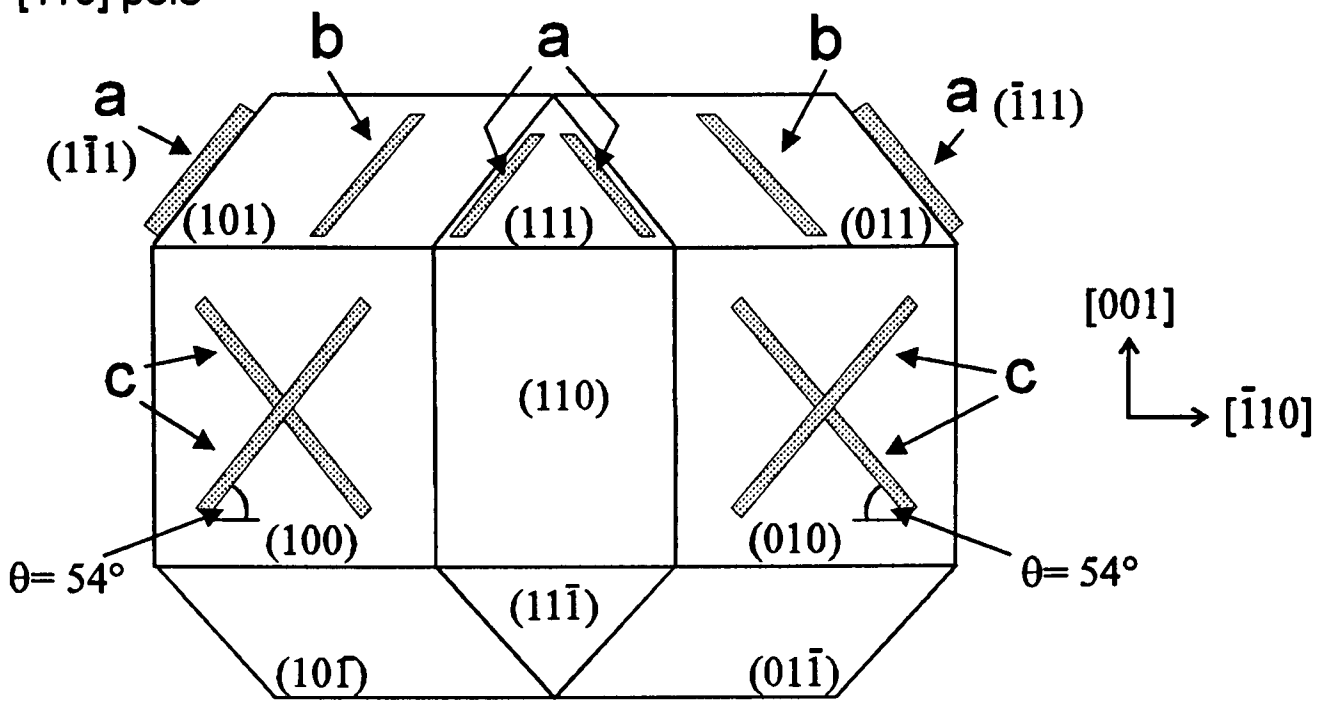

ii) [100] pole

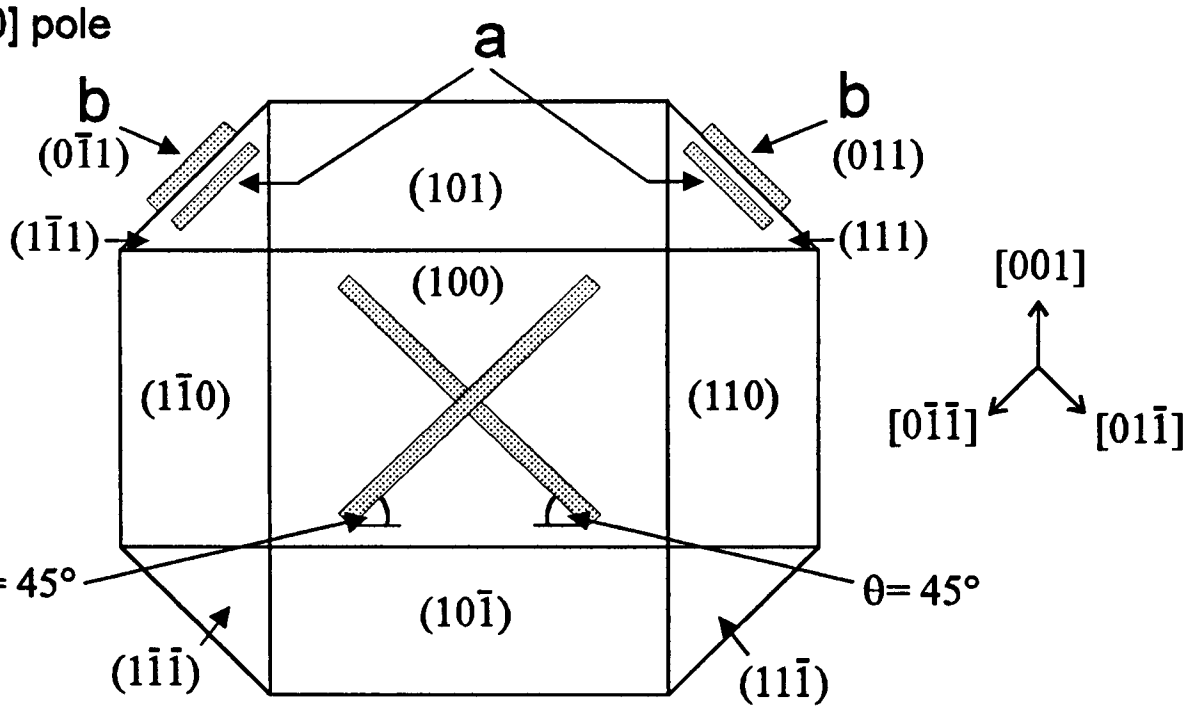

iii) [111] pole

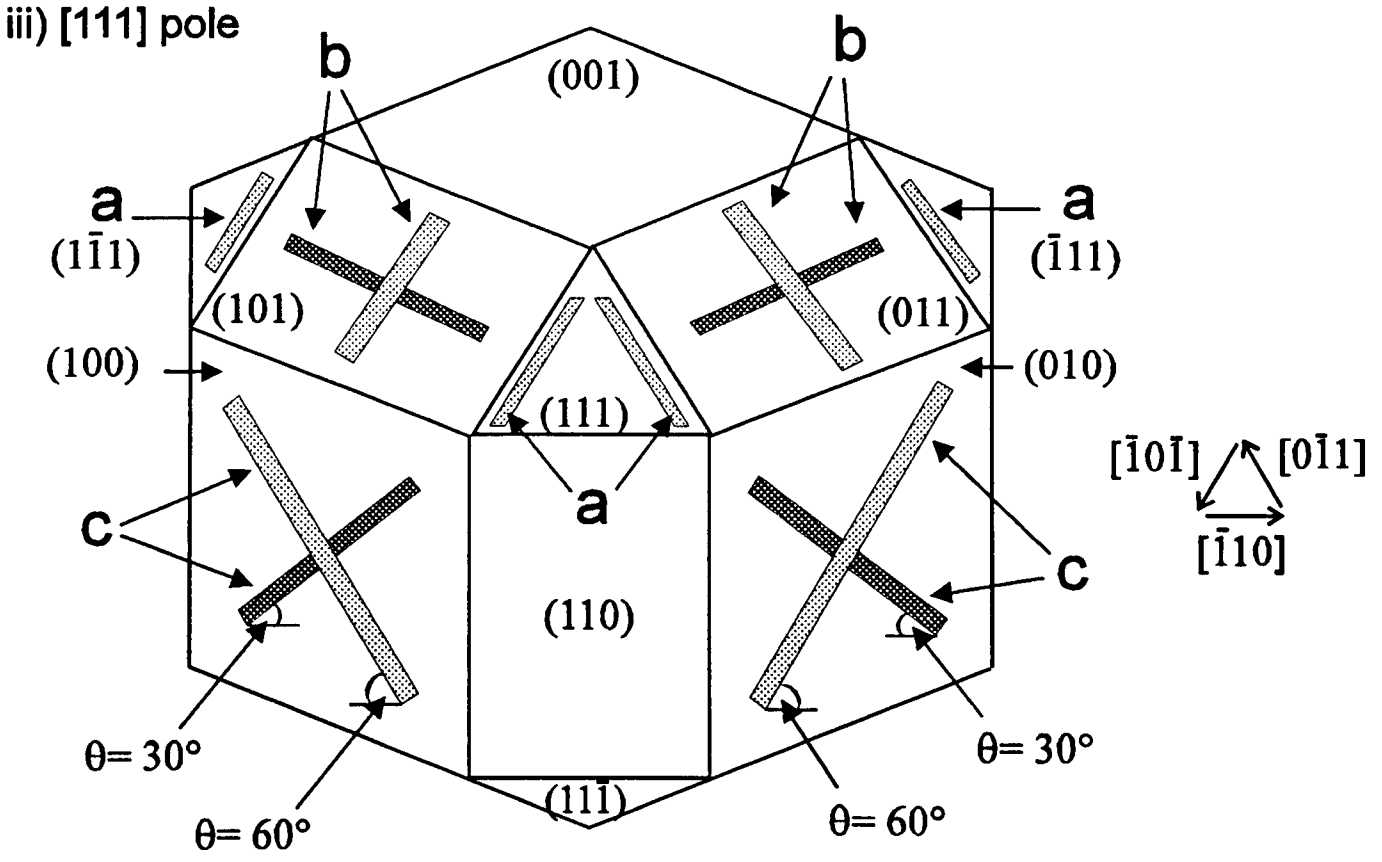

directions and those inclined at 30° to the $\pm[\bar{1}10]$ direction have their length in the <100> directions (fig. 3.26). If the length of the defects lying in the <100> and <110> directions on the inclined {110} planes was limited by the thickness of the c.s., then at the [111] pole the projected length of the defects lying in the <100> directions, i.e. those inclined at 30° to the $\pm[\bar{1}10]$ direction, would be longer than for the defects lying in the <110> directions, i.e. those inclined at 60° to the $\pm[\bar{1}10]$ direction. This was not observed experimentally and hence if the defects lie on the {110} planes then their length is not determined by the thickness of the c.s.. If the defects lying in the <100> and <110> directions were of the same length, or if the defects in the <100> directions were shorter, then their projected lengths at the [111] pole would be shorter for the defects in the <100> directions, i.e. those inclined at 30° to the $\pm[\bar{1}10]$ direction. This was observed experimentally and hence such defects are also consistent with the experimental results.

The two different line directions (<110> and <100>) might explain why the defects parallel to the $\pm[\bar{1}10]$, $\pm[0\bar{1}1]$ or $\pm[\bar{1}01]$ directions are more easily observed under two beam diffraction conditions, than the defects in the $\pm[\bar{1}\bar{1}2]$ direction or the defects inclined at 30° to the $\pm[\bar{1}10]$ direction (fig. 3.25). Dislocations with <110> line direction are more common in bulk Si than dislocations with <100> line direction[15] and hence if these defects are dislocations this suggests that it is more likely that these defects lie on the {100} planes with edges along <110> line directions, rather than on the {110} planes with edges along <110> and <100> line directions (if defects are present on both the {100} and {110} planes, then the defects inclined at 30° to the $\pm[\bar{1}10]$ direction could all lie on the {100} planes, and not on the {110} planes, and hence the edges of all the defects could have <110> line directions). Some of the defects inclined at 30° to the $\pm[\bar{1}10]$ direction are broader, more planar defects (fig. 3.25). These defects contain under $\mathbf{g}(\bar{2}20),3\mathbf{g}$ weak beam diffraction conditions weak fringes inclined at 40-50° to the $\pm[\bar{1}10]$ direction (fig. 3.25). As discussed previously displacement fringes are parallel to the intersection of the plane of the defect and the sample surface[6]. Hence for a parallel faced (110) c.s., (010), (100) and inclined {110} planes would intersect the c.s. surface in lines whose projection at this pole would make angles of 90° and 30° to the $\pm[\bar{1}10]$ direction respectively. As discussed above the electron transparent edge of the c.s. has a wedge shape and as a

consequence the (010), (100) and inclined {110} planes would intersect the c.s. surface in lines, and hence defects on these planes would contain fringes, at angles <90° and >30° to the $\pm[\bar{1}10]$ direction respectively. Hence the broad defects with fringes at 40-50° to the $\pm[\bar{1}10]$ direction are more likely to be lying on the inclined {110} planes than on the {100} planes.

The images and the streaking in the SADP at the [100] and [110] poles (figs. 3.21 & 23) strongly suggest that some of the defects lie on the {100} planes. The images and SADP at the [111] pole are consistent with defects lying on either, or both, the {100} or the {110} planes. All the results, except the displacement fringes observed in some of the broader defects using $\mathbf{g}(\bar{2}20),3\mathbf{g}$ weak beam diffraction conditions at the [111] pole, could be explained in terms of defects lying in the two orthogonal <110> directions on the {100} planes (at the [100] and [110] poles no evidence was observed which suggested that the defects did not lie only on the {100} planes). The displacement fringes observed in some of the broader defects using $\mathbf{g}(\bar{2}20),3\mathbf{g}$ weak beam diffraction conditions at the [111] pole suggest that some defects lie on the {110} planes inclined to the wafer surface (the shape of the defects on the {110} planes has not been completely determined but the images at the [111] pole suggest they are broader than the defects on the {100} planes). Hence the conclusions are that the defects are present on both the {100} and {110}planes, where the defects on the {100} planes are elongated with their length in the two orthogonal <110> directions, and the defects on the {110} planes may be either elongated in the <110> directions or broader (fig. 3.27).

Hence summarising the experimental results, at the [100] pole, the vertical and horizontal defects lie on the [010] and [001] planes respectively, and the defects inclined at 45° to the wafer surface lie on either the {110} planes or the [100] plane. At the [110] pole, the inclined defects lie on either the (010) or (100) planes or the {110} planes inclined to the wafer surface. At the [111] pole, the elongated defects parallel to the $\pm[\bar{1}10]$ direction, and the short vertical defects, lie in the $\pm[\bar{1}10]$ and $\pm[110]$ directions on the (001) plane; the elongated defects at 60° to the $\pm[\bar{1}10]$ direction, i.e. in the $\pm[0\bar{1}1]$ and $\pm[\bar{1}01]$ directions, lie on the (100) or (010) planes respectively; the elongated defects inclined at 30° to the $\pm[\bar{1}10]$ direction lie in the orthogonal <110> directions on the vertical (010) and (100) planes, and the broader defects inclined at 30° to the $\pm[\bar{1}10]$ direction lie on the {110} planes inclined to the surface.

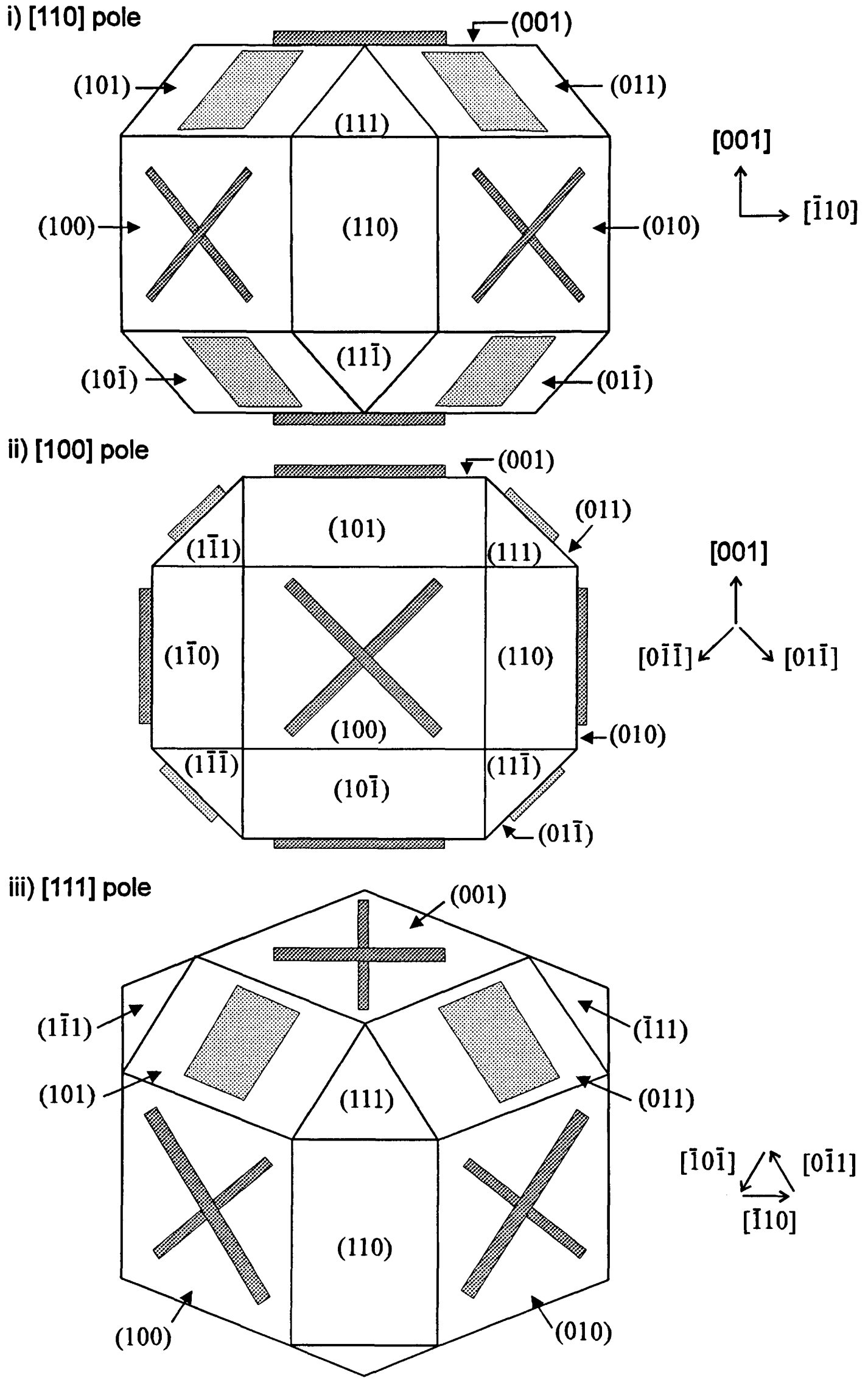

Figure 3.27 Projections of a rhombicuboctahedron, six {100}, twelve {110} and eight {111} faces, i) at the [110] pole, projected onto the (110) plane, ii) at the [100] pole, projected onto the (100) plane and iii) at the [111] pole, projected onto the {111} plane, showing what are thought to be the habit plane, shape and orientation of the defects below the buried oxide layer.

3.5.2 Defect displacement vector

At the [110] pole the "line" defects parallel to the wafer surface are invisible for **g**($\bar{2}$20) (fig. 3.22a) and visible at **g**(004) (fig. 3.22b). Hence the directions of the displacement vectors of the defects are not <110>, but could be <111> or $\pm$[001] (the magnitude of the defect displacement vector will depend on whether the defect is a dislocation loop, a platelet or a rod. This is discussed at the end of this section. For a dislocation loop or platelet the displacement vector of each individual defect has one direction while a rod defect has a radial displacement vector at right angles to the length of the rod). If the directions of the displacement vectors are <111> then at the [100] pole defects, with the displacement vectors in four of the eight possible <111> directions would be invisible for **g**(022), while defects with displacement vectors in the other four possible <111> directions would be invisible for the orthogonal **g**(0$\bar{2}$2). Hence if defects with displacement vectors in all of the eight possible <111> directions are present with equal probability then half the defects would be invisible for **g**(0$\bar{2}$2) and the other half for **g**(022). Experimentally all the defects parallel to the wafer surface are observed for both **g**(0$\bar{2}$2) and **g**(022) (fig. 3.24) and therefore the directions of the displacement vectors are not <111>. As the directions of the displacement vectors are not <110> or <111>, this suggests that the direction is $\pm$[001]. The defects inclined at 54° to the surface are visible for **g**($\bar{2}$20) and show only faint contrast for **g**(004), suggesting that $\pm$[010], $\pm$[100] or <011> could be the direction of the displacement vector.

At the [111] pole the elongated "line" defects in the $\pm$[$\bar{2}$20], $\pm$[0$\bar{2}$2] or $\pm$[$\bar{2}$02] directions are invisible for either **g**(0$\bar{2}$2), **g**($\bar{2}$02) or **g**($\bar{2}$20), when **g** is parallel to the projected line direction of the defect at this pole (fig. 3.25). The shorter elongated "line" defects inclined at 30° to the $\pm$[$\bar{2}$20] direction are visible for **g**(0$\bar{2}$2) and invisible for **g**($\bar{2}$02) or **g**($\bar{2}$20), when **g** is perpendicular to the projected line direction of these defects, at this pole (fig. 3.25). Hence the directions of the displacement vectors of these defects could be <100>, <110> or <111>.

At the {100} pole the vertical "line" defects are visible for **g**(040), **g**(0$\bar{2}$2) and **g**(022) but show only faint contrast for **g**(004) (fig 3.24). This faint contrast is similar to that observed for the defects parallel to the wafer surface at **g**(040) and suggests the direction of the displacement vector of these defects could be [010]. The defects inclined at 45° show only faint

contrast for **g**(040), **g**(004) and for either **g**(022) or **g**(0$\bar{2}$2), when **g** is not parallel to the line direction of the defect, and are invisible for either **g**(022) or **g**(0$\bar{2}$2), when **g** is parallel to the line direction (fig. 3.24), suggesting that the directions of the displacement vectors of these defects could be <110> or <111>. The faint contrast when these defects are visible suggests that ±[001] is the direction of the displacement vector (see below).

As discussed in the previous section the majority of the "line" defects are thought to lie on the {100} planes with edges in the <110> directions. The results described above suggest that the direction of the displacement vectors are perpendicular to the {100} planes of the defects. Tables 3.4 & 3.5 compares the observed contrast for the defects with values for $\mathbf{g} \cdot \mathbf{R}$ and $\mathbf{g} \cdot \mathbf{R} \times \mathbf{u}$ for defects lying on the three {001} planes, bounded by <110> line directions (**u**) and with displacement vectors (**R**) perpendicular to the planes of the defects, for the values of **g** used to form the images at the [110], [100] and [111] poles (figs. 3.22, 3.24 & 3.25). Table 3.4 shows there is good agreement between the presence of defects in the images when $\mathbf{g} \cdot \mathbf{R} \neq 0$, faint contrast in the images when $\mathbf{g} \cdot \mathbf{R} = 0$ and $\mathbf{g} \cdot \mathbf{R} \times \mathbf{u} \neq 0$, and invisibility of the defects when $\mathbf{g} \cdot \mathbf{R} = 0$ and $\mathbf{g} \cdot \mathbf{R} \times \mathbf{u} = 0$. At the [111] pole there is one diffraction condition for each of the defects inclined at 30°, and the small vertical defects, at which faint defect contrast was not observed when $\mathbf{g} \cdot \mathbf{R} = 0$ and $\mathbf{g} \cdot \mathbf{R} \times \mathbf{u} \neq 0$ (table 3.4). These defects were not studied extensively under these diffraction conditions and the faint contrast may have been overlooked.

Fig. 3.27 and Table 3.5 show that at the [100] pole the "line" defects inclined at 45° to the wafer surface could lie on either the edge on {110} planes inclined to the wafer surface or on the face on (100) plane (where the contrast is faint due to $\mathbf{g} \cdot \mathbf{R} \times \mathbf{u} \neq 0$). Table 3.6 compares the experimental images of these defects with values for $\mathbf{g} \cdot \mathbf{R}$ and $\mathbf{g} \cdot \mathbf{R} \times \mathbf{u}$ for defects lying on the inclined {110} planes, bounded by <110> line directions and with displacement vectors perpendicular to the planes of the defects, for the values of **g** used to form the images at the [100] pole (fig. 3.24). Table 3.6 shows that for defects lying on the {110} planes with displacement vector at right angles to the plane and bounded by <110> line direction there is good agreement between these defects when both $\mathbf{g} \cdot \mathbf{R} = 0$ and $\mathbf{g} \cdot \mathbf{R} \times \mathbf{u} = 0$ and when the defects in the experimental images are invisible, but when these defects are not invisible $\mathbf{g} \cdot \mathbf{R} \neq 0$, suggesting that the contrast from these defects would be "visible" and not "faint" as is

a) [110] pole

Defect morphology	**g**	contrast in image	**R**	**g · R**	**u**	**g · R x u**
—	$\bar{2}20$	invisible	±[001]	0	±[$\bar{1}$10]	0
	004	visible	"	±4	-	-
/	$\bar{2}20$	visible	±[100]	±2	-	-
($\theta = 54°$)	"	"	±[010]	±2	-	-
	004	faint	±[100]	0	±[011]	±4
	"	"	±[010]	0	±[$\bar{1}$01]	±4
\	$\bar{2}20$	visible	±[100]	±2	-	-
($\theta = 54°$)	"	"	±[010]	±2	-	-
	004	faint	±[100]	0	±[01$\bar{1}$]	±4
	"	"	±[010]	0	±[101]	±4

b) [111] pole

Defect morphology	**g**	contrast in image	**R**	**g · R**	**u**	**g · R x u**
—	$\bar{2}20$	invisible	±[001]	0	±[$\bar{1}$10]	0
	0$\bar{2}$2	visible	"	±2	-	-
	$\bar{2}$02	visible	"	±2	-	-
|	$\bar{2}20$	invisible*	"	0	±[110]	±4*
	0$\bar{2}$2	visible	"	±2	-	-
	$\bar{2}$02	visible	"	±2	-	-
\	$\bar{2}20$	visible	±[100]	±2	-	-
($\theta = 60°$)	0$\bar{2}$2	invisible	"	0	±[0$\bar{1}$1]	0
	$\bar{2}$02	visible	"	±2	-	-
\	$\bar{2}20$	visible	±[010]	±2	-	-
($\theta = 30°$)	0$\bar{2}$2	visible	"	±2	-	-
	$\bar{2}$02	invisible*	"	0	±[101]	±4*
/	$\bar{2}20$	visible	±[010]	±2	-	-
($\theta = 60°$)	0$\bar{2}$2	visible	"	±2	-	-
	$\bar{2}$02	invisible	"	0	±[10$\bar{1}$]	0
/	$\bar{2}20$	visible	±[100]	±2	-	-
($\theta = 30°$)	0$\bar{2}$2	invisible*	"	0	±[011]	±4*
	$\bar{2}$02	visible	"	±2	-	-

Table 3.4 The shape, angle of inclination to the [$\bar{2}$20] direction and contrast of the defects in the images and values of **g** · **R** and **g** · **R** x **u** (when **g** · **R** = 0) for defects lying on the {100} planes bounded by edges with <110> line directions, for different values of **g** at the a) [110] and b) [111] poles (for the [100] pole see table on the following page). * faint contast was not observed for these diffraction conditions (to obtain the correct magnitude of **g** · **R** and **g** · **R** x **u**, the values in the tables need to be multiplied by a constant, where the value of the constant depends on the type of defect, see text).

Defect morphology	g	contrast in image	**R**	**g · R**	**u**	**g · R x u**
—	004	visible	±[001]	±4	-	-
	040	faint	"	0	±[$\bar{1}$10]	±4
	"	"	"	"	±[110]	±4
	022	visible	"	±2	-	-
	0$\bar{2}$2	visible	"	±2	-	-
|	004	visible	±[010]	0	±[101]	±4
	"	"	"	"	±[$\bar{1}$01]	±4
	040	visible	"	±4	-	-
	022	visible	"	±2	-	-
	0$\bar{2}$2	visible	"	±2	-	-
/	004	faint	±[100]	0	±[011]	±4
($\theta = 45°$)	040	faint	"	0	"	±4
	022	invisible	"	0	"	0
	0$\bar{2}$2	faint	"	0	"	±4
\	004	faint	"	0	±[0$\bar{1}$1]	±4
($\theta = 45°$)	040	faint	"	0	"	±4
	022	faint	"	0	"	±4
	0$\bar{2}$2	invisible	"	0	"	0

Table 3.5 [100] pole. The shape, angle of inclination to the [$\bar{2}$20] direction and contrast of the defects in the images and values of **g** · **R** and **g** · **R** x **u** (when **g** · **R** = 0) for defects lying on the {100} planes bounded by edges with <110> line directions, for different values of **g** at the [100] pole (to obtain the correct magnitude of **g** · **R** and **g** · **R** x **u**, the values in the tables need to be multiplied by a constant, where the value of the constant depends on the type of defect).

Defect morphology	g	contrast in image	**R**	**g · R**	**u**	**g · R x u**
/	004	faint	±[0$\bar{1}$1]	±4	-	-
($\theta = 45°$)	040	faint	"	±4	-	-
	022	invisible	"	0	±[011]	0
	0$\bar{2}$2	faint	"	±4	-	-
\	004	faint	±[011]	±4	-	-
($\theta = 45°$)	040	faint	"	±4	-	-
	022	faint	"	±4	-	-
	0$\bar{2}$2	invisible	"	0	±[0$\bar{1}$1]	0

Table 3.6 [100] pole. The shape, angle of inclination to the [$\bar{2}$20] direction and contrast of the defects in the images and values of **g** · **R** and **g** · **R** x **u** (when **g** · **R** = 0) for defects lying on the {110} planes, bounded by <110> line directions, with displacement vectors at right angles to the planes of the defects for different values of **g** at the [100] (to obtain the correct magnitude of **g** · **R** and **g** · **R** x **u**, the values in the table need to be multiplied by a constant, where the value of the constant depends on the type of defect).

experimentally observed (fig. 3.24). Therefore the fainter contrast from the defects in the experimental images compared to the contrast from the vertical and horizontal defects (fig. 3.24), assuming that this contrast difference is not due to the different habit plane ({110} as opposed to {100} for the vertical and horizontal defects), suggests that the defects lie on the {100} rather than the {110} planes.

The comparisons in Tables 3.4, 3.5 & 3.6 support the idea that the "line" defects lie on the {100} planes, bounded by <110> line direction and with displacement vectors perpendicular to the plane of the defects. The magnitude of the values of $\mathbf{g} \cdot \mathbf{R}$ and $\mathbf{g} \cdot \mathbf{R} \times \mathbf{u}$ in Tables 3.4, 3.5 & 3.6 depend on whether the defects are dislocation loops, platelets or rods. For dislocation loops the displacement vector (**R**) in Tables 3.4, 3.5 & 3.6 is replaced by the Burgers vector (**b**). For **R** = <100> and **b** = a<100> then the $\mathbf{g} \cdot \mathbf{R}$ and $\mathbf{g} \cdot \mathbf{R} \times \mathbf{u}$ values given in the tables are correct. For **R** = <110> and **b** = <100>a/2 then the $\mathbf{g} \cdot \mathbf{R}$ and $\mathbf{g} \cdot \mathbf{R} \times \mathbf{u}$ values given in the tables need to be multiplied by ½. For platelets the values of $\mathbf{g} \cdot \mathbf{R}$ and $\mathbf{g} \cdot \mathbf{R} \times \mathbf{u}$ in Tables 3.4, 3.5 & 3.6 need to be multiplied by a constant which can be larger or smaller than 1 depending on the morphology of the platelets. Although for platelets the magnitude of **R** are not known the contrast analysis can nevertheless be used to deduce the direction of **R**. For rods the displacement vector **R** does not lie along a single direction but is perpendicular to the rod. Consequently the rods only go out of contrast when **g** is parallel to the rod. As the defects are invisible for more than one **g** the defects can not be rods. The presence of streaks in the <100> directions in the SADP (figs. 3.21c & 3.23b) suggest the defects are platelets, rather than dislocation loops, where because oxygen is being implanted Si oxide is the most likely composition.

At the [130] and [121] poles, edge-on and planar defects are visible (figs. 3.28 & 3.29). Some of the defects are invisible for $\mathbf{g}(1\bar{3}1)$ or $\mathbf{g}(\bar{1}31)$, at the [130] pole (fig. 3.28), and invisible for $\mathbf{g}(\bar{3}11)$ or $\mathbf{g}(11\bar{3})$, at the [121] pole (fig. 3.29), suggesting that the displacement vectors of these defects could be <110> or <301>. As these defects can not have a <100> displacement vector two different types of displacement vector must be present, suggesting that two different defects are present. As described in section 3.5.1 the displacement fringes observed in some of the broader defects, using $\mathbf{g}(\bar{2}20)$,3**g** weak beam diffraction conditions at the [111] pole, suggest

Figure 3.28 Cross-section micrographs (of the same area), at or close to the [130] pole, showing the defects below the buried damage/oxide layer in the sample implanted at 200keV, $\Phi = 1.2\text{x}10^{18}\text{O/cm}^2$, $T_i = 700°\text{C}$, $I' = 5.6\mu\text{A/cm}^2$,

a) bright field many beam diffraction condition at the [130] pole,

b) bright field $\mathbf{g}(\bar{1}31)$,

c) bright field $\mathbf{g}(1\bar{3}1)$.

Figure 3.29 Cross-section micrographs (of the same area), at or close to the [121] pole, showing the defects below the buried damage/oxide layer in the sample implanted at 200keV, $\Phi = 1.2\text{x}10^{18}\text{O/cm}^2$, $T_i = 700°\text{C}$, $I' = 5.6\mu\text{A/cm}^2$,

a) bright field many beam diffraction condition at the [121] pole,

b) bright field $\mathbf{g}(\bar{3}11)$,

c) bright field $\mathbf{g}(11\bar{3})$.

Figure 3.28

a)

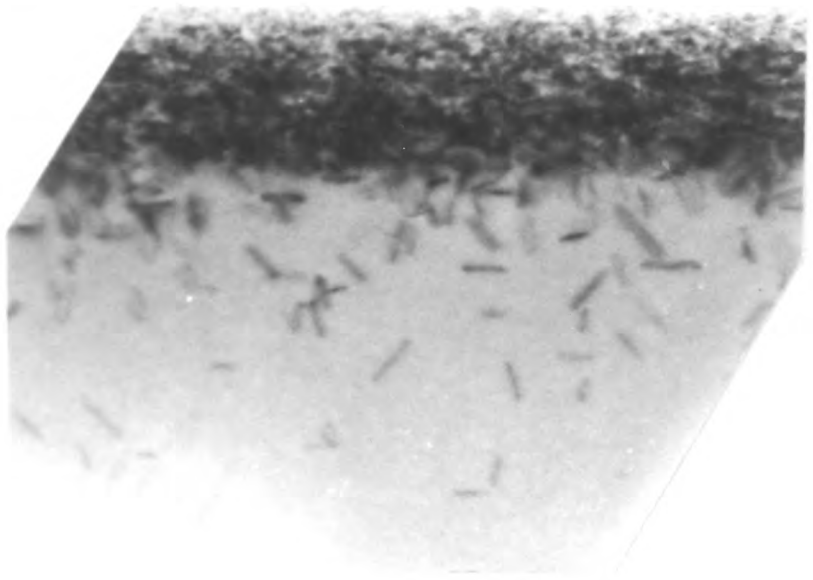

b)

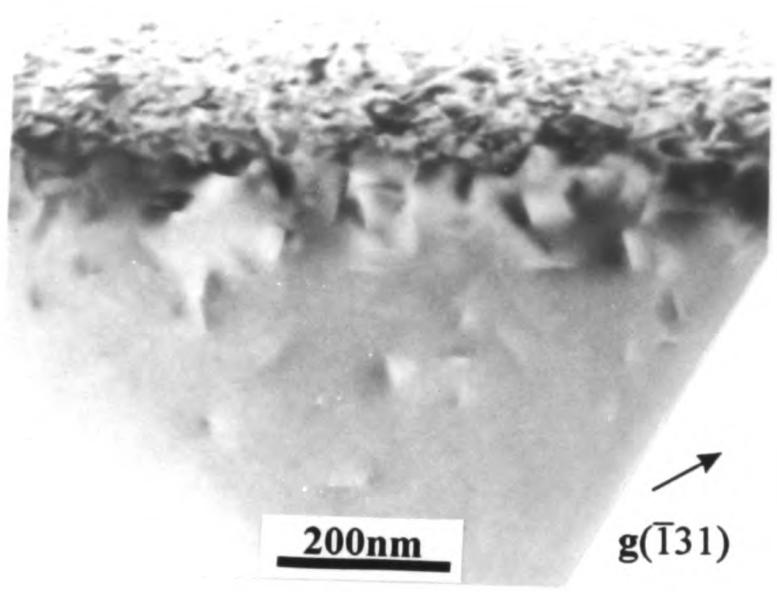

c)

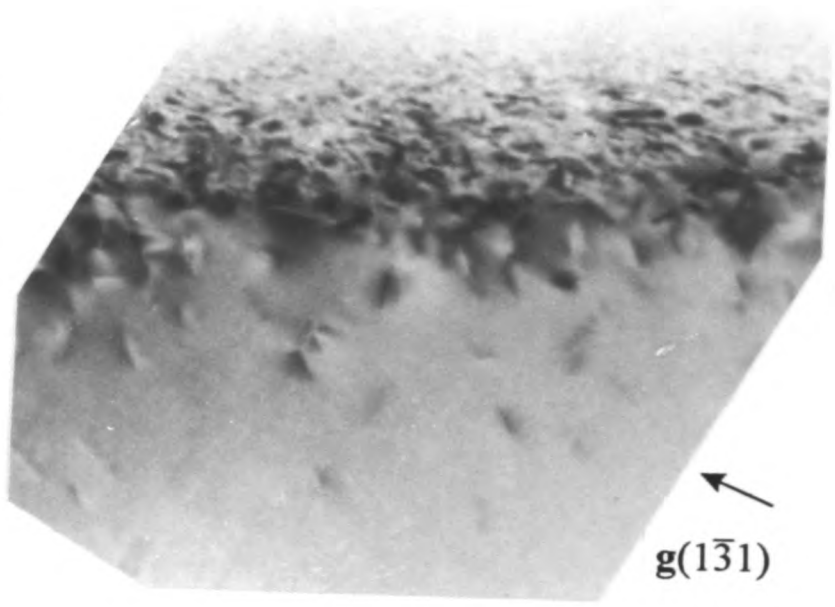

Figure 3.29

a)

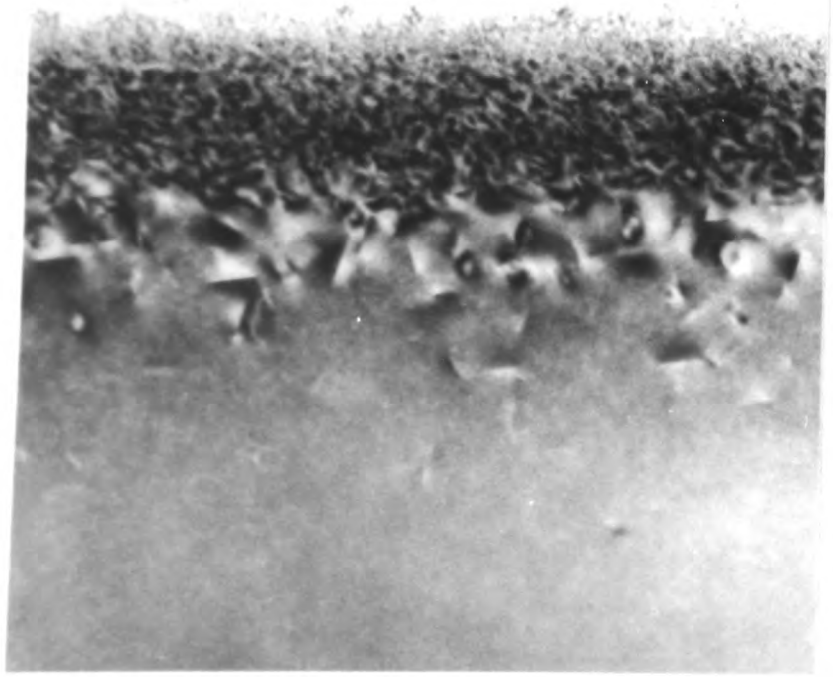

b)

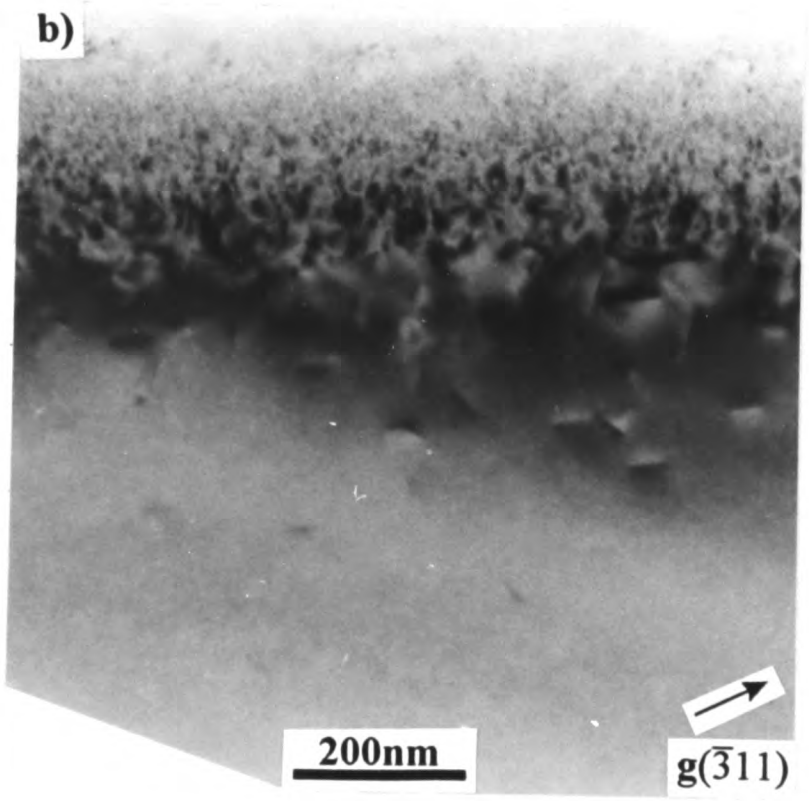

c)

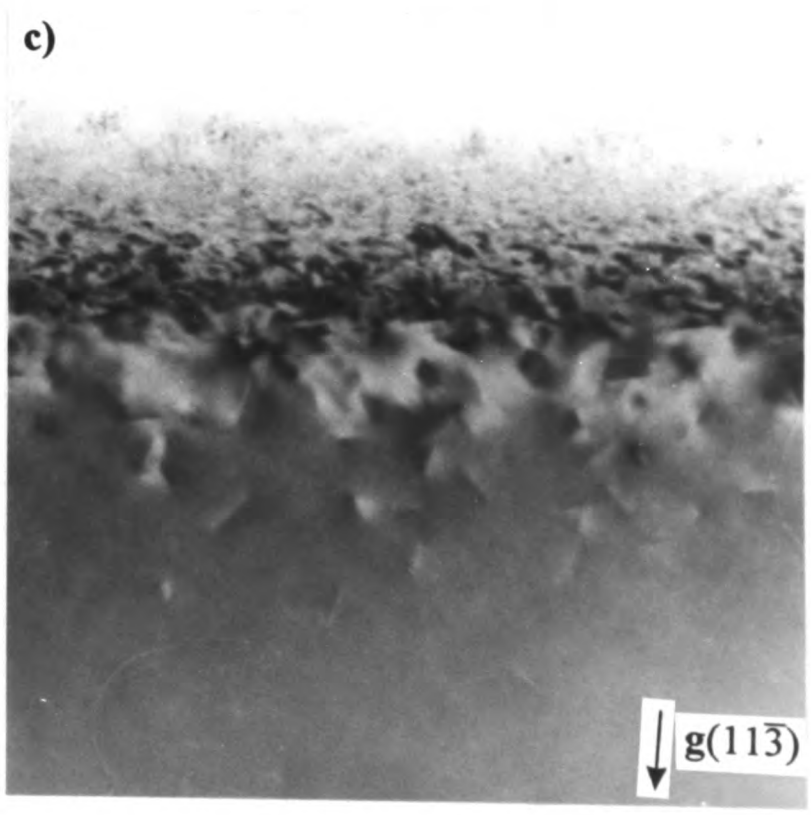

that some of the "line" defects lie on the {110} planes, and therefore it is possible that some of the defects that were observed to go invisible for g{311} at the [130] and [121] poles are lying on the {110} planes with displacement vectors perpendicular to the plane of the defect. These defects could also be oxide platelets, but no streaking in <110> directions was observed in the SADP suggesting that these defects are not platelets. Edge dislocation loops, which have their Burgers vector perpendicular to the plane of the loop, are often observed in ion implanted Si. Hence it seems likely that these "line" defects are {110} edge loops, formed from the excess Si_i.

Hence the results suggest that the "line" defects both inclined to and parallel with the wafer surface (fig. 3.21) consist of both oxide platelets and dislocation edge loops. The micrographs taken at the [110] pole show that for the same dose, the length and density of the "line" defects inclined to and parallel with the wafer surface depend on the implant energy, with the defect length increasing and the density decreasing with increasing implant energy (fig. 3.21). In previous work implanting similar doses at 200keV and 550°C using beam heating only, these defects were not observed and hence their presence is probably due to the higher implant temperature (680-700°C) used in this work.

3.6 Oxygen Concentration

3.6.1 SIMS results

SIMS profiles of the samples implanted with doses $0.1x10^{18}O/cm^2$ to $1.6x10^{18}O/cm^2$ at energies of 50keV, 70keV, 90keV and 200keV are shown in Figs. 3.30 & 3.31. For all four energies the SIMS profiles show, in agreement with reports in the literature, that for low doses the oxygen profiles are skewed gaussians. The depths of the peaks in the oxygen profiles for the four implant energies show good agreement with the depths predicted by TRIM90 (table 3.7). With increasing dose the oxygen concentration increases at all depths and the profiles change from skewed gaussians to flat topped distributions, with the oxygen concentration at the flat peak corresponding to stochiometric SiO_2. For the low energy implants, in agreement with previous reports of high energy implants[12-14], once the oxygen concentration at the peak reaches

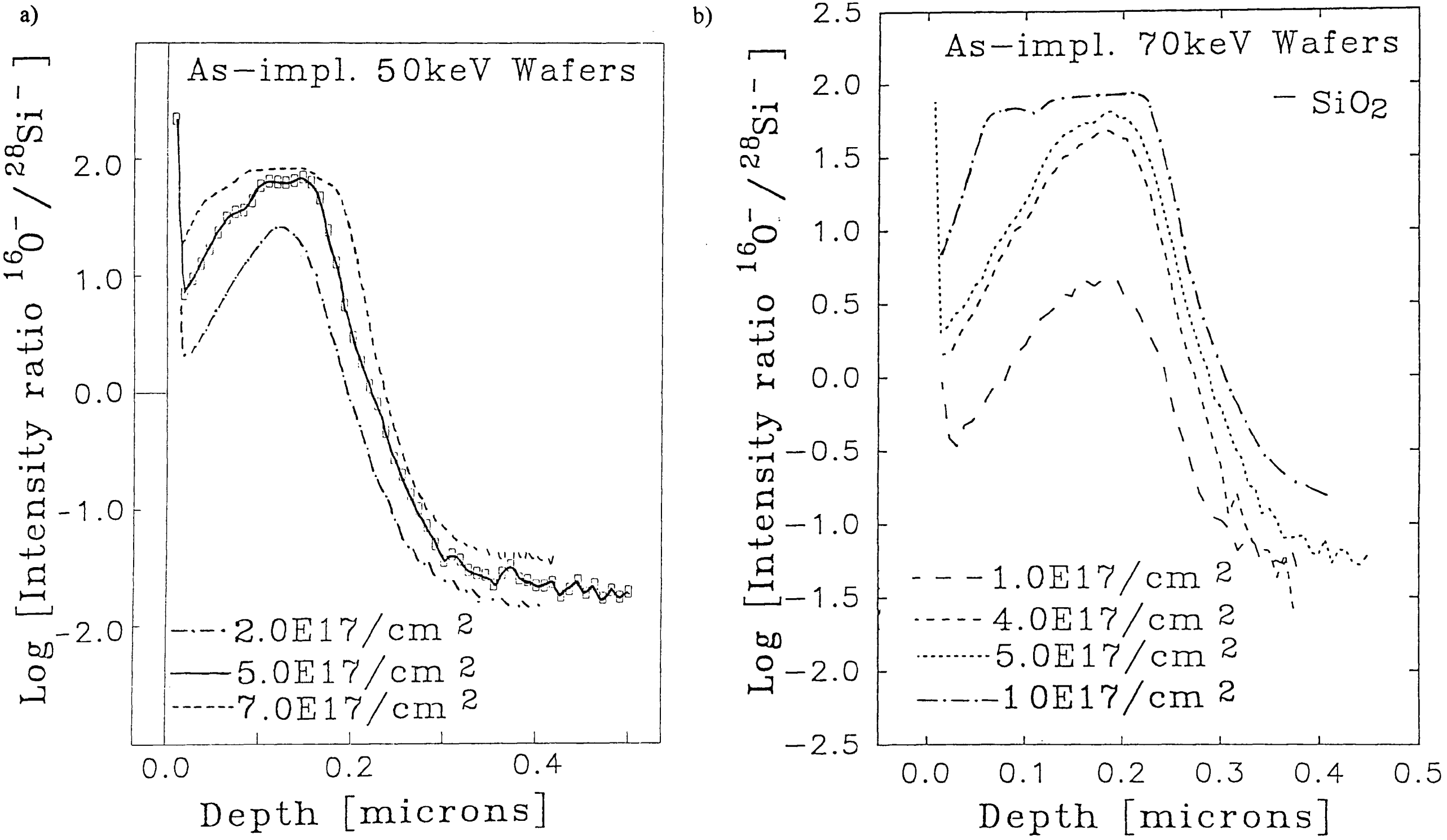

Figure 3.30 SIMS profiles of the oxygen distributions for various doses implanted at a) 50keV and b) 70keV.

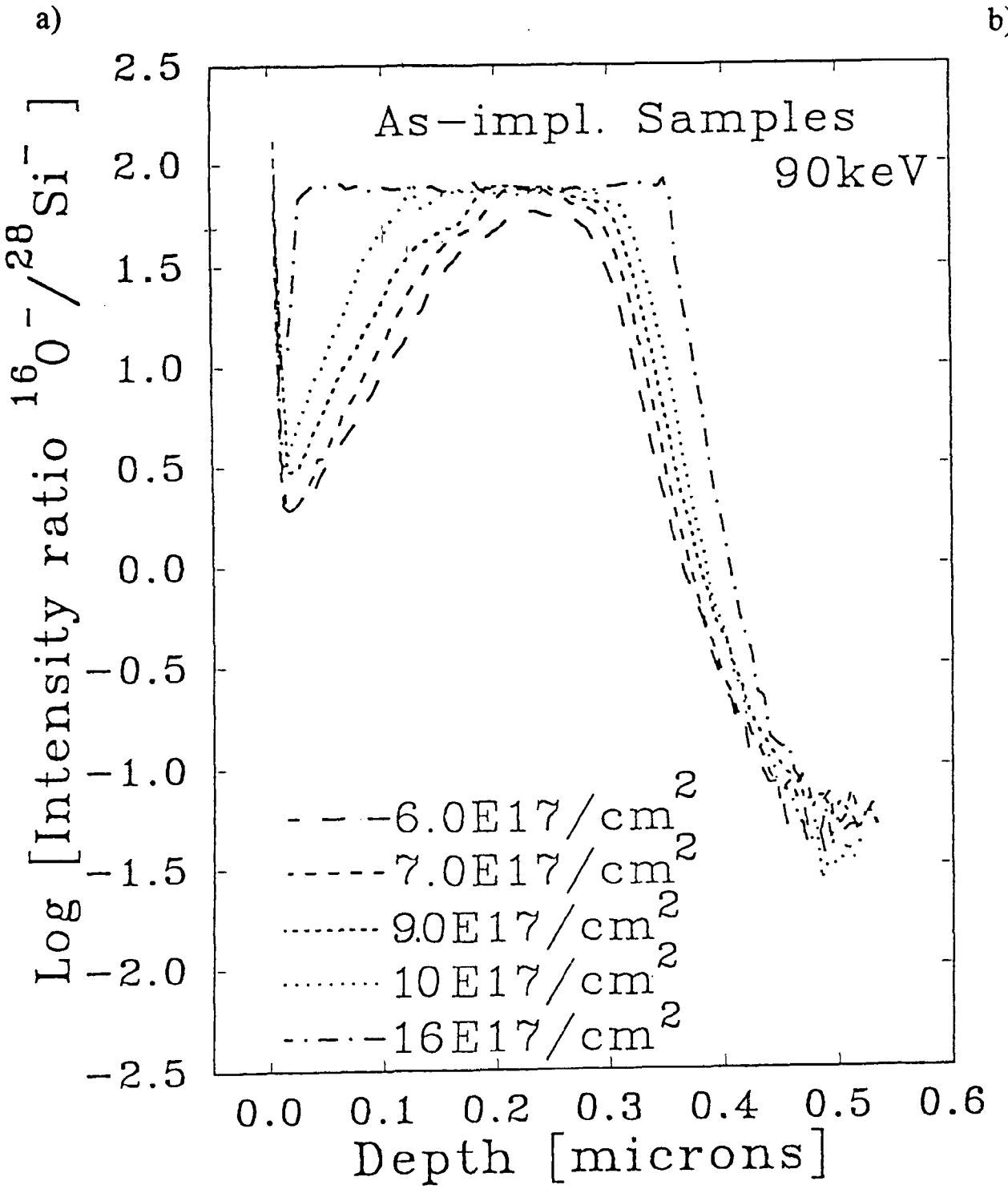

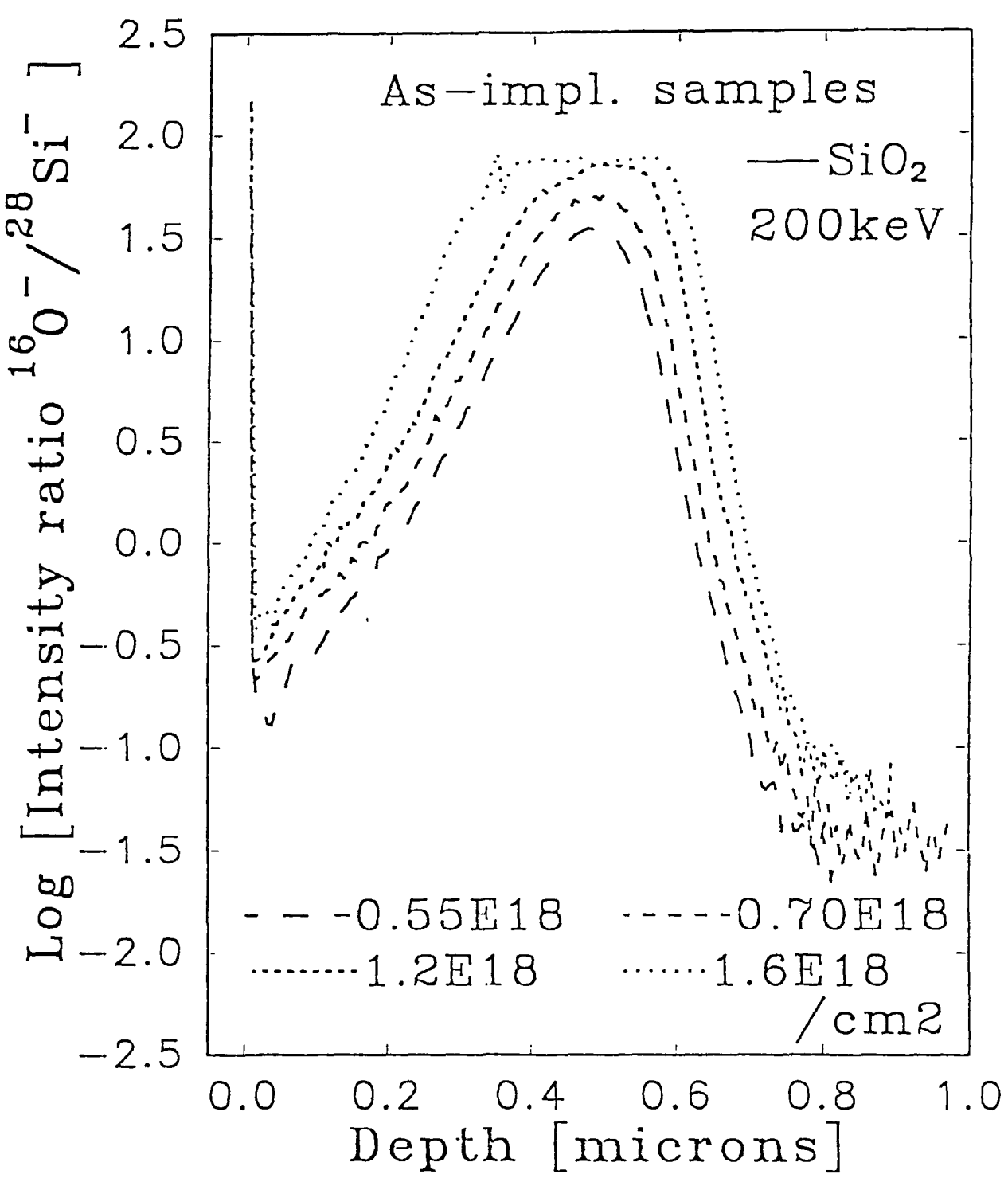

Figure 3.31 SIMS profiles of the oxygen distributions for various doses implanted at a) 90keV and b) 200keV.

Energy (keV)	Depth of the peak of the oxygen profile for doses < $^{I}\Phi c$ (nm)		Minimum dose ($^{I}\Phi c$) for forming an oxide layer after implantation ($x10^{18}O^{+}/cm^{2}$)	
	SIMS	TRIM90	TEM & SIMS	Model*
50	130±7	121	0.5	0.54
70	181±9	167	0.7	0.67
90	227±12	209	$0.7<\Phi<0.9$	0.8
200	481±25	446	1.2	1.16

Table 3.7 Comparisons of the depth of the peak of the oxygen profile from the SIMS results and the predictions from the computer program TRIM90, for doses less than the minimum dose to form a buried oxide layer after implantation ($^{I}\Phi c$), and of the value of the $^{I}\Phi c$ estimated from the TEM and SIMS results and the prediction of this dose from a semi-empirical model (*Li *et al* [16]).

Log [O^{+}/Si ratio]	Oxygen concentration ($/cm^{3}$)	Equivalent volume fraction of SiO_2
1.92	$4.48x10^{22}$	100 %
1.7	$2.8x10^{22}$	65 %
1.6	$2.2x10^{22}$	50 %
1.5	$1.8x10^{22}$	40 %
1.2	$1.3x10^{22}$	30 %
1	$1.0x10^{22}$	22 %
0.5	$4.7x10^{21}$	10 %
0.3	$3.9x10^{21}$	9 %
0	$1.9x10^{21}$	4 %
-0.5	$6x10^{20}$	1.3 %
-1	$2x10^{20}$	0.4 %
-1.5	$6x10^{19}$	0.1 %

Table 3.8 Calibration of the output signal from the SIMS equipment (log[O^{+}/Si ratio]) in terms of the oxygen concentration and the equivalent volume fraction of the material that is silicon dioxide if all the oxygen present is in the form of silicon dioxide.

the value corresponding to SiO_2 ($4.48x10^{22}/cm^3$) then with further increases in dose the oxygen concentration does not increase further, i.e. an oxygen rich $SiO_x(x>2)$ layer does not form.

The conversion of the log of the intensity ratio of the oxygen to Si SIMS signals, as plotted on the vertical axis of the SIMS profiles, to an oxygen concentration has been carried out using the results of Griffin, for the enhancement factor of the intensity ratio[15], and by assuming that the peak value of the intensity ratio, 1.92, corresponds to stochiometric SiO_2, i.e. an oxygen concentration of $4.48x10^{22}/cm^3$. The conversions are summarised in Table 3.8.

3.6.2 Volume of stochiometric silicon dioxide

If it is assumed that all the oxygen measured by the SIMS is present as stochiometric SiO_2 then the volume fraction of the material that is SiO2 can be estimated for each point on the SIMS profiles. The corresponding values are shown in Table 3.8.

3.7 Correlation of the Microstructure and Oxygen Concentration

By calibrating the SIMS profiles and overlaying them on the TEM micrographs the local oxygen concentration at the depths of the seven different SiO_2/precipitate morphologies observed in the TEM results can be estimated (the magnification of the TEM micrographs used was the same as in Figs. 3.14, 3.17 & 3.18 and hence the corresponding depth scale of the SIMS profiles used was approximately twice the scale of the profiles in Figs. 3.30 & 3.31).

1) Precipitate denuded zone The SIMS signal at the depth of the precipitate denuded zone, present at the surface in the low dose 200keV and 70keV implants, is in the range -1 to -0.5, corresponding to oxygen concentrations of $2x10^{20}/cm^3$ to $\approx 6x10^{20}/cm^3$. Conversely, when the SIMS signal is in this range, a denuded zone is observed in the micrographs.

2) Spheroidal inclusions The SIMS signal at the depth of the spheroidal inclusions observed only in the 200keV implants is -0.5, corresponding to an oxygen concentration of $\approx 6x10^{20}/cm^3$.

3) Spherical precipitates The SIMS signal at the depth of the spherical precipitates, present in <100> linear or cubic arrays, is in the range -0.5 to 0.5, corresponding to oxygen concentrations between $\approx 6x10^{20}/cm^3$ & $5x10^{21}/cm^3$. The SIMS signal at the depths of the randomly distributed

spherical precipitates is in the range 0.5 to 1.6, corresponding to oxygen concentrations between $5x10^{21}/cm^3$ and $2.2x10^{22}/cm^3$.

4) [001] columnar precipitates The SIMS signal at the depths of these precipitates is in the range 1.2 to 1.6, corresponding to oxygen concentrations of $1.3x10^{22}/cm^3$ to $2.2x10^{22}/cm^3$.

5) Irregular precipitates The SIMS signal at the depths of these precipitates is in the range 1.6 to 2.0, corresponding to oxygen concentrations between $2.2x10^{22}/cm^3$ and $4.48x10^{22}/cm^3$.

6) Elongated precipitates The SIMS signal at the depths of these precipitates is in the range 1.2 to 1.6, corresponding to oxygen concentrations between $1.3x10^{22}/cm^3$ and $2.2x10^{22}/cm^3$.

7) Continuous oxide layer The minimum doses at each energy at which a stochiometric SiO_2 layer is formed at the peak of the oxygen profile is in good agreement with the doses for which a buried amorphous layer is observed by TEM, confirming that the buried amorphous layer is stochiometric SiO_2. The minimum doses, at each energy, at which a stochiometric SiO_2 layer is formed are in good agreement with the predictions of these doses from the semi-empirical model of Li *et al*[16] (table 3.7).

The correlations between the microstructure and the oxygen concentration described above apply to all the energies and doses at which that microstructure is observed. The results are summarised in Fig. 3.32. For oxygen concentrations $<1.3x10^{22}/cm^3$ and $>2.2x10^{22}/cm^3$ only one type of precipitate morphology was observed at each oxygen concentration, i.e. the precipitate morphology is independent of the depth, suggesting that the oxygen concentration is playing the critical role in determining the precipitate morphology. For oxygen concentrations between $1.3x10^{22}/cm^3$ and $2.2x10^{22}/cm^3$ three different precipitate morphologies at three different depths are present. Hence the morphology of the SiO_2 precipitates is found to depend on both the local oxygen concentration and the depth below the surface. This suggests that a factor other than the local oxygen concentration helps to determine at least two of the three precipitate morphologies present for oxygen concentrations between $1.3x10^{22}/cm^3$ and $2.2x10^{22}/cm^3$. This is discussed in section 3.9.2. The implantation energy and dose determine the local oxygen concentration as a function of depth and hence the precipitate morphology depends indirectly on both. If the as-implanted structure is divided approximately into three regions, a near surface region, a region close to the peak of the oxygen distribution and the region between

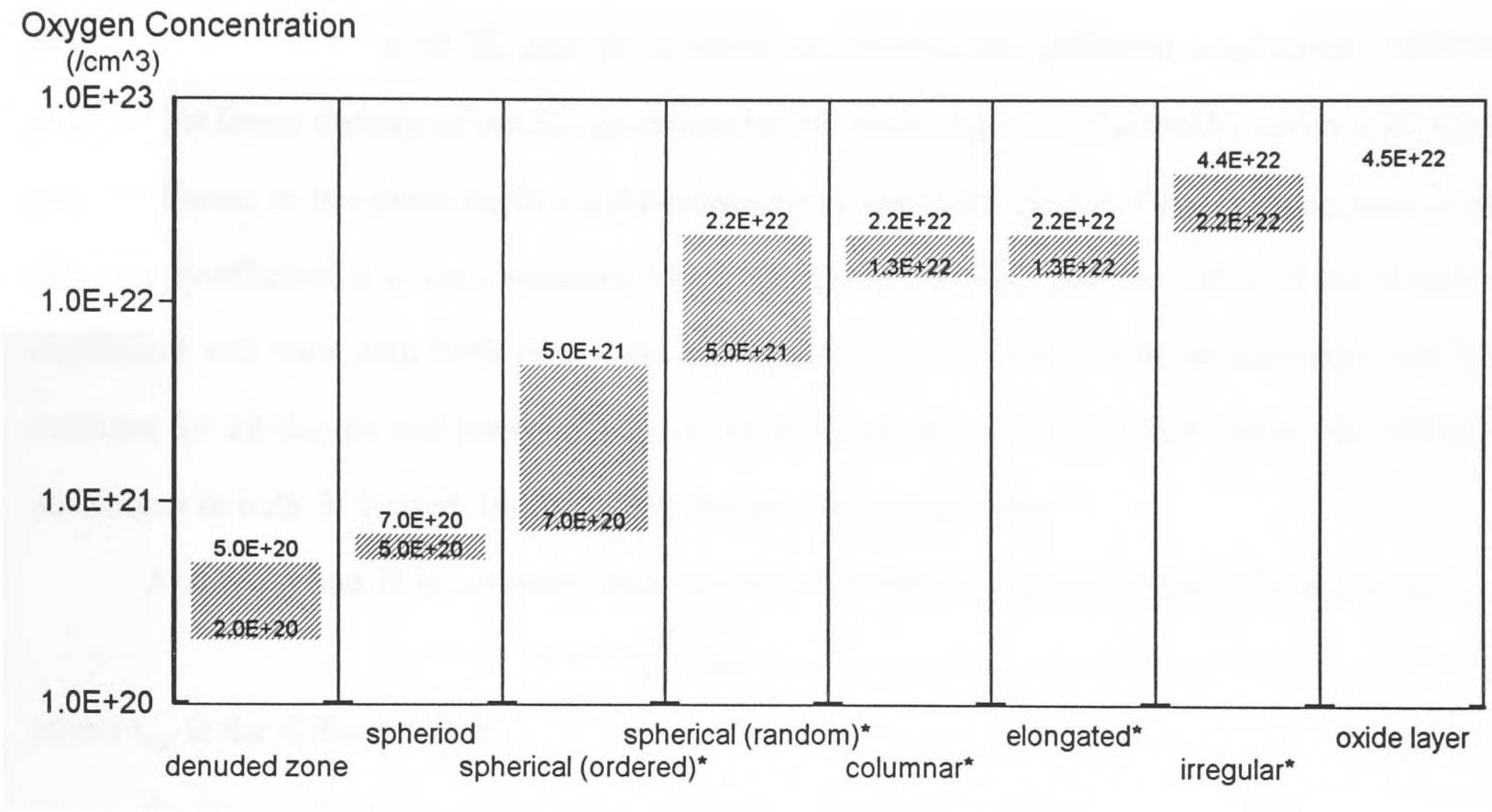

Figure 3.32 The range of oxygen concentrations at which the denuded zone and the seven different precipitate/oxide morphologies were observed.

these two, then in each of these regions only one precipitate morphology is present for oxygen concentrations between $1.3x10^{22}/cm^3$ and $2.2x10^{22}/cm^3$ and therefore in these regions only one precipitate morphology is present for any oxygen concentration (fig. 3.33).

3.8 Oxygen Diffusion Coefficient and Diffusion Length

The diffusion coefficient (D) of oxygen in bulk Si at the implantation temperature, 680°C, is $3.3x10^{-15}cm^2/s$ [17]. In the non-equilibrium situation of ion implantation the value of the diffusion coefficient is likely to be different from the bulk value. The generation by the incoming ions of a large number of Si_v and Si_i is likely to increase the diffusion coefficient. TRIM90 predicts the linear density of the Si_v generated by the incoming ions (Si_v/ion/Å) varies with depth and is different at the same depth for different energy implants. Hence if the enhancement of the diffusion coefficient is a very localised phenomena it is possible that the value of the diffusion coefficient will vary with both depth and ion energy. In this work it will be assumed that D is constant for all depths and energies and, in the absence of a more accurate value, the diffusion coefficient in bulk Si is used, but it is regarded as a minimum value.

Assuming that D is constant, then the diffusion length is given by the usual expression,

$$x = 2\sqrt{D\,t_{diff}} \quad \text{.....Eq. 3.1}$$

where t_{diff} is the diffusion time.

During implantation the time available for the first implanted ions to diffuse is equal to the implantation time, but for subsequent ions the time available for diffusion decreases linearly, assuming a constant beam current, with the time from the start of the implant. Hence during implantation there is a spread in the time available for the oxygen ions to diffuse and hence a spread in the diffusion lengths. The time available for diffusion (t_{diff}) as a function of the time (t) from the start of the implant is given by,

$$t_{diff} = t_{im} - t \quad \text{.....Eq. 3.2}$$

where t_{im} is the total implantation time. Hence the value of the diffusion length (x) for an ion implanted at time "t" is given by,

$$x = 2\sqrt{D\,(t_{im} - t)} \quad \text{.....Eq. 3.3}$$

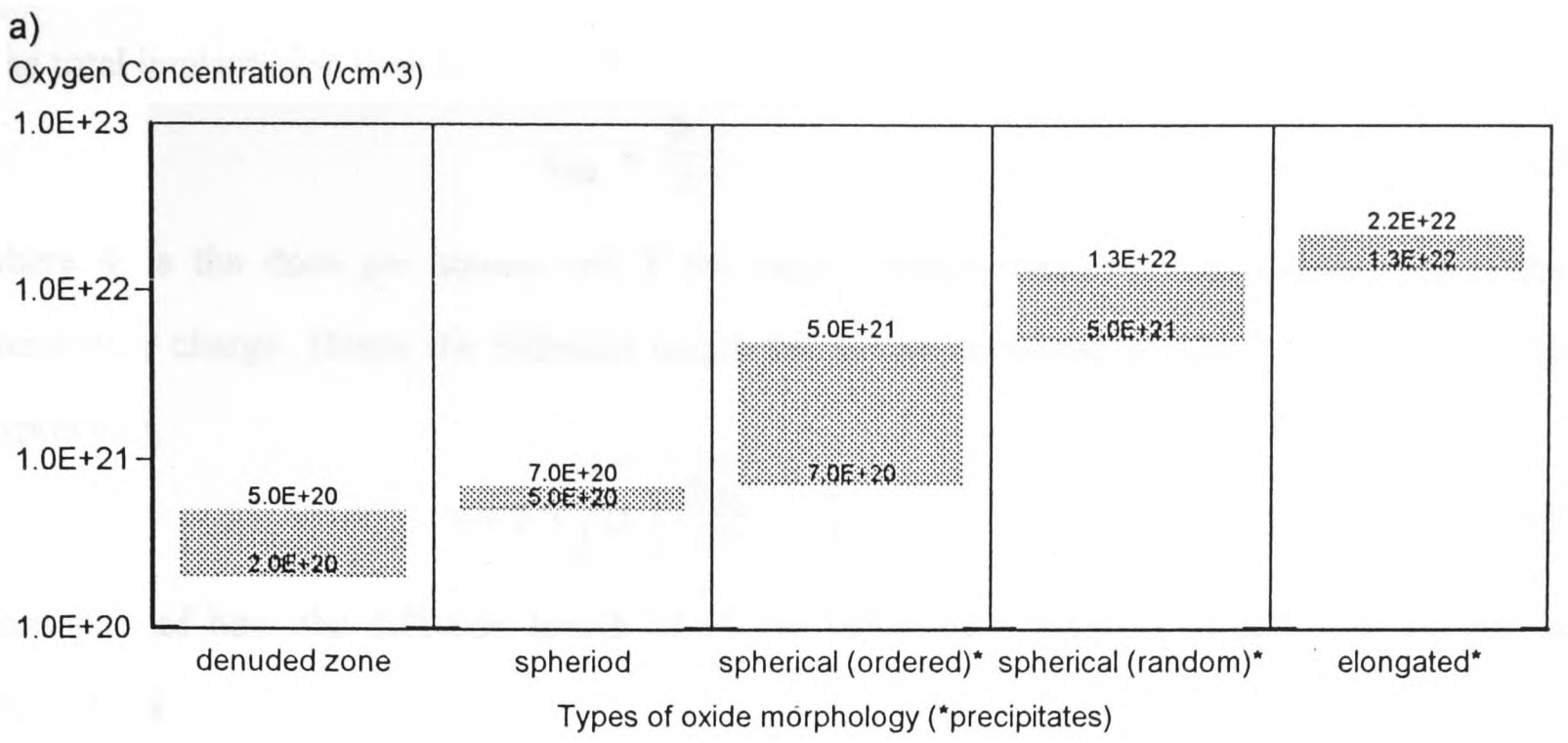

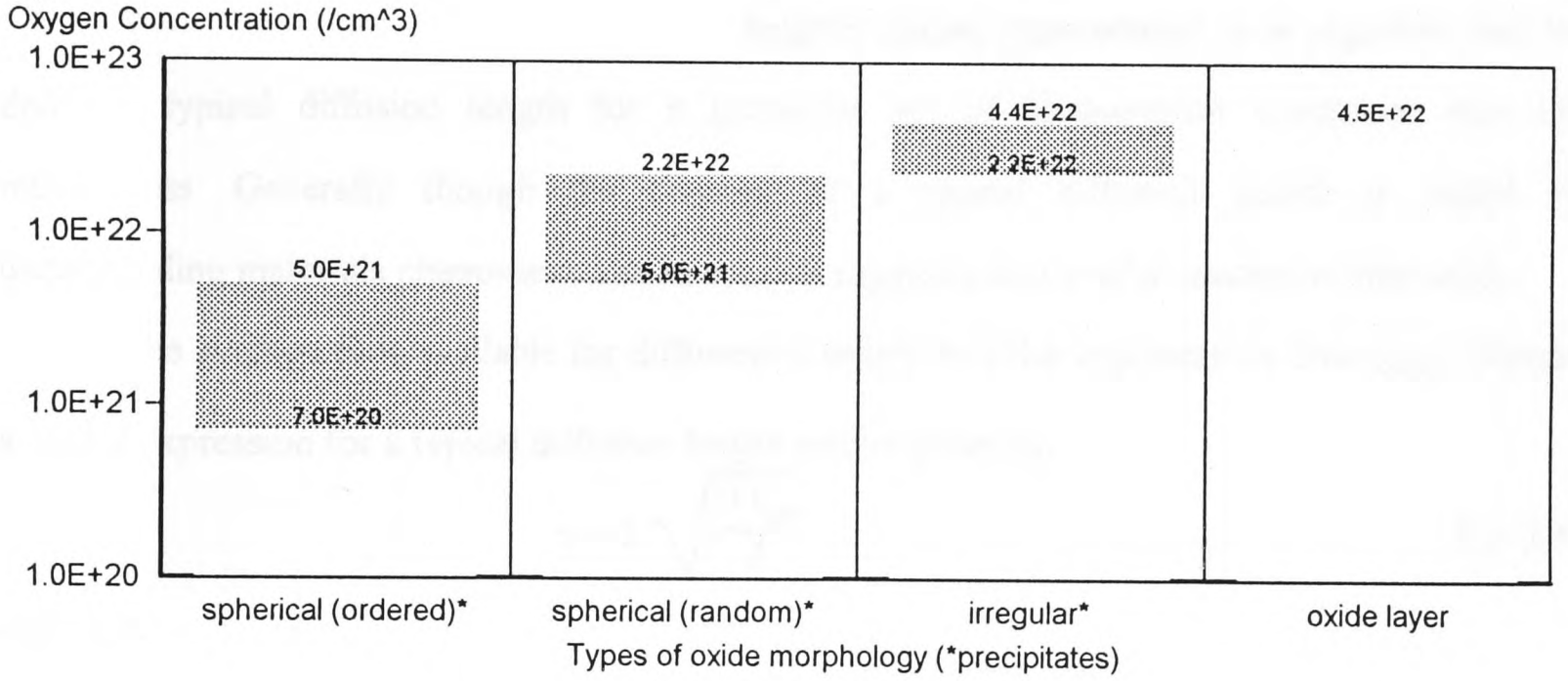

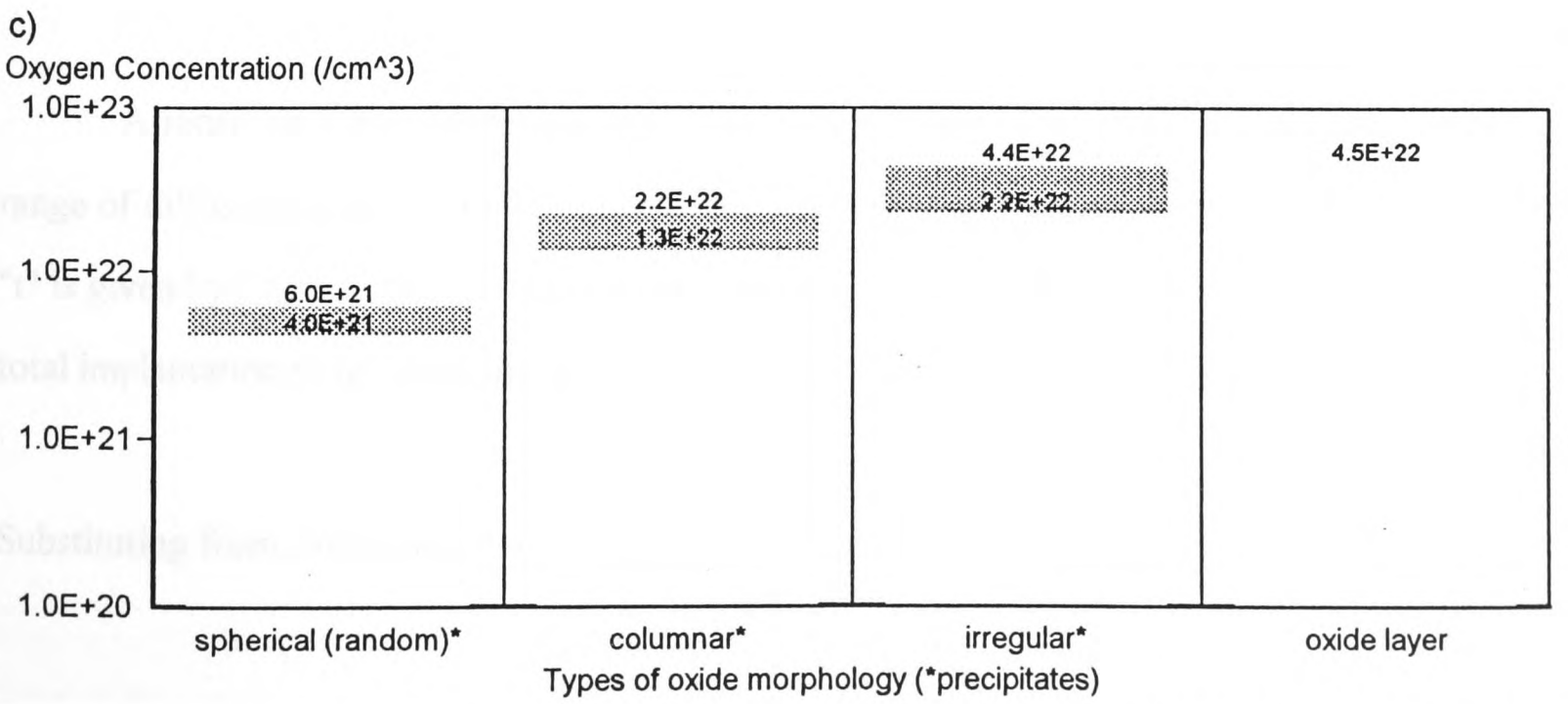

Figure 3.33 The range of oxygen concentrations over which the denuded zone and the different oxide morphologies were observed at a) the near surface region, b) throughout the rest of the surface silicon layer and c) near the peak of the oxygen profile.

The total implantation time (t_{im}) for the O_2^+ ions is given by,

$$t_{im} = \frac{\Phi q}{2 I'} \quad \text{.....Eq. 3.4}$$

where Φ is the dose per square cm, I' the time-averaged beam current density and q the elementary charge. Hence the diffusion length for an ion implanted at time "t" is given by the expression,

$$x = 2\sqrt{D\left[\frac{\Phi q}{2 I'} - t\right]} \quad \text{.....Eq. 3.5}$$

Examples of how the diffusion length of an ion varies as a function of the time the ion is implanted after the start of the implantation, for values of dose and beam current density used in this work, are shown in fig. 3.34.

With such a spread in the diffusion lengths during implantation it is arguable that to define a typical diffusion length for a particular set of implantation conditions may be meaningless. Generally though the concept of a typical diffusion length is useful in understanding materials phenomena and hence it is regarded as a useful concept in this work.

The average time available for diffusion is simply half the implantation time (t_{im}). Hence a simple expression for a typical diffusion length can be given by,

$$x = 2\sqrt{\frac{D\, t_{im}}{2}} \quad \text{.....Eq. 3.6}$$

and substituting from Eq. 3.4 for t_{im},

$$x = 2\sqrt{\frac{D \Phi q}{4 I'}} \quad \text{.....Eq. 3.7}$$

A more accurate value for a typical diffusion length would be the average value of the range of diffusion lengths during implantation. The diffusion length for an ion implanted at time "t" is given by Eq. 3.5. Integrating this expression over the implantation time and dividing by the total implantation time, gives the expression for the average diffusion length as,

$$x_{av} = \frac{4}{3}\sqrt{D\, t_{im}} \quad \text{.....Eq. 3.8}$$

Substituting from expression 3.4 for t_{im}, the average diffusion length is given by,

$$x_{av} = \frac{4}{3}\sqrt{\frac{D \Phi q}{2 I'}} \quad \text{.....Eq. 3.9}$$

Examples of the average diffusion lengths for beam currents and doses used are indicated in Fig. 3.34. The average diffusion length increases with implantation dose, i.e with implantation time,

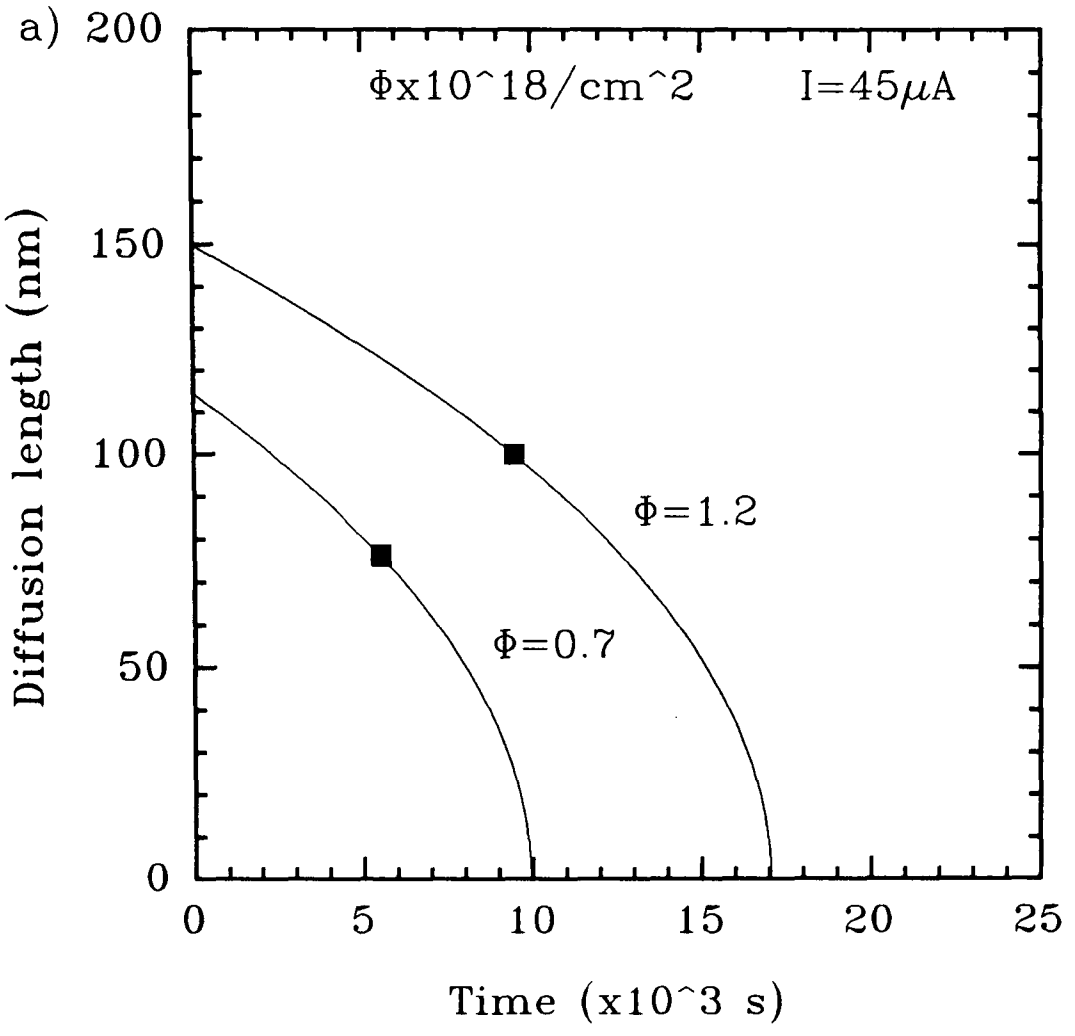

Figure 3.34 Calculated diffusion length of an implanted ion as a function of the time after the start of the implant that the ion was implanted, for different a) doses (Φ) and b) beam currents (I). The calculated average diffusion lengths and the time at which ions with the average diffusion length are implanted are indicated for each set of implant conditions by the squares.

and with decreasing beam current density, as expected. The average diffusion lengths as a function of the doses and beam current densities used in this work are shown in fig. 3.35.

For the implanter used in this work, due to the greater efficiency of extracting oxygen ions from the ion source with increasing energy, the maximum available beam current increased with increasing energy (table 2.1). Fig. 3.36a shows that over the energy range used in this work the beam current was closely proportional to the square root of the energy,

$$I \propto \sqrt{E} \quad \text{.....Eq. 3.10}$$

Substituting Eq. 3.10 into Eqs. 3.4 and 3.9, gives, when implanting a fixed dose and area, and for the beam currents shown in Table 2.1, gives the following expressions for the dependence of the total implantation time (t_{im}) and average diffusion length (x_{av}) on the energy,

$$t_{im} \propto \frac{1}{\sqrt{E}} \quad \text{and} \quad x_{av} \propto \frac{1}{\sqrt[4]{E}} \quad \text{.....Eqs. 3.11a \& b}$$

Hence when implanting the same dose at different energies the average diffusion length decreases with increasing energy. An example of how the average diffusion length varies as a function of the implant energy is shown in Fig. 3.36b.

For producing SIMOX substrates at different energies, where the same peak oxygen concentration (e.g. corresponding to SiO_2) is required for any energy, the variation of the diffusion length with implantation energy for constant peak oxygen concentrations is of interest. The straggle of the implanted ions increases with increasing energy (table 2.3) and hence, to produce the same peak oxygen concentration at higher energies, a larger dose has to be implanted. The required dose to form a peak oxygen concentration (N_p) is given[18] by,

$$\Phi = \sqrt{2\pi}\ \Delta R_p\ N_p \quad \text{.....Eq. 3.12}$$

where ΔR_p is the straggle in the projected range of the oxygen ions. A plot of the straggle (table 2.3) against the energy, over the energy range used in this work (fig. 3.37), shows that ΔR_p is approximately proportional to the square root of the implant energy,

$$\Delta R_p \propto \sqrt{E} \quad \text{.....Eq. 3.13}$$

Hence,

$$\Phi \propto \sqrt{E}\ N_p \quad \text{.....Eq. 3.14}$$

From Eqs. 3.4 and 3.9, for a constant implant area,

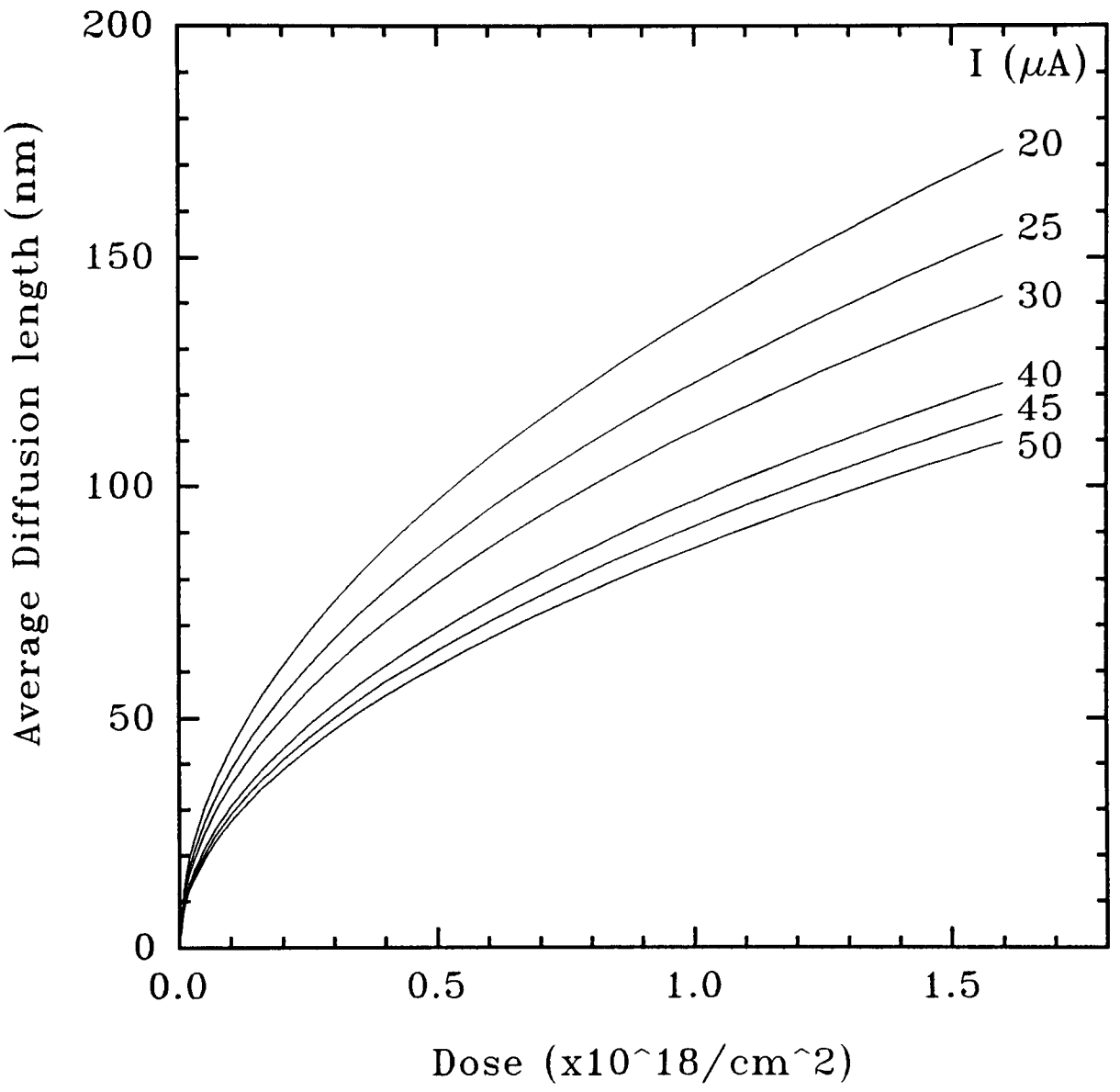

Figure 3.35 The calculated average diffusion length of the implanted ions as a function of the implanted dose and beam current (I).

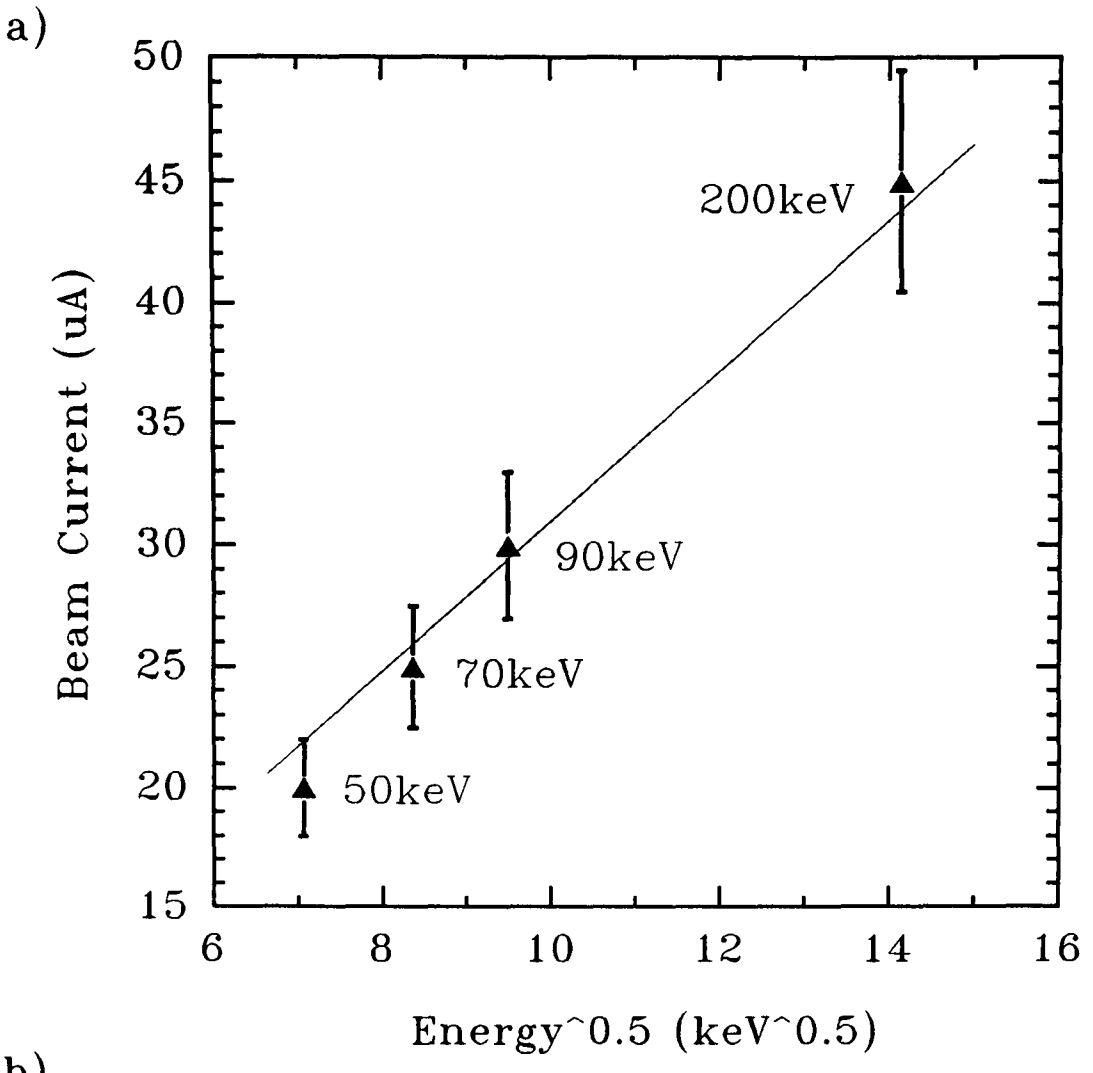

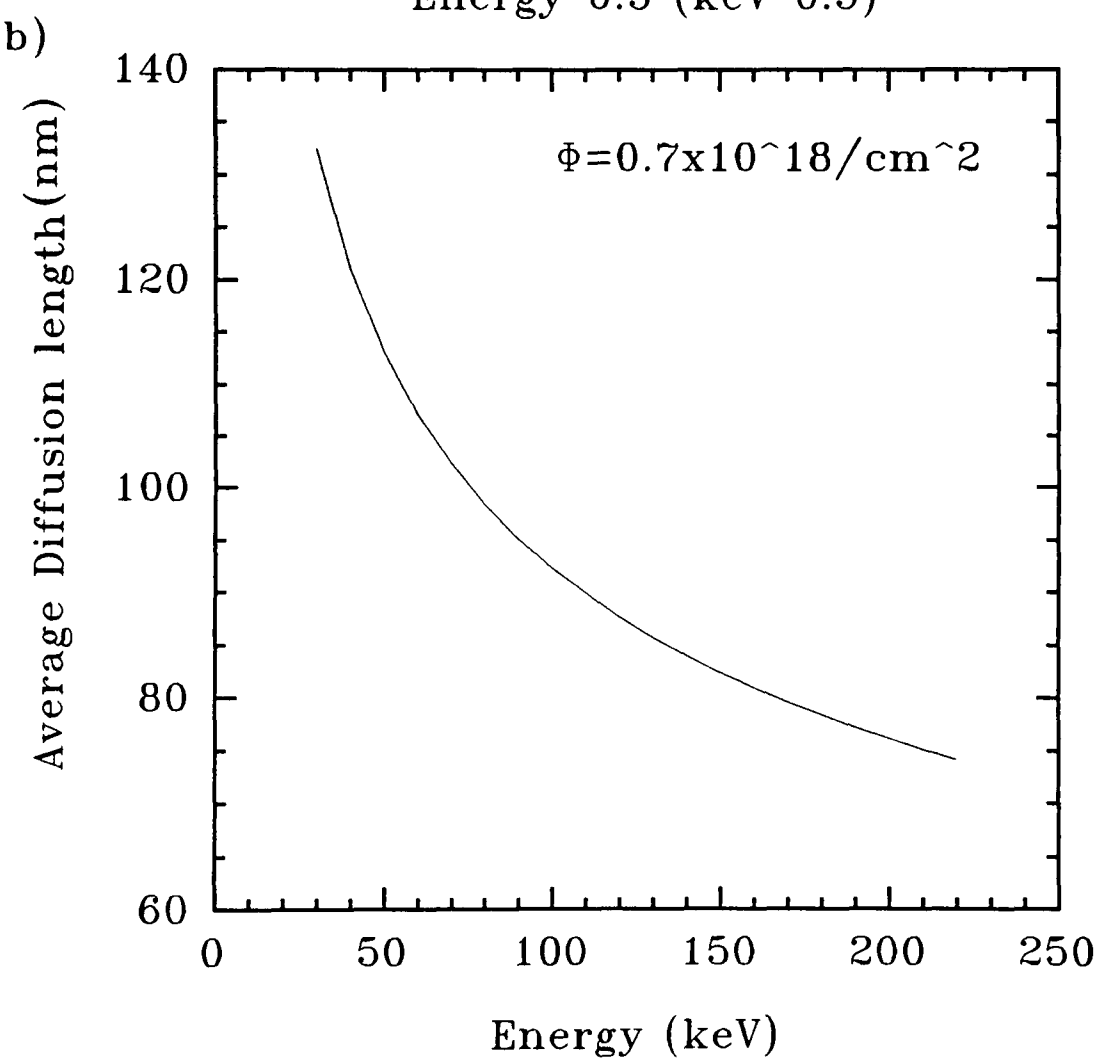

Figure 3.36 a) The available beam current of the implanter plotted against the square root of the implant energy. The implant energies are indicated. The straight line is a least squares fit to the four points and the origin, generated by the computer program Sigmaplot, showing that within experimental errors the beam current is proportional to the square root of the energy and b) an example of the average diffusion length as a function of the energy for the beam currents indicated by the line in a).

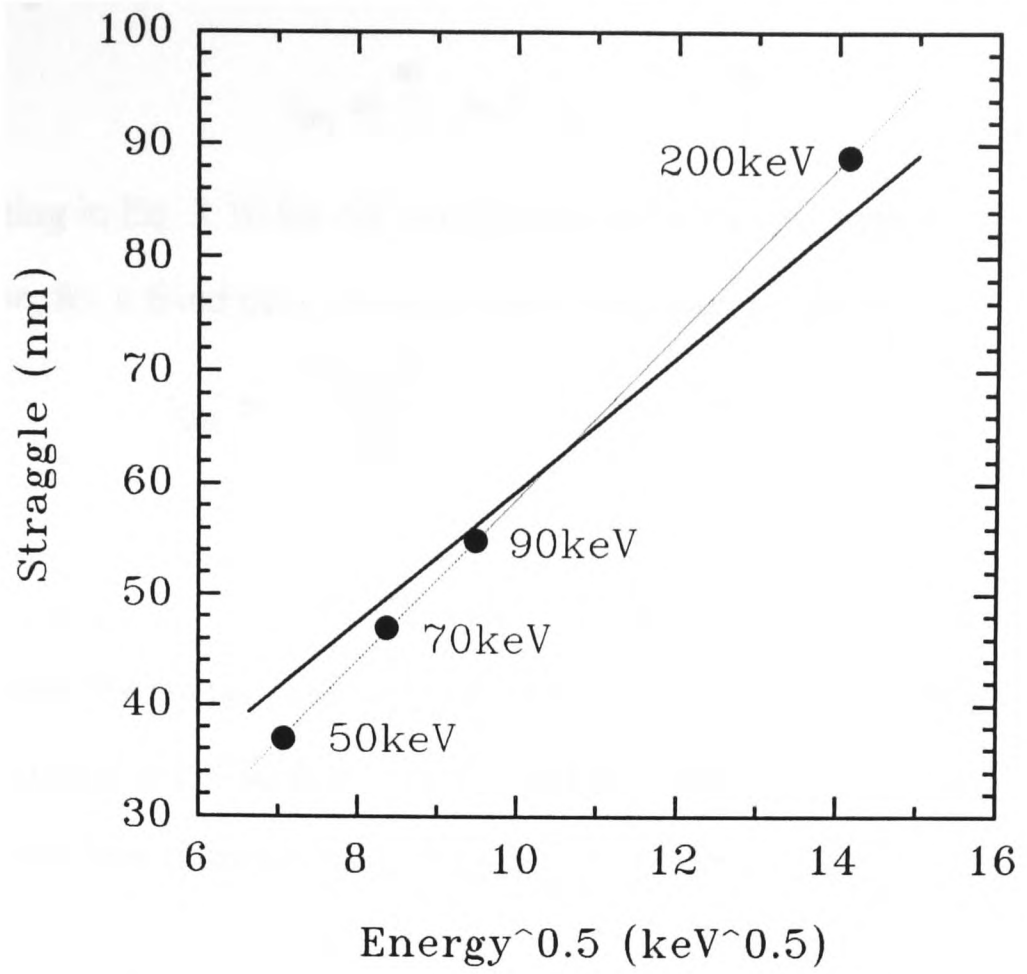

Figure 3.37 The straggle of the implanted ions, as predicted by TRIM90, plotted against the square root of the energy (circles). The implant energies are indicated. The darker line is a least squares fit to the four points and the origin, generated by the computer program Sigmaplot, showing that the straggle is approximately proportional to the square root of the energy (The thinner line through the points is a least squares fit to just the points, showing that the relationship between the straggle (ΔR_P) and energy (E) is more accurately represented by an expression of the type $\Delta R_P = m\sqrt{E} + b$, where in this case b = -14nm and m = 7.3 nm/(keV)^{½}).

Peak oxygen concentration from SIMS (/cm^3)	Energy (keV)	Dose (x10^{18}O$^+$/cm^2)	Implantation time (s)	Diffusion length (nm)
2.2x10^{22}	70	0.4	10240	78
	90	0.43	9173	73
	200	0.7	9956	76
2.8x10^{22}	70	0.5	12800	87
	90	0.6	12800	87
4.48x10^{22}	50	0.5	16000	97
	70	0.7	17920	103
	90	0.75	16000	97
	200	1.2	17067	100

Table 3.9 Doses that were observed experimentaly to result in the same peak oxygen concentration for the different energies and the calculated implantation time (eq 3.4), for three different peak oxygen concentrations. Note that because the implantation times required to produce the same peak oxygen concentration at different energies are very similar, the diffusion length for each peak oxygen concentration is independent of the energy.

$$t_{im} \propto \frac{\Phi}{I} \quad \text{and} \quad x_{av} \propto \sqrt{\frac{\Phi}{I}} \qquad \text{.....Eqs. 3.15a \& b}$$

Hence substituting in Eq. 3.10 for the variation in beam current with energy and Eq. 3.14 for the variation in dose, for a fixed peak concentration, with energy, gives,

$$t_{im} \propto \frac{N_p\sqrt{E}}{\sqrt{E}} \quad \text{and} \quad x_{av} \propto \sqrt{\frac{N_p\sqrt{E}}{\sqrt{E}}} \qquad \text{.....Eqs. 3.16a \& b}$$

i.e.,

$$t_{im} \propto N_p \quad \text{and} \quad x_{av} \propto \sqrt{N_p} \qquad \text{.....Eqs. 3.17a \& b}$$

Hence to produce the same peak oxygen concentration (N_p) at different energies both the implantation time and the diffusion length are independent of the energy. This was confirmed experimentally for three different peak oxygen concentrations (table 3.9).

3.9 Oxygen Precipitation

3.9.1 Nucleation

The driving force for the nucleation of the SiO_2 precipitates is the decrease in the free energy associated with the precipitation. When oxygen precipitation occurs consideration needs to be given to both mass conservation,

$$Si + 2O^+ <-> SiO_2 \qquad \text{.....Eq. 3.18}$$

and volume conservation,

$$V(Si_{Si}) + 2V(O) + \delta V(SiO_2) = V(SiO_2) \qquad \text{.....Eq. 3.19}$$

(where V(a) denotes the volume of atom or molecule "a" and $\delta V(SiO_2)$ is the accommodation volume required per SiO_2 molecule for strain free precipitation). The volume occupied by a molecule of SiO_2 is 2.25 times that occupied by one Si atom on its lattice site. This increase in volume leads to stress in the surrounding Si unless an accommodation volume is provided. The accommodation volume can be created either by the ejection, by the lattice, of interstitials (Si_i) or by the absorption, by the precipitate, of vacancies (Si_v). In bulk Si at temperatures around 680°C these processes are ineffective, but during ion implantation many Si_v and Si_i are created by collisions of the incident ions with atoms on the lattice sites (Si_{Si}).

$$Si_{Si} <-> Si_i + Si_v \quad \text{.....Eq. 3.20}$$

TRIM90 predicts that for 200keV O^+ implants into Si an average of >700 Si_v and Si_i are created per incident ion (table 2.3). These Si_v could provide the accommodation volume for oxidation .

Nucleation at small vacancy clusters is a possible mechanism for the nucleation of the SiO_2 precipitates. With such a large number of Si_v being produced a large number of these nucleation sites could be created. The Si_v are created randomly in the surface Si layer by the implantation process and therefore the formation of nucleation sites will be a random process. Hence a random distribution of heterogeneously nucleated precipitates will result. The actual nucleation process may vary with depth as the vacancy production profile is a skewed gaussian (fig. 2.2). The other parameter which will effect the nucleation is the oxygen concentration, the higher the concentration the greater the probability of precipitation. The SIMS results (figs. 3.30 & 3.31) show that the oxygen depth profile is a skewed gaussian and hence the influence of the oxygen concentration will also vary with depth. At a constant depth the nucleation and growth process will be influenced by the energy because the projected range and straggle of the implanted ions (and hence the oxygen distribution) and the linear density of Si_v generated per ion (Si_v/ion/Å) changes with energy (table 2.3 & TRIM90[19], respectively).

3.9.2 Precipitate denuded zone

Precipitate denuded zones are present only in the top 25nm of the wafers implanted with $0.1x10^{18}O/cm^2$ at 70keV (fig. 3.17) and in the top $\leq$60nm for doses of $\leq 1.2x10^{18}O/cm^2$ implanted at 200keV (fig. 3.9 & table 3.10). The oxygen concentration at the end of the implantation at these depths is in the range $2x10^{20}/cm^3$ to $6x10^{20}/cm^3$ (figs. 3.30 & 3.31)

The solid solubility of oxygen in Si at the implantation temperature of 680°C is $<10^{16}/cm^3$ [17]. Hence the oxygen concentration at the depths of the denuded zones is above the solid solubility, and therefore a supersaturation of oxygen is present. In the top 60nm of the wafers implanted at 200keV, Si_v are being produced at a linear density of 0.1/ion/Å, which for a dose of $0.7x10^{18}O/cm^2$ amounts to a total of $2.8x10^{19}Si_v/cm^2$ (TRIM90[19]). With such a large number of Si_v being generated the likelihood of small Si_v clusters being formed and acting as

nucleation centres seems reasonable. Hence something must be preventing the Si_v forming nucleation sites in order to explain the supersaturation of oxygen indicated by the SIMS results.

Dose ($x10^{18}O/cm^2$)	Denuded zone width (nm)	Diffusion length (nm)
0.4	60	58
0.6	45	71
1.2	20	100
1.6	not observed	116

Table 3.10 Comparison of the calculated oxygen diffusion length, as defined in the text, with the width of the denuded zone for different doses implanted at 200keV with a beam current of 45μA and a beam current density of 5.6$\mu A/cm^2$.

The critical minimum radius for the stability of an SiO_2 precipitate depends on the local oxygen, Si_v and Si_i concentrations. An expression for the critical radius (r_c) is given by Vanhellemont and Claeys[20] as,

$$r_c = \frac{2\sigma}{AT \ln \left\{ \frac{c_o}{C_o} \left[\frac{c_v}{C_v} \right]^{\gamma} \left[\frac{C_i}{c_i} \right]^{\beta} \right\} - F} \quad \text{..... Eq. 3.21}$$

where σ is the interface energy, F the strain energy, C_o, C_v, C_i the thermal equilibrium concentrations of oxygen, Si_v and Si_i, respectively, c_o, c_v, c_i the concentrations of oxygen, Si_v and Si_i, respectively, and A is a constant. β and γ are the number of Si_i ejected into the Si matrix and the number of Si_v absorbed from the Si matrix per precipitating oxygen ion, respectively. Hence the lower the excess oxygen and Si_v concentrations and the higher the excess Si_i concentration, the larger the critical radius.

During implantation the oxygen concentration increases at all depths but the skewed gaussian oxygen concentration profile means that in the surface Si layer the oxygen concentration increases with depth and the lowest oxygen concentration is present at the wafer surface. Hence during and at the end of the implantation the oxygen concentration contribution to Eq. 3.21 results in the critical radius in the surface Si layer being largest at the wafer surface. The oxygen concentration in the denuded zones at the end of the implants is up to 4 orders of

magnitude above the solid solubility and therefore precipitation might still be expected. Oxide precipitation is known to decrease in the presence of an excess of Si_i[21] and Eq. 3.21 predicts that the higher the excess Si_i concentration the larger the critical radius. Hence the supersaturation of oxygen, for concentrations between $10^{16}/cm^3$, the thermal equilibrium value, and $6x10^{20}/cm^3$, the lowest oxygen concentration at which precipitates are observed, is thought to be due to the excess Si_i concentration at the surface being sufficiently high that the critical radius is too large for any precipitates to be stable. The reasons for a high Si_i concentration in the surface Si is discussed in section 3.10.

The oxygen that does not precipitate out in the denuded zones can do one of, or a combination of, three possibilities; be gettered by the nearest stable oxide precipitates (or other oxygen sinks), out-diffuse via the surface, or remain as a supersaturation, as is indicated by the SIMS results. If some of the oxygen is gettered by the nearest stable precipitates this would explain why the spheroidal inclusions, at the edge of the denuded zone, are larger than the deeper precipitates. Typical oxygen diffusion lengths (using the definition proposed previously) for the implants at 200keV, are shown in Table 3.10. These lengths are larger than the observed denuded zone widths, so the out diffusion of some of the oxygen from these depths is possible. The SIMS results indicate that an oxygen supersaturation forms during implantation but it is possible that one or both of the other two processes are also taking place during implantation.

The presence of a denuded zone has been observed by other workers[22,23,24], although none of them reported the presence of larger inclusions at the edge of the denuded zone. Van Ommen[24] observed for one sample that, when the bulk Si value was taken for the diffusion coefficient and the time available for diffusion was taken to be the implantation time, the width of the denuded zone was equal to the diffusion distance. He therefore suggested that the width of the denuded zone was determined by the out-diffusion of oxygen to the surface from depths equal to the diffusion distance. The typical diffusion lengths (using the average diffusion length definition proposed in section 3.9) shown in Table 3.10 indicate that the diffusion length increases with increasing dose while the observed denuded zone width decreases, suggesting that the denuded zone width is not being determined by the oxygen diffusion length. The deeper edge of the denuded zone occurs for all samples at the depth where the oxygen concentration

equals $\approx 6x10^{20}/cm^3$, suggesting the oxygen concentration is playing a major role in determining the width of the denuded zones.

In the samples implanted with $\Phi \approx 0.7x10^{18}O/cm^2$ at 200keV the experimentally observed decrease in the thickness of the denuded zone with increasing time-averaged beam current density (I') suggests, in terms of the idea of the oxygen concentration determining the width of the denuded zones, that the oxygen concentration near the surface at the end of the implantation increases with increasing beam current density or that the oxygen concentration near the surface does not change but the higher beam current enables precipitates to nucleate at lower oxygen concentrations. SIMS analysis on these samples implanted with $I' = 5\mu A/cm^2$ and $3.75\mu A/cm^2$ showed almost identical as-implanted oxygen distributions (not shown), hence the first hypothesis is not true, although the second hypothesis is still possible. The TEM micrographs suggest that it is only the spheroidal inclusions that occur nearer the surface with increasing beam current density (fig. 3.10). Hence if the spheroidal inclusions are not oxide precipitates, the precipitate denuded zone would be approximately the same width for all the beam current densities. The possibility that the spheroidal inclusions are voids is discussed in section 3.11.

3.9.3 Precipitate morphology

The results summarised in figs. 3.32 & 3.33 indicate that the precipitate morphology depends on the oxygen concentration and the depth below the surface. For oxygen concentrations between $6x10^{20}/cm^3$ and $1.3x10^{22}/cm^3$, at any depth, only one type of precipitate morphology was observed. These precipitates, present in either an ordered cubic or randomly distributed array, are spherical, suggesting they have formed without any pronounced local strain and the minimisation of the surface energy has determined the shape. The lack of distortion in the Si {111} planes in HREM images of regions containing precipitates also suggests that the precipitates have formed without any pronounced local strain. The distances between the precipitates (typically a few nm) are more than an order of magnitude smaller than the average oxygen diffusion lengths for the implant conditions used (fig. 3.35). Hence the size of the precipitates is not being limited by the oxygen diffusion. The high density and small size

of the precipitates is probably determined by the high density of nucleation sites created during implantation.

Ordered cubic arrays of SiO_2 precipitates, similar to those observed in the 90keV and 200keV implants in this work, have been reported for higher doses ($\geq 1.8x10^{18}O/cm^2$) in 200keV implants by several authors[9,22,25]. This is the first report of an ordered cubic array of SiO_2 precipitates for an implant energy as low as 90keV. Similar to the situation of ordering in metals[56,57] the minimisation of long-range elastic strain has been proposed as the driving force for this ordering and the negative elastic anisotropy of Si has been proposed as the reason for a simple cubic ordered array in the diamond cubic lattice of Si[9]. The ordered precipitates could have developed from either an ordered array of nucleation sites, or developed from a random distribution of nucleation sites, where the long range strain makes it favourable for the precipitates on the cubic array sites to grow at the expense of other precipitates. The discussion of the nucleation (section 3.9.1) suggests that the latter is more probable. The observation of ordered spherical precipitates only at final oxygen concentrations between $2x10^{21}/cm^3$ and $4x10^{21}/cm^3$ and randomly distributed spherical precipitates for oxygen concentrations $>4x10^{21}/cm^3$ suggests that the oxygen concentration plays a role in determining the ordering. Higher oxygen concentrations may introduce a long range strain which disrupts the ordering.

For oxygen concentrations between $1.3x10^{22}/cm^3$ and $2.2x10^{22}/cm^3$ (30% to 50% SiO_2) three types of precipitate morphologies are observed, depending on the depth below the surface. This suggests that two or all three of these precipitate morphologies are not being determined by only the local oxygen concentration. The three depths at which the different precipitate morphologies are present are, at the wafer surface, at the peak of the oxygen distribution and in the surface Si layer between these two regions. In the surface Si layer, between the regions close to the wafer surface and at the peak of the oxygen concentration, spherical randomly distributed precipitates are present at these oxygen concentrations (fig. 3.33).

At the wafer surface when the oxygen concentration is between these values elongated platelet precipitates, parallel to the wafer surface, are present (fig. 3.33). In bulk Cz Si wafers after annealing at temperatures (650-950°C) similar to the implantation temperature (680-700°C) platelet precipitates parallel to the {100} planes have been reported as the equilibrium

700°C) platelet precipitates parallel to the {100} planes have been reported as the equilibrium morphology[26]. It has also been shown that for an oxide precipitate, the shape with the theoretical minimum strain energy is a disc[26]. In general, when lattice strain accompanies precipitation, in order to minimise the strain the habit plane of the precipitate lies normal to the direction of minimum elastic constant. In Si these are the <100> directions. Hence the tendency of these precipitates to form platelets parallel to the (001) wafer surface suggests that strain is accompanying the precipitation, and the minimisation of the lattice strain is dominating over the minimisation of surface energy as the driving force for the platelet morphology. The presence of strain suggests that for the implant conditions which result in an oxygen concentration in this range at the surface, the required volume for strain free precipitation is not being provided. The generation of strain is discussed in section 3.10.5.

At the peak of the oxygen profile columnar [001] precipitates are present for oxygen concentrations between these values (fig. 3.33). The [001] columnar nature suggests that the morphology is influenced by the beam direction. The minimum depth at which these precipitates are present is 75% of the depth of the oxygen peak. This coincides approximately with the peak of the vacancy production profile from TRIM90, suggesting that a high concentration of Si_v may be involved in determining the shape of these precipitates. Si_v are created along the oxygen ion tracks, the average direction of these tracks is along the beam direction, which is approximately perpendicular to the wafer surface. The Si_v created along the tracks will, by providing the accommodation volume in the direction of the surface, enable precipitates nucleated at any depth to grow preferentially towards the surface, although this is not observed experimentally. The maximum density of Si_v are produced at the peak of the vacancy production profile which occurs at depths less than the peak of the oxygen concentration profile. This will particularly enable precipitates nucleated near the peak of the oxygen concentration to grow towards the surface. The [001] columnar precipitates would also only be present near the peak of the oxygen profile if a large oxygen concentration is necessary for the precipitates to grow in the [001] direction before the Si_v and Si_i generated along the tracks recombine. The presence of spherical precipitates at the peak of the oxygen profile for the dose of $0.1 \times 10^{18} O/cm^2$ at 70keV suggests that the columnar precipitates originate as spherical precipitates. A combination of beam

direction, high vacancy concentration and high oxygen concentration may then enable growth in the [001] direction to take place. The role of the Si_i at the wafer surface may also effect the morphology of these precipitates, this is discussed in section 3.10.2.

For oxygen concentrations between $2.2x10^{22}/cm^3$ and $2.8x10^{22}/cm^3$ irregular precipitates are present, either at the peak of the oxygen profile or in the surface Si layer adjacent to a buried SiO_2 layer. These irregularly shaped precipitates probably result from the coalescing of adjacent precipitates, spherical precipitates in the surface Si layer and columnar precipitates at the peak of the oxygen profile. The oxygen concentration of $2.2x10^{22}/cm^3$ corresponds to 50% of the sample volume being SiO_2 (table 3.8). Hence this change in morphology corresponds to the depth at which the SiO_2 volume fraction exceeds 50%. For oxygen concentrations $>2.8x10^{22}/cm^3$ (60% to <100% SiO_2), bands approximately parallel to the wafer surface of amorphous SiO_2 and Si ribbons are present. The [001] columnar and irregular precipitate structures are present within the ribbons of Si. The horizontal nature of the SiO_2 bands suggests that the lateral coalescing of adjacent columnar precipitates plays a role in the evolution of the SiO_2 layer. The ribbons of Si are usually connected to the surface Si layer or the substrate, but many, especially with increasing dose, appear isolated in the c.s. Hence for higher doses the evolution of a homogeneous SiO_2 layer is determined by the oxidation of the isolated Si rather than oxygen precipitation.

3.10 The Role of Silicon Interstitials

3.10.1 Generation

Since the volume occupied by a molecule of SiO_2 is 2.25 times the volume occupied by the one Si atom on its lattice site ($V(Si_{Si})$) an accommodation volume ($\delta V(SiO_2)$) of,

$$\delta V(SiO_2) = 1.25\ V(Si_{Si}) \quad \text{.....Eq. 3.22}$$

is required to form every SiO_2 molecule. Hence for every incident oxygen ion the required accommodation volume ($\delta V(O)$) is,

$$\delta V(O) = 0.625\ V(Si_{Si}) \quad \text{.....Eq. 3.23}$$

If this accommodation volume is being provided by the Si_v generated during the implantation and assuming all the other Frenkel pairs recombine, then for every incident oxygen ion 0.625 Si_i are generated in the lattice. For the doses in this work the oxygen concentrations after implantation ranged from $10^{20}/cm^3$ to $4.48x10^{22}/cm^3$, so during implantation the total concentrations of Si_i generated are between $0.625x10^{20}/cm^3$ and $2.8x10^{22}/cm^3$. At these concentrations and assuming no Si_i diffuse away, a large density of extrinsic SF might be expected to form[10]. Extrinsic SF have been observed experimentally (section 3.4) but not at a large density. Further these extrinsic stacking faults are thought to be present only as a part of intrinsic and extrinsic SF pairs which are not net sinks for interstitials.

3.10.2 Epitaxial growth of the surface

It has been suggested that the excess Si_i migrates towards the surface which then acts as a sink[22]. This would explain the absence of extrinsic SF without a neighbouring intrinsic SF in the TEM results, but depends on the ability of the Si_i to diffuse to the surface and of the surface to absorb the Si_i. Morehead[29] gives the diffusivity of Si_i in bulk Si as,

$$D(Si_i) = 4000 \exp\left[\frac{-5.0\ eV}{kT}\right] \quad cm^2/s \quad \text{.....Eq. 3.23}$$

Using this equation the diffusivity of Si_i in bulk Si at 680°C is $1.5x10^{-23}cm^2/s$. This value is too low to enable a significant number of the Si_i generated during the implantation to diffuse to the surface. The diffusion of Si_i consists of two processes, the formation of the Si_i-Si_v pair and the Si_i migration. It has been shown[30] that although the formation energy of Si_i is high ($\approx$5eV) the migration energy is very low (0.3eV), and it has been suggested[25] that during ion implantation, where Si_i are easily created, it is the low migration energy which determines the diffusion. Replacing the combined formation and migration energy of 5eV in Eq. 3.23 with the migration energy of 0.3eV gives a diffusion coefficient at 680°C of $104cm^2/s$. This large diffusivity would enable the Si_i to diffuse to the wafer surface almost instantaneously ($\approx 10^{-15}$ s) resulting it >>99% of the Si_i generated by the implantation to reach the front surface. It is considered that the far from equilibrium situation in the implanted region during implantation will also modify the number in front of the exponential term in Eg. 3.23. This term is related to the jumping

frequency and the jumping distance of the Si_i. If the presence of the radiation damage is aiding the migration of the Si_i, by enabling a higher jumping frequency or larger jumping distance, this would further increase the diffusivity and would enable more Si_i to reach the front surface of the wafer rather than the back surface. The back surface of the wafer is also significantly further away from the implanted region than the front surface which will also result in fewer Si_i reaching the back surface.

Once the Si_i reach the front surface if they are absorbed on the surface they produce epitaxial growth. For a molecular (O_2^+) beam, current density (I'), the rate of arrival of oxygen atoms (O') is given by,

$$O' = \frac{2\,I'}{q} \qquad \text{.....Eq. 3.24}$$

and for ß Si_i generated per incident ion the generation rate of Si_i (α) is,

$$\alpha = ß\,O' = \frac{2\,ß\,I'}{q} \qquad \text{.....Eq. 3.25}$$

If all these Si_i are incorporated into the surface then taking account of the atomic density (N) the surface growth rate (S') is given by,

$$S' = \frac{\alpha}{N} = \frac{2\,ß\,I'}{q\,N} \qquad \text{.....Eq. 3.26}$$

The largest time-averaged beam current density used in this work was 6.25μA/cm² (O_2^+ ions) which is equivalent to an arrival rate, for oxygen atoms, of $7.8\text{x}10^{13}$/cm² s. With 0.625 Si_i being created per incident oxygen ion the net generation rate of Si_i is $4.9\text{x}10^{11}$/cm²s. The atomic density of Si is $5\text{x}10^{22}$/cm³, hence if all these Si_i are absorbed epitaxially at the surface the growth rate would be 0.6nm/minute. In practice the oxygen beam is scanned across the wafer during implantation and the instantaneous beam current, typically 118μA/cm², is larger than the time-averaged current density. The instantaneous beam current results in a Si_i generation rate of $9\text{x}10^{14}$/cm²s. The dwell time of the beam spot is 0.1ms. If all the Si_i are to be epitaxially incorporated at the surface during this time then the epitaxial growth rate at the surface would have to be 11nm/minute. The dwell time of the spot leads to the generation of $9\text{x}10^{10}$/cm² Si_i. If the lattice can accommodate this concentration of Si_i, the Si_i would not have to be incorporated into the surface during the dwell time, but would have to be incorporated during the time before

the beam returns. The surface growth rate is then between the growth rates determined by the time-averaged and instantaneous beam current densities.

During implantation atoms are also removed from the surface by sputtering. Taking sputtering into account, if all the Si_i are incorporated in the surface the net growth of the surface (S), for a dose (Φ), is given by,

$$S = \frac{(\beta - Y)\,\Phi}{N} \qquad \text{.....Eq. 3.27}$$

where Y is the sputtering yield per incident ion. This equation assumes that all the excess Si_i epitaxially grow on the surface and therefore gives the maximum possible growth due to the internal oxidation. The calculated surface growth as a function of dose, for the energies used in this work, is shown in fig. 3.38.

3.10.3 Generation of defects at the wafer surface

For low doses, i.e. $<0.5\text{x}10^{18}\text{O/cm}^2$ at 200keV, no defects are observed at the surface, while for higher doses the density of defects at the surface increases suggesting that they grow down with increasing dose (fig. 3.1). This suggests that the lattice annealing during implantation is not quite keeping up with the increasing damage during implantation and the wafer surface is acting as the nucleation site for the defects.

If the rate of surface growth is slower than the arrival rate of Si_i this might lead to imperfections in the epitaxial growth, generating defects at the surface. The typical rates used to grow defect free MBE Si at 500-535°C are 4-66nm/minute[31,32]. A growth rate of 66nm is faster than the growth rates required to incorporate all the Si_i into the surface, irrespective of whether it is the time-averaged beam current density or the instantaneous beam current density which determines the growth rate. Hence it is possible for the surface to grow fast enough not to incorporate any defects (this analogy may not be entirely appropriate as during MBE growth the Si atoms arrive at the growing surface from the vacuum, whereas in the implantation case the Si atoms arrive from within the Si, and this difference may influence the epitaxial process).

A surface growth rate slower than the arrival rate of Si_i would lead to an increase in the concentration of Si_i in the surface Si layer with dose. Potentially once the Si_i concentration

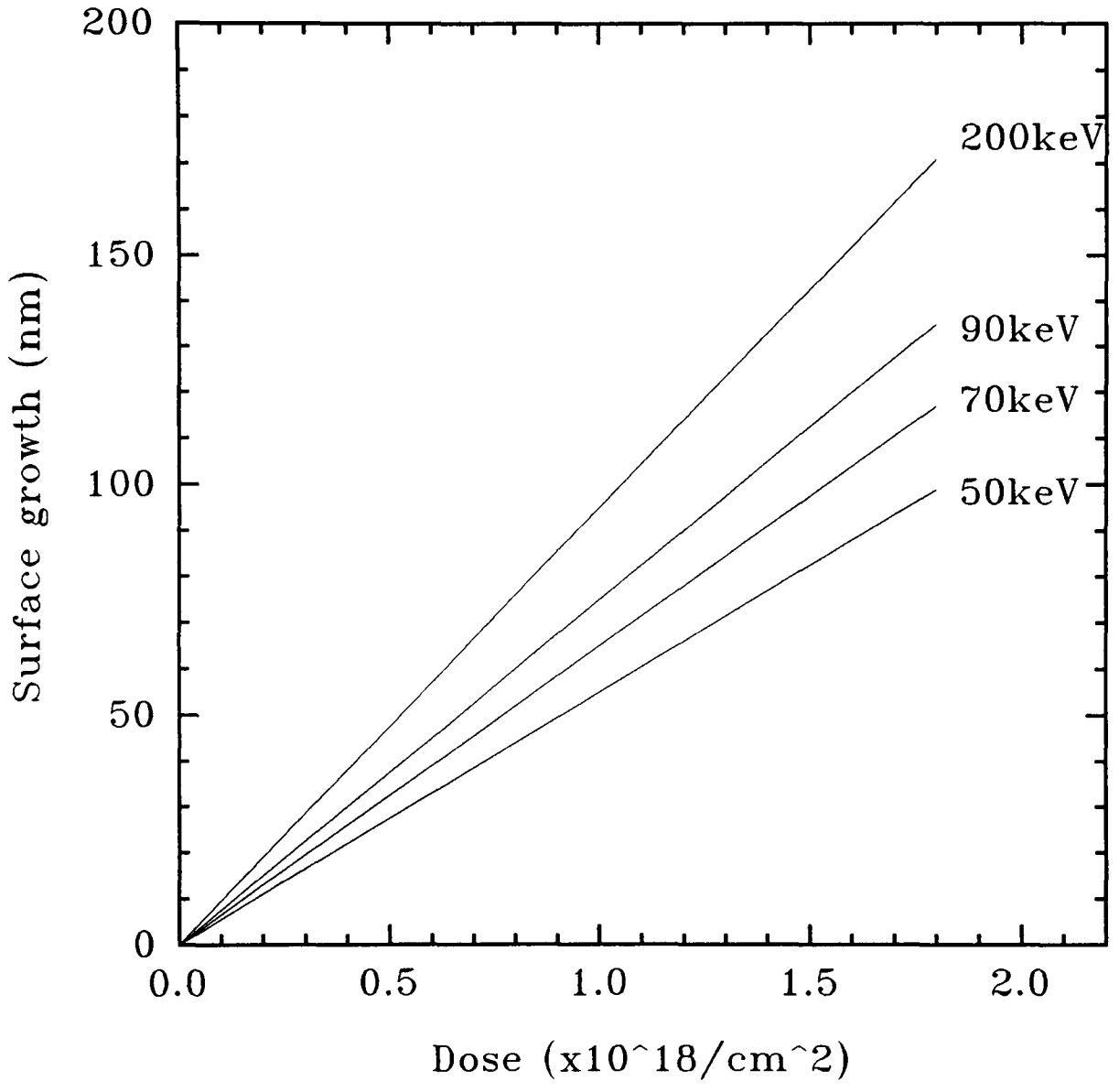

Figure 3.38 Calculated surface growth by the silicon interstitials generated during internal oxidation, as a function of the dose and the implantation energies used in this work.

reaches a threshold value the Si_i could precipitate out, directly forming defects, or the large Si_i concentration might disrupt the lattice annealing during implantation, leading to the formation of defects. These two hypotheses can explain why defects are observed only for the higher doses.

Another possible source of nucleation for defects at the surface is contamination on the wafer surface as the surface grows or knocked-in by the oxygen ions. This could be either hydrocarbon contamination from the implanter vacuum (the vacuum in the implanter is 10^{-7} torr, which compares to 10^{-10} torr for an MBE growth kit[31,32]) or due to unintentional sputtering in the beam line during implantation[33]. Although the wafer surface is cleaned by the sputtering of atoms during implantation, contamination from both these sources could arrive at the surface at any time during the implants.

If any of these mechanisms are the origin of the defect nucleation, a random distribution of nucleation centres across the wafer surface would be expected. For the 200keV implants when the defects at the surface are not uniformly distributed across the implanted area, the random distribution of the regions of Si containing defects supports the idea that the nucleation is random. Once nucleated at the surface the defects could then grow with the growing surface and/or act as sinks for further Si_i enabling them to grow down from the surface. This would explain the increase in the thickness of the surface damage region with increasing dose for high doses (fig. 3.1). The dislocations which are the predominant defect in the surface damage probably nucleate at the wafer surface as loops, formed from the excess Si_i. Once nucleated the dislocations will probably grow quickly in the denuded zone, due to the constant flux of Si_i, until they meet the SiO_2 precipitates which slow further growth. Therefore the dislocations tend to be present in the precipitate denuded zone, or when they are present at the depths of the SiO_2 precipitates they are also present at a higher density in the denuded zone, and because the precipitates are aligned along the <100> directions this gives the defect regions approximate <100> edges.

If the spheroidal inclusions are SiO_2 precipitates (see also section 3.11) the lower density of the spheroidal inclusions when dislocations are present at the same depth suggests that the dislocations are either modifying the oxygen distribution, reducing the gettering of the oxygen to these precipitates or increasing the out-diffusion of oxygen.

The intrinsic SF at the surface are observed only in the denuded zone of the 200keV implants. The thickness of Si in which the SF are observed is less than the thickness of epitaxial surface growth predicted by Eq. 3.27. This and their intrinsic nature at depths where, because of the expected high Si_i concentration, extrinsic defects might be expected, suggests that the SF are regrowth defects and not due to the coalescence of point defects (see also section 3.11.2). The SF could have nucleated at the wafer surface, i.e. may be due to surface contamination, and as the surface epitaxially grew the SF grew with the surface. This is analogous to the early work on homo-epitaxy of Si in the presence of carbon contamination. Similar {111} defects have been reported for higher dose implants at 200keV but they were not characterised[34]. The SF were not observed at the surface of the low energy implants. This may be because for all but one of the low energy samples no precipitate denuded zone was present at the surface and the presence of precipitates may have prevented the growth of the SF as the surface epitaxially grew.

The small pits in the surface and the larger SiO_2 precipitates close to the surface after the low energy (50-90keV) implants were also only observed to depths which were less than the thickness of epitaxially surface growth predicted by Eq. 3.27. This suggests that these could also be regrowth defects. The large SiO_2 precipitates might be heterogeneously nucleated precipitates which have then gettered further oxygen and the pits might be regrowth defects which have grown with the surface. The appearance of both these defects only after the low energy implants may be due to the higher oxygen concentrations at the surface, for the doses implanted at these energies, compared to the oxygen concentrations for the doses implanted at 200keV (see also 3.11.2).

In the samples implanted at 200keV the decrease in the fraction of the implanted area containing defects with increasing beam current density is thought to be due to greater local thermal annealing, due to increasing local beam heating with increasing beam current density. In this work the depth of the surface damage was less, for the same dose, than in the samples implanted at 550°C, using only beam heating[35]. This shows the importance of the higher implantation temperature, and the use of background and pre-heating, in reducing the defects.

3.10.4 Defects below the peak of the oxygen distribution

During implantation, due to the low diffusivity of Si in SiO_2, the increasing volume of SiO_2 at the peak of the oxygen distribution makes the migration to the surface of Si_i generated at depths deeper than the oxygen peak more difficult. When the buried SiO_2 becomes continuous, migration to the surface is stopped. The next nearest sink for these Si_i is the back of the wafer but because it is significantly further away, few Si_i are expected to reach it. Therefore at depths below the peak of the oxygen profile, the concentration of Si_i would be expected to increase during implantation and increase more rapidly once a buried SiO_2 layer has formed, as then all the Si_i generated are trapped. A high concentration of Si_i is known to decrease the oxidation rate of Si[21]. So when the Si_i concentration at this depth increases rapidly the oxidation rate at this depth would be expected to decrease significantly. This is in agreement with marker layer[36] and isotope tracer experiments[37] which have shown that once a continuous SiO_2 layer has formed, further oxidation takes place preferentially at the upper interface. After implanting doses large enough to form a continuous SiO_2 layer the oxygen concentration at this depth is of the order 10^{20}-$10^{22}/cm^3$, so a Si_i concentration $\geq 10^{20}/cm^3$ would be expected. At this concentration extrinsic defects might be expected to be formed[10] and this is precisely the depth where the {311}, {100} and {110} defects were observed experimentally.

Defects on {311} planes have been seen by other workers in thermally treated Cz wafers[10,11], electron irradiated Si[38], ion implanted wafers[39,40] and in SIMOX[9]. The defects were initially interpreted as coesite[9,10,11] but more recently it has been suggested they are Si_i precipitates with a hexagonal Si (wurtzite type) structure[41,42]. Hexagonal Si has the same volume per atom as the cubic diamond phase but extra atoms are concentrated at the interface between the two phases[52]. Hence thin {311} defects with a large surface area to volume ratio would act as effective Si_i sinks. The {311} defects observed in this work are thin and planar, and therefore have a large surface area to volume ratio. Therefore if they are hexagonal Si they would act as effective Si_i sinks. The damage enhanced diffusion of Si_i to the wafer surface at depths less than the peak of the oxygen implantation would explain why no {311} defects are observed above the buried SiO_2 layer.

The observation of {110} edge loops at this depth suggests they are also formed from the excess Si_i. The decrease in density of these defects with increasing energy suggests that their nucleation could be due to the coalescence of Si_i. Thus, as the straggle of the implanted ions increases, the profile of the excess Si_i broadens with increasing energy, and therefore the probability of Si_i coalescing to form nucleation sites decreases. The longer length of the defects, for the same dose, for 200keV implants rather than the low energy implants would then result from the same number of excess Si_i (because the dose is the same) having fewer defects to act as sinks and hence those that have nucleated grow larger.

3.10.5 Stress and strain

As mentioned in section 3.9.3 the presence of platelet precipitates parallel to the wafer surface for implants of $0.7x10^{18}O/cm^2$, $1x10^{18}O/cm^2$ and $1.3x10^{18}O/cm^2$, at 50keV, 70keV & 90keV respectively, suggests strain is present and plays an important role in determining the precipitate morphology.

The diffusivity of Si in thermal SiO_2 at 680°C is very low ($10^{-29}cm^2/s$ [43]) and because the SiO_2 is amorphous the diffusivity of Si is not expected to be significantly enhanced by radiation damage during implantation. Hence the presence of SiO_2 precipitates in the surface Si layer would hinder the diffusion of Si_i towards the surface. As the volume of SiO_2 precipitates in the surface Si increases with increasing dose, the Si_i would find it increasingly difficult to reach the surface, leading to an increase in the Si_i concentration in the surface Si layer. If the Si_i concentration becomes sufficiently large, i.e. after high doses, to annihilate the Si_v before they can provide the accommodation volume, strain will accompany any subsequent precipitation and the strain will modify the precipitate shape. This mechanism would depend on both the number of excess Si_i, which is related to the dose, and the thickness of the surface Si layer. The effect would be expected to be more pronounced for a combination of thinner surface Si layers and higher doses. This could explain why, because the surface Si layer is thinner, precipitates elongated parallel to the wafer surface were only observed for the high dose, low energy implants, i.e. not observed for the 200keV implants even though higher doses were implanted,

and also why for the same range of oxygen concentrations ($1.3x10^{22}/cm^3$ to $2.2x10^{22}/cm^3$) platelet precipitates were only in the thinner surface Si layers.

For doses $<{}^{I}\Phi c$ a tensile strain, i.e. Si lattice expansion, perpendicular to the wafer surface has been reported at the depth of the peak of the oxygen distribution[44,45,46]. If the volume effect of the oxidation is only partially compensated by the emission of Si_i then, in order to accommodate the extra volume of SiO_2, the lattice at this depth would wish to expand. The Si at this depth though is constrained by the substrate underneath (resulting in the buried damage layer being under compressive stress parallel to the wafer surface) and therefore, to accommodate the extra volume, the lattice would expand perpendicular to the wafer surface and hence be under tensile strain in this direction, which is in agreement with these reports[44,45,46].

3.11 The Role of Silicon Vacancies

3.11.1 Voids

Using TEM, either by diffraction contrast or HREM techniques, it is difficult to distinguish between small (<10nm) amorphous precipitates and small voids containing gases of the same elements as in the precipitates[6,7]. In high energy as-implanted SIMOX voids have been reported in the surface Si layer by several authors[47,48,49,50,51,52,53]. The voids were either aligned along the beam direction[47,48,49,50] and randomly distributed across the wafer[50], or randomly distributed throughout the near surface region[51,52,53]. The aligned voids were observed in material implanted on the high current (100mA) Eaton Nova NV-200 dedicated oxygen implanters[54] and the randomly distributed voids were observed in material implanted on a conventional implanter using electrostatic scanning[51,52,53]. In both cases the voids were reported when the instantaneous beam current density (for O^+ ions) was >0.8mA. This is equivalent to a molecular ion instantaneous beam current density of 0.4mA. Hence for the higher instantaneous beam current densities used in this work voids might be expected (because of the type of implanter used only randomly distributed voids might be expected).

The reported randomly distributed voids in <110> c.s. were either spherical (diameters up to 30nm), or spheroidal with the longer dimension parallel to the wafer surface[51,52,53]. Both morphologies were determined to be voids, rather than oxide precipitates, from electron energy loss spectroscopy measurements on the larger voids. The reports showed that, under some implant conditions, the voids were present below a void-free surface region[51,52,53]. No p.v. TEM results were reported[51,52,53] and therefore it is not known if the voids randomly distributed in c.s. were aligned in p.v., though the ordering of voids in implanted Si[54] and metals[55,56] has been reported.

In the present work the different shape, larger size and linear distribution in <110> c.s. indicate a difference between the spheroidal inclusions observed at the edge of the denuded zone and the other inclusions considered to be oxide precipitates. The shape, larger size, presence below a denuded zone, the linear distribution in <110> c.s. of these inclusions and the fact that they do not align along the beam direction, are consistent with the previous reports of voids using a conventional implanter with electrostatic scanning[51,52,53]. The linear distribution in <110> c.s. of these inclusions in this work are closely similar to the linear distribution in <110> c.s. observed in the previous reports[51,52,53] (e.g. fig. 2 in ref. 53). The size of the voids in the previous reports[51,52,53] are generally larger, the density higher and they are present to greater depths than the spheroidal inclusions at the edge of the denuded zone in this work. The low density and small size in this work suggests that the implantation conditions were only just favourable for the spheroidal inclusions to form. In this work though a lower equivalent O^+ ion instantaneous beam current density was used and according to a proposed formation mechanism of the voids[49,50], a lower density and smaller size might be expected for a lower instantaneous beam current density. Similarly both the increase in size of the largest of the inclusions and the presence of the inclusions closer to the wafer surface with increasing beam current density observed in this work might be expected if the inclusions are voids. Further in the reports of both the randomly distributed[51,52,53] and aligned voids[47,48,49,50] the surface Si layer was free from dislocations whenever voids were present. Hence if the inclusions in this work are voids the observation that the inclusions were present at lower densities in areas where dislocations are present (fig. 3.7) is consistent with the reports of voids in the literature. Nothing has been

observed in this work which suggests that the spheroidal inclusions at the edge of the denuded zone are not SiO_2 precipitates but, comparing the experimental results in this work with the reports of voids in SIMOX in the literature, suggests that these inclusions could be voids.

Defects formed from Si_v, i.e. voids, initially seem to contradict the model of an excess of Si_i diffusing through the surface Si layer, where they either cause the surface to grow epitaxially or create defects, used to explain the results so far in this work. So far in this thesis it has been assumed that the Si_v and Si_i (Frenkel pairs) created by the implantation process quickly recombine. The Si_v will diffuse more slowly than the Si_i and hence the fast recombination is primarily due to the rapid diffusion of the Si_i. In the reports of voids it has been suggested that the rapid arrival rate of the oxygen ions enables small Si_v clusters to fill with oxygen gas, which prevents the Si_v from being annihilated by the Si_i. The Si_i then diffuse to the surface as previously discussed. This is similar to the ordering of voids in radiation environments[56].

In the reports of voids observed in higher current implants it was suggested that the voids were formed due to the overlapping of thermal spikes in the ion damage process[50]. A further possible mechanism is the knock-on effect of Si atoms displaced from their lattice site by the incoming oxygen ions. This process results in the peak of the Si_v distribution being closer to the surface than the peak of the Si_i distribution (because oxygen ions are lighter than Si atoms the distance between the two peaks would be small) and at all depths less than the peak of the Si_v distribution there is an excess of Si_v (because the distance between the two peaks is expected to be small the excess of Si_v is also small)[18,58]. If the excess of Si_v formed small voids, stabilised by oxygen gas, a distribution of voids in the surface Si layer would then result.

3.11.2 Defects at the wafer surface

An excess of Si_v in the surface Si layer could explain the presence of the intrinsic SF observed at the surface in the 200keV implants. i.e they could be formed from the coalescence of Si_v. If this was the case though an explanation would have to be found as to why the Si_v forming the SF were not annihilated by the Si_i from the Frenkel pairs and the internal oxidation. This could be due to an energy barrier to the recombination. The existence of energy or entropy barriers to the recombination of point defects in Si has been proposed in other work[59,60].

If the spherical inclusions are voids the lower density when dislocations are present at the same depth suggests that the dislocations and the voids could be formed from the same point defects, i.e. Si_v. It is also possible that the pits and larger precipitates at the surfaces of the low energy implant samples could also be voids rather than precipitates. The different formation process would explain the different morphology from that of the precipitates.

3.11.3 Stress and strain

It has been reported from 5 crystal x-ray and Raman measurements that for low doses ($<^{I}\Phi c$) and low beam currents[44] and for high doses ($>^{I}\Phi c$) and high beam currents[45] the Si lattice in the surface Si layer contracts perpendicular to the wafer surface.

The ideas discussed in section 3.11.1 of an excess of Si_v resulting from the implantation might be expected to lead to a shrinking of the Si lattice. For doses $<^{I}\Phi c$, because the surface Si layer is constrained by the substrate, a shrinking of the surface Si layer would to lead to tensile stress parallel to the wafer surface and therefore compressive strain, i.e. lattice contraction, perpendicular to the wafer surface. For doses $>^{I}\Phi c$, using our experimental conditions where only the centre of a wafer is implanted, the surface Si layer is still partially constrained at the edge of the implanted area, and therefore some tensile stress parallel to the wafer surface and compressive strain perpendicular to the wafer surface would be expected. For doses $>^{I}\Phi c$ if the whole wafer is implanted, the surface Si layer is no longer constrained by the substrate and compressive strain both parallel and perpendicular to the wafer surface might be expected.

No strain measurements were made in this work but the possibility that the inclusions at the edge of the denuded zone are voids suggests that an excess of Si_v and therefore compressive strain in part of the surface Si layer may have resulted from the implant conditions used.

3.12 Thermal Contraction

At the implantation temperature of 680°C SiO_2 is not viscous[61,62] and therefore the difference in thermal expansion coefficients of SiO_2 and Si would introduce stress during the cool down at the end of the implant. The thermal expansion coefficient of SiO_2 is smaller than

that of Si[63] and therefore on cooling the surrounding Si contracts more than the SiO_2 precipitates putting the precipitates under compressive stress[62]. Strain might then be expected in the Si surrounding the precipitates. Strain was not observed by TEM suggesting, assuming that relaxation due to the c.s. sample being thin is negligible, that the difference in the thermal expansion coefficients contributes a negligible amount to the stress in the surface Si layer.

At the peak of the oxygen distribution a large density of defects is present. For low doses, i.e. $<{}^{I}\Phi c$, SiO_2 precipitates are present at this depth but the oxygen concentration is significantly higher than in the surface Si layer and this may result, due to the difference in the thermal expansion coefficients, in the formation of the defects during the cool down at the end of the implant. For doses $>{}^{I}\Phi c$ a continuous buried SiO_2 layer is present at this depth. On cooling down a separate layer of SiO_2 will contract less than a layer of Si but in this situation where the SiO_2 is attached to the Si substrate, the greater thickness of the Si substrate will force the SiO_2 layer to contract further and hence the SiO_2 layer will be under compressive stress parallel to the interfaces. Hence the Si at both interfaces will be under tensile stress parallel to the interfaces.

The rod-like defects observed at the interface of the buried damage/SiO_2 layer and the surface Si layer are SF pairs, of opposite type, suggesting they are not net sinks for point defects but were created by a shear mechanism due to the presence of stress[64]. Similar rod-like defects, referred to as multiple faulted defects (MFD), have been reported by other workers in 200keV implants[25,47,65]. Visitserngtrakul *et al*[25] also observed that some MFDs consisted of parallel intrinsic and extrinsic SF and suggested stress as the driving force for their generation. During the thermal oxidation of bulk Si at 800°C, stresses attributed to the difference in the thermal expansion coefficients can result in shear stresses that are higher than the critical stress for shear flow of Si[62]. Hence the stresses due to the difference in the thermal expansion coefficients could be large enough to generate defects. Further it has been reported that the yield strength of Si is reduced by the presence of SiO_2 precipitates[66] which would make it easier for defects to form in as-implanted SIMOX than in bulk Si. Hence the cooling down at the end of the implantation may be playing an important role in the formation of the SF pairs in this work and the defects referred to as MFD by other authors[25,47,65].

3.13 Summary

The main new work of the present chapter is summarised as follows. The first detailed TEM investigation reported on as-implanted SIMOX structures;

a) formed at energies of 90keV, 70keV and 50keV and the changes in the microstructure as a function of the implanted dose,

b) formed by implanting lower than standard doses (<1.4 x10^{18}O/cm^2) at 200keV and the first known report of the non-uniform distribution across the implanted area of the defects at the wafer surface and their occurrence in regions with precise rectangular shapes,

c) of previously unreported "line" defects below the peak of the oxygen distribution for energies of 90keV, 70keV, 50keV and 200keV,

d) the influence of time-averaged beam current densities between 2.5μA/cm^2 and 6.25μA/cm^2 for a constant implantation temperature of 680°C, a dose of $\approx$0.7x10^{18}O/cm^2 and an energy of 200keV,

and;

a) the as-implanted oxide precipitate morphology is correlated with the as-implanted oxygen distribution, from SIMS analysis, over a range of energies (90keV, 70keV, 50keV and 200keV) and doses (0.1-1.6x10^{18}O/cm^2) and hence as a function of the depth below the surface and the oxygen concentration ($\approx 10^{18}$-4.48x10^{22}/cm^3),

b) a simple model is proposed to calculate typical oxygen diffusion lengths during implantation as a function of the implantation conditions,

c) the likely role of the oxygen concentration, Si_i, Si_v, stress and thermal contraction in determining the as-implanted precipitate morphologies and defect microstructure are described.

3.14 References

[1] A Nejim, Dept. Electronic Engineering, University of Surrey, private communication.

[2] A Olsen & J C H Spence, Phil. Mag. A 43, p945 (1981).

[3] P Lu, R W Glaisher & D J Smith, Proc. 47th USA Elect. Micro. Soc. Conf., p576 (1989).

[4] P Rez & O L Krivanek, Proc. 9th Int. Congress. Elec. Micro. 1, p288 (1978).

[5] R E Mallard, Dept. of Materials, University of Oxford, private communication.

[6] P B Hirsch, A Howie, R B Nicholson, D W Pashley & M J Whelan, *Electron Microscopy of Thin Crystals* (Robert E Krieger, Florida, 1965).

[7] J W Edington, *Monographs in Practical Electron Microscopy in Materials Science* (Philips Technical Library, 1975).

[8] J Van Landuyt, R Gevers & S Amelinckx, Pys. Stat. Sol. 10, p319 (1965).

[9] A H Van Ommen, B H Koek & M P A Viegers, Appl. Phys. Lett. 49, p1063 (1986).

[10] A Bourret, J Thibault-Dessaux, & D N Seidman, J. Appl. Phys. 55, p825 (1984).

[11] W Bergholtz, J L Hutchinson & P Pirouz, Inst. Phys. Conf. Ser. 76, p11 (1985).

[12] S Maeyama & K Kajiyama, Jap. J. Appl. Phys. 21, p744 (1982).

[13] D Fathy, O L Krivanek, R W Carpenter & S Wilson, Inst. Phys. Conf. Ser. 67, p479 (1983).

[14] J A Kilner, R J Chater, P L F Hemment, R F Peart, E A Maydell-Ondrusz, M R Taylor & R P Arrowsmith, Nucl. Inst. & Meths. B7/8, p293 (1985).

[15] C Griffin, Ph D Thesis, University of London (1989).

[16] Y Li, J A Kilner, A K Robinson, P L F Hemment & C D Marsh, J. Appl. Phys. 70, p3605 (1991).

[17] R C Newman, M J Binns, W P Brown, F M Livingston, S Messoloras, R J Stewart & J G Wilkes, Physica 116B, p264 (1983).

[18] J W Mayer, L Eriksson & J A Davis, *Ion Implantation in Semiconductors* (Academic, New York, 1970).

[19] J F Ziegler, J P Biersack & U Littmark, *The Stopping and Ranges of Ions in Solids* vol 1, ed. J F Ziegler (Pergamon, New York, 1985).

[20] J Vanhellemont & C Claeys, J. Appl. Phys. 62, p3690 (1987).

[21] T Y Tan & C Y Kung, J. Appl. Phys. 59, p917 (1986).

[22] C Jaussaud, J Margail, J Stoemenos & M Bruel, Mats. Res. Soc. Proc. 107, p17 (1988).

[23] T P Sjoreen, O W Holland, D Fathy & R F Davis, Nucl. Inst. & Meths. B10, p579 (1985).

[24] A H Van Ommen, Mats. Res. Soc. Proc. 107, p79 (1988).

[25] J Stoemnos, J Margail, M Dupuy & C Jaussaud, Physica Scripta 35, p42 (1987).

[26] W A Tiller, S Hahn & F A Ponce, J. Appl. Phys. 59, p3255 (1986).

[27] L Kalinowski & R Seguin, Appl. Phys. Lett. 35, p211 (1979).

[28] K Taniguchi, D A Antoniades & Y Matsushita, Appl. Phys. Lett. 42, p961 (1983).

[29] F Morehead, Mats. Res. Soc. Proc. 104, p99 (1987).

[30] G D Watkins, Inst. Phys. Conf. Ser. 23, p1 (1975).

[31] M Hockly, C G Tuppen, C J Gibbings, A S R Martin, Z A Shafi & P Ashburn, Inst. Phys. Conf. Ser. 117, p445 (1991).

[32] D J Eaglesham, H J Gossman, M Cerullo, L N Pfeiffer & D Windt, Inst. Phys. Conf. Ser. 117, p431 (1991).

[33] P L F Hemment, Vacuum 29, p439 (1979).

[34] A De Veirman, J Van Landuyt, J Vanhellemont, H E Maes & K Yallup, Vacuum 42, p367 (1991).

[35] K J Reeson, A K Robinson, P L F Hemment, C D Marsh, K N Christensen, G R Booker, R J Chater, K J Kilner, G Harbeke, E F Steigmeir & G K Celler, Microelectron. Eng. 8, p163 (1988).

[36] K J Reeson, Nucl. Inst. & Meths. B19/20, p269 (1987).

[37] R J Chater, J A Kilner, P L F Hemment, K J Reeson & R F Peart, Proc. Electrochem. Soc. 86-4, p652 (1986).

[38] S Takeda, Jap. J. Appl. Phys. 30, p639 (1991).

[39] Z Lilental, R W Carpenter, D Fathy & J C Kelly, Mats. Res. Soc. Proc. 25, p525 (1984).

[40] M Pasemann, D Hoehl, A L Assev & O Pchelyakov, Phys. Stat. Solidi A 80, p135 (1983).

[41] A Bouret, Inst. Phys. Conf. Ser. 87, p39 (1987).

[42] H Bender & J Vanhellemont, Phys. Stat. Sol. A 107, p455 (1988).

[43] G Brebec, R Seguin, J Bevenot & C Martin, Acta Metal 28, p327 (1980).

[44] D Venables, K S Jones & F Namavar, Appl. Phys. Lett. 60, p3147 (1992).

[45] A Seidl, M Takai, H Sayama, K Haramura, H Ryssel & R Schork, presented at IBMM Conf. (1992) & to be published in Nucl Inst. & Meths. (1993).

[46] A Perez-Rodriguez, A Romano, J Macai, J R Morante, E Martin & J Jimenez, presented at the Euro. Mats. Res. Soc. Conf. (1993) & to be published in Nucl Inst. & Meths. (1993).

[47] J Margail, J M Lamure & A M Papon, Mats. Sci. & Eng. B12, p27 (1992).

[48] S Visitserngtrakul, S J Krause & B F Cordts, J. Appl. Phys. 69, p1784 (1991).

[49] S Nakashima & K Izumi, J. Mat. Res. 5, p1919 (1990).

[50] W P Maszara, J. Appl. Phys. 64, p123 (1988).

[51] M K El-Ghor, S J Pennycock, F Namavar & N Karam, Appl. Phys. Lett. 57, p156 (1990).

[52] M K El-Ghor, S J Pennycock, T P Sjoreen C W White & J Narayan, Mats. Res. Soc. Proc. 107, p235 (1988).

[53] M K El-Ghor, S J Pennycock & J Narayan, Mats. Res. Soc. Proc. 74, p591 (1987).

[54] J P Ruffel, D H Douglas-Hamilton & K Izumi, Nucl. Inst. & Meths. B21, p229 (1987).

[55] J Narayan & O W Holland, J. Electrochem. Soc. 131, p2651 (1984).

[56] K Krishan, Radiat. Eff. 66, p121 (1982).

[57] P B Johnson, *Fundamental Aspects of Inert Gases in Solids*, eds. S E Donnelly & J H Evans (Plenum Press, New York, 1991).

[58] G Dearnley, J H Freeman, R S Nelson & J Stephens, *Ion Implantation,* Defects in Crystalline Solids vol 8, eds. S Amelinckx, R Gevers & J Nihoul (North Holland, Amsterdam, 1973).

[59] U Gosele, W Frank & A Seeger, Solid State Commun. 45, p31 (1983).

[60] D A Antoniades & I Moskowitz, J. Appl. Phys. 53, p6788 (1982).

[61] E A Irene, E Tierney & J Angilello, J. Electrochem. Soc. 129, p2594 (1982).

[62] S M Sze, *VLSI Technology* (McGraw-Hill International, Singapore, 1988).

[63] R J Jaccadine & W A Schlegel, J. Appl. Phys. 37, p2429 (1966).

[64] S G Roberts, Dept.of Materials, University of Oxford, private communication.

[65] S Visitserngtrakul, S J Krause, B F Cordts & P Roitman, Vacuum 42, p353 (1991).

[66] B Leroy & C Ploughoven, J. Electrochem. Soc. 127, p961 (1980).

[67] J Margail, LETI, CEN, Grenoble, France, private communication.

Chapter 4

Annealed Microstructure

4.1 Introduction

In this chapter a detailed investigation is made of the post-anneal microstructures of the as-implanted samples investigated in chapter 3 after a subsequent anneal in either N_2, at 1310°C, 1320°C or 1360°C or Ar + ½ % O_2 at 1300°C (sections 4.2, 4.3 & 4.4). This is in order to determine the experimental parameters for forming the optimal structures for "fully depleted" high performance CMOS devices and for radiation hard devices with reduced circuit self-heating, and using the detailed knowledge of the as-implanted structures obtained in chapter 3 to develop an understanding of the mechanisms taking place during annealing. After the single implants in chapter 3 and the anneals mentioned above, Si islands in a buried oxide layer and threading dislocations in a surface Si layer are present. To try to reduce the density of Si islands other samples given either graded low energy implants and an anneal at 1320°C (section 4.5) or single standard implants and either a rapid thermal anneal (RTA) or a RTA and conventionally annealed are also investigated (section 4.6). The c.s. micrographs in this chapter are taken using the many beam diffraction condition at a <110> pole and the p.v. micrographs using the many beam diffraction condition at the [001] pole.

4.2 Dose and Energy Dependence

4.2.1 Introduction

Cross-section (c.s.) and plan-view (p.v.) TEM micrographs of samples implanted at energies of 200keV, 90keV, 70keV and 50keV with doses (Φ) in the range of $0.1x10^{18}O/cm^2$ to $1.6x10^{18}O/cm^2$ after annealing in N_2 at either 1320°C for 2hrs or 1310°C, 1320°C or 1360°C for 6hrs, or in Ar + ½ % O_2, at 1300°C for 6hrs, are shown in Figs. 4.1, 4.2, 4.3, 4.4, 4.5, 4.6 & 4.7. The layer thicknesses and defect densities are summarised in Table 4.1. The c.s. micrographs show the structures consist of a buried amorphous oxide layer (continuous, discontinuous or a series of precipitates, see section 4.2.2) below a single crystal Si surface

Figure 4.1 Cross-section micrographs, at a <110> pole, of samples implanted at 50keV, Φ = a) $0.2x10^{18}O/cm^2$, b) $0.5x10^{18}O/cm^2$ and c) $0.7x10^{18}O/cm^2$, T_i = 680°C, I' = 2.5μA/cm^2 and annealed in nitrogen at 1320°C for 2hrs, and,
plan-view micrographs, at the [001] pole, of the same samples, d), e) and f) respectively.
O = discontinuous buried oxide layer, H = silicon pinholes through the buried oxide layer, D = dislocations parallel to the wafer surface in the Si pinholes and S = silicon islands within the buried oxide layer. Figs. d) and e) show the plan-view microstructure in both the surface silicon layer and the buried oxide. Fig. f) shows the plan-view microstructure in only the surface silicon layer (the directions shown in the bottom right hand corner of f) apply also to d) and e)).

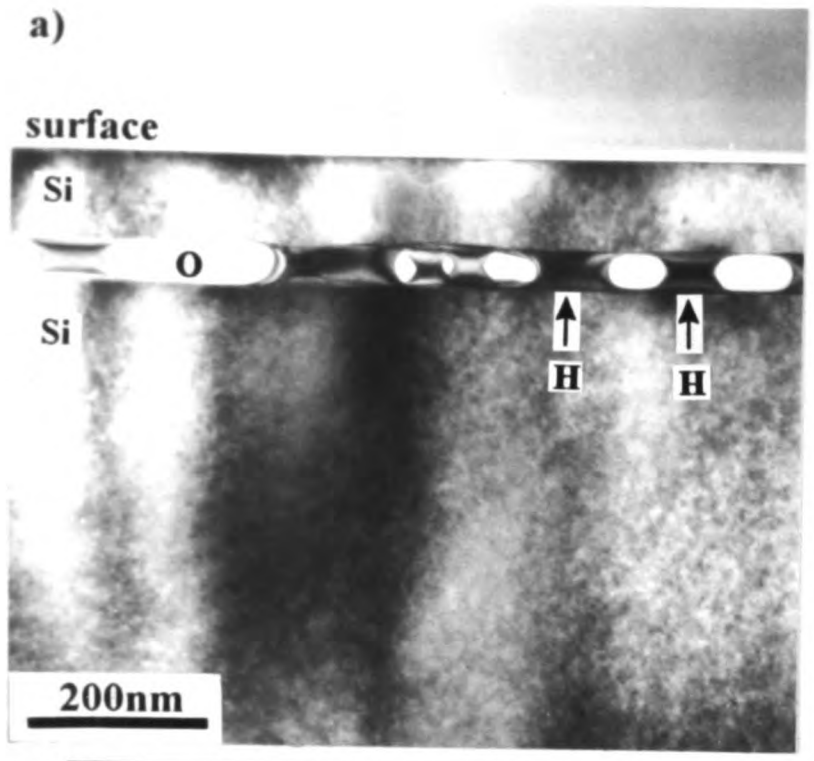
a)
surface
Si
O
Si
H
H
200nm

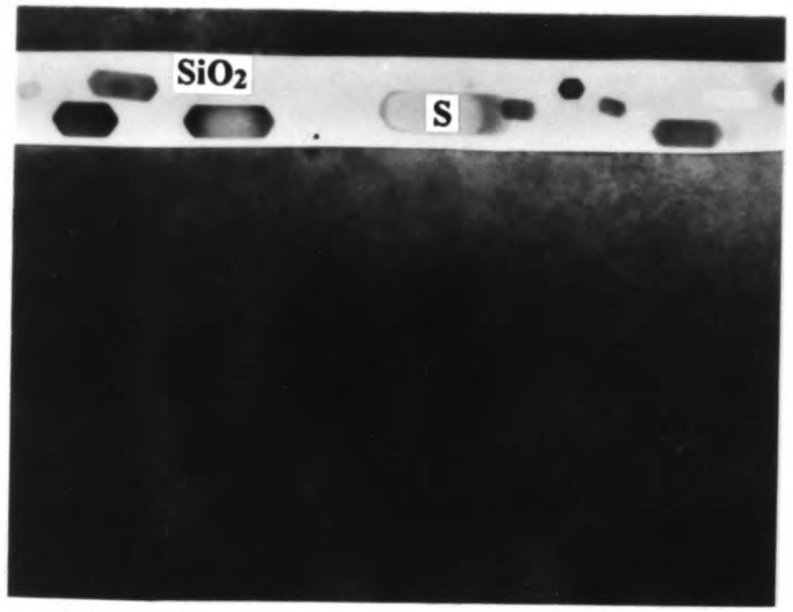
b)
SiO2
S

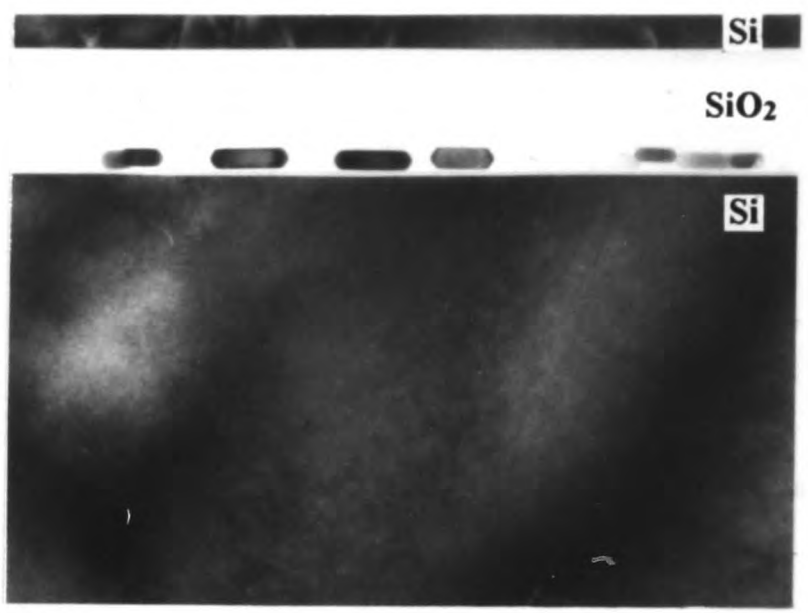
c)
Si
SiO2
Si

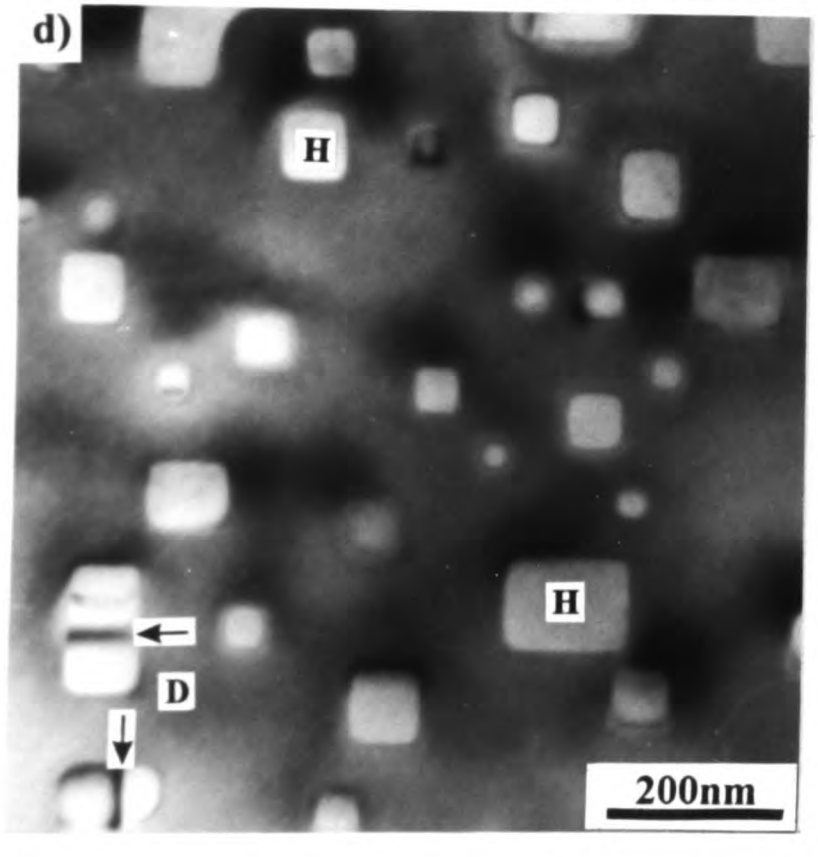
d)
H
H
D
200nm

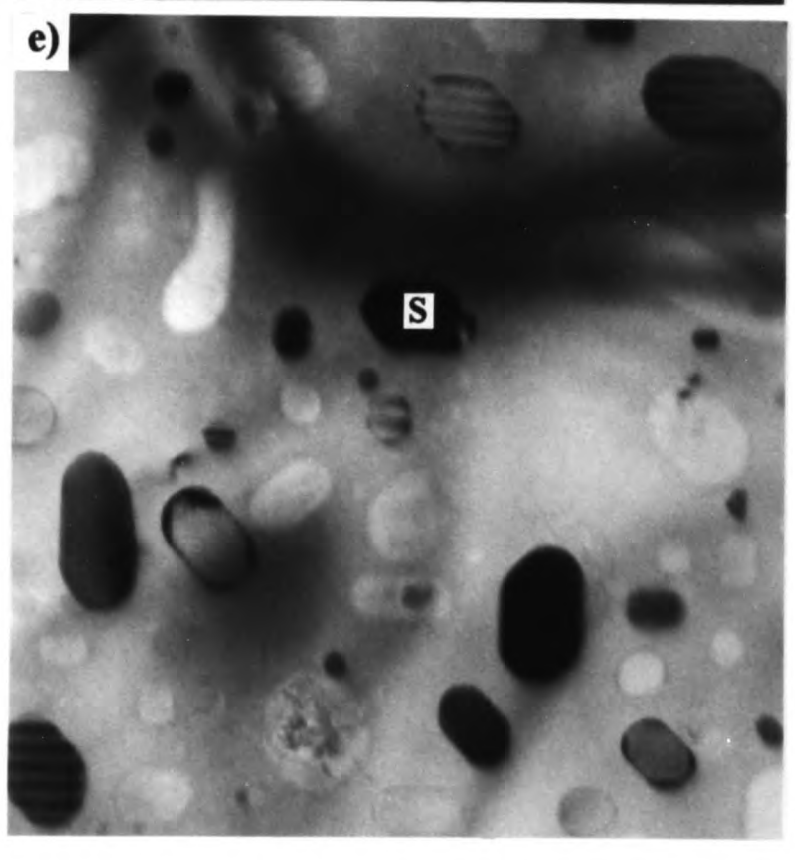
e)
S

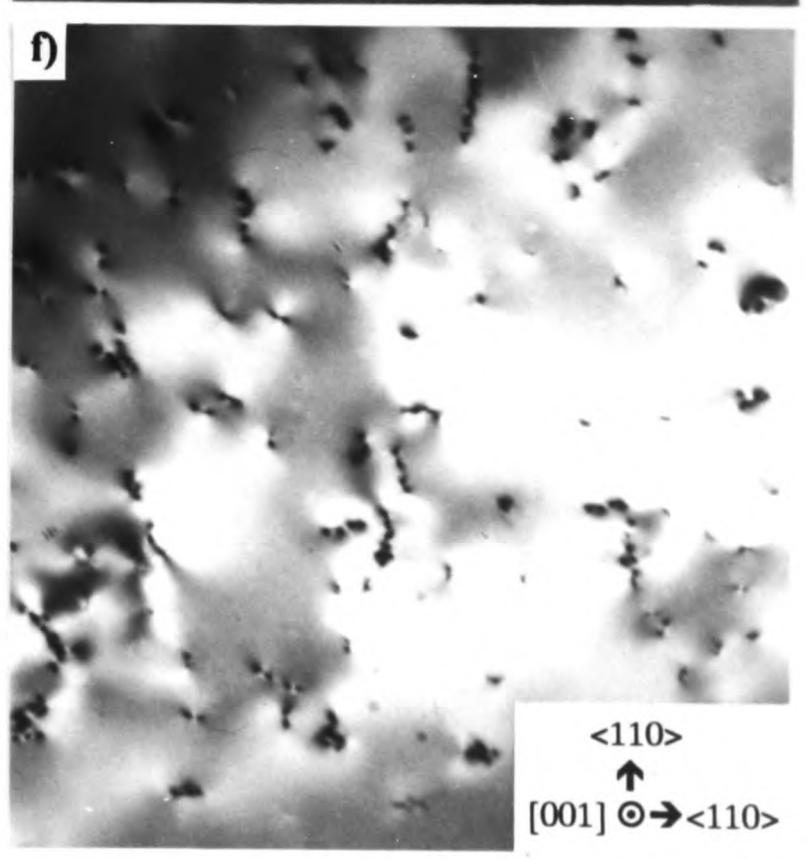
f)
<110>
[001] ⊙→<110>

Figure 4.2 Cross-section micrographs, at a <110> pole, of samples implanted at 70keV, Φ = a) $0.1x10^{18}O/cm^2$, b) $0.4x10^{18}O/cm^2$ and c) $0.5x10^{18}O/cm^2$, T_i = 680°C, I' = 3.1μA/cm^2 and annealed in nitrogen at 1320°C for 6hrs, and,
plan-view micrographs, taken at the [001] pole, of the same samples, d), e) and f) respectively. O = oxide precipitates, D = dislocations pinned between oxide precipitates, E = dislocations pinned between oxide precipitates and the surface, S = silicon islands within the buried oxide layer, M = silicon islands within the buried oxide layer exhibiting moiré fringes and P = silicon protrusion into the buried oxide layer. The plan-view micrographs show the microstructure in both the surface silicon layer and the buried oxide precipitates/continuous layers (the directions shown in the bottom right hand corner of f) apply also for d) and e)).

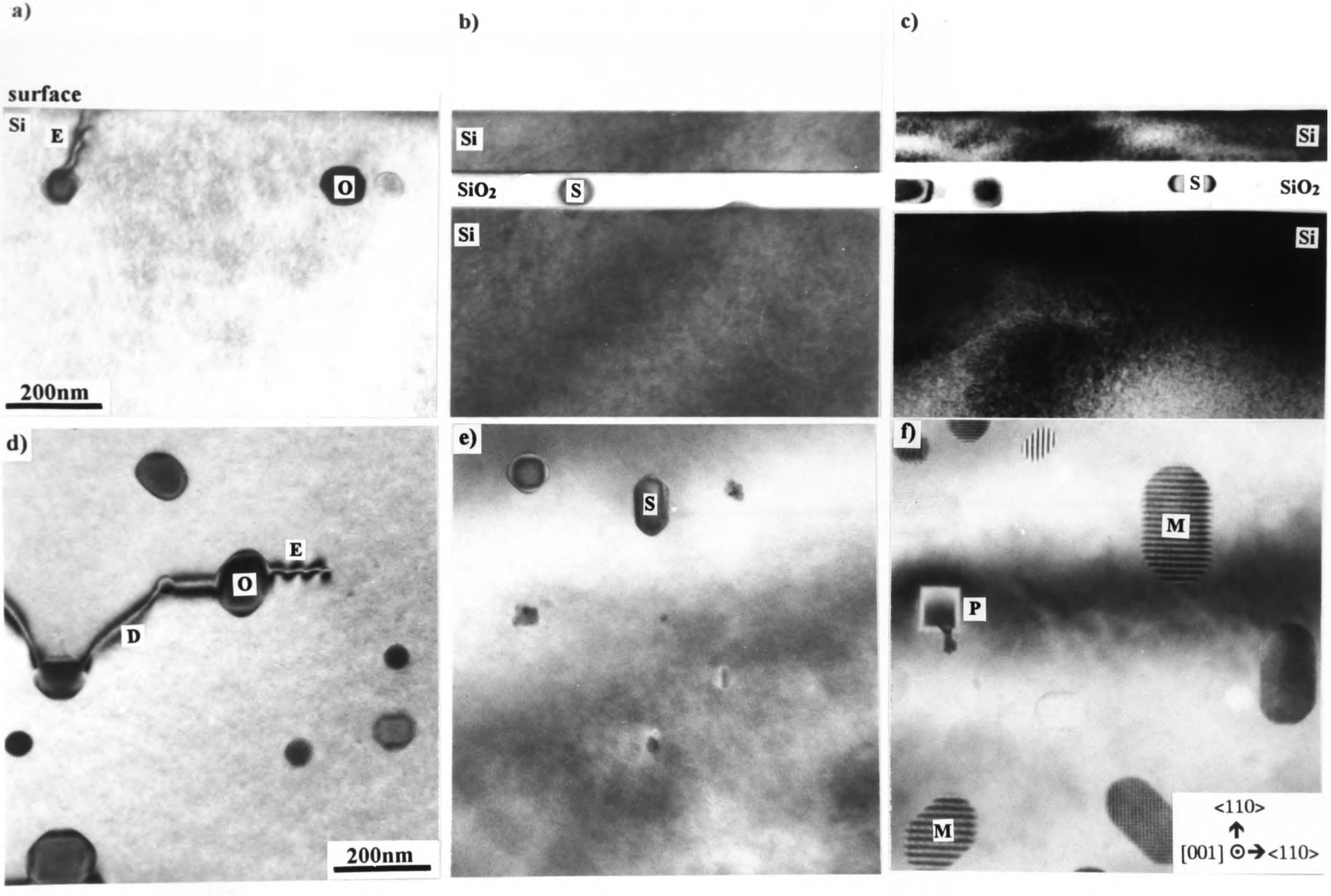
a)
surface
Si
E
O
200nm
b)
Si
SiO2
S
Si
c)
Si
S
SiO2
Si
d)
E
O
D
200nm
e)
S
f)
M
P
M
<110>
[001] ⊙→<110>

Figure 4.3 Cross-section micrographs, at a <110> pole, of samples implanted at 70keV, Φ = a) $0.25x10^{18}O/cm^2$, b) $0.35x10^{18}O/cm^2$, c) $0.45x10^{18}O/cm^2$ and d) $0.5x10^{18}O/cm^2$, T_i = 680°C, I' = $3.1\mu A/cm^2$ and annealed in argon + ½ % oxygen at 1300°C for 6hrs, and,
plan-view micrographs, taken at the [001] pole, of the same samples, e), f), g) and h) respectively. O = oxide precipitates, D = dislocations parallel with the wafer surface pinned between the oxide precipitates, E = dislocations pinned between oxide precipitates and the surface, S = silicon islands within the buried oxide layer and M = silicon islands within the buried oxide layer exhibiting moiré fringes. The plan-view micrographs show the microstructure in both the surface silicon layer and the buried oxide precipitate/continuous layers (the directions shown in the bottom right hand corner of h) apply also for e), f) and g)).

a)

surface

Si

O

200nm

b)

Si

SiO_2 S

Si

c)

M

d)

Si

SiO_2

Si

e)

O

E

D

O

O

200nm

f)

g)

S

M

h)

M

<110>

[001] ⊙→<110>

Figure 4.4 (part 1) Cross-section micrographs, at a <110> pole, of samples implanted at 90keV, Φ = a) $0.22x10^{18}O/cm^2$, b) $0.29x10^{18}O/cm^2$, c) $0.4x10^{18}O/cm^2$ and d) $0.6x10^{18}O/cm^2$, T_i = 680°C, I' = 3.75μA/cm^2 and annealed in nitrogen at 1320°C for 6hrs, and,
plan-view micrographs, taken at the [001] pole, of the samples implanted with Φ = e) $0.22x10^{18}O/cm^2$, f) $0.4x10^{18}O/cm^2$ and g) $0.6x10^{18}O/cm^2$.
O = discontinuous buried oxide layer, H = silicon pinholes through the buried oxide layer, D = dislocations parallel with the wafer surface within silicon pinholes, S = silicon island showing thickness fringe contrast, P = silicon protrusion, N = small dislocation network and DP = dislocation pairs. Fig. e) shows the plan-view microstructure of both the surface silicon and buried oxide layer. Figs. f) and g) show the plan-view microstructure in only the surface silicon layer (the directions shown in the bottom right hand corner of g) apply also for e) and f)).

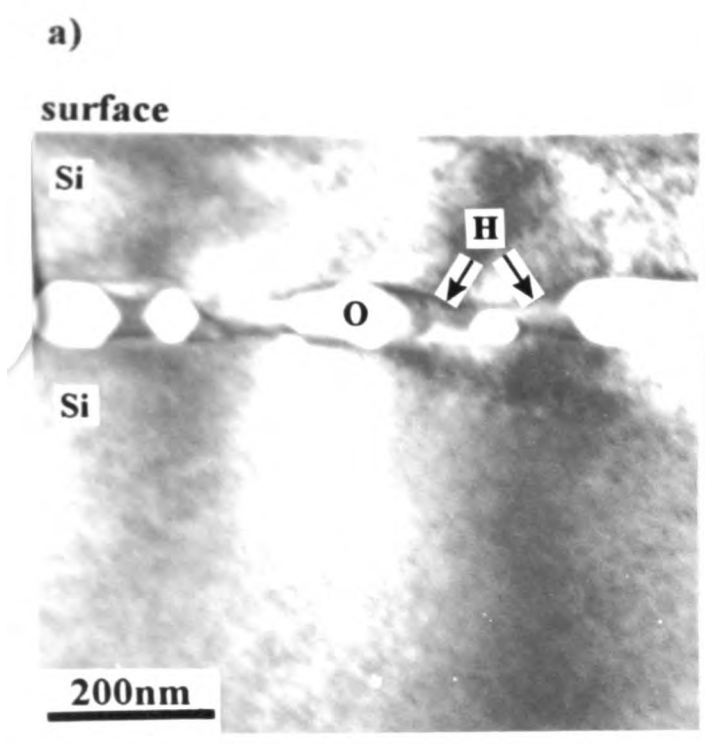
a)
surface
Si
H
O
Si
200nm

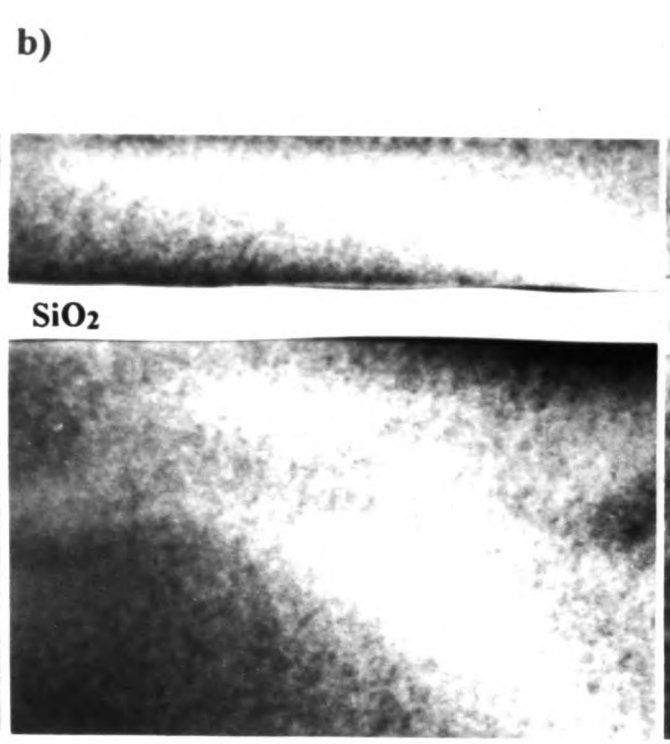
b)
SiO2

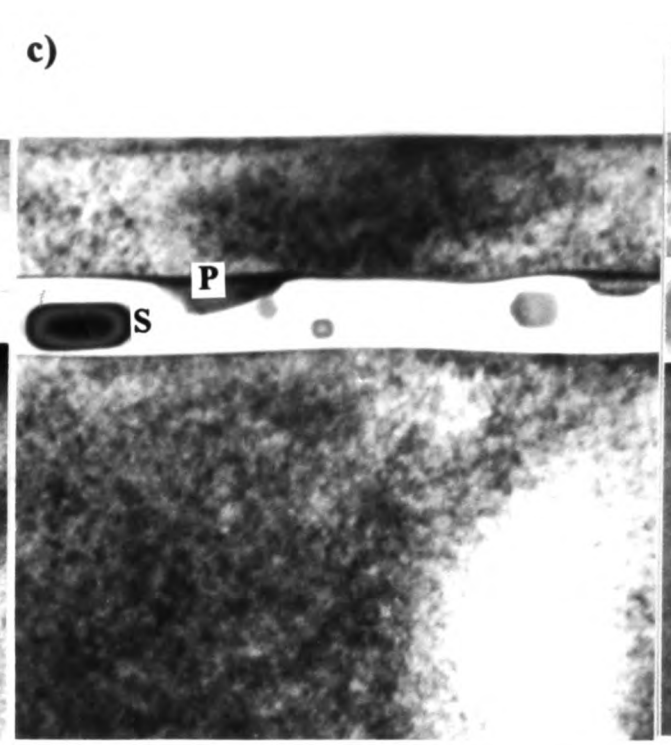
c)
P
S

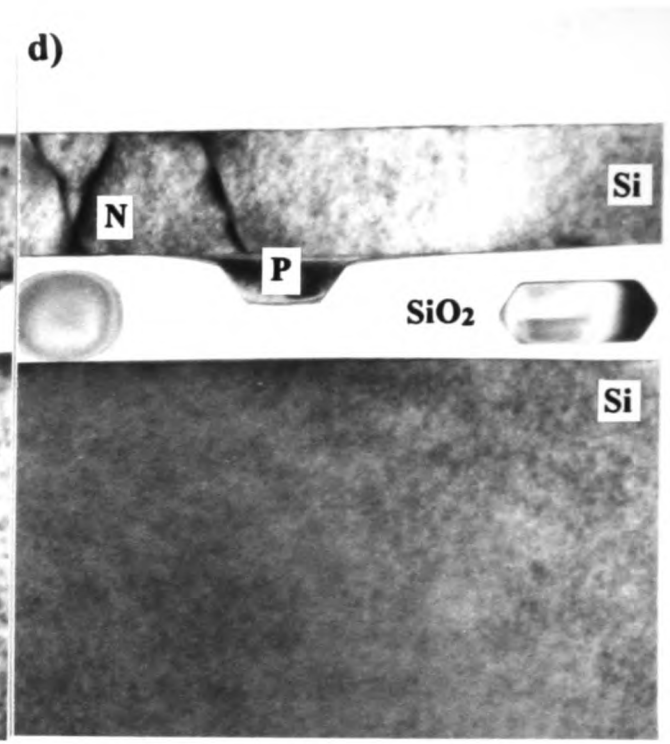
d)
Si
N
P
SiO2
Si

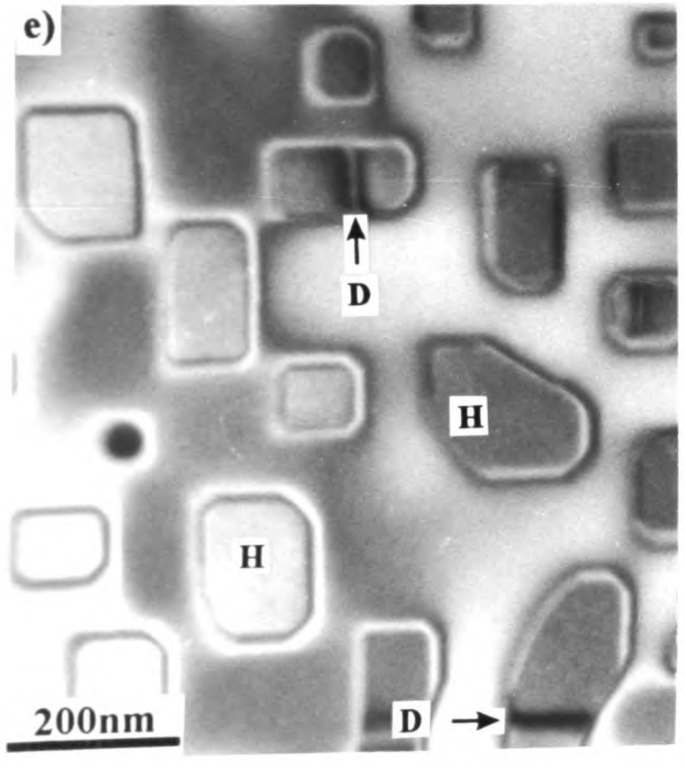
e)
D
H
H
200nm
D

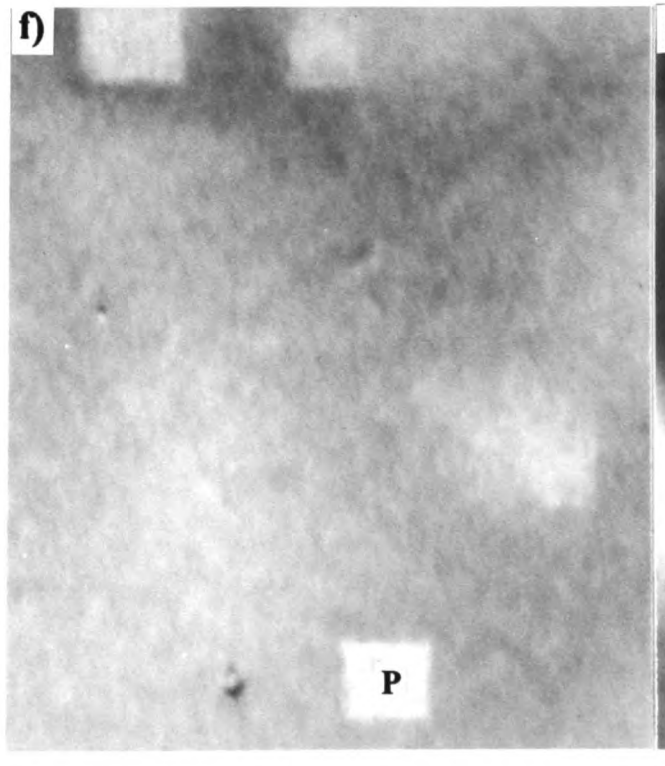
f)
P

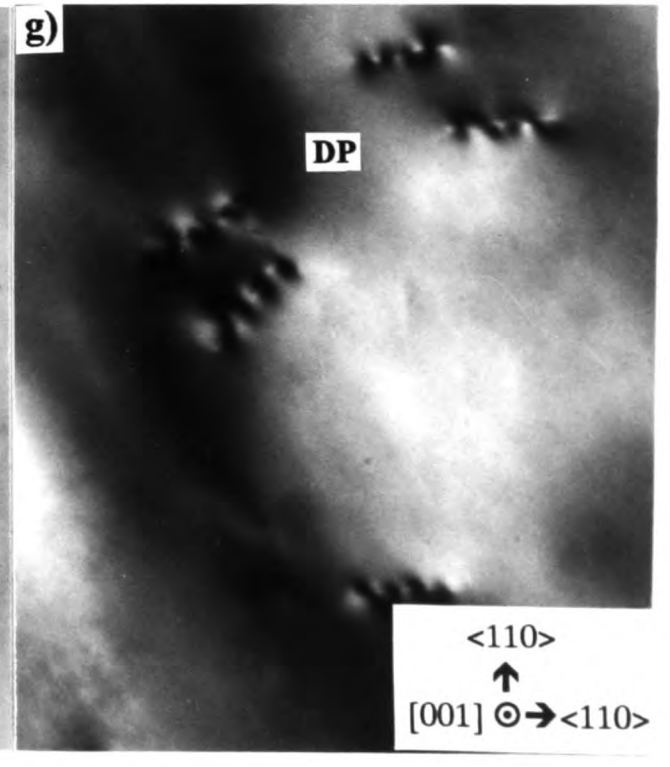
g)
DP
<110>
[001] ⊙→<110>

Figure 4.4 (part 1) Cross-section micrographs, at a <110> pole, of samples implanted at 90keV, Φ = a) $0.22x10^{18}O/cm^2$, b) $0.29x10^{18}O/cm^2$, c) $0.4x10^{18}O/cm^2$ and d) $0.6x10^{18}O/cm^2$, T_i = 680°C, I' = 3.75μA/cm^2 and annealed in nitrogen at 1320°C for 6hrs, and,
plan-view micrographs, taken at the [001] pole, of the samples implanted with Φ = e) $0.22x10^{18}O/cm^2$, f) $0.4x10^{18}O/cm^2$ and g) $0.6x10^{18}O/cm^2$.
O = discontinuous buried oxide layer, H = silicon pinholes through the buried oxide layer, D = dislocations parallel with the wafer surface within silicon pinholes, S = silicon island showing thickness fringe contrast, P = silicon protrusion, N = small dislocation network and DP = dislocation pairs. Fig. e) shows the plan-view microstructure of both the surface silicon and buried oxide layer. Figs. f) and g) show the plan-view microstructure in only the surface silicon layer (the directions shown in the bottom right hand corner of g) apply also for e) and f)).

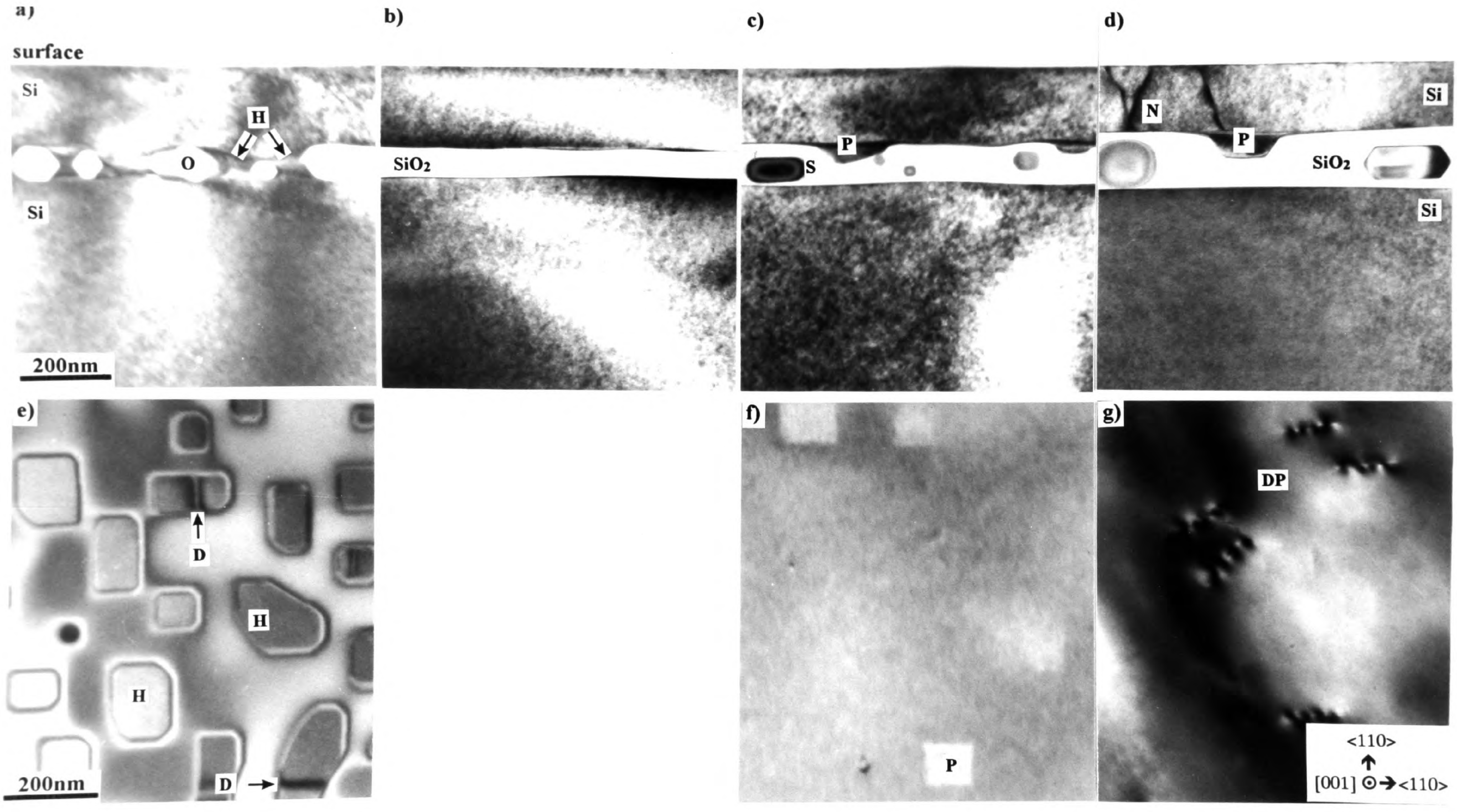
a)
surface
Si
H
O
Si
200nm
b)
SiO2
c)
P
S
d)
N
Si
P
SiO2
Si
e)
D
H
H
200nm
D
f)
P
g)
DP
<110>
[001] ⊙→<110>

Figure 4.4 (part 2) Cross-section micrographs, at a <110> pole, of samples implanted at 90keV, Φ = h) $0.7x10^{18}O/cm^2$, i) $0.9x10^{18}O/cm^2$, j) $1.0x10^{18}O/cm^2$ and k) $1.5x10^{18}O/cm^2$, T_i = 680°C, I' = $3.75\mu A/cm^2$ and annealed in nitrogen at 1320°C for 6hrs, and,
plan-view micrographs, taken at the [001] pole, of the same samples l), m), n) and o) respectively. S = silicon islands within the buried SiO_2 layer. Fig. l) shows the plan-view microstructure in only the surface silicon layer. Figs. m), n) and o) show the plan-view microstructure in both the surface silicon layer and the buried SiO_2 layer (the directions shown in the bottom right hand corner of o) apply also for l), m) and n)).

h)

surface

Si

SiO_2

S

Si

200nm

i)

j)

k)

Si

SiO_2

Si

l)

200nm

m)

S

n)

S

o)

<110>

[001] ⊙→<110>

Figure 4.5 Cross-section micrographs, at a <110> pole, of samples implanted at 90keV, Φ = a) $0.35x10^{18}O/cm^2$, b) $0.4x10^{18}O/cm^2$, c) $0.52x10^{18}O/cm^2$ and d) $1.0x10^{18}O/cm^2$, T_i = 680°C, I' = $3.75\mu A/cm^2$ and annealed in argon + ½ % oxygen at 1300°C for 6hrs, and,
plan-view micrographs, taken at the [001] pole, of the samples implanted with Φ = e) $0.35x10^{18}O/cm^2$, f) $0.52x10^{18}O/cm^2$ and g) $1.0x10^{18}O/cm^2$.
P = silicon hillock/protrusion at the silicon/SiO_2 interface, S = silicon islands within the buried SiO_2 layer and M = silicon islands (showing no facets) within the buried SiO_2 layer exhibiting moiré fringes. Figs. e) and f) show the plan-view microstructure in both the surface silicon layer and the buried SiO_2 layer. Fig. g) shows the plan-view microstructure in only the surface silicon layer (the directions shown in the bottom right hand corner of g) apply also for e) and f)).

a)

surface

Si

SiO_2

Si

200nm

b)

S

P

c)

S

d)

Si

SiO_2

Si

e)

200nm

f)

M

M

g)

<110>

[001] ⊙→<110>

Figure 4.6 (part 1) Cross-section micrographs, at a <110> pole, of samples implanted at 200keV, Φ = a) $0.4x10^{18}O/cm^2$, b) $0.46x10^{18}O/cm^2$, and c) $0.56x10^{18}O/cm^2$, T_i = 680-700°C, I' = 5.6μA/cm^2 and annealed in nitrogen at 1360°C for 6hrs, and,
plan-view micrographs, taken at the [001] pole, of the same samples d), e) and f) respectively. O = discontinuous buried oxide layer, H = silicon pinholes through the buried oxide layer and D = dislocation parallel with the wafer surface within a pinhole. The plan-view figures show the microstructure in both the surface silicon and buried oxide/SiO_2 layers (the directions shown in the bottom right hand corner of f) apply also for d) and e)).

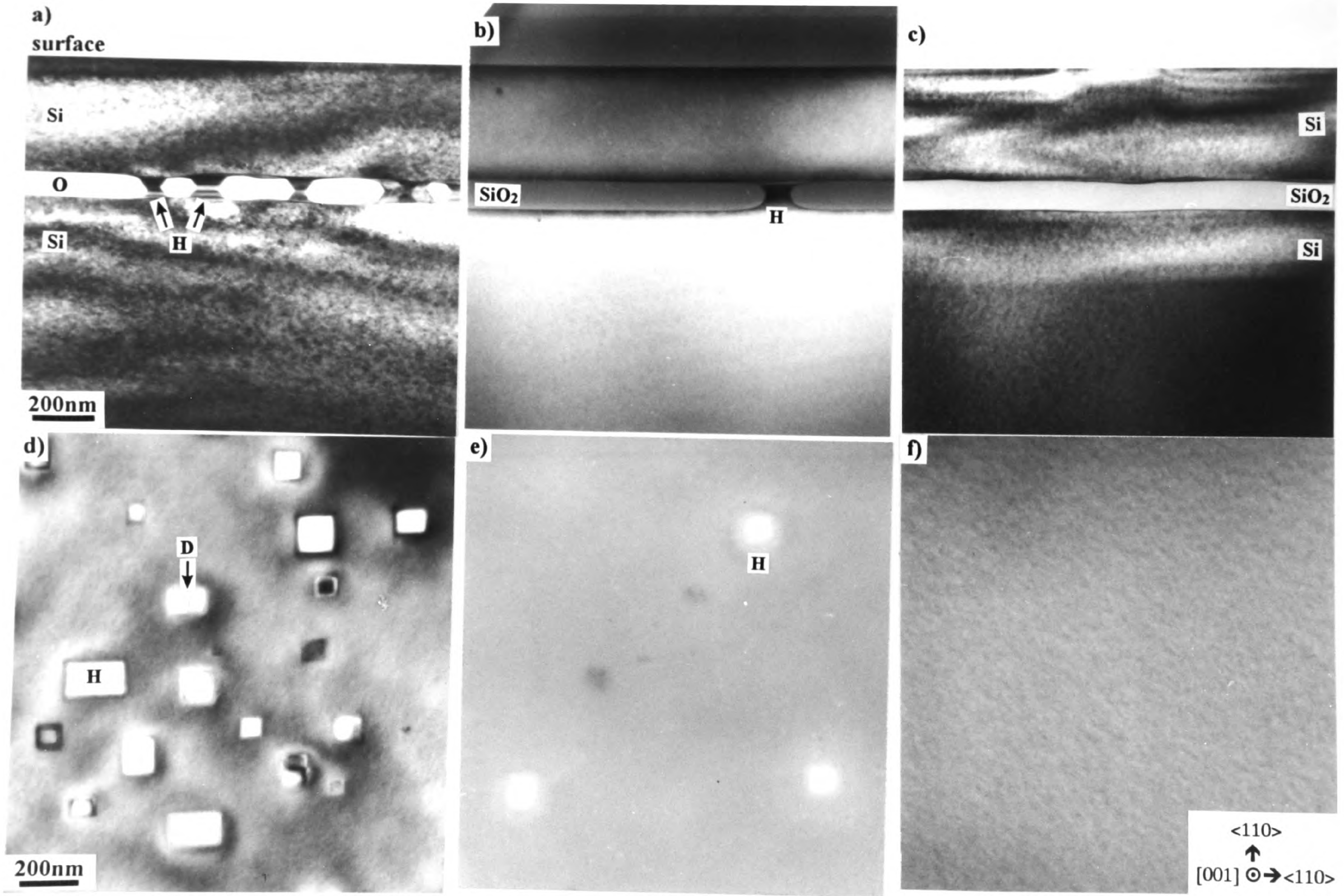
a)
surface
Si
O
Si
H
200nm
b)
SiO2
H
c)
Si
SiO2
Si
d)
D
H
200nm
e)
H
f)
<110>
[001] <110>

Figure 4.6 (part 2) Cross-section micrographs, at a <110> pole, of samples implanted at 200keV, T_i = 700°C, Φ = g) $0.6x10^{18}O/cm^2$ (I' = $5.6\mu A/cm^2$), h) $0.72x10^{18}O/cm^2$ (I' = $5\mu A/cm^2$), i) $1.2x10^{18}O/cm^2$ (I' = $5.6\mu A/cm^2$) and j) $1.6x10^{18}O/cm^2$ (I' = $5.6\mu A/cm^2$) and annealed in nitrogen at 1360°C, 1360°C, 1310°C and 1320°C, respectively, for 6hrs, and, plan-view micrographs, taken at the [001] pole, of the samples implanted with doses of k) $0.6x10^{18}O/cm^2$and l) $0.72x10^{18}O/cm^2$.

S = silicon islands connected to one or both of the silicon/SiO_2 interfaces and N = small dislocation network. The plan-view micrographs show the microstructure in both the surface silicon and the buried SiO_2 layers (the directions shown in the bottom right hand corner of l) apply also for k)).

g)
surface
Si
SiO_2
Si
200nm
h)
S
i)
N
S
j)
Si
SiO_2
Si
k)
200nm
l)
<110>
[001] ⊙→<110>

Figure 4.7 Cross-section micrographs, at a <110> pole, of samples implanted at 200keV, Φ =, a) $0.56 \times 10^{18} O/cm^2$, b) $0.65 \times 10^{18} O/cm^2$, c) $1.6 \times 10^{18} O/cm^2$ and d) $1.7 \times 10^{18} O/cm^2$, T_i = 650°C, 700°C, 700°C and 680°C, respectively, I' = 5.6μA/cm^2 and annealed in argon + ½ % oxygen at 1300°C for 6hrs, and,
plan-view micrographs, taken at the [001] pole, of the same samples e), f), g) and h) respectively.
P = silicon protrusion/silicon island connected to substrate, D = "dog-leg" dislocations, S = straight dislocations, and N = small dislocation network. Figs. e) and h) show the plan-view microstructure in both the surface silicon layer and the buried SiO_2 layer. Figs. f) and g) show the plan-view microstructure in only the surface silicon layer (the directions shown in the bottom right hand corner of h) apply also for e), f) and g)).

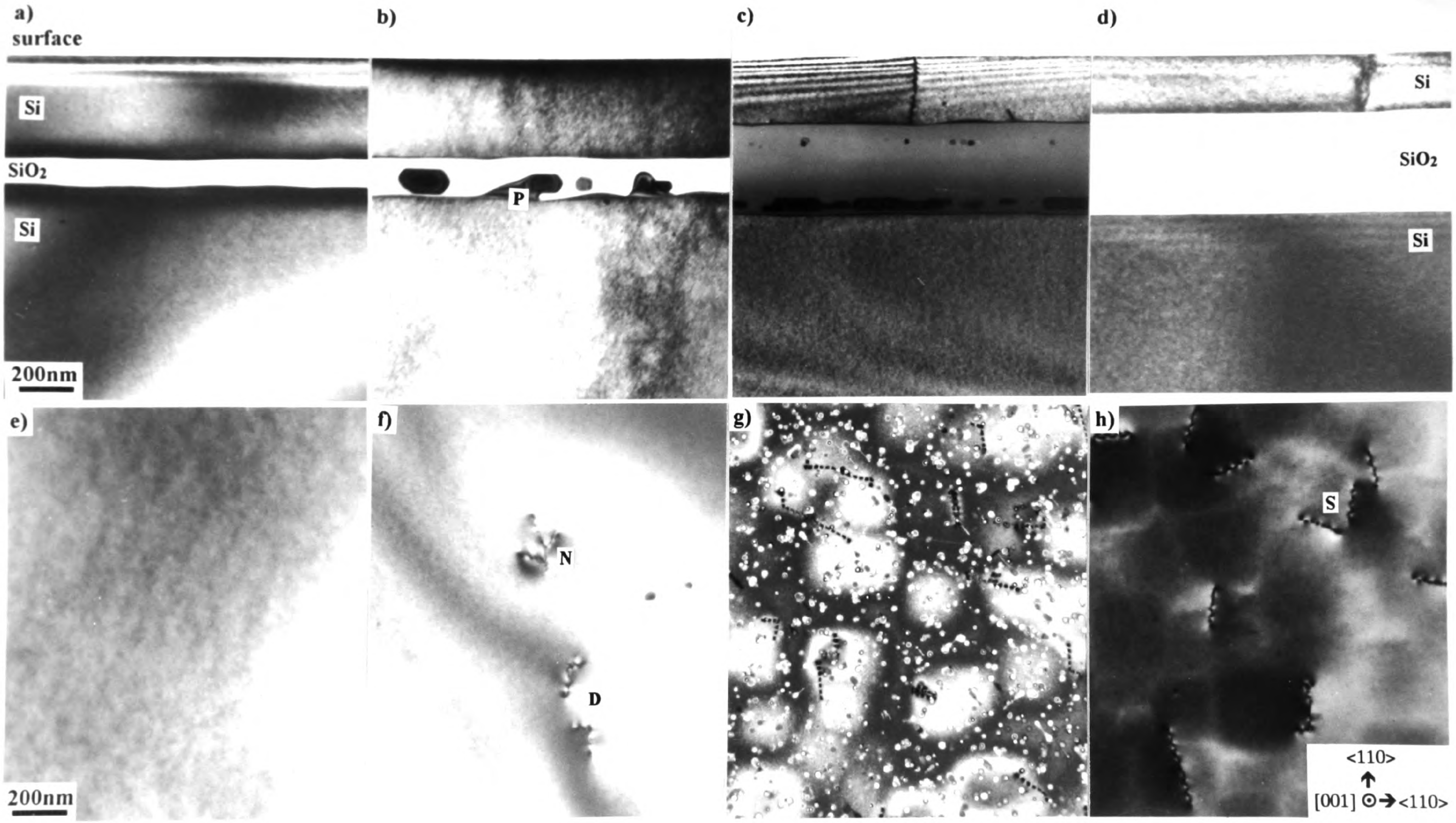
a)
surface
Si
SiO2
Si
200nm
b)
P
c)
d)
Si
SiO2
Si
e)
200nm
f)
N
D
g)
h)
S
<110>
[001] ⊙→<110>

Sample	Energy (keV)	Dose ($x10^{18}/cm^2$)	Anneal ambient	T_{Si} (nm)	T_{SiO_2} (nm)	Dislocation density ($/cm^2$)	Si island density ($/cm^2$)
Ho3a	50	0.2	N_2	-	#	$<10^6$	-
Ho3b	"	0.5	"	55	105	$8x10^7$	$5x10^9$
Ho3c	"	0.7	"	40	150	$1x10^9$	$1x10^9$
H56a	70	0.25	$Ar + O_2$	-	#	-	-
H57	"	0.35	"	110	75	$<10^5$	$4x10^8$
H114	"	0.36	"	120	75	$1x10^7$	$6x10^8$
H89	"	0.45	"	105	90	$5x10^7$	$1x10^9$
H90	"	0.5	"	85	120	$4x10^8$	$2x10^9$
H36a	"	0.1	N_2	-	#	10^8	-
K339a	"	0.3	"	-	#	$<10^7$	$<10^7$
H11	"	0.33	"	140	70	$<10^5$	$5x10^7$
H36c	"	0.4	"	130	80	$5x10^6$	$1.4x10^8$
H36b	"	0.5	"	110	110	$5x10^7$	$2x10^9$
K339c	"	0.7	"	95	155	$4x10^8$	-
K339b	"	1.0	"	50	220	$7x10^8$	-
H100	90	0.35	$Ar + O_2$	160	75	$1x10^7$	$4x10^7$
H99	"	0.4	"	135	110	$9x10^7$	$9x10^8$
H97	"	0.48	"	125	140	$2x10^8$	$2x10^{10}$
H106	"	0.52	"	150	110	$5x10^7$	$1x10^9$
H113	"	0.56	"	130	140	$3x10^8$	$1x10^{10}$
H41	"	1.0	"	75	230	$7x10^8$	-
H103	"	1.05	"	60	250	$5x10^8$	-
H124	"	0.22	N_2	-	#	$6x10^5$	-
H123	"	0.29	"	-	#	$<5x10^6$	$5x10^6$
H122	"	0.4	"	180	90	$5x10^7$	$6x10^8$
H142	"	0.43	"	160	100	$5x10^7$	$3x10^8$
H42a	"	0.6	"	155	135	$3x10^8$	$1.5x10^9$
H42b	"	0.7	"	135	165	$1.6x10^8$	$>1x10^{10}$
H42c	"	0.9	"	120	210	$9x10^8$	$1x10^{10}$
H42d	"	1.0	"	90	235	$1.2x10^9$	$3x10^9$
H42e	"	1.5	"	20#	340	$8x10^9$	-
H93	200	0.56	$Ar + O_2$	390	110	$<10^5$	$4x10^7$
H104	"	0.65	"	380	145	$1x10^7$	10^9
H43	"	1.6	"	260	350	$7x10^8$	-
H88	"	1.7	"	225	380	$4x10^8$	-
H135	"	0.4	N_2	-	#	$1x10^6$	-
H133	"	0.46	"	-	#	$<5x10^5$	$5x10^6$
H35	"	0.56	"	405	110	$<1x10^5$	$5x10^6$
H136	"	0.6	"	400	120	$5x10^6$	$2x10^7$
H130	"	0.7	"	390	145	$5x10^6$	$2x10^9$
H121	"	1.2	"	345	265	$3x10^8$	$>10^{11}$
H128	"	1.6	"	280	360	$4x10^8$	-

Table 4.1 Silicon (T_{Si}) and oxide (T_{SiO_2}) layer thicknesses and defect densities. Anneal in N_2 was 1310°C, 1320°C or 1360°C for 6hrs. Anneal in $Ar + O_2$ was 1300°C for 6hrs (# discontinuous).

layer. The p.v. micrographs show the structure within both the buried oxide layer and the surface silicon layer for all the samples except for those in Figs. 4.1f, 4.5g & 4.7g, because the chemical (HF) etching method of p.v. sample preparation was used to prepare these p.v. samples (section 2.5), and Figs. 4.4f, 4.4g, 4.4l & 4.7f, as these micrographs illustrate structure within only the surface Si layer to be discussed in section 4.2.3. The p.v. samples shown in the later micrographs were prepared by ion beam thinning and the microstructure within only the surface Si layer was observed by examining the p.v. samples close to the edge of the hole made by the ion beam thinning process. The p.v. microstructure in both the surface Si layer and the buried oxide layer was observed by examining the p.v. sample further from the edge of the hole.

4.2.2 Buried Oxide Layer

The TEM results show that the amorphous oxide layer is either a) continuous, i.e. the surface Si layer and the substrate are not observed to be connected by Si at any points (e.g. figs. 4.1b & 4.4b), b) discontinuous, i.e. the surface Si layer and the substrate are connected at some points by Si through the oxide layer (e.g. figs. 4.1a, 4.4a & 4.4a,b), or c) consisted of a series of discrete oxide precipitates (e.g. figs. 4.2a & 4.3a). For the discontinuous oxide layer the Si columns running through the oxide layer are referred to as Si pinholes. For the continuous oxide layers SIMS measurements (not included) show that the oxide is stochiometric SiO_2 and hence the continuous buried oxide layers in the c.s. micrographs in Figs. 4.1b,c, 4.2b,c, 4.3b-d, 4.4b-k, 4.5a-d, 4.6b-j and 4.7a-d are labelled SiO_2. As the SIMS analysis is an average measurement over a area of many thousands of square microns, when a large number of Si pinholes are present in the discontinuous oxide layers, or the oxide layers consist of oxide precipitates, the SIMS signal at the depth of the oxide layer does not give a value corresponding to SiO_2. Based on selected area diffraction patterns (SADP) from areas containing the oxide of the discontinuous layers and oxide precipitates, the oxide is considered to be stochiometric SiO_2 but as this is not proved by the SIMS results for these samples the oxide layers in the c.s. micrographs in Figs. 4.1a, 4.2a, 4.3a, 4.4a and 4.6a are labelled as oxide rather than SiO_2.

A remark may be made concerning the contrast of the oxide/SiO_2 under the many beam diffraction condition. In figures 4.3a and 4.3b the oxide/SiO_2 appears lighter than the adjacent

Si. In figures 4.2a, 4.2d & 4.3e however the oxide/SiO_2 precipitates appear darker than the surrounding Si. It is likely that this difference arises from the fact that in the former case the SiO_2 layer is continuous through the TEM cross section specimen, whilst in the latter case there are regions of Si above and below the buried oxide/SiO_2. This has not been investigated systematically.

For most of the dose range investigated a continuous SiO_2 layer is formed but for the lowest doses at each energy the SiO_2 layer is either discontinuous or consists of oxide precipitates. The minimum implanted doses for which continuous SiO_2 layers are formed after annealing ($^{A}\Phi_c$) at energies of 70keV, 90keV and 200keV are shown in Table 4.2. The values of $^{A}\Phi_c$ are different for the different energies and therefore the formation of a continuous SiO_2 layer after annealing is not simply a case of implanting a minimum dose. The latter may have been expected if the formation of a continuous SiO_2 layer was simply due to the segregation of all the implanted oxygen towards the depth of the peak of the as-implanted oxygen distribution ($\hat{R}_p$). The values of $^{A}\Phi_c$ are smaller than the critical dose to form a continuous layer after implantation ($^{I}\Phi_c$) for all energies (table 4.2) and hence the formation of a continuous SiO_2 layer after implantation is not a prerequisite for the formation of a continuous SiO_2 layer after annealing.

Energy (keV)	$^{A}\Phi_c$ ($x10^{18}O^+/cm^2$)	$^{M}T_{SiO_2}$ (nm)	$^{I}\Phi_c$ ($x10^{18}O^+/cm^2$)	$^{A}\Phi_c$ (model) ($x10^{18}O^+/cm^2$)
70	0.33	70	0.7	0.22
90	0.35	75	$0.7<\Phi<0.9$	0.28
200	0.56	110	1.2	0.56

Table 4.2 Values of the minimum dose to form a continuous oxide layer after annealing ($^{A}\Phi_c$) and the minimum thickness of a continuous oxide layer ($^{M}T_{SiO_2}$) after annealing, i.e. the thicknesses for dose $^{A}\Phi_c$. The values of $^{A}\Phi_c$ at each energy are the same for both the nitrogen and the argon + ½ % oxygen anneal ambients. Values of the minimum dose to form a continuous oxide layer after implantation ($^{I}\Phi_c$) and values of $^{A}\Phi_c$ from the model of Li *et al*[44] are shown for comparison.

Energy (keV)	$^{A}\Phi_{dc}$ (O^+/cm^2)	SIMS signal at peak Φ_{dc}	oxygen conc. at peak ($/cm^3$)	$^{A}\Phi_c$ (O^+/cm^2)	SIMS signal at peak $^{A}\Phi_s$	oxygen conc. at peak ($/cm^3$)
70	$0.3x10^{18}$	1.5	$1.8x10^{22}$	$0.33x10^{18}$	1.6	$2.2x10^{22}$
90	$0.29x10^{18}$	1.5	$1.8x10^{22}$	*$0.35x10^{18}$	-	-
200	$0.5x10^{18}$	1.5	$1.8x10^{22}$	$0.56x10^{18}$	1.6	$2.2x10^{22}$

Table 4.3 The maximum doses for which a discontinuous oxide layer is present after annealing ($^{A}\Phi_{dc}$), the minimum doses for continuous oxide layers present after annealing ($^{A}\Phi_c$) and the SIMS signal and oxygen concentration at the peak of the as-implanted oxygen distribution for these doses. *This sample was annealed in argon + ½ % oxygen and therefore the as-implanted oxygen distribution was not examined by SIMS. A sample (H122) implanted with a dose of $0.4x10^{18}O^+/cm^2$ has a continuous oxide layer after annealing and the SIMS signal at the peak of the as-implanted distribution was 1.7, corresponding to an oxygen concentration of $2.8x10^{22}$.

The SIMS signal at the depth of $\hat{R}_p$, taken from as-implanted SIMS profiles (figs. 3.31 & ref 1), for experimentally observed doses of ${}^{A}\Phi_c$ is 1.6 for energies of 70keV and 200keV, and 1.7 for an energy of 90keV (table 4.3). For the energy of 90keV a sample (H100) implanted with a dose (Φ) of $0.35x10^{18}O/cm^2$ has a continuous layer after annealing, but because this sample was annealed in the Ar + ½ % O_2 furnace SIMS measurements could not be carried out on the as-implanted material. As this dose is lower than that for the sample with a SIMS signal of 1.7 at $\hat{R}_p$ it is considered that the value of the SIMS signal at $\hat{R}_p$ for this sample would be <1.7. Hence at each energy the value of the SIMS signal at $\hat{R}_p$ for the minimum implanted dose that results in a continuous buried SiO_2 layer after annealing is $\approx$1.6, corresponding to an oxygen concentration of $2.2x10^{22}/cm^3$ (table 3.8). This suggests that a critical as-implanted minimum oxygen concentration at $\hat{R}_p$ is an important criterion in forming a continuous buried SiO_2 layer after annealing. The SIMS signal at $\hat{R}_p$ for the closest implanted dose $<{}^{A}\Phi_c$ for which the SiO_2 layer was discontinuous (Φ_{dc}) is 1.5 for all the energies (table 4.3), corresponding to an oxygen concentration of $1.8x10^{22}/cm^3$ (table 3.8). Hence the minimum dose that could result in a continuous SiO_2 layer after implantation and annealing (as opposed to the minimum dose that was observed experimentally to result in a continuous SiO_2 layer) would lie between the values of ${}^{A}\Phi_{dc}$ (table 4.3) and ${}^{A}\Phi_c$ (table 4.2) and therefore the as-implanted minimum oxygen concentration at $\hat{R}_p$ that results in a continuous SiO_2 layer after annealing, for these energies, is between $1.8x10^{22}/cm^3$ and $2.2x10^{22}/cm^3$.

The results in chapter 3 of this work show a close correlation between the oxygen concentration and the as-implanted oxide precipitate morphology. After implantation of doses equal to ${}^{A}\Phi_c$ (table 4.2) at 70keV and 200keV (50keV and 90keV were not examined) the microstructure at $\hat{R}_p$ consists of [001] columnar precipitates. This precipitate morphology was also observed, at different depths, for oxygen concentrations down to $1.3x10^{22}/cm^3$. The as-implanted microstructure of samples with an oxygen concentration of $1.3x10^{22}/cm^3$ at $\hat{R}_p$ were not examined by TEM, but the results of chapter 3 suggest that the microstructure would also be [001] columnar precipitates. Therefore, although the microstructure of the precipitates after implantation may be playing a role, it is not primarily determining whether or not the SiO_2 layer will be continuous after annealing.

It is expected that during annealing the buried SiO_2 layer grows by an Ostwald ripening process[2,3], i.e. the larger of the [001] columnar precipitates grow at the expense of the smaller ones, until the growing precipitates coalesce forming a continuous layer parallel to the wafer surface. Such a process also enables the redistribution of the implanted oxygen towards the buried layer. Hence if at depth $\hat{R}_p$, in one area, the equivalent radius of the [001] columnar precipitates is smaller than the critical radius for the precipitate to be stable[4,5], while in the surrounding areas the equivalent radius of the [001] columnar precipitates is larger than the critical radius for the precipitates to be stable, then the smaller precipitates would dissolve. This could lead to the formation of a pinhole through the oxide at that point at the end of the annealing. Although the formation of a pinhole, width typically <150nm (fig. 4.6b), is a localised structure compared to the area over which the SIMS measures the average oxygen concentration (chapter 2), a minimum average oxygen concentration may ensure that across the whole of the implanted area the equivalent radius of the [001] columnar precipitates is large enough for all the precipitates at depth $\hat{R}_p$ to be stable.

Due to the increasing straggle with increasing energy (table 2.3), a larger dose has to be implanted with increasing energy in order to reach the same as-implanted oxygen concentration at the peak of the oxygen distribution. This explains why the dose ${}^{A}\Phi_c$ increases with increasing energy. A consequence of the value of ${}^{A}\Phi_c$ increases with increasing energy and all the implanted oxygen segregateing to the SiO_2 layer during annealing is that the width of the thinnest continuous SiO_2 layers after annealing, i.e. the width of the SiO_2 layers for doses of ${}^{A}\Phi_c$, also increases with increasing energy. For the 200keV implants the minimum thickness is 110nm, compared to $\approx$70nm for the 70keV and $\approx$75nm for the 90keV implants (table 4.2).

For doses $\geq {}^{A}\Phi_c$ the thicknesses of the SiO_2 layer after annealing increases with increasing dose (figs. 4.1 to 4.7). The relationship between the thickness of the SiO_2 layer and the dose is linear and within experimental error the thickness is proportional to the dose (fig. 4.8). The same linear relationship holds independent of the energy (50keV, 70keV, 90keV or

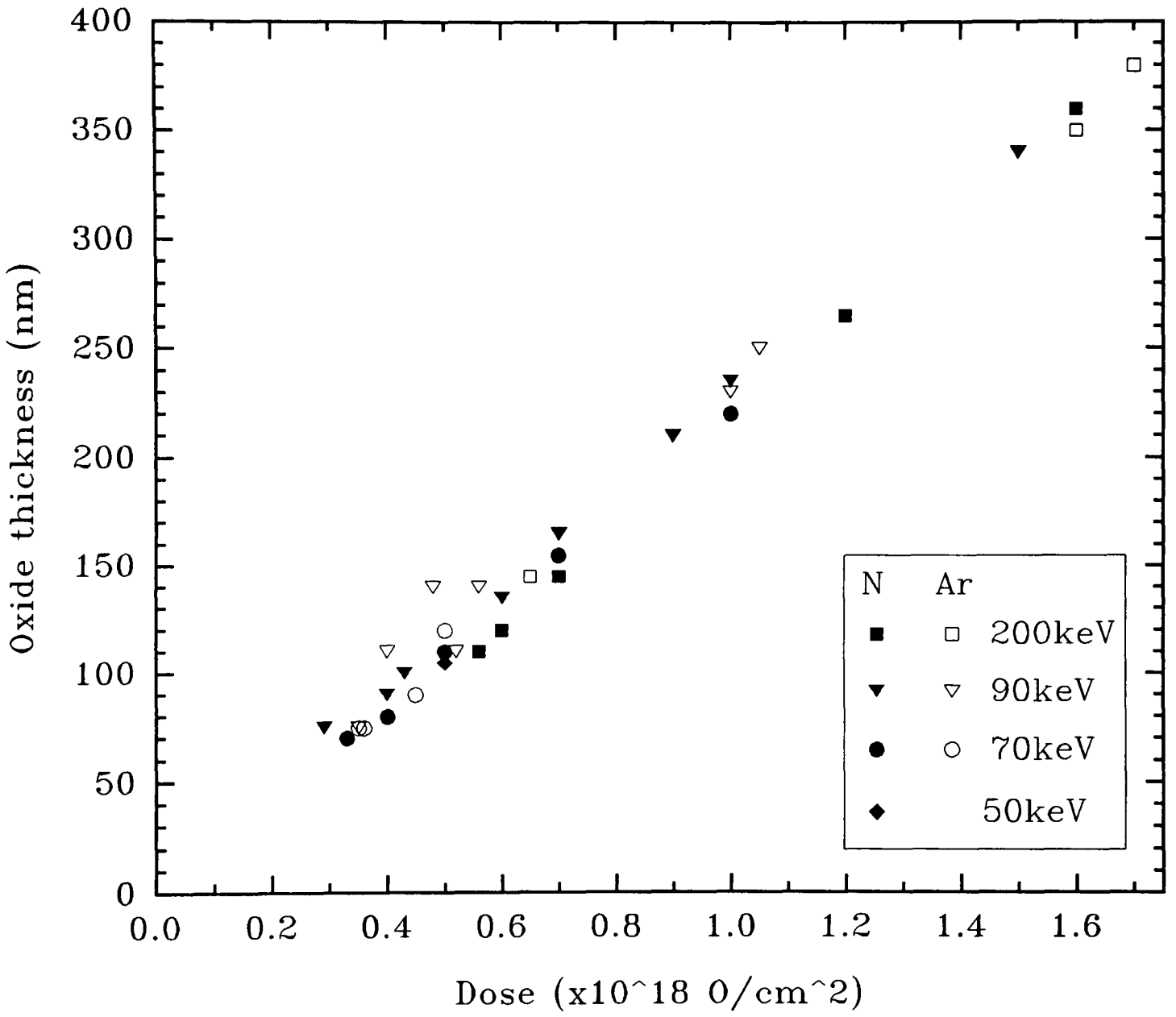

Figure 4.8 Buried oxide layer thickness as a function of dose, energy and anneal ambient (T_i = 680°C or 700°C, I' = 5.6μA/cm^2, 3.75μA/cm^2 and 3.1μA/cm^2 at 200keV, 90keV and 70keV respectively, N = annealed at 1320°C or 1360°C for 6hrs in nitrogen, Ar = annealed at 1300°C for 6hrs in argon + ½ % oxygen).

200keV) or the annealing ambient (N_2 or Ar + ½ % O_2) (fig. 4.8). After implanting doses equal to or just $>{}^{A}\Phi_c$ at 200keV (i.e. just $\geq 0.56 \times 10^{18} O/cm^2$) the structures have a thin ($\geq 110nm$) continuous buried SiO_2 layer below a standard thickness ($\approx 400nm$) surface Si layer (figs. 4.6c,g & 4.7a) which are suitable for the subsequent fabrication of radiation hard circuits with reduced circuit self-heating.

Although for doses $\geq {}^{A}\Phi_c$ the SiO_2 layer is continuous, Si islands are present in the SiO_2 for all doses $\geq {}^{A}\Phi_c$. For doses of ${}^{A}\Phi_c$ and just $>{}^{A}\Phi_c$ the density of Si islands is low (table 4.1) and the islands are present in the centre of the buried SiO_2 layer (figs. 4.2 to 4.7). At these low doses the larger islands span approximately 75% of the SiO_2 layer width (figs. 4.2b, 4.3b & 4.5a). With increasing dose the islands decrease in size and increase in density (figs. 4.4 & 4.6). The islands are larger and at a higher density close to the interface with the substrate (figs. 4.1b & 4.3d). With further increases in dose the density decreases and the islands are present only close to the buried SiO_2 layer substrate interface (figs. 4.1c, 4.4i & 4.7c). A general increase of SiO_2 thickness with increasing dose has also been reported by ourselves earlier for 70keV using different annealing conditions[6], and for 180keV[7,8] and 200keV[9] implants, under different implantation and anneal conditions. Twins or dislocations are sometimes observed in the Si islands.

At each energy the dose ${}^{A}\Phi_c$ is smaller than the dose ${}^{I}\Phi_c$ (table 4.2) and therefore for the samples implanted with doses between ${}^{A}\Phi_c$ and ${}^{I}\Phi_c$ a continuous SiO_2 layer is not present after implantation (chapter 3). Dark field TEM images using g(220) two beam diffraction condition showed that after implantation the microstructure at the depth of $\hat{R}_p$ consists of [001] columnar oxide precipitates in a matrix of Si. Hence the Si at this depth is at the same crystallographic orientation as the substrate. No evidence was observed for Si isolated from either the substrate or the surface Si layer. The columnar precipitates are small, only a few nm across, and therefore it is considered unlikely that they contain any isolated Si that can not be resolved by the TEM. Therefore in this dose range the islands must originate from Si isolated from the substrate and surface Si layer during annealing. The diffusivity of Si in SiO_2 is very low[10], even at the anneal temperature of 1320°C ($3.5 \times 10^{-17}/cm^2$), and is eight orders of magnitude lower than the diffusivity of oxygen in SiO_2 at this temperature ($1.6 \times 10^{-9}/cm^2$ [11]). Hence the coalescence of

SiO_2 precipitates during annealing could isolate regions of unoxidised Si. Samples implanted with doses $>{}^{I}\Phi_c$ have a continuous SiO_2 layer present after implantation (chapter 3) and the islands in this dose range originate from Si isolated from the substrate and surface Si layer by the synthesis of the SiO_2 layer during implantation (fig. 3.12). When these small volumes of Si become surrounded by SiO_2, during either annealing or implantation, any subsequent oxidation will eject the Si_i required to provide the accommodation volume into either the remaining island or into the surrounding SiO_2. As the diffusivity of Si in SiO_2 is very low[10] the rate of injection of Si_i into the surrounding SiO_2 will be low. As the volume of the islands is small, injection into the remaining island will quickly lead to an increase in the Si_i concentration which is known to decrease the rate of oxidation[12]. Both of these processes will slow down the oxidation rate of the islands and explains why the Si islands are still present even after the anneals at 1300°C or 1360°C for 6hrs.

During annealing the Si islands develop (001) and {111} facets (figs 4.1 to 4.7). In p.v. the shape of the Si islands is either irregular (e.g. figs. 4.3c,d,g,h) or they have edges parallel to the <110> and <100> directions in the (001) plane (e.g. figs. 4.2f & 4.4m). Both irregular and regular islands can exist in the same sample (figs. 4.1e & 4.5f). For doses $\geq {}^{I}\Phi_c$ the large (001) facets parallel to the wafer surface probably originate because the isolated Si ribbon-like structure within the buried oxide after implantation that the islands form from, lie approximately parallel to the wafer surface (fig. 3.12). It has also been suggested[13] that the formation of the facets is a result of the crystallographic orientation dependence of the oxidation rate of Si. In this case the development of the {100} facets is due to the slower oxidation rate in this direction. For doses between ${}^{A}\Phi_c$ and ${}^{I}\Phi_c$ this is probably the dominating mechanism. The {111} planes of Si have the lowest surface energy[14] and therefore their presence is probably the result of the minimisation of the interface energy. A minority of islands have small {110} facets present at the apex of the {111} facets. Of the low index planes the {110} planes have a low oxidation rate, between that of the {100} and {111} planes[13], which might explain their presence, but have a higher surface energy than that of the {111} planes[14] and therefore they may only be present because the anneal temperature was not high enough or the anneal time not long enough for the lower energy {111} facets to completely develop.

The large Si islands (size $\geq$50% of the width of the buried SiO_2) are only observed for doses between $^{A}\Phi_c$ and $<^{I}\Phi_c$ (figs. 4.2b,c, 4.3b,c, 4.4c,d, 4.5a, 4.5b,c 4.6h & 4.7b). Hence as well as being determined by the dose the size of the islands may also be depend on whether the Si forming the island was isolated during implantation or annealing. In the c.s. micrographs contrast is present within the large islands resulting from variations in the island thickness (figs. 4.3d & 4.4c). Some of the Si islands are at the same orientation as the substrate but the majority are at a slightly different orientation. This mis-orientation with respect to the substrate and the surface Si layer shows up as moiré fringes in the Si islands in the p.v. micrographs (e.g. figs. 4.2f, 4.3h & 4.5f). In c.s. where two Si islands overlap, moiré fringes are also visible (fig. 4.3c). At the anneal temperature the SiO_2 is viscous[15] and the difference in the orientation of the Si islands and the substrate is due to the viscous flow of the SiO_2 during annealing. The driving mechanism for the flow of the viscous SiO_2 is most probably the relief of internal stresses. Hence the observation of Si islands at orientations different from that of the substrate suggests the presence of internal stresses. For doses $>^{I}\Phi_c$ the islands close to the interface with the substrate originate from the ribbon-like structure at the lower edge of the SiO_2 layer which is still connected to the substrate after implantation (fig. 3.12). The observation that these islands tend to be at the same orientation as the substrate suggests either the stress in the SiO_2 is lower at this depth in the oxide, or the Si island formed, i.e. became disconnected from the substrate, at a later point during the anneal when any stress within the SiO_2 has already been relieved.

After annealing, Si protrusions into the SiO_2 layer are present at the Si interfaces in some samples (figs. 4.4c & 4.6h). The protrusions are present for doses $>^{A}\Phi_c$ and $<<^{I}\Phi_c$. Some of the Si protrusions have the appearance of "hillocks" on the interfaces (fig. 4.5b), while others have developed facets (fig. 4.4c). In p.v., in the samples containing the faceted protrusions, well developed square or rectangular structures are present (figs. 4.2f & 4.4f). Associated with some of these regular structures is irregular structure which is similar in shape to protrusions seen in c.s. (fig. 4.2f). The dimensions of these regular structures is also similar to the width of the faceted protrusions present in c.s. and hence these regular structures are thought to be the faceted protrusions in p.v.. The regular shape contrast probably originates from where the protrusions join either the surface Si layer or the Si substrate. Some of the protrusions connect

both irregular (fig. 4.6i) and faceted (fig. 4.7b) Si islands to either the surface Si layer or the substrate and in one sample ($0.7x10^{18}O/cm^2$, 200keV) a minority of the Si islands are connected by two protrusions to both the surface Si layer and the substrate (fig. 4.6h). In this sample the two protrusions are not observed one above the other, but are laterally offset and hence the structure is slightly different from the Si pinholes to be discussed later in this chapter. The formation mechanism of the protrusions though is probably similar to that of the Si pinholes except in the case of the protrusions the Si path does not go all the way through the SiO_2 layer. Broader and shallower undulations in the interface of the surface Si layer and the SiO_2 layer are present in higher dose samples. For example these are thought to be the cause of the changes in the background contrast visible in the p.v. micrographs of the two samples implanted with doses of $1.6x10^{18}O/cm^2$ and $1.7x10^{18}O/cm^2$ at 200keV (figs. 4.7g & 4.7h).

The presence of the Si islands and protrusions may be undesirable if they are harmful to the electrical isolation achieved by the SiO_2 layer. For each energy the density of the Si islands and protrusions is lowest for doses of ${}^{A}\Phi_c$ and hence this dose represents the optimum dose at each energy for minimising any potential harmful effects on the electrical properties. The areal density of the islands alone though is not the best method for predicting the effect on the electrical properties, such as the breakdown voltage, as the breakdown voltage will also depend on the size of the islands and their distribution within the SiO_2 and, as previously described, these depend strongly on the dose (e.g. fig. 4.4). Similarly the density and length of the protrusions and whether they are connected to Si islands will play an important role in determining the electrical properties. The TEM results show that at each energy the density and length of the protrusions is minimal for doses of ${}^{A}\Phi_c$ but large Si islands are present within the SiO_2 layer. Electrical measurements need to be carried out to determine the influence of these large islands. The presence of Si islands though, even for doses of ${}^{A}\Phi_c$, suggests that further process optimisation is required.

For doses just $< {}^{A}\Phi_c$ the SiO_2 layer contains Si pin-holes connecting the surface Si layer to the substrate (figs. 4.6b & 4.6e). The pinholes have {111} facets and are thinnest approximately half way between the surface Si layer and the substrate (figs. 4.4a & 4.6a,b). In p.v. the pinholes are rectangular with edges parallel to the <110> directions (figs. 4.1d, 4.3d,

4.4e & 4.6d). Hence the shape of the pinholes is being determined by the minimisation of the Si surface energy. In some pinholes dislocations lying parallel to the wafer surface in <110> directions are present (figs. 4.1d, 4.4e & 4.6d). For lower doses the density of pinholes increases until the layer becomes a band of faceted SiO_2 precipitates (figs. 4.2a & 4.3a). The facets are not determined by the SiO_2 but the precipitates are effectively negative crystals within the Si[16] and the facets are determined by the surrounding Si, for the same reasons as described above for the Si islands in the SiO_2 layer. In these samples dislocations are present pinned between neighbouring SiO_2 precipitates (figs. 4.2d, 4.3a & 4.3e) and between the precipitates and the surface Si layer (figs. 4.2a, 4.2d & 4.2e). For the sample implanted with $0.1x10^{18}O/cm^2$ at 70keV (H36a) the structure of the buried oxide was different in different parts of the implanted area (fig. 4.9). Four different areas of the implanted area were examined by c.s and p.v. TEM and a further four areas examined by only c.s. TEM. A continuous SiO_2 layer is present in the TEM samples from two of the areas, a band of faceted oxide precipitates is present in TEM samples from four different areas and no evidence of oxide was found in the TEM samples from the two further areas. In one area where oxide precipitates are present, the precipitates are thicker than the thickness of the continuous oxide layer (fig. 4.9). This suggests that in the area of these precipitates the minimisation of surface energy may have resulted in the formation of oxide precipitates rather than a continuous oxide layer. The different structures were randomly distributed across the implanted area. This variation of structure across the implanted area is only observed in this low dose sample and it is considered that the presence of the variation in the structure is critically dependent on the dose, for doses close to the dose of this sample.

During annealing if the size of the SiO_2 precipitates is smaller than the critical radius for a stable precipitate[4,5] the buried SiO_2 precipitates will dissolve and the SiO_2 cap could act as an infinite SiO_2 precipitate, causing the implanted oxygen to segregate to the cap and be lost from the buried layer. If the precipitates that result from the implantation are close to this critical radius or there is lateral non-uniformity in the implanted dose this could lead to the variations in structure observed for the above sample (H36a). Any swelling of the cap for such a low dose is difficult to determine because the uniformity and precise thickness of the cap prior to annealing

Figure 4.9 Cross-section micrographs, at a <110> pole, of the sample implanted with ^{16}O at 70keV, $\Phi = 0.1x10^{18}O/cm^2$, $T_i = 680°C$, $I' = 3.1\mu A/cm^2$ and annealed at 1360°C for 6hrs in nitrogen, showing in different parts of the implanted area,

a) a continuous oxide layer,

b) a band of large oxide precipitates (O), where the width of the precipitates is larger than the width of the continuous oxide layer shown in a),

c) a band of smaller oxide precipitates (O) where the width of the precipitates is smaller or approximately equal to the width of the continuous oxide layer shown in a) (D = dislocations).

a)

b)

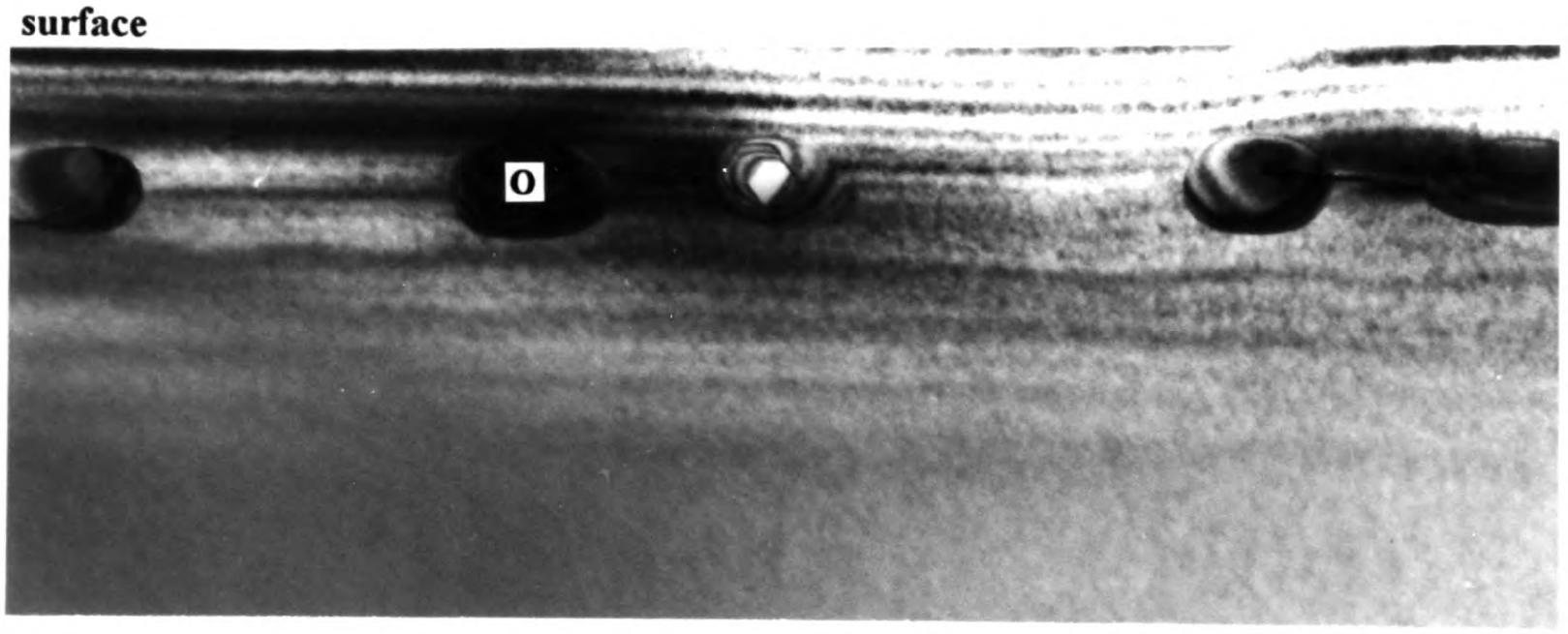

c)

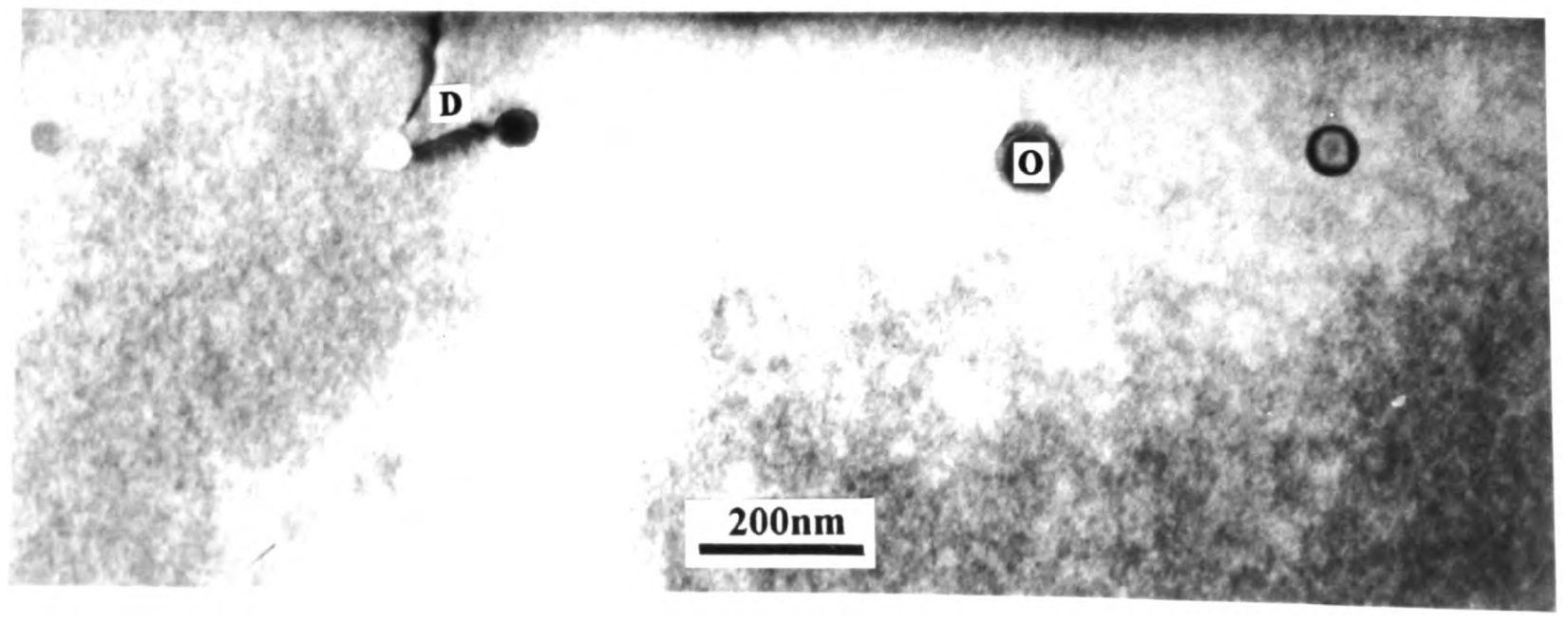

are not known, but SIMS measurements (not shown) on a sample implanted with ^{18}O at a nominal $\Phi = 0.1x10^{18}O/cm^2$ (H151) under the same conditions, and annealed with a ^{16}O cap under the same conditions, show that after annealing that 95% of the implanted ^{18}O is present in the ^{16}O cap[17]. No oxide layer or precipitates were observed by TEM in this sample. TEM analysis confirmed that the ^{18}O was present prior to annealing and the as-implanted microstructure was similar to the as-implanted structure of the sample implanted with ^{16}O (H36a). The absence of any oxide precipitates in sample H151 ($\Phi = 0.1x10^{18}O/cm^2,^{18}O$) suggests that a larger fraction of the implanted oxygen has segregated to the cap. This could be explained if this sample was actually implanted with a lower dose than sample H36a ($\Phi = 0.1x10^{18}O/cm^2,^{16}O$). The distance of the precipitates from the cap is expected to play a role in determining the loss of the implanted oxygen to the cap. The higher the energy the larger the distance between the precipitates and the cap and the more stable the precipitates are expected to be. This is thought to be the reason why in the work of Reeson *et al*[18] implanting the same dose ($0.1x10^{18}O/cm^2$) at 200keV resulted after annealing in a layer of oxide precipitates. For a sample implanted with ^{18}O at 90keV, $\Phi = 0.43x10^{18}O/cm^2$ (H143) and annealed with a ^{16}O cap under nominally the same conditions, there was exchange between the implanted ^{18}O and the ^{16}O in the cap but there was no net transport of oxygen to the cap[17,31]. Hence it is considered that for doses $\geq {}^{A}\Phi_c$ there is no net transport of oxygen to the cap and hence this process does not effect the thickness of the buried oxide layers for the samples shown in Fig. 4.8.

4.2.3 Surface silicon layer

For any particular implant energy, with increasing dose, as the thickness of the buried SiO_2 layer increases, the thickness of the surface Si layer decreases (figs. 4.1 to 4.7 & table 4.1). For the same implanted dose because of the increasing mean projected range of the oxygen ions with increasing energy (table 2.3) the thickness of the surface Si layer increases with increasing energy. These two trends are shown graphically in Fig. 4.10. The structures formed after implanting doses of $\geq 0.35x10^{18}O/cm^2$ and $\geq 0.33x10^{18}O/cm^2$ at 90keV and 70keV, respectively, have a surface Si layer of thicknesses $\leq 160nm$ above a continuous buried SiO_2

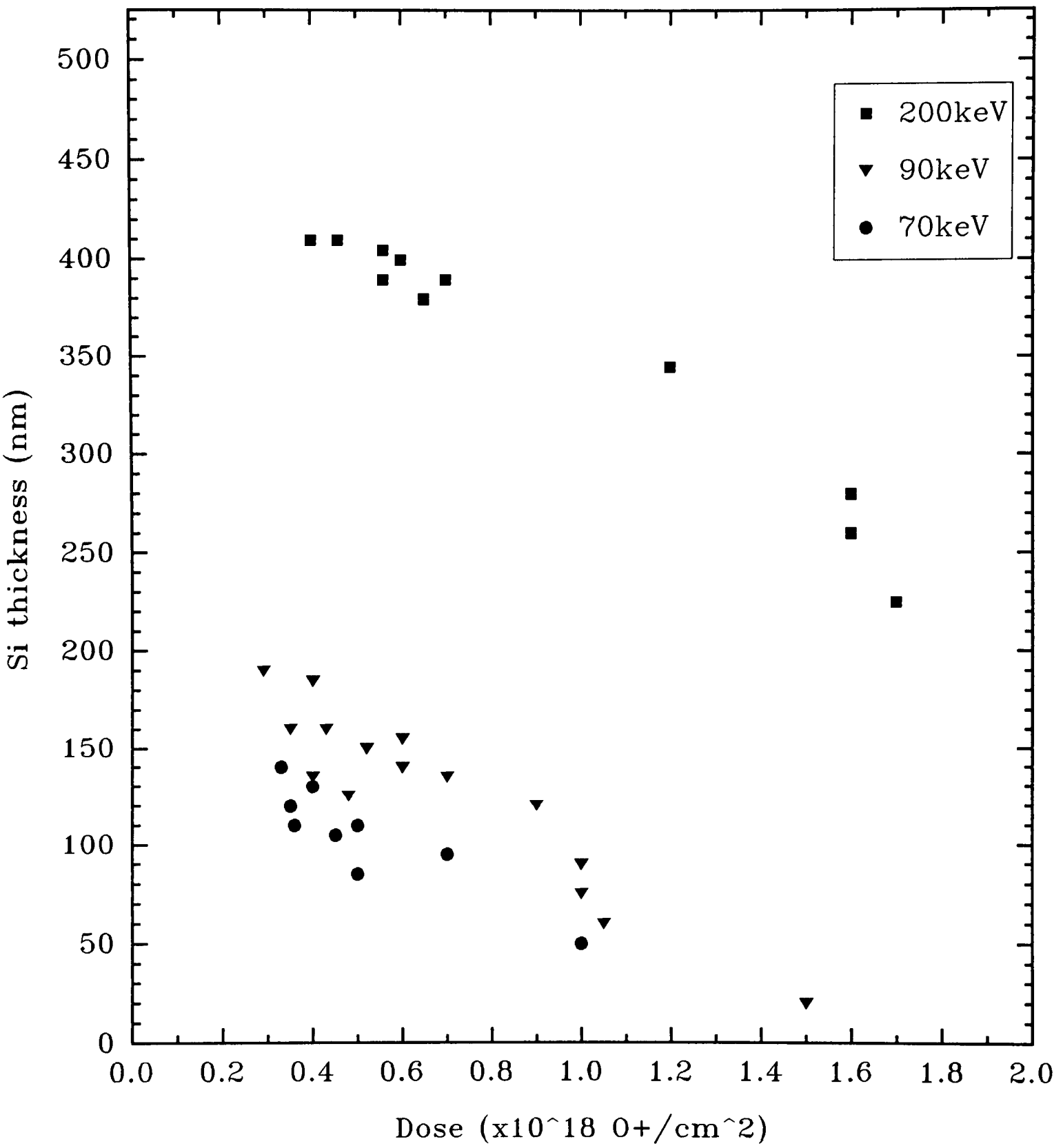

Figure 4.10 Surface silicon layer thickness as a function of the dose and energy (T_i = 680°C or 700°C, I' = 5.6μA/cm^2, 3.75μA/cm^2 and 3.1μA/cm^2 at 200keV, 90keV and 70keV respectively, annealed at 1320°C or 1360°C for 6hrs in nitrogen or at 1300°C for 6hrs in argon + ½ % oxygen).

layer (figs. 4.2b,c, 4.3b-d 4.4b-d,h-j & 4.5a-d) which is suitable for the subsequent fabrication of "fully depleted" high performance CMOS devices.

When the surface Si layer becomes very thin, holes filled with oxide occur in the surface Si layer and these connect the buried SiO_2 layer and the oxide anneal cap. For example after implanting a dose of $1.5x10^{18}O/cm^2$ at 90keV the surface Si layer is only 20nm thick but holes through the surface Si layer are present (fig. 4.11a). At the edge of these holes the Si is faceted and slightly thicker than the rest of the surface Si layer (fig. 4.11a). In the oxide at the centre of all the holes that were observed a small piece of Si appears to be present (fig. 4.11a). Some of the Si that made up the surface Si layer where the oxide filled hole now exists is absorbed in the formation of the oxide in the hole and the thickening of the Si around the holes suggests that the excess Si_i may have redistributed to the Si at the edge of the holes. By dipping the sample in buffered HF the anneal cap is completely removed and through each hole the buried oxide layer is locally etched. In p.v. the shape of the region of buried oxide etched away is a circle centred on the hole (fig 4.11b). The size of the circle depends on the thickness of the buried oxide, the size of the hole and the etch time. Hence in p.v. after the HF dip, one circle is present for every hole (fig. 4.11b). This enables the number of holes to be easily counted at low magnifications and using this approach the hole density was determined to be $2x10^7/cm^2$. Fig. 4.11b also illustrates one difficulty with this technique in that when the pits are close together the regions of buried oxide removed by the HF dip overlap. Where this is the case though the regular, circular shape of the regions of buried oxide removed by the HF usually enable the number of regions and hence the number of pits to be determined. It should also be noted that for this sample, once the buried oxide had been etched away the thin surface Si layer above the etched region of oxide was in most cases too weak to support itself and broke off, between the etching and viewing in the microscope. Hence in the p.v. shown in Fig. 4.11b, where the back of the sample to the buried oxide layer has been thinned away, no structure is present within the circles.

The holes may have been caused by a non-uniform distribution in the as-implanted oxygen or by a non-uniform redistribution of Si and oxygen during annealing. In the c.s. TEM specimen of the unetched sample the anneal cap above the holes is intact. Therefore the holes

Figure 4.11,

a) a cross-section micrograph, at a <110> pole, of the sample implanted at 90keV, Φ = $1.5x10^{18}O/cm^2$, T_i = 680°C, I' = $3.75\mu A/cm^2$ and annealed at 1360°C for 6hrs in nitrogen, showing a hole in the surface Si layer filled with SiO_2, at the centre of which a piece of silicon is present,

b) a plan-view micrograph, at the [001] pole, after the same sample had been dipped in buffered HF. The HF dissolves the anneal cap and, because the hole in the surface Si layer was filled with SiO_2, the HF etches away some of the buried SiO_2 layer. The shape in plan-view of the region of SiO_2 etched away is approximately a circle. Hence each circle in b) represents one etch pit, which corresponds to one initial hole in the surface silicon layer.

a)

SiO_2 (anneal cap)

Si

surface

Si

SiO_2 (buried oxide)

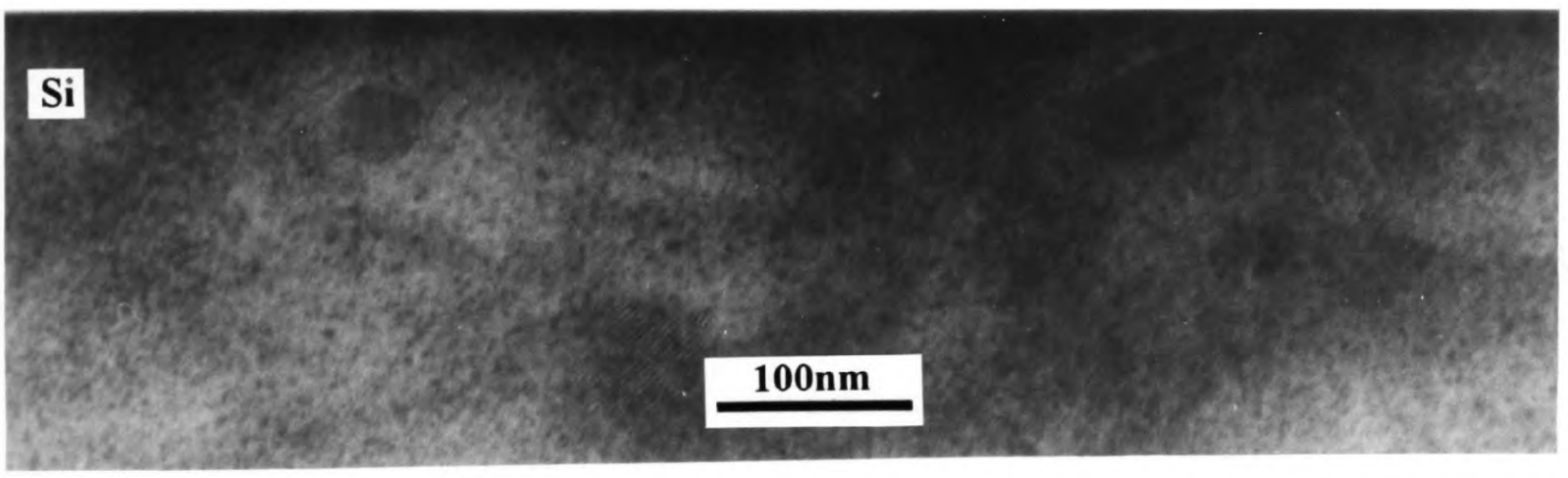

b)

<110>

[001] ⊙→<110>

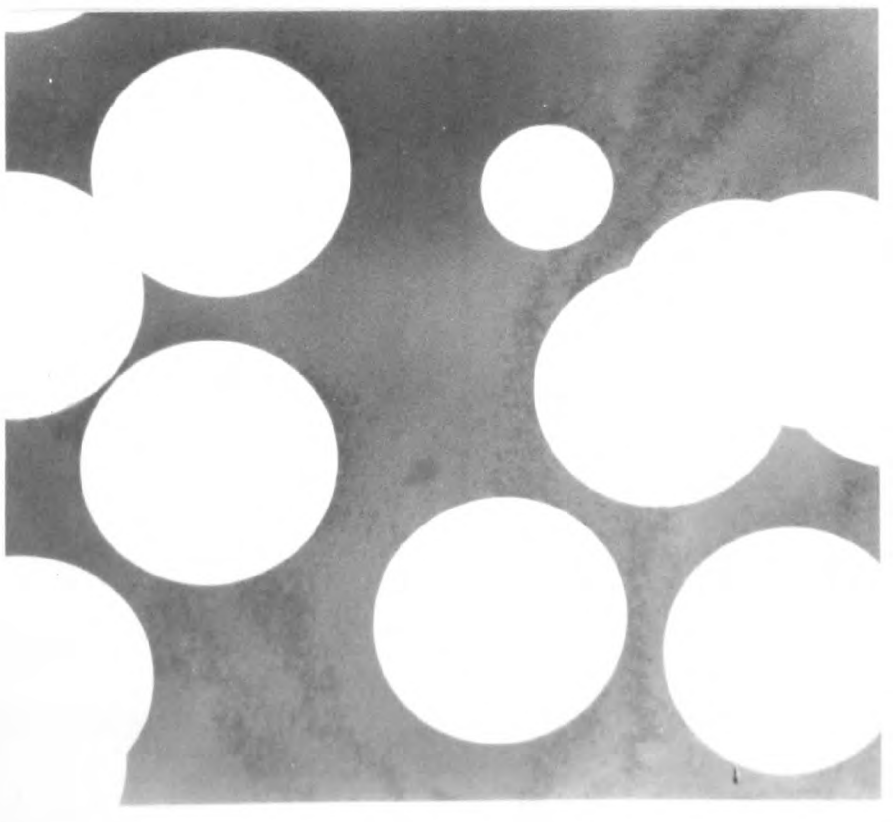

5μm

can not arise because the SiO_2 anneal cap has broken down into silicon monoxide (SiO) during annealing, which then evaporates exposing the Si surface which is then etched. For thin films the surface energy can play an important role in determining the stability of the film and the minimisation of the Si surface energy may be contributing to the formation of these holes. The presence of facets at the edge of the holes suggests that the minimisation of the interface energy has played a role in determining the structure of the holes, even if it did not play a role in the creation of the holes.

In the surface Si layer the main defects present are dislocations, threading between the surface and the interface with the buried SiO_2 layer. The areal densities of these threading dislocations are shown in Table 4.1 and graphically as a function of dose and energy in Fig. 4.12. For all energies at low doses either no or only a low density of dislocations are present. With increasing dose the threading dislocation density increases for all energies (fig. 4.12). This trend is observed for both anneal ambients and has also been reported elsewhere for high energy implants using different implantation and anneal conditions[8,18,19]. At each energy a dose window exists in which a low threading dislocation density is present above a continuous buried oxide layer (table 4.1). At each energy this dose window exists for doses close to $^{A}\Phi c$. Implanting the same dose at lower energies, i.e. at 70keV or 90keV as opposed to 200keV, results in a threading dislocation density more than an order of magnitude higher (fig. 4.12). At first this may seem to work against the idea of directly fabricating thin-film SIMOX structures by implanting at low energies but, as discussed above, the optimum dose window exists for doses close to $^{A}\Phi c$ which decreases with decreasing energy (section 4.2.2). The net result, suggested by the results in Table 4.1, is that the same low threading dislocation density can be achieved for any energy by implanting a dose close to $^{A}\Phi c$ for that energy.

The majority of the threading dislocations are single, straight dislocations randomly distributed across the implanted area (e.g. figs. 4.7c & 4.7h). Some dislocations have a "dog-leg" geometry (fig. 4.7f), are present in pairs (figs. 4.4g & 4.7f) or are present in small dislocation networks usually consisting of only one (figs. 4.4d & 4.6i) or two dislocation nodes (fig. 4.7f). The projected line direction in the (001) plane, i.e. in p.v., of many dislocations are <110> directions, although these are not the only projected line directions (figs. 4.7h).

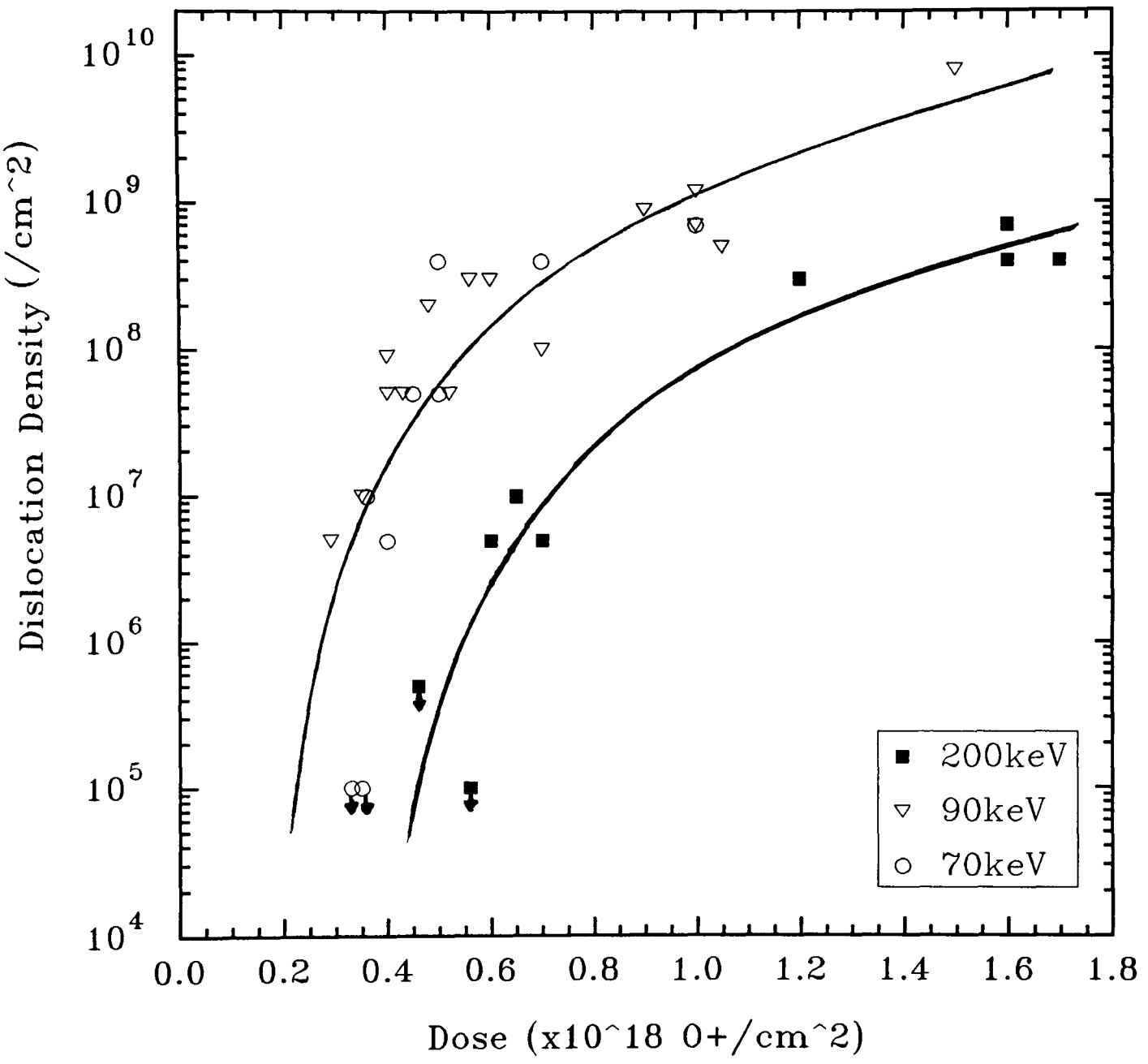

Figure 4.12 Threading dislocation density in the surface Si layer as a function of dose and energy. Points with arrows indicate the highest density limit for samples in which no dislocations were observed. The two lines are drawn through either the points from the 200keV implants or the points from both the 90keV and 70keV implants (T_i = 680°C or 700°C, I' = 5.6μA/cm^2, 3.75μA/cm^2 and 3.1μA/cm^2 at 200keV, 90keV and 70keV respectively, annealed at 1320°C or 1360°C for 6hrs in nitrogen or at 1300°C for 6hrs in argon + ½ % oxygen).

Comparison of the as-implanted microstructure (figs. 3.1, 3.3 to 3.5, 3.14, 3.17 & 3.18) and the threading dislocation densities after annealing (table 4.1 & fig. 4.12) shows that for the 50keV, 70keV and 90keV implants the annealed samples with the lowest dislocation densities have no crystallographic defects, or associated strain contrast, at the wafer surface of the as-implanted samples (fig. 4.13). For the 200keV implants the samples with the lowest dislocation densities have either no crystallographic defects at the wafer surface (fig. 4.13) or the defects are present only in small regions of the wafer surface (figs. 3.3 to 3.5). Further for the 200keV implants, both the thickness of the defects at the wafer surface in the as-implanted samples (fig. 3.1) and the threading dislocation density after annealing increase with dose (fig. 4.12 & table 4.1). These points suggest that the defects at the wafer surface after implantation and the threading dislocation density after annealing are related. The defects at the wafer surface could act as a source of dislocation loops which once nucleated grow during annealing by acting as sinks for Si_i. The loops could grow down until they reach the buried oxide, at which point two threading dislocations would be formed. This mechanism could explain the straight threading dislocations most frequently observed (e.g. figs. 4.7c & 4.7h) and why some defects are present in pairs (figs. 4.4g & 4.7f). It is also in agreement with the suggestions of De Vireman *et al*[20], that the threading dislocations may grow down from the surface, and of Visitserngtrakul *et al*[21] that the defect density may be reduced after annealing if defects in the surface Si layer do not form during implantation. It should be pointed out that during annealing, because of the presence of the oxide cap, the surface is prevented from acting as a sink for Si_i.

During annealing the oxygen is considered to redistribute by an Ostwald ripening process[2,3], where the larger precipitates grow at the expense of the smaller ones until eventually the only precipitate left is the buried oxide layer (which acts as a two dimensional infinite size precipitate). The loops growing down from the surface could become pinned by the oxide precipitates during the Ostwald ripening process or new dislocation loops could nucleate on these precipitates. If a dislocation loop nucleates on a precipitate and the precipitate grows during annealing, the precipitate will eject Si_i enabling the loop to grow, but if the oxide precipitate starts to dissolve it will eject Si_v which could cause the loop to shrink. The experimental results indicate that threading dislocations are difficult to remove by annealing and

Figure 4.13 Cross-section micrographs at a <110> pole of samples implanted at,
a) & b) 70keV, $\Phi = 0.33 \times 10^{18} O/cm^2$, $T_i = 680°C$, $I' = 3.1 \mu A/cm^2$,
a) as-implanted (X = surface silicon layer, Y = buried damage/oxide layer),
b) annealed at 1320°C for 6hrs in nitrogen,
c) & d) 200keV, $\Phi = 0.56 \times 10^{18} O/cm^2$, $T_i = 680°C$, $I' = 5.6 \mu A/cm^2$,
c) as-implanted (X = surface silicon layer, Y = buried damage/oxide layer),
d) annealed at 1320°C for 6hrs in nitrogen,
showing, for both high and low energies, that the samples in which no threading dislocations are observed after annealing contained no defects at the wafer surface after implantation.

Figure 4.14 Cross-section micrographs, at a <110> pole, of the sample implanted with ^{16}O at 70keV, $\Phi = 0.1 \times 10^{18} O/cm^2$, $T_i = 680°C$, $I' = 3.1 \mu A/cm^2$, and annealed at 1320°C for 6hrs in nitrogen, showing two examples of the dislocations (D) pinned between neighbouring oxide precipitates (P) which suggest that for this specimen the dislocations originate at the depth of the oxide precipitates and grow towards the surface during annealing.

Figure 4.13

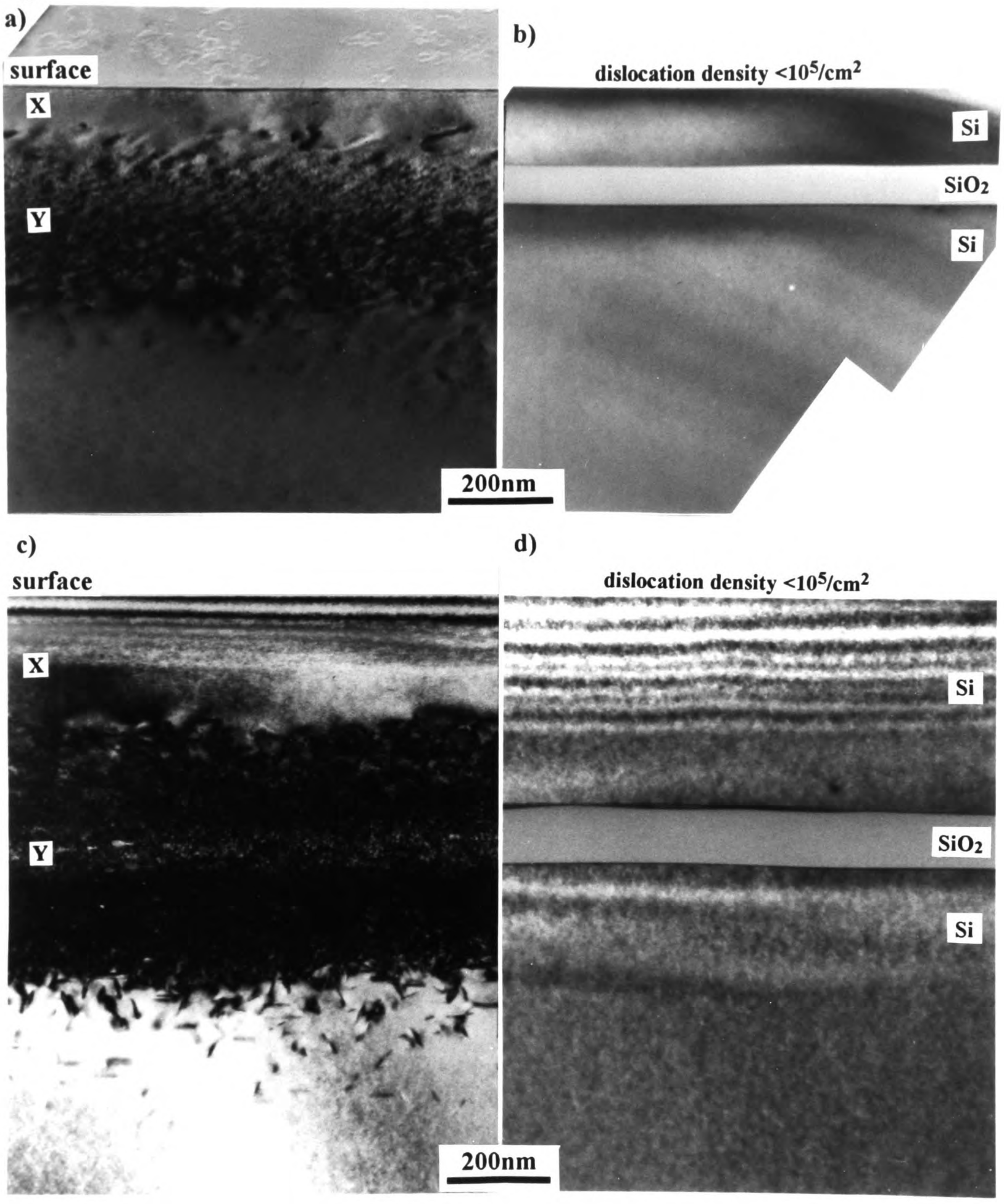

Figure 4.14

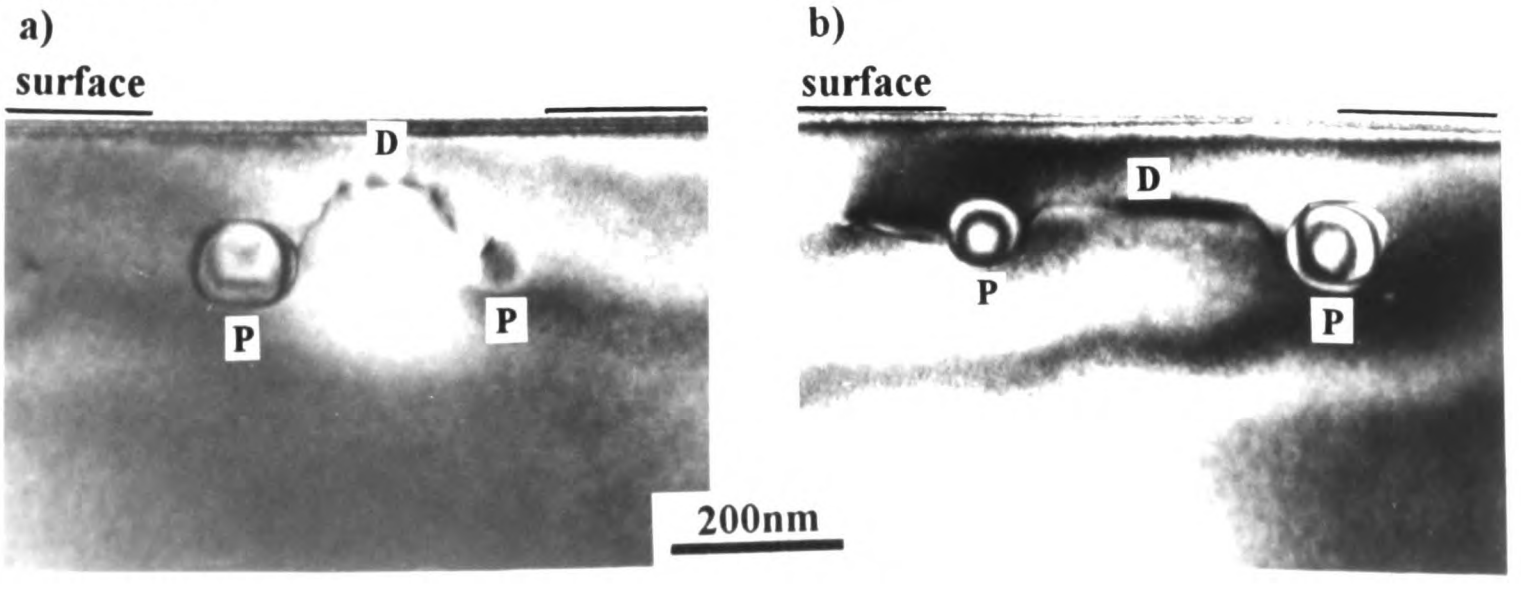

hence it is considered that once a dislocation loop reaches the buried oxide and surface, to form two threading dislocations, the dislocations are very stable. Hence for loops that nucleate on oxide precipitates what is important is whether they reach the buried oxide and surface, and become stable, before the precipitate starts to dissolve. The loops that reach the surface and interface before the precipitate starts to dissolve will then remain even after the precipitate has completely dissolved. This mechanism could explain the straight dislocations (e.g. figs. 4.7c & 4.7h), "dog-leg" dislocations (fig. 4.7f), pairs of dislocations (fig. 4.4g) and small dislocation networks (figs. 4.4d, 4.6i & 4.7f). For the "dog-leg" dislocations, the loop nucleates at a precipitate originally present at the point where the dislocation changes direction and for the small dislocation networks, one or more dislocation loops nucleate at precipitates originally present at each node of the final dislocation network. Alternatively if a loop growing down from the surface is pinned in one place by an oxide precipitate which subsequently dissolves, this could explain the "dog-leg" dislocations and if two loops growing down from the surface are pinned by the same oxide precipitate which subsequently dissolves, this could explain the small dislocation networks. For either model the observation that above a continuous buried oxide layer the small dislocation networks contain only one or two dislocation nodes suggests that only one or two precipitates are involved in the formation of each network. Hence these two mechanisms both can potentially explain the different dislocation geometries observed and during annealing both mechanisms could be taking place, but the experimental results discussed in the previous paragraph suggest that threading dislocations originating from defects at the wafer surface is the mechanism that occurs more often.

For either mechanism if the growth of dislocation loops in directions parallel to the wafer surface is significantly larger than the growth towards the surface and buried oxide layer, then when the loops do reach the surface and buried oxide layer the two threading dislocations formed would be a distance apart significantly greater than the thickness of the surface Si layer. If this distance was larger than the average distance between dislocations then even though the threading dislocations are formed in pairs the resulting distribution could give the impression of single randomly distributed dislocations.

Hence two criteria for the formation of a low dislocation density SIMOX structure are an as-implanted structure free from defects at the wafer surface and the absence of loops formed during the growth and dissolution of oxide precipitates during annealing. For the 200keV implants of Reeson *et al*[18], where no pre-heating, an implant temperature of 550°C and only beam heating was used during implantation, after implantation defects were present at the wafer surface and after annealing for all doses when the buried SiO_2 layer was continuous the threading dislocation density was high ($10^8/cm^2$ to $10^{10}/cm^2$). In this work, for low doses ($\leq 0.7x10^{18}O/cm^2$) at 200keV, defects are either not present or present only in small regions of the wafer surface after implantation (figs. 3.3 to 3.5), and a low threading dislocation density is present above a continuous SiO_2 layer after annealing (table 4.1). This suggests that the use of pre-heating and a higher implant temperature (680°C or 700°C) due to the use of lamp heating during implantation, in this work is playing an important role in reducing the defects at the wafer surface and hence reducing the threading dislocation densities after annealing. The higher implant temperature obviously increases the rate of annealing, leading to a reduction in the defect density and strain during implantation. The use of pre-heating increases the annealing of the damage generated by the ions at the start of implant, i.e. during the time it takes the beam-only heated wafer to reach the implant temperature. For beam-only heating, any defects nucleated as the wafer temperature rises to the implant temperature may be subsequently difficult to anneal out.

Threading dislocations could also be generated during annealing by stress (strain) present within the material. The rapid increase in the threading dislocation density with increasing dose, e.g. by three orders of magnitude between doses of $0.29x10^{18}O/cm^2$ and $1.0x10^{18}O/cm^2$ at 90keV (table 4.1), suggests that the increase in the dislocation density is only partially due to the increase in defects at the surface and that stress within the implanted region may be playing an important role. This increase in stress with increasing dose may be due to the blocking of the migration of Si_i to the surface because of the build up of oxide precipitates during implantation. The stress may increase further for doses $>{}^I\Phi_c$ because during implantation for dose increments $>{}^I\Phi_c$ the Si_i generated can no longer escape to the substrate which may lead to an increase in the rate of build up of the Si_i concentration in the surface Si layer with

increasing dose. Moreover because the oxidation preferentially takes place at the oxide/surface Si interface, the edge of the oxide layer grows more rapidly towards the surface, reducing the volume of the surface Si layer in which the Si_i are to be accommodated. An increase in stress in the surface Si layer would increase the likelihood of dislocations nucleating at precipitates and could provide the driving force for dislocations to move by a glide mechanism. An increase in the concentration of Si_i would increase the likelihood of dislocations moving by a climb mechanism. These two points may help explain why high threading dislocation densities are observed for high doses. Due to the decreasing straggle with decreasing energy, implanting the same dose at lower energies results in the same dose of oxygen in a smaller volume of Si. This would lead to a greater stress (strain) in the surface Si with decreasing energy and may explain why a higher threading dislocation density results from implanting the same dose at lower energies (fig. 4.12). Hence the minimisation of stresses during implantation is a further criterion for the formation of low dislocation density SIMOX structures. Higher implantation temperatures may help to reduce the build up of stress during implantation. Temperature homogeneity during implantation may also be important. Thermal stresses during annealing could also generate dislocations and because of the higher temperature, temperature homogeneity and controlled ramp rates are thought to be significantly more important during annealing than during implantation.

Contamination on the wafer surface could act as nucleation sites for the formation of defects during implantation. Then as the surface epitaxially grows during implantation defects are generated as the contamination is grown over. Even if the contamination does not nucleate defects during implantation, because the surface is growing epitaxially during implantation (section 3.10) the contamination could become incorporated within the surface Si layer and then during annealing act as nucleation sites for the formation of threading dislocations. The nodes of the small "X" shape dislocation networks observed in the sample implanted with a dose of $1.2x10^{18}O/cm^2$ at 200keV (fig. 4.6i), are at a depth of 120nm, which is very close to the calculated depth of the original surface, given by Eq. 3.27, of 114nm. This suggests that for this sample contamination on the original wafer surface may have played a role in the formation of the "X" shape threading dislocations networks. Hence clean wafer handling prior to implantation

and an implanter free from contamination are important for minimising the threading dislocation density. Even if the surface after implantation is free from defects, contamination on the surface during annealing could also act as nucleation sites for dislocations and hence clean capping and wafer handling facilities between implantation and capping are also important.

It is interesting that in the low dose sample (fig. 4.9), in which the structure of the SiO_2 layer varied in different parts of the implanted area (H36a), no threading dislocations are observed in the two TEM c.s. samples where a continuous SiO_2 layer is present, suggesting a threading dislocation density $<5x10^6/cm^2$, while in the TEM samples where the oxide layer consisted of precipitates, an average threading dislocation density of $10^8/cm^2$ is present. In this sample as the dose was low the internal stress after implantation is expected to be low and the TEM results in chapter 3 showed that the as-implanted material contained no defects at the wafer surface. This suggests that when the oxide layer consists of oxide precipitates after annealing the mechanism generating the threading dislocations may be different from that when the oxide layer is continuous after annealing. In sample H36a the geometry of some of the dislocations pinned between neighbouring oxide precipitates suggests that the dislocations are growing up towards the surface (fig. 4.14). Hence it is speculated that when the buried oxide layer consists of discrete oxide precipitates, the precipitates generate dislocations which then grow up to the surface. Conversely, the formation of the continuous oxide layer does not result in the formation of dislocations but, as the implanted dose increases and stress and defects at the wafer surface increase, the dislocations form at the wafer surface and grow down.

The formation of the threading dislocations is very complex. Several of the above mechanisms and possibly others probably occur. The effect of the threading dislocations on devices is not completely understood and although it is generally desirable to totally remove them, high performance CMOS transistors have been successfully fabricated in non-optimised thick-film SIMOX material containing a dislocation density as high as $10^8/cm^2$ [22]. The overall results show though that for each energy a dose window exists in which a surface Si layer containing a low threading dislocation density is present above a continuous buried SiO_2 layer (table 4.1). For all the energies used in this work this optimum dose window exists for doses close to ${}^A\Phi_c$.

4.3 Anneal Ambient

Fig. 4.15 shows the thickness of the surface Si layer (table 4.1) as a function of dose for the two anneal ambients and indicates that for each energy the samples annealed in Ar + ½ % O_2 show a consistently thinner, by on average 20nm, surface Si layer than similar samples annealed in N_2. This is thought to be due to oxidation of the Si surface layer through the anneal cap, which reduces the thickness of the surface Si layer, during annealing, due to the oxygen in the Ar + ½ % O_2 ambient. The values of the thickness of the surface Si layer for the samples annealed in Ar + ½ % O_2 show a greater scatter as a function of dose (fig. 4.15) than for similar samples annealed in N_2. This suggests that although the Ar + ½ % O_2 anneal conditions are nominally constant the thickness of the Si oxidised by the oxygen in the Ar + ½ % O_2 ambient may be varying slightly between anneals, suggesting that the anneal conditions affecting the oxidation of the surface Si layer through the cap are varying slightly between anneals. This may be due to practical difficulties in controlling the oxygen flow while running the particular furnace used at 1300°C for 6hrs, rather than a fundamental difficulty in annealing in an Ar + ½ % O_2 ambient. Under the present conditions where the thickness of the surface Si layer oxidised by the oxygen in the Ar + ½ % O_2 ambient is not controlled this is obviously undesirable. If the amount of Si lost could be controlled then this is not necessarily an undesirable effect. Figs. 4.8 & 4.17 show the thickness of the buried SiO_2 layer and the threading dislocation density, respectively, as a function of dose for the two anneal ambients and indicate that the ambient has no noticeable effect on either the thickness of the buried SiO_2 layer or the threading dislocation density. For low doses close to ${}^{A}\Phi_c$ and high doses $>>{}^{A}\Phi_c$ the ambient has no noticeable influence on the SiO_2/Si interfaces, but for doses just $>{}^{A}\Phi_c$ the structure of the SiO_2 layer/surface Si layer interface shows a dependence on the ambient. In this dose range for the N_2 ambient both of the SiO_2/Si interfaces have Si protrusions into the SiO_2, while for the Ar + ½ % O_2 ambient the SiO_2/surface Si layer interface has no protrusions and little waviness (fig. 4.16). Smoother interfaces after annealing in an Ar + ½ % O_2 ambient have also been reported elsewhere[23]. For bulk Si it has been reported that nitrogen diffuses rapidly[24] to SiO_2/Si interfaces where it chemically reacts and reduces the rate of oxidation[25]. It has also been reported that annealing SIMOX structures in a N_2 ambient leads to the accumulation of nitrogen

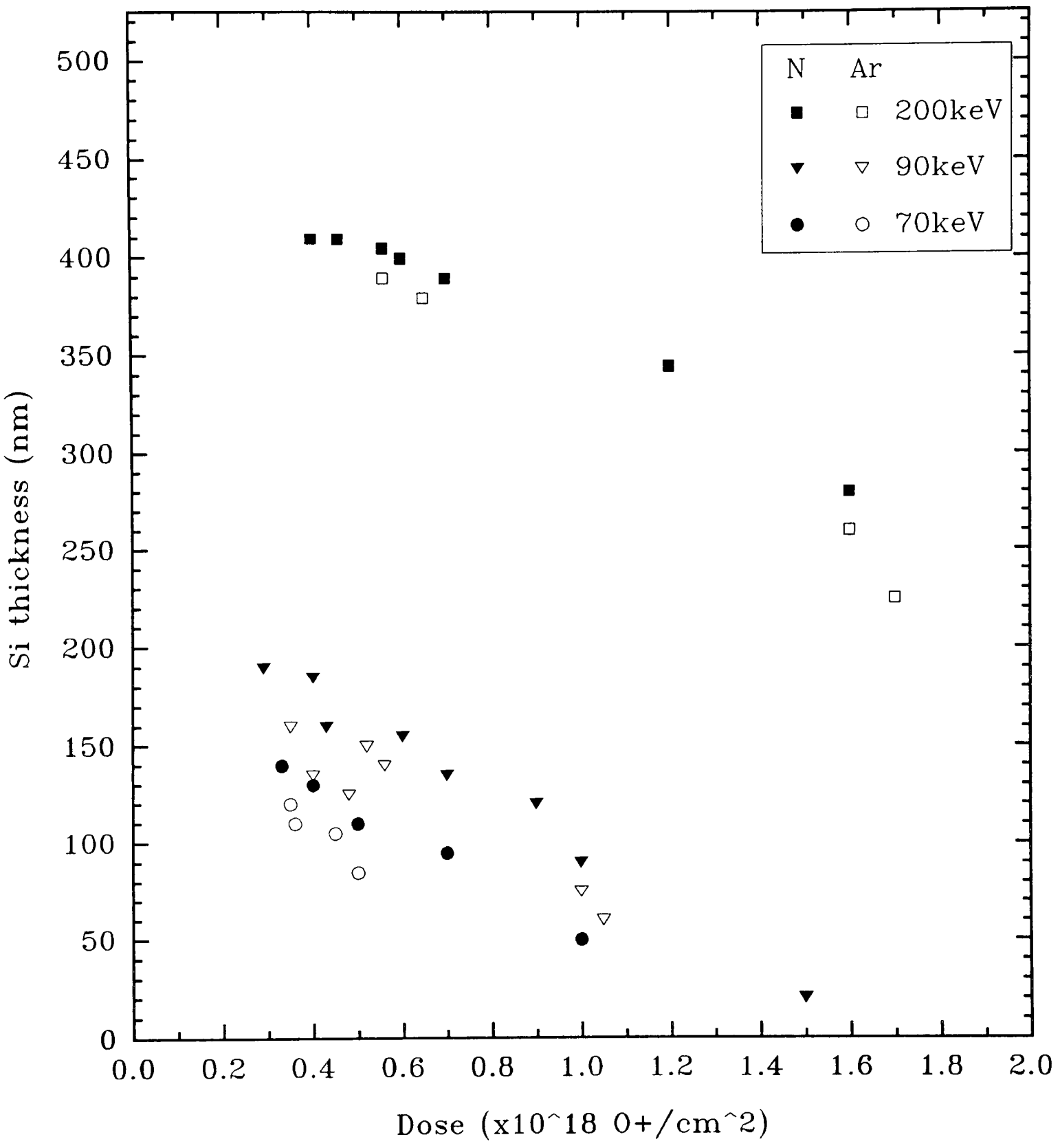

Figure 4.15 Silicon surface layer thickness as a function of the energy, dose and anneal ambient. N = annealed in nitrogen at 1320°C or 1360°C for 6hrs, Ar = annealed in argon + ½ % oxygen at 1300°C for 6hrs (T_i = 680°C or 700°C, I' = 5.6μA/cm^2, 3.75μA/cm^2 and 3.1μA/cm^2 at 200keV, 90keV and 70keV respectively).

Figure 4.16 Cross-section micrographs, at a <110> pole, of samples implanted at,
a) & b) 90keV, $\Phi = 0.4 \times 10^{18} O/cm^2$, $T_i = 680°C$, $I' = 3.75 \mu A/cm^2$,
a) annealed in nitrogen at 1320°C for 6hrs,
b) annealed in argon + ½ % oxygen at 1300°C for 6hrs,
c) & d) 200keV, $T_i = 700°C$,
c) $\Phi = 0.72 \times 10^{18} O/cm^2$, $I' = 5 \mu A/cm^2$ and annealed in nitrogen at 1320°C for 6hrs,
d) $\Phi = 0.65 \times 10^{18} O/cm^2$, $I' = 5.6 \mu A/cm^2$ and annealed in argon + ½ % oxygen at 1300°C for 6hrs,
showing that the buried SiO_2/surface Si layer interface is more planar after the anneals in the argon + ½ % oxygen ambient at 1300°C for 6hrs.

a)

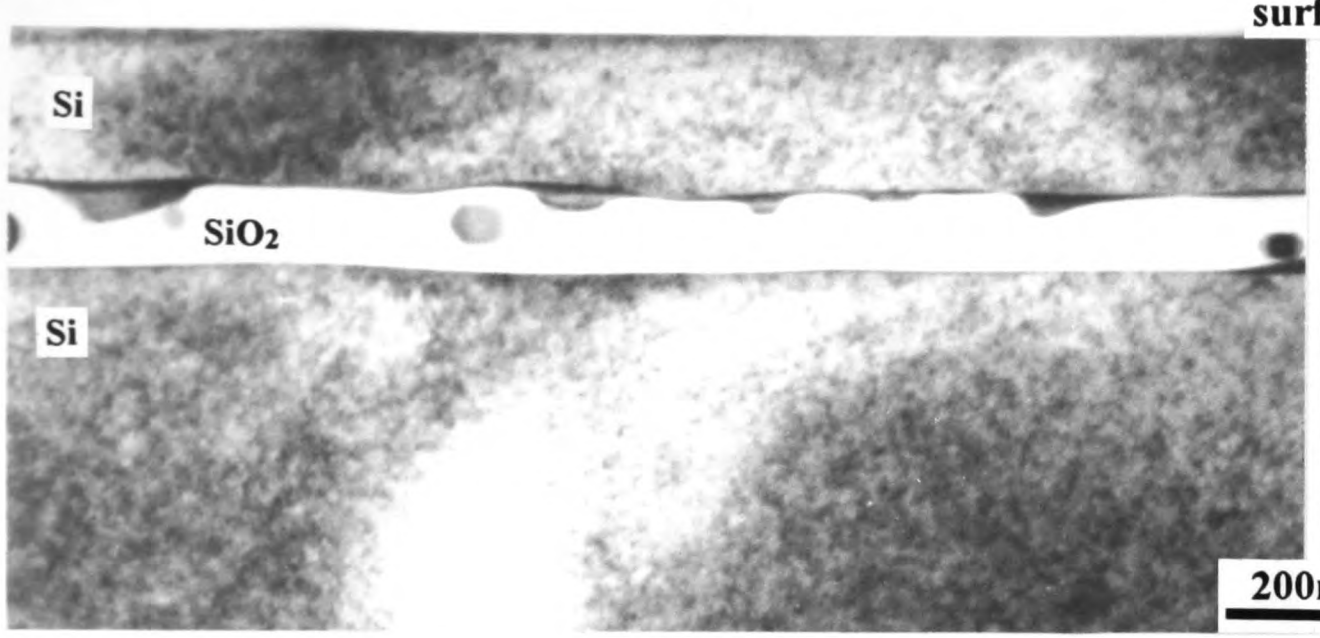

b)

surface

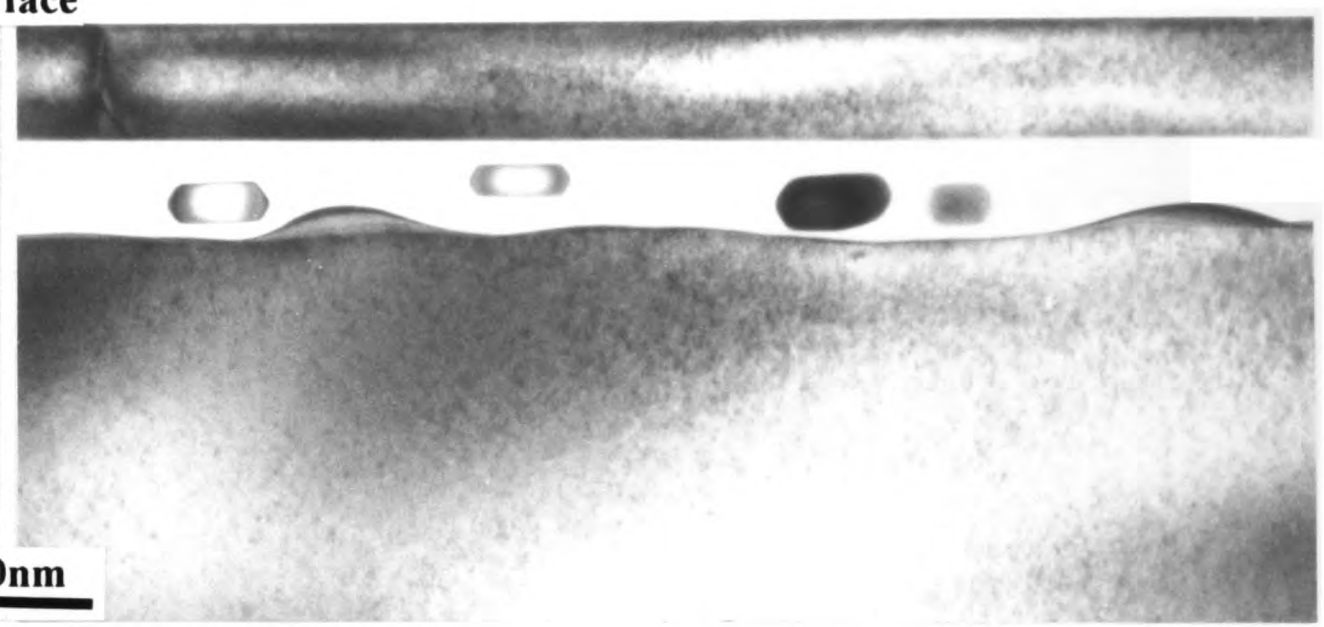

c)

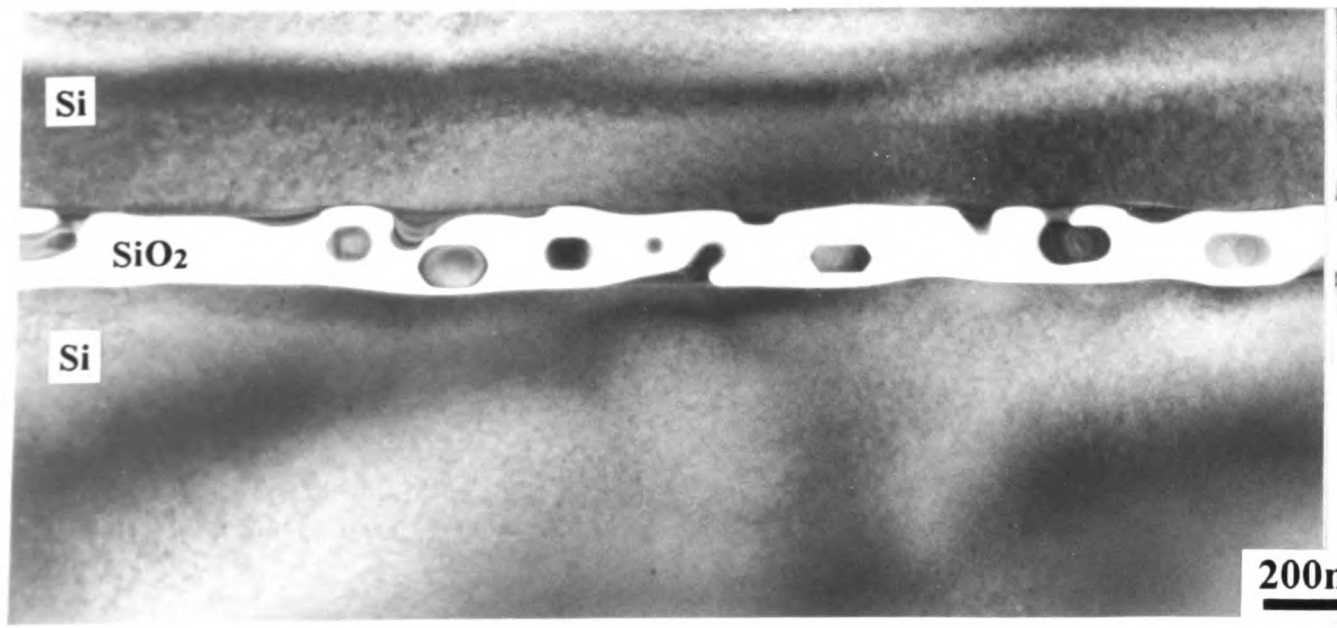

d)

surface

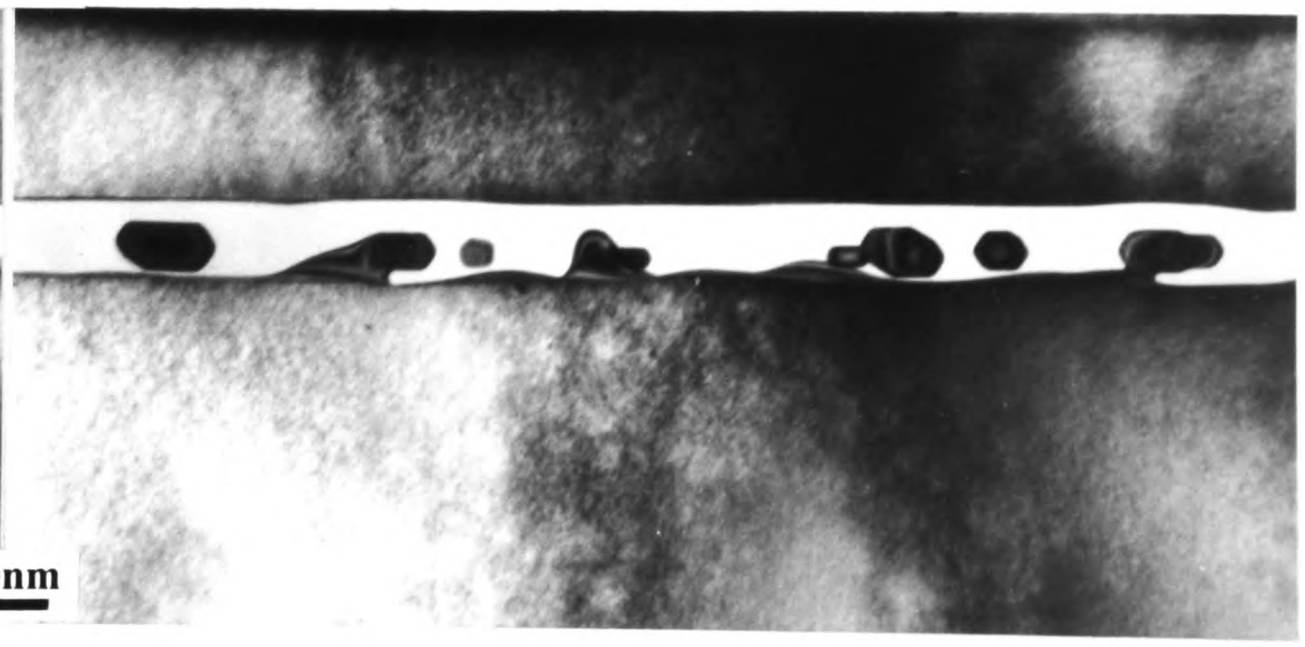

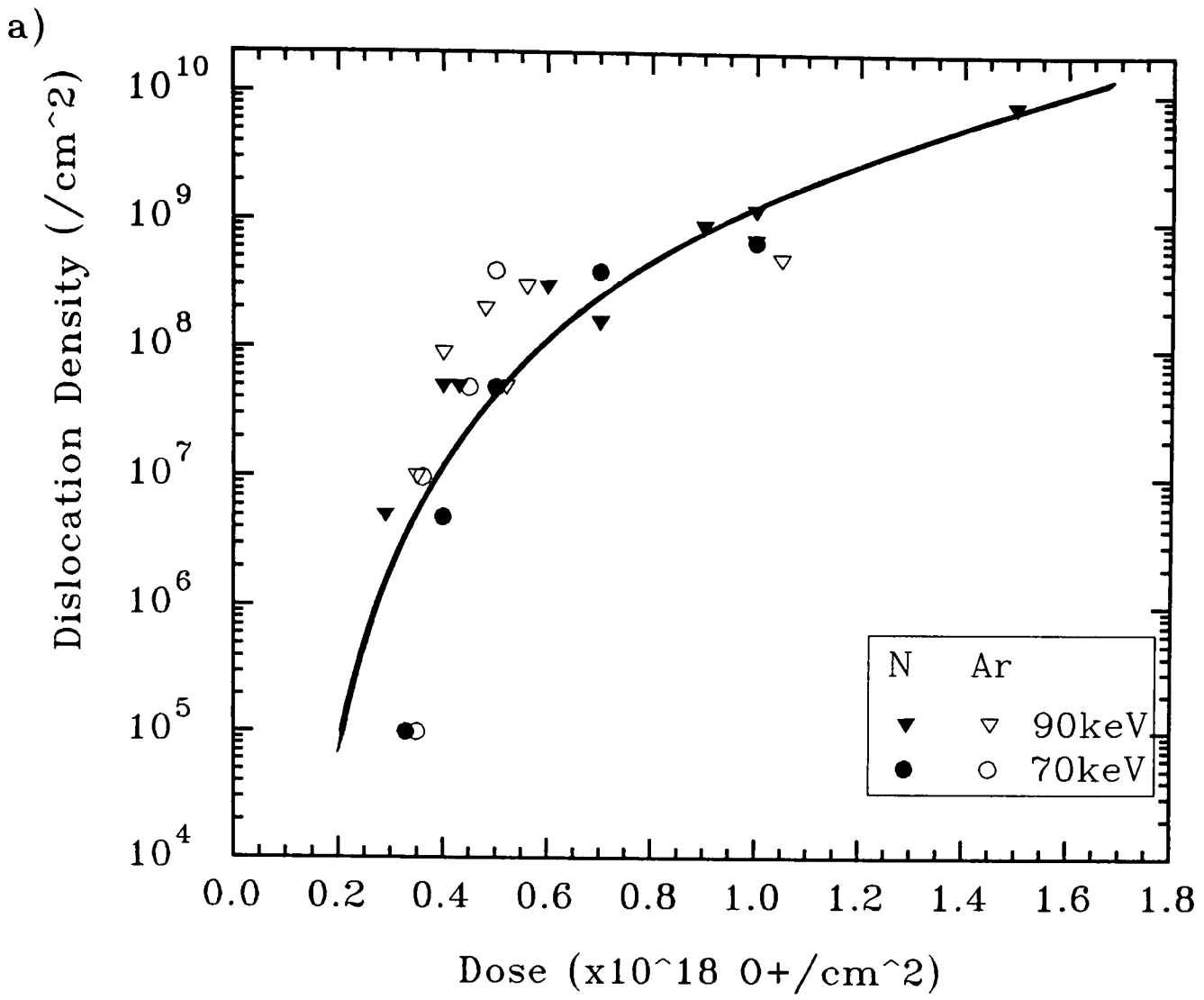

Figure 4.17 Threading dislocation density as a function of the dose and anneal ambient, a) 70keV & 90keV and b) 200keV. N = annealed in nitrogen at 1320°C or 1360°C for 6hrs, Ar = annealed in argon + ½ % oxygen at 1300°C for 6hrs.

at both of the SiO_2/Si interfaces[23]. These reports suggest that the oxidation rate at the buried SiO_2/Si interfaces would be slower in a N_2 ambient than in an Ar + ½ % O_2 ambient. As the formation of abrupt planar interfaces involves the oxidation of Si protrusions this would lead to rougher interfaces, i.e. more protrusions, after annealing in N_2. Hence this effect might be expected to apply to both of the SiO_2/Si interfaces, but experimentally only the SiO_2/surface Si layer interface was smoother after the Ar + ½ % O_2 anneal. It should be noted that these two anneals also had different ramp rates and starting and finishing temperatures (section 2.2) and these may also be influencing the difference in the upper SiO_2/Si interface. Smother interfaces potentially result in better electrical properties for the buried SiO_2 layer[26] suggesting that if SIMOX structures were to be fabricated in this dose regime, then from this point of view annealing in an Ar + ½ % O_2 ambient would be better.

Based on these results it is difficult to draw conclusions about which ambient results in the better overall structure. Hence further work is required to clarify the influence of the anneal ambient and also to investigate the effect of the ramp rate and starting/finishing temperature.

4.4 Beam Current Density

The results and discussion in section 4.2.3 suggest that if the defects present at the wafer surface after implantation could be reduced or eliminated this would reduce or eliminate the threading dislocations after annealing. One possible cause of the defects at the wafer surface is that the arrival rate of the Si_i generated by the internal oxidation arrive at the surface at a rate faster than they can be incorporated in the surface (section 3.10.3). Hence if the generation rate of Si_i is reduced this may result in a reduction in the threading dislocation density. The generation rate of Si_i can be reduced by implanting with a lower time-averaged beam current density, which can be achieved by using lower beam currents while keeping the implant area constant. If the size of the beam spot remains constant this results in both lower time-averaged and instantaneous beam current densities. The implantation temperature can be maintained at 680°C by increasing the power to the halogen lamps which provides the background heating. For the low energies (90keV,70keV and 50keV) used in this work, the range of beam currents available from the implanter was limited and therefore an energy of 200keV was used for this

experiment. A dose of $0.7x10^{18}O/cm^2$ was chosen as this is close to the dose that would be of interest for fabricating thin buried SiO_2 layers at this energy. The dependence of the as-implanted microstructure on the beam current density was discussed in chapter 3. Fig. 4.18 shows the structure, after annealing in N_2 at 1360°C or 1320°C, of samples implanted with this dose and energy using beam current densities of $2.5\mu A/cm^2$, $3.75\mu A/cm^2$ and $5\mu A/cm^2$. For the low threading dislocation densities in these specimens the TEM data has been supplemented by etch pit data using a new chemical etch[28], for which each etch pit is considered to equal one or two (if the dislocations are present as closely spaced pairs so that the two etch pits overlap) threading dislocations[27]. The layer thicknesses and defect densities are summarised in Table 4.4. In these three samples there is no noticeable influence of the beam current density on the Si island density or the surface Si or buried SiO_2 layer thicknesses (table 4.4). In all three samples some of the Si islands are connected to the surface Si layer or the substrate, with the number of connected islands being greatest in the highest beam current sample. All three samples contain Si protrusions into the SiO_2 layer from both SiO_2/Si interfaces. The density of the protrusions was highest for the sample implanted with a beam current of $5\mu A/cm^2$. For samples implanted with beam currents of $2.5\mu A/cm^2$ and $3.75\mu A/cm^2$ the Si islands and protrusions have better developed facets. This may not be connected with the differences in the beam current densities but may be because of the slightly higher anneal temperature, 1360°C, used for annealing the samples implanted with beam current densities of $2.5\mu A/cm^2$ and $3.75\mu A/cm^2$, as opposed to 1320°C used for annealing the sample implanted with the beam current density of $5\mu A/cm^2$.

There is no clear relationship between the beam current density and the threading dislocation density, but the threading dislocation density is lowest for the two higher beam current densities and this trend is supported by two etch pit dislocation density measurements (table 4.4)[27]. These results suggest that the threading dislocation density decreases with increasing beam current density. In the as-implanted samples the percentage of the surface containing defects after implantation decreased with increasing beam current density (table 3.2). Therefore such a trend of decreasing dislocation density with increasing beam current density is consistent with the model of the defects at the wafer surface acting as the source of the threading dislocations (i.e. the highest threading dislocation density and the highest fraction of

Figure 4.18 Cross-section micrographs, at a <110> pole, of samples implanted at 200keV, T_i = 680°C,

a) $I' = 2.5\mu A/cm^2$, $\Phi = 0.7x10^{18}O/cm^2$ and annealed at 1360°C for 6hrs in nitrogen,

b) $I' = 3.75\mu A/cm^2$, $\Phi = 0.69x10^{18}O/cm^2$ and annealed at 1360°C for 6hrs in nitrogen,

c) $I' = 5\mu A/cm^2$, $\Phi = 0.72x10^{18}O/cm^2$ and annealed at 1320°C for 6hrs in nitrogen.

a)

surface

Si

SiO_2

Si

b)

surface

Si

SiO_2

Si

c)

surface

Si

SiO_2

Si

200nm

Sample	Current density (μA/cm^2)	Layer thicknesses (nm) silicon	oxide	Defect densities (/cm^2) dislocations	etch pits*	Si islands
H130	5	390	140	< 5 x 10^6	-	1 x 10^9
H134	3.75	370	160	< 5 x 10^6	2 x 10^6	2 x 10^8
H132	2.5	380	160	5 x 10^6	1 x 10^7	1 x 10^8

Table 4.4 Layer thicknesses and defect densities for the samples implanted at 200keV using different beam current densities (H130, Φ = 0.72x10^{18}O/cm^2, annealed at 1320°C for 6hrs in nitrogen, H134, Φ = 0.69x10^{18}O/cm^2, annealed at 1360°C for 6hrs in nitrogen and H132, Φ = 0.7x10^{18}O/cm^2, annealed at 1360°C for 6hrs in nitrogen). *ref 27.

Sample	Energy (keV)	Layer thicknesses (nm) silicon	oxide	Defect densities (/cm^2) dislocations	pinholes	Si islands
H127	65,70,75	150	65	< 5 x 10^6	1 x 10^7	1 x 10^8
H131	75,70,65	150	65	< 5 x 10^6	3 x 10^7	1 x 10^8
H11	70	140	75	< 10^5	none	5x10^7

Table 4.5 Layer thicknesses and defect densities for samples implanted with a total dose of 0.33x10^{18}O$^+$/cm^2, either by implanting doses of 0.1x10^{18}O$^+$/cm^2, at 65keV, 70keV and 75keV (H127) or at 75keV, 70keV and 65keV (H131) or by implanting a dose of 0.33x10^{18}O$^+$/cm^2 at 70keV (H11). Specimens annealed at 1320°C for 6hrs in nitrogen.

Sample (energy)	Anneal	Layer thickness (nm) silicon	oxide	Defect densities (/cm^2) dislocations	pinholes	Si islands
H143b	CA 6hrs	160	90	1.5 x 10^8	5x10^7	4x10^8
" c	RTA 1min	-	-	2 x 10^9	-	-
" d	3 x RTA 1min	-	-	5 x 10^8	-	-
" e	RTA 1min + CA 6hrs	165	100	1.5 x 10^8	1x10^7	3x10^8
H136b	CA 6hrs	400	120	5 x 10^6	<10^7	2x10^7
" c	RTA 1min	-	-	<10^7	-	-
" d	3 x RTA 1min	-	-	<10^7	-	-
" e	RTA 1min + CA 6hrs	400	105	<10^7	5x10^7	2x10^7

Table 4.6 Layer thicknesses and defect densities for sample H143 (90keV, Φ = 0.43x10^{18}O/cm^2, ^{18}O) and sample H136 (200keV, Φ = 0.6x10^{18}O/cm^2, ^{16}O) that were rapid thermally annealed (RTA) at 1300°C in nitrogen. Results from pieces of the same samples conventionally annealed (CA) at 1360°C in nitrogen are included for comparison.

the implanted surface containing defects are both for the sample implanted with the lowest, 2.5μA/cm^2, beam current density). A difficulty is that these preliminary studies have resulted in insufficient TEM and etch pit results to strongly support this hypothesis. Trends of decreasing defect density at the wafer surface after implantation and decreasing threading dislocation density after annealing, with increasing beam current density are the opposite to that predicted at the beginning of this section. Increasing the beam current density increases the power loading on the wafer, e.g. increasing the beam current density from 2.5μA/cm^2 to 5μA/cm^2 increases the power loading from 4 to 8 watts, and hence increases the localised beam heating and annealing. This increase in local heating could account for the reduction of the defects at the wafer surface after implantation and the threading dislocation density after annealing, even though the arrival rate of Si_i at the wafer surface is expected to double with this increase in the beam current density.

The results suggest that the dislocation density decreases with increasing beam current density, but based on these results from only three samples, it is difficult to draw any strong conclusions. Further work is required to confirm this relationship. A potential disadvantage of using high beam current densities ($\geq$6.25μA/cm^2) for partially implanted wafers is that they often generate slip lines during annealing that span the implanted area[29]. These are obviously detrimental to any subsequent device fabrication, although by relieving stress they may result in a lower dislocation density in regions between the slip lines.

4.5 Graded Energy Implants

For all the energies used in this work the results in section 4.2 show that for the optimum doses, i.e. doses just $>^{A}\Phi_c$, Si islands are present within the SiO_2 layer. At 70keV the optimum dose is close to 0.33x10^{18}O/cm^2 and for this dose the Si island density is 5x10^7/cm^2 (table 4.1). If the oxygen distribution could be altered during implantation so that more of the silicon is oxidised rather than isolated during annealing it may be possible to reduce the density of the Si islands. With this aim two samples were implanted with doses of 3 x 0.11x10^{18}O/cm^2, with each implant at a different energy at or close to 70keV. The total dose still equals 0.33x10^{18}O/cm^2 but the final oxygen distributed will not be gaussian but results from the three

Figure 4.19 Cross-section micrographs at a <110> pole of,

a) a sample implanted with doses of $0.11x10^{18}O/cm^2$ at each of the energies 65keV, 70keV and 75keV, and annealed at 1360°C for 6hrs in nitrogen,

b) a sample implanted with doses of $0.11x10^{18}O/cm^2$ at each of the energies 75keV, 70keV and 65keV, and annealed at 1360°C for 6hrs in nitrogen,

c) the as-implanted structure of the annealed sample shown in a) (X = surface silicon layer, Y = buried damage/oxide layer),

d) a sample implanted with a dose of $0.33x10^{18}O/cm^2$ at 70keV, and annealed at 1360°C for 6hrs in nitrogen.

T_i = 700°C and I' = $2.5\mu A/cm^2$ for all of the implants.

Note the absence of defects at the surface of the as-implanted sample shown in c) and the difference in the size of the typical silicon islands (S) in the two samples shown in b) and d).

a)

200nm

surface

Si

SiO_2

Si

b)

surface

Si

SiO_2

Si

S

c)

d)

surface

X

Y

surface

Si

SiO_2

S

Si

overlapping distributions. One sample (H127) was implanted with the doses of $0.11x10^{18}O/cm^2$ first at 65keV, then at 70keV and finally at 75keV. The second sample (H131) was implanted with the doses of $0.11x10^{18}O/cm^2$ first at 75keV, then at 70keV and finally at 65keV. Both samples were then annealed at 1320°C for 6hrs in N_2 (table 2.2). The samples after annealing are shown in Fig. 4.19 and layer and defect densities are summarised in Table 4.5. Table 4.5 shows that both samples consist of surface Si layers above an oxide layer containing Si pinholes. SIMS analysis confirms that the oxide is SiO_2 [1]. The results show that neither the layer thicknesses nor the Si island, threading dislocation or Si pinhole densities are influenced by the order of the three different energy implants (table 4.5). In both samples no threading dislocations are observed after annealing. The as-implanted structure of sample H131 contained no defects at the wafer surface (fig. 4.19) which supports the hypothesis that defects present at the wafer surface after implantation can lead to the threading dislocations and when these defects are absent the dislocation density is low (section 4.2.3).

Comparison with the sample implanted with a dose of $0.33x10^{18}O/cm^2$ in one implant at 70keV (H11) shows that the graded energy implants have a slightly thinner SiO_2 layer, a slightly thicker surface Si layer and similar Si island and threading dislocation densities (table 4.5). In sample H11 the oxide layer was continuous but in samples H127 and H131 Si pinholes are present in the oxide (table 4.5). The presence of Si pinholes, slightly thinner buried SiO_2 layers and thicker surface Si layers in samples H127 and H131, compared to H11, may be because the layers were formed from the graded energy implants, but these differences are also consistent with the total implanted doses in samples H127 and H131 being slightly lower than the implanted dose for H11. For a slightly lower total dose the pinholes arise because the nominal total dose ($0.33x10^{18}O/cm^2$) is very close to the dose ${}^{A}\Phi_c$ for the energy of 70keV. The size of the islands in c.s for both samples H127 and H131 are typically 25-35nm across which is approximately 30-45% of the thickness of the buried SiO_2 layer. This compares to the typical island size in c.s for H11 of 55nm across which is about 75% of the thickness of the buried SiO_2 layer. Hence although the densities of the Si islands in samples H127 and H131 are similar to that in sample H11, the islands are smaller (fig. 4.19). As they span a smaller fraction of the buried oxide thickness they are potentially less harmful to the electrical isolation achieved by the

presence of the buried SiO_2 layer. This potentially makes this technique useful for fabricating thin-film SIMOX structures, although the greater complexity involved with the implantation is a potential disadvantage.

4.6 Rapid Thermal Anneals

The results in section 4.2 show that the range of doses (Φ) of interest for fabricating thin-film SIMOX structures is ${}^{A}\Phi_c<\Phi<{}^{I}\Phi_c$. As discussed in section 4.2, for doses in this range the Si islands form from Si isolated during the annealing. Hence an alternative method to try and oxidise all the Si at the depth of the buried SiO_2 layer, and hence reduce the density of Si islands, is to alter the oxygen distribution after implantation, but before the standard high temperature 6 hour anneal required for all the implanted oxygen to segregate to the buried SiO_2 layer. This could be done by using an interim rapid thermal anneal (RTA). It has also been suggested that altering the thermal ramping cycle may reduce dislocation densities and for high doses ($1.8x10^{18}O/cm^2$ at 200keV) may also reduce the density of Si islands close to the interface with the substrate[30]. Hence with the aim of reducing the density of the Si islands, pieces of two samples, implanted at 90keV (H143) and 200keV (H136), were given RTA at 1300°C for 1 minute prior to the standard 6 hour anneal. Doses of $0.43x10^{18}O/cm^2$ and $0.6x10^{18}O/cm^2$ were implanted at these two energies, respectively, as these doses are just $>{}^{A}\Phi_c$, the optimum dose, for 90keV and 200keV, respectively (section 4.2). Sample H143 was implanted with ^{18}O because this sample was also used for SIMS studies of oxygen exchange between the implanted oxygen and the cap during the anneals[31]. The structure of these two samples after a 6 hour anneal at 1360°C (H143b & H136b), a 1 minute RTA (H143c & H136c), and a 1 minute RTA followed by a 6 hour anneal at 1360°C (H143e & H136e) are shown in Figs. 4.20 & 4.21. The layer thicknesses and defect densities are summarised in Table 4.6.

After the 1 minute RTA the structure is very different from the structure after the conventional anneal at 1360°C for 6 hours (fig. 4.20). In the RTA samples for both energies (H143c & H136c) an oxide precipitate denuded zone exists at the surface to a depth of $\approx$40nm. Below this is a high density of oxide precipitates and/or oxide ribbons. At the depth of the peak of the oxygen distribution the structure consists of uneven bands of oxide and Si running

Figure 4.20 Cross-section micrographs, at a <110> pole, of samples implanted with ^{18}O at 90keV, $\Phi = 0.43x10^{18}O/cm^2$, $T_i = 680°C$, $I' = 3.1\mu A/cm^2$ and,

a) conventionally annealed at 1360°C for 6 hours in nitrogen,

b) rapid thermally annealed at 1300°C for 1 minute in nitrogen showing a region (A) of uneven bands of oxide and silicon running approximately parallel with the wafer surface,

c) rapid thermally annealed at 1300°C for 1 minute in nitrogen followed by a conventional anneal at 1360°C for 6 hours in nitrogen.

Figure 4.21 Cross-section micrographs, at a <110> pole, of samples implanted with ^{16}O at 200keV, $\Phi = 0.6x10^{18}O/cm^2$, $T_i = 680°C$, $I' = 5.6\mu A/cm^2$ and,

a) conventionally annealed at 1360°C for 6 hours in nitrogen,

b) rapid thermally annealed at 1300°C for 1 minute in nitrogen showing a region (A) of uneven bands of oxide and silicon running approximately parallel with the wafer surface and a region of oxide precipitates (B),

c) rapid thermally annealed at 1300°C for 1 minute in nitrogen followed by a conventional anneal at 1360°C for 6 hours in nitrogen.

Figure 4.20

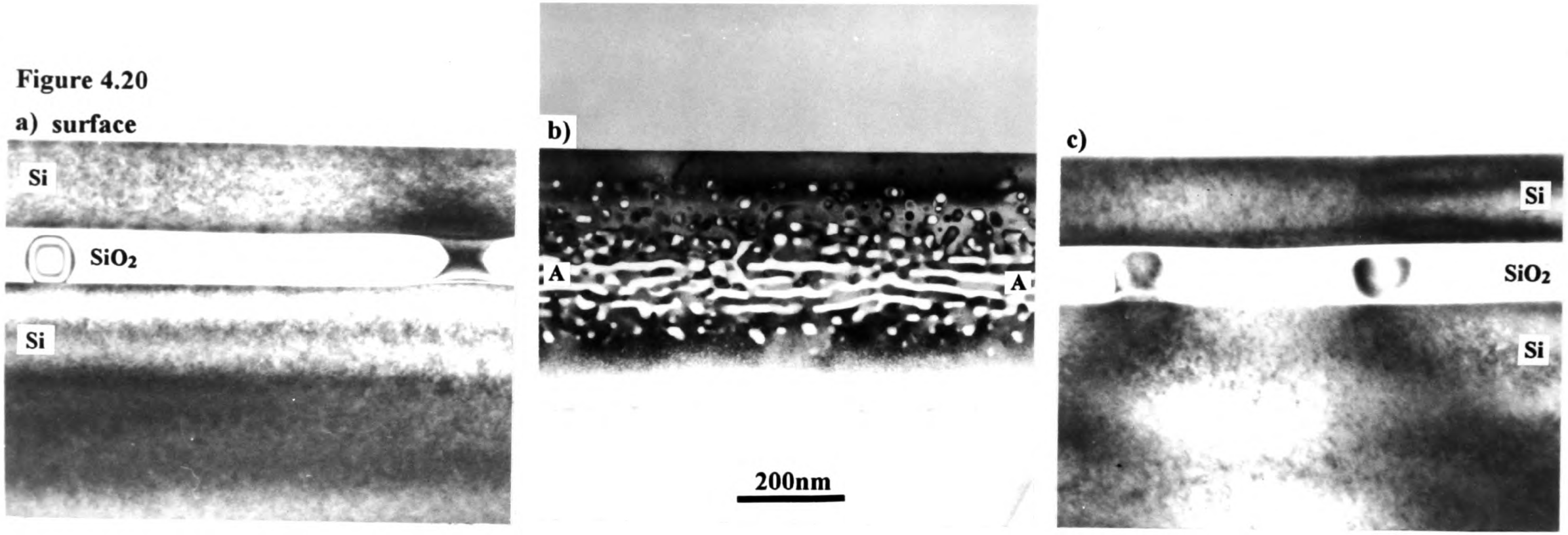

Figure 4.21

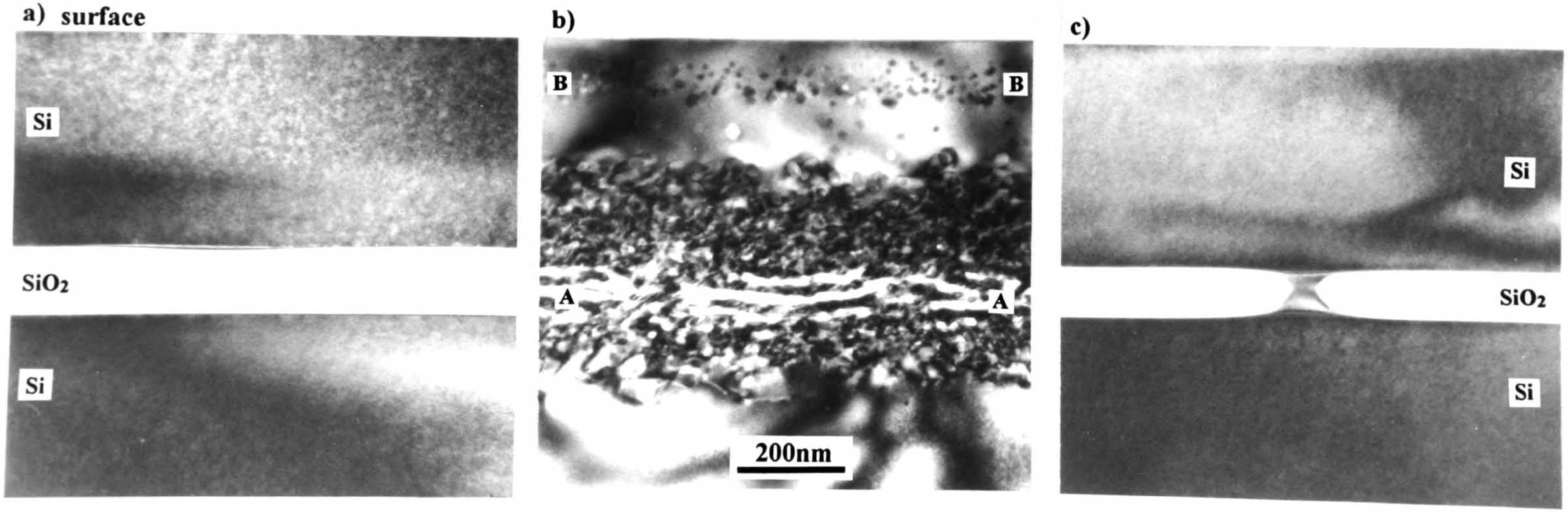

approximately parallel to the wafer surface. Both of the uneven bands of oxide and Si, for both energies, are ≈20nm thick. The bands of Si are connected to either the surface Si layer, which is at the same orientation as the substrate, or to the substrate and hence are also at the same orientation as the substrate. No Si islands are present within the uneven oxide bands. Oxide precipitates are present in the Si below the banded structure. Even though the anneal was only for 1 minute many of the oxide precipitates, both in the surface Si layer and below the banded Si/oxide structure, have developed {100} and {111} facets. The similar structure present at the depth of the peak of the oxygen distribution for these two different energies may be explained by the fact that the two doses chosen are both just $>^{A}\Phi_c$ for the two energies and hence, as explained in section 4.2, a similar oxygen concentration is expected at the peak of the oxygen distribution after implantation.

Plan view micrographs of the RTA sample implanted at 90keV (H143c) both near the edge of the hole created by the ion beam thinning process and further away from the hole are shown in Fig. 4.22. These micrographs show that closest to the surface the oxide is present in a network of ribbons while slightly deeper the oxide is present as discrete precipitates. These oxide ribbons and discrete precipitates at different depths can be seen in thick c.s. (fig 4.23). In the sample implanted at 200keV (H136c) a region, width 80nm, of oxide precipitates is present below the denuded zone (fig. 4.21b). The precipitates, typical size 20nm, are faceted mainly by {111} planes with small {001} planes parallel to the wafer surface (fig. 4.24). In this sample between this region of faceted precipitates and the banded structure at the peak of the oxygen distribution is a region of Si, 100nm wide, containing a lower density of larger, typical size 30nm in c.s., faceted oxide precipitates.

The oxide ribbons near the surface in sample H143c, the region of oxide precipitates in sample H136c and the oxide denuded zones at the wafer surface of both samples probably result from an Ostwald ripening process during annealing. After the short 1 minute anneal the oxide ribbons and precipitate particles are the precipitates that have grown at the expense of other precipitates present in the as-implanted samples. In the sample implanted at 200keV (H136) the region of Si containing a lower density of oxide precipitates below the region of oxide precipitates is probably the result of the oxygen at this depth in the as-implanted sample

Figure 4.22 Plan-view micrographs, at the [001] pole, of the sample implanted with ^{18}O at 90keV, Φ = 0.43x10^{18}O/cm^2, T_i = 680°C, I' = 3.1μA/cm^2 and rapid thermally annealed at 1300°C for 1 minute in nitrogen,
a) structure near the edge of the hole formed by the ion beam thinning (thin foil),
b) structure further from the edge of the hole (thin foil),
showing oxide "ribbons" (R) and precipitates (P).

Figure 4.23 Cross-section micrograph, at a <110> pole, of the sample implanted with ^{18}O at 90keV, Φ = 0.43x10^{18}O/cm^2, T_i = 680°C, I' = 3.1μA/cm^2 and rapid thermally annealed at 1300°C for 1 minute in nitrogen, from a thicker part of the TEM cross-section foil than shown in Fig. 4.20b, showing the band of oxide "ribbons" (R) above the discrete oxide precipitates (P).

Figure 4.24 Cross-section micrograph, at the <110> pole, of the sample implanted at 200keV, Φ = 0.6x10^{18}O/cm^2, T_i = 680°C, I' = 5.6μA/cm^2 and rapid thermally annealed at 1300°C for 1 minute in nitrogen, showing the shape of the oxide precipitates (O) near the wafer surface (this region is labelled (B) in fig. 4.21).

Figure 4.25 Cross-section micrographs, at the <110> pole, of samples implanted,
a) with ^{18}O at 90keV, Φ = 0.43x10^{18}O/cm^2, T_i = 680°C, I' = 3.1μA/cm^2 and rapid thermally annealed three times, each time in nitrogen at 1300°C for 1 minute,
b) with ^{16}O at 200keV, Φ = 0.6x10^{18}O/cm^2, T_i = 680°C, I' = 5.6μA/cm^2 and rapid thermally annealed three times, each time in nitrogen at 1300°C for 1 minute.

Figure 4.22

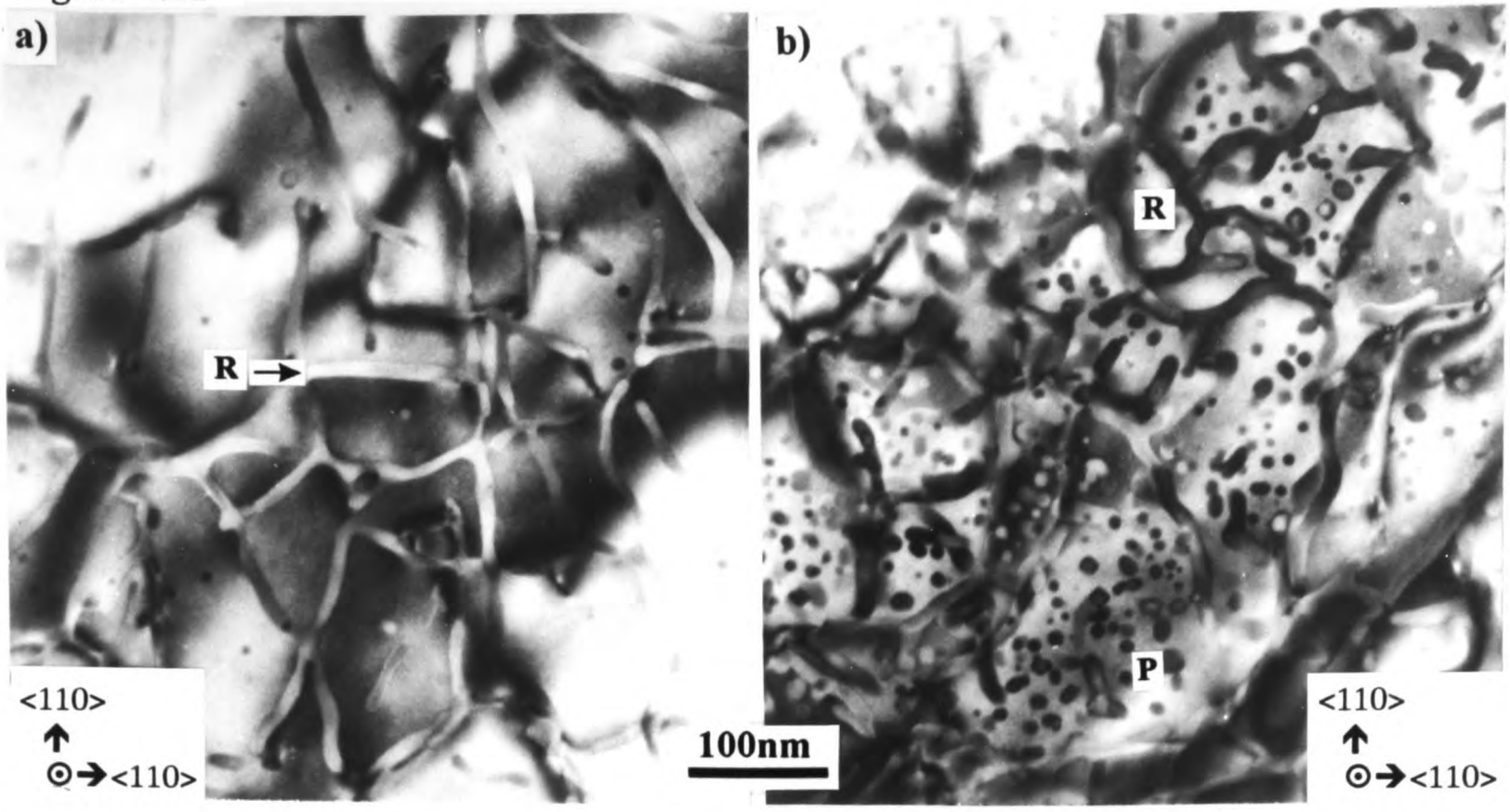

Figure 4.23

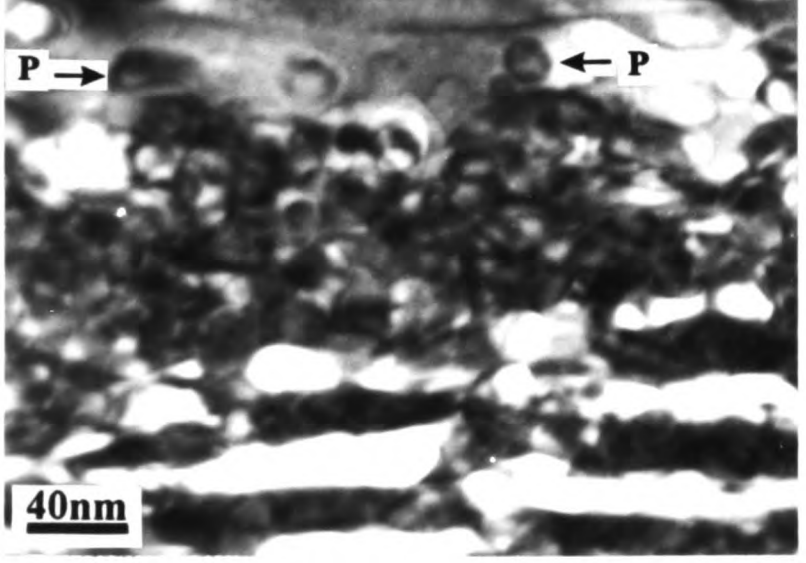

Figure 4.24

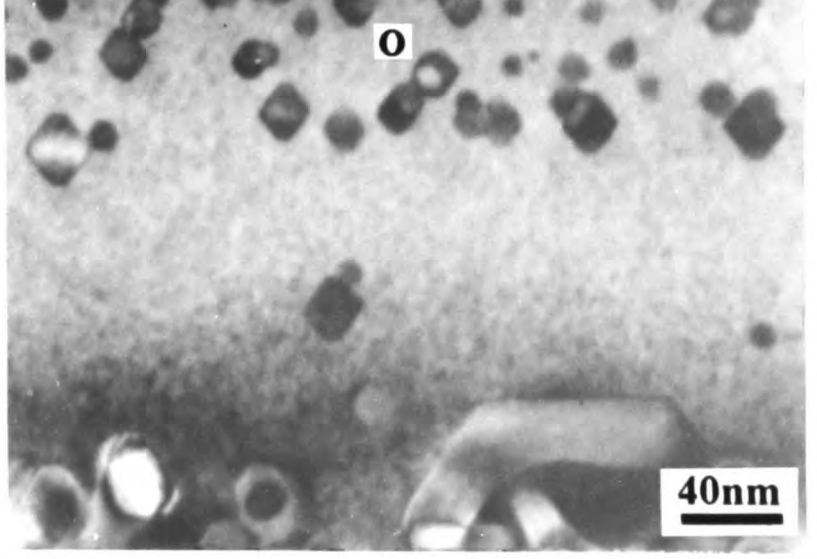

Figure 4.25

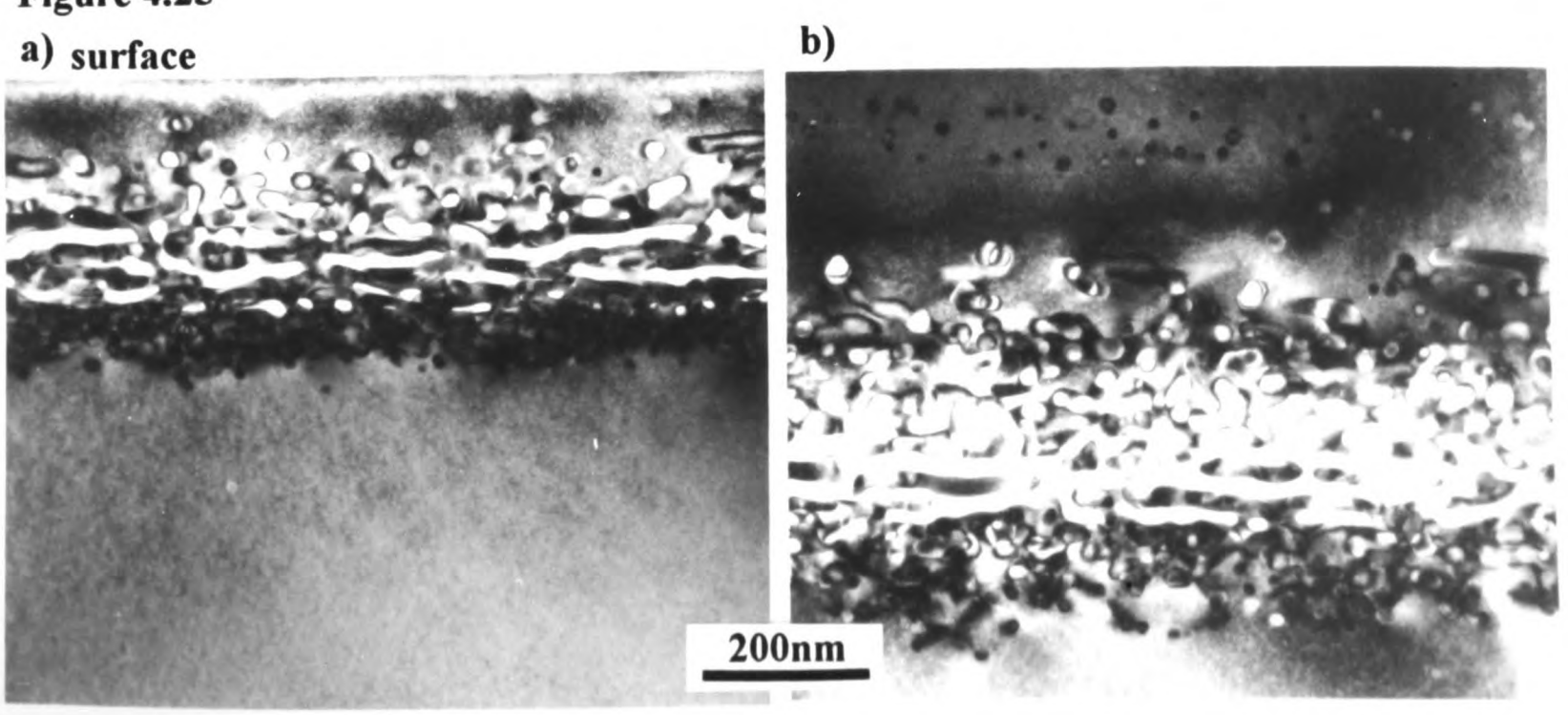

segregating to the depths of the banded structure at the peak of the as-implanted oxygen distribution during the annealing. Oxide precipitates are present in the region near the wafer surface after the 1 minute anneal because these are further from the peak of the as-implanted oxygen distribution. A similar mechanism may also partly explain why oxide ribbons are present nearer to the surface than oxide precipitates in sample H143c. An oxide ribbon with the same diameter as a number of oxide precipitates, where the total volume of these precipitates is the same as the volume of the oxide ribbon, has a smaller surface area than the total surface area of the precipitates and hence the minimisation of surface energy may be playing a role in the formation of the oxide ribbons. Regions of oxide precipitates in 200keV implants after annealing (2 hrs at 1150°C) have been observed by other workers[32]. Pieces of these two samples (H143e & H136e) were also given 3 RTA each for 1 minute (fig. 4.25). The microstructure and the threading dislocation densities of these samples is similar to the microstructure and threading dislocation density after the single RTA for 1 minute (H143c & H136c). Hence these two samples were not annealed further. Comparing the structure of the two samples given RTA for just 1 minute with the as-implanted structure (chapter 3) shows that even a short, high temperature anneal results in large changes in the microstructure. The SIMS analysis on sample H143c also shows that 7% of the implanted ^{18}O has exchanged with an equal amount of ^{16}O in the cap, even though the RTA was only for 1 minute[17].

After conventionally annealing a piece of the two RTA samples for a further 6 hours (H143e & H136e) a buried SiO_2 layer has formed below a high quality surface Si layer. The structure of these two samples is very similar to the structure of the samples (H143b & H136b) conventionally annealed at the same time, but without the prior RTA (figs. 4.20 & 4.21, table 4.6). Based on the results of section 4.2 the presence of Si pinholes in the SiO_2 layers after the conventional anneals of samples H143b and H143e suggest that the implanted dose for sample H143 was lower than the nominal dose. For both energies the Si island densities are very similar after the RTA plus conventional anneal and just the conventional anneal (table 4.6), suggesting that the use of interim RTA to redistribute the oxygen prior to the conventional anneal is not an appropriate technique for reducing the Si island density.

Threading dislocations are present in H143c after the 1 minute RTA while no dislocations are observed in sample H136c after the RTA (table 4.6). TEM analysis of the as-implanted samples showed the presence of defects at the surface of sample H143a and no defects present at the surface of sample H136a (fig. 3.1). Hence these results further support the hypothesis that the source of the threading dislocations is related to the defects present at the wafer surface after implantation. The threading dislocation density in the top 70nm of sample H143 is an order of magnitude higher after the RTA (H143c) than in the surface Si layers after the conventional anneal (H143b) (table 4.6). This may be explained by the faster ramp rate of the RTA generating more stress than the conventional anneal ramp rate. For sample H136 only one threading dislocation was observed (table 4.6) after the 6 hour conventional anneal (H136b). Hence no relationship between the threading dislocation density and the anneal treatments can be established from this sample. For sample H143 after a piece given a RTA for 1 minute was given a further conventional 6 hour anneal (H143e), the threading dislocation density was the same as after just the 6 hour conventional anneal (H143b) (table 4.6). Hence the conventional anneal may reduce the threading dislocation density present after the 1 minute RTA, but as the density is the same as after only the conventional anneal this suggests that the interim RTA has not had a positive influence on the final threading dislocation density.

The accuracy of the comparison of the Si island and threading dislocation densities between the RTA plus conventional anneal (CA) samples and the only CA samples could be improved by performing p.v. TEM, but the results from c.s. TEM suggest that the use of interim RTA is not an appropriate technique for reducing the Si island or dislocation densities.

4.7 Other Defects

4.7.1 Stacking fault pyramids and stacking fault tetrahedra

In many annealed samples small stacking fault pyramids (SFP) or stacking fault tetrahedra (SFT) are present in the surface Si layer, in the substrate close to the interface with the buried oxide layer and in Si islands within the buried oxide layer (fig. 4.26). In the substrate, based on c.s. observations, the combined areal density with respect to the wafer surface of these

Figure 4.26,

a) cross-section micrograph, at a <110> pole, showing a small stacking fault defect (arrowed) in the surface Si layer of the sample implanted at 90keV, $\Phi = 0.29x10^{18}O/cm^2$, $T_i = 680°C$ and $I' = 3.75\mu A/cm^2$ and annealed at 1320°C for 6hrs in nitogen,

b) cross-section micrograph, at a <110> pole, showing two small stacking fault defects (arrowed) in the substrate close to the interface with the buried SiO_2 layer and a stacking fault defect (arrowed) in one of the Si islands, in the sample implanted at 90keV, $\Phi = 0.6x10^{18}O/cm^2$, $T_i = 680°C$ and $I' = 3.75\mu A/cm^2$ and annealed at 1320°C for 6hrs in nitogen,

c) plan-view, at a [001] pole, of an elongated stacking fault pyramid (arrowed) in either the surface silicon layer or the substrate close to the buried SiO_2 layer, in the sample implanted at 70keV, $\Phi = 0.5x10^{18}O/cm^2$, $T_i = 680°C$ and $I' = 3.1\mu A/cm^2$ and annealed at 1320°C for 6hrs in nitogen,

d) cross-section micrograph, at a <110> pole, showing an example of the small stacking fault defects in the sample implanted with ^{18}O at 70keV, $\Phi = 0.1x10^{18}O/cm^2$, $T_i = 680°C$ and $I' = 3.1\mu A/cm^2$ after annealing at 1360°C for 6hrs in nitrogen. Note the absence of any oxide precipitates.

For all samples the small stacking fault defects are only observed at depths less than maximum depth of the as-implanted oxygen distribution.

Figure 4.27,

a) cross-section micrograph, at a <110> pole, of a "pit" in the surface Si layer, in the sample implanted at 200keV, $\Phi = 1.6x10^{18}O/cm^2$, $T_i = 700°C$, $I' = 5.6\mu A/cm^2$ and annealed at 1320°C for 6hrs in nitrogen,

b) plan-view micrograph, at the [001] pole, of a "pit" (P) in the surface Si layer, in the sample implanted at 90keV, $\Phi = 0.9x10^{18}O/cm^2$, $T_i = 680°C$, $I' = 3.75\mu A/cm^2$ and annealed at 1320°C for 6hrs in nitrogen,

c) plan-view micrograph, at the [001] pole, of the area around the pit shown in b) showing the circular shape of the region of buried oxide etched away by dipping the sample in HF,

d) plan-view micrograph, at the [001] pole, of the same sample as in b) and c) at low magnification showing it is easy to count the number of etch circles over a wide area and hence calculate the pit density.

Figure 4.26

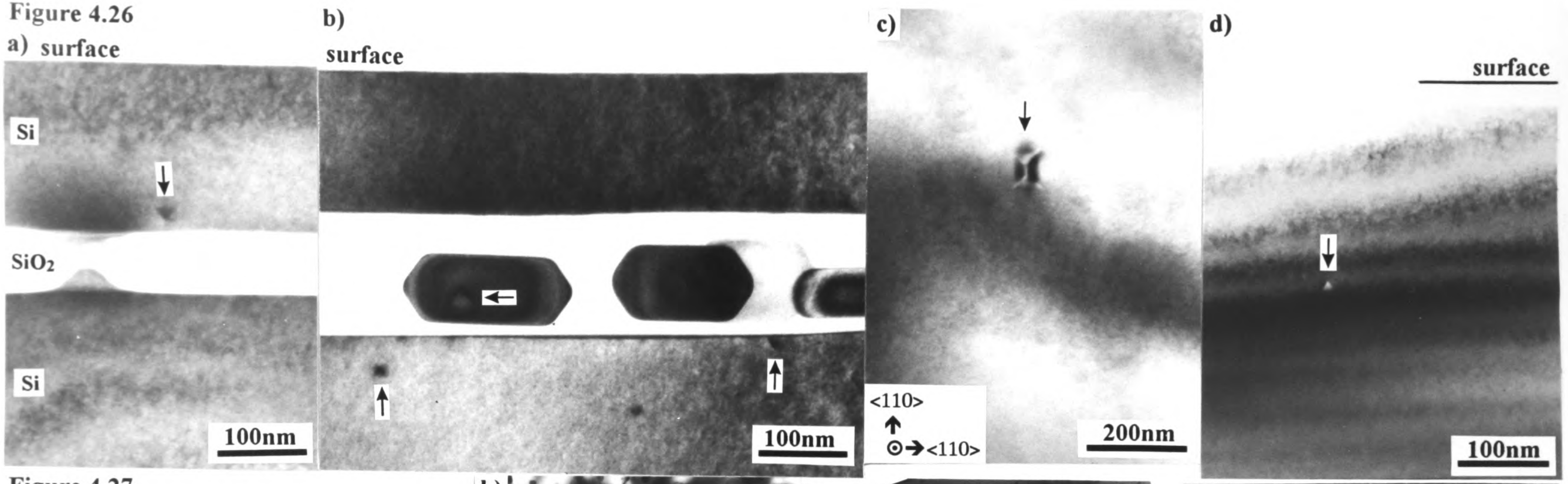

Figure 4.27

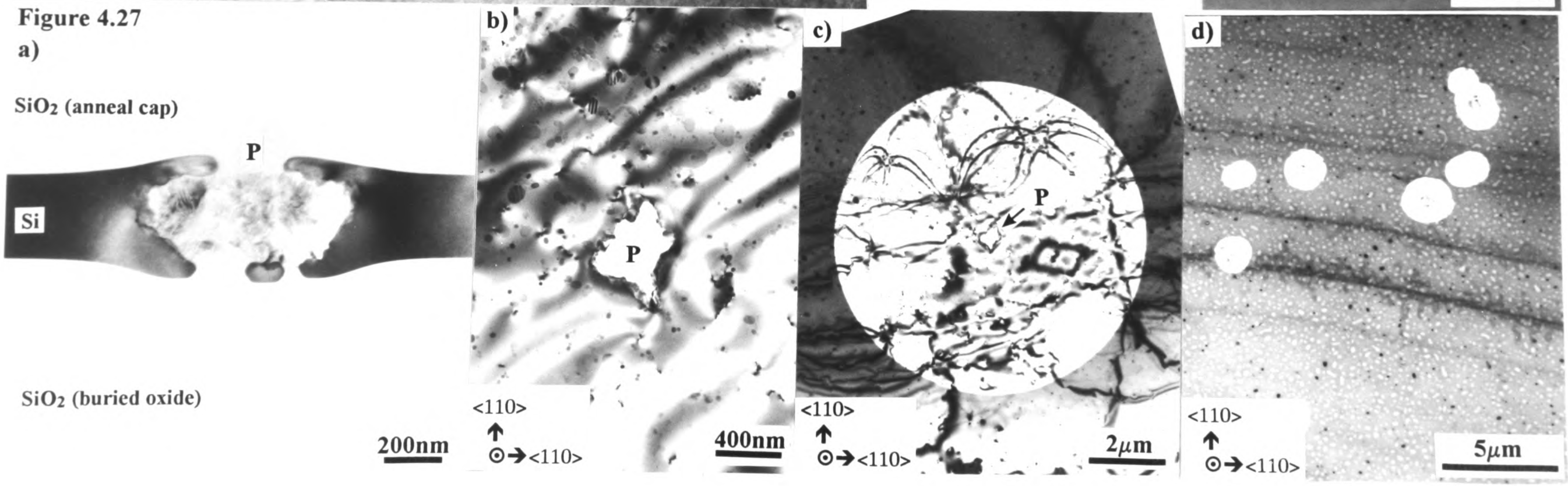

two SF defects is of the order 10^7-10^8/cm^2. In the surface Si layer one or two of these SF defects are observed in some samples while in others none are observed. This suggests the densities are around the limit detectable by c.s. TEM and are therefore of the order of 10^6-10^7/cm^2. In c.s. the apexes of the SFP or SFT, in both the surface Si layer and the substrate, point both towards and away from the buried oxide layer. In <110> c.s. the SFT and SFP can not be distinguished. In <001> p.v. the projected image of the SFP and SFT can both be square, but the edges of the squares for the SFP are parallel to the <110> directions in the (001) plane (fig. 4.26), while the edges of the square for the SFT are parallel to the <100> directions in the (001) plane. In p.v. SFP and SFT can also be distinguished in the standard way, by observing which part of the defects go invisible under g{220} two beam diffraction conditions. The samples in which the SF defects were observed in p.v. suggest that the SFP are more common than the SFT. Some of the SF defects observed are rectangular in p.v. and these can not be SFT. No "elongated hexagon" SFT defects[33] were observed in this work.

In the sample implanted with ^{18}O (H151), in which after annealing no buried oxide was observed, small SFT or SFP (height $\approx$7nm, width $\approx$10nm) in c.s. with apexes pointing both towards and away from the surface are present (fig. 4.26). The density of these SF defects is 1x10^8/cm^2. The SFT or SFP are present at depths between 200nm and 270 nm (fig. 4.26). This compares to the depths of between 150nm and 225nm in which oxide is observed in the sample implanted with ^{16}O (H36a), using the same implantation and anneal conditions, and 300nm, the maximum depth the as-implanted oxygen distribution is above the background oxygen concentration detectable by the SIMS (6x10^{19}/cm^3) for this dose (fig. 3.30). Hence these SF defects are present only at depths at which oxygen was present after implantation.

SFT and SFP have also been reported for higher dose implants at 200keV using the commercial Eaton Nova NV200 dedicated oxygen implanter[34]. The SFT and SFP could be small oxidation induced SF, and therefore the SF would be of interstitial (extrinsic) type. Alternatively during the segregation of the oxygen to the buried oxide or the cap by the Ostwald ripening process, when the oxide precipitates dissolve they will emit Si_v which could coalescence to form the SFT and SFP. Hence in this case the SF would be vacancy (intrinsic) type. Therefore it is conceivable that the SFT and SFP could be of either type. The defect type could be determined

by c.s. HREM, but the small size and low density of the SFT and SFP reduce the probability of producing a TEM c.s. in which the defects are present in thin enough material for interpretable HREM images to be formed.

4.7.2 Pits

In some samples, e.g. 90keV, $\Phi = 0.9x10^{18}O/cm^2$, after annealing in the N_2 ambient, pits are present in the surface Si layer (fig. 4.27). The pits, typically $\leq 0.5\mu m$ across, contain polycrystalline material, go through the surface Si layer to the buried oxide layer (fig. 4.27a) and are irregular in shape (figs. 4.27a & 4.27b). When the samples are dipped in buffered HF the material within the pits is etched away (fig. 4.27b). As the pits reach the buried oxide, by dipping the samples in buffered HF some of the buried oxide is etched away. As discussed above in p.v. the shape of the region of buried oxide etched away is a circle, centred on the pit (fig. 4.27c). Note that in the sample shown in Figs 4.27b & 4.27c the back of the sample has been thinned away to the buried oxide layer, by the ion beam thinning process and hence no structure is visible through the pit shown. Hence after the HF dip for every pit a circle is present (fig. 4.27d). This makes it easier to count the number of pits at low magnifications in p.v.. Using this technique the pit density was found to vary between samples from $<10^5/cm^2$ to $5x10^7/cm^2$. In the example shown in Fig. 4.27d the pit density is $3x10^6/cm^2$.

In some of the samples annealed in the N_2 ambient in which pits are absent, polycrystalline defects are present in the cap (fig. 4.28). Although not identified these defects are thought to be silicon nitride or silicon oxynitride. In the few c.s. samples in which these polycrystalline defects are present they are not observed to reach as far as the surface Si layer, but if in other samples they were to reach the surface Si layer they may play a role in the generation of the pits. Alternatively, for high temperature anneals if the partial pressure of oxygen is too low the SiO_2 cap can be broken down into silicon monoxide which evaporates exposing the Si, which is then etched leading to the formation of a pit. The pits were observed in c.s. in only one sample (H128) and for this sample the TEM c.s. was prepared without removing the anneal cap. The cap above the pits in this sample is intact and does not contain polycrystalline defects. This suggests that the previous two mechanisms discussed are not the

origin of the pits. The shape of the pits in c.s. suggests that the material within these pits has formed within the surface Si layer, causing the Si above and below to swell (fig. 4.27a). This suggests that the origin of some of the pits may lie in contamination introduced below the final surface during implantation. This contamination may be unintentionally implanted or may be contamination on the surface near the start of the implant which has subsequently been incorporated within the surface Si layer as the surface epitaxially grows during implantation. This contamination may then react with the Si and buried oxide/cap during the high temperature anneal and the material is then dissolved by the HF dip, resulting in the pits. The observation that the material within the pits is easily removed by dipping in HF suggests that the material contains some form of oxide.

Hence the origin of the pits is not completely understood, but their presence is obviously undesirable and reinforces the importance of good control of the parameters during fabrication.

4.7.3 Stacking faults below the buried oxide layer

Stacking faults (SF) are sometimes observed in the Si below the buried oxide layer (fig. 4.29). All the SF are present at the interface of the buried oxide layer and the substrate and they may have nucleated at this interface. The SF probably form from the high concentration of Si_i at this depth after implantation and hence would be similar to oxidation induced SF in bulk Si[35]. The presence of SF at this depth would not be harmful to any subsequent device fabrication. Some of the SF are decorated with precipitate colonies which have dislocations associated with them (fig. 4.29). Plan view SADP from an area containing a precipitate colony, i.e. many precipitates, contains extra diffraction spots in the position of Si **g**{200} spots (fig. 4.29e) and energy dispersive x-ray (EDX) analysis suggests that copper is present in the precipitate colony (fig. 4.30). The stable chemical composition of copper silicide precipitates at room temperature is Cu_3Si with a base-centered (C) orthorhombic lattice[38] but metastable copper silicide precipitates with chemical composition CuSi and a diamond cubic lattice, isomorphous with the Si lattice and lattice parameter (5.72Å) similar to that of Si have been reported[36]. Hence the colonies are thought to be copper silicide precipitates[36,37,38,39]. In this work the Si wafers were purchased from two vendors. The copper colonies are only present in the wafers purchased

Figure 4.28 Cross-section micrograph at a <110> pole showing an example of the polycrystalline defects (A) observed in the surface of the SiO_2 anneal cap after annealing at 1360°C for 6 hours in nitrogen (this sample implanted at 90keV, $\Phi = 0.43x10^{18}O/cm^2$ (^{16}O), T_i = 680°C and I' = 3.75μA/cm^2).

Figure 4.29,

a) cross-section micrograph at a <110> pole showing an undecorated stacking fault (SF) below the buried SiO_2 layer in the sample implanted at 200keV, $\Phi = 0.6x10^{18}O/cm^2$, T_i = 680°C and I' = 5.6μA/cm^2 and annealed at 1320°C for 6hrs in nitrogen,

b) & c) cross-section micrographs at a <110> pole showing stacking faults (SF) below the buried SiO_2 layer, decorated with precipitate colonies (C) and associated dislocations (D), in samples implanted at 90keV, $\Phi = 0.4x10^{18}O/cm^2$ and $0.35x10^{18}O/cm^2$ respectively, T_i = 680°C and I' = 3.75μA/cm^2 and annealed at 1300°C for 6hrs in argon + ½ % oxygen,

d) plan-view micrograph at the [001] pole of a precipitate colony (C) associated with stacking faults (to improve the visibility of the precipitates the diffraction conditions were chosen so that stacking fault fringes are invisible), in the sample implanted at 70keV, $\Phi = 0.5x10^{18}O/cm^2$, T_i = 680°C and I' = 3.1μA/cm^2 and annealed at 1300°C for 6hrs in argon + ½ % oxygen,

e) plan-view long exposure SADP, at the silicon [001] pole, from a region of the same sample as in d) containing a large precipitate colony, showing extra weaker diffraction spots, originating from the precipitates, in the positions of silicon **g**{200} spots (T = transmitted spot).

Figure 4.28

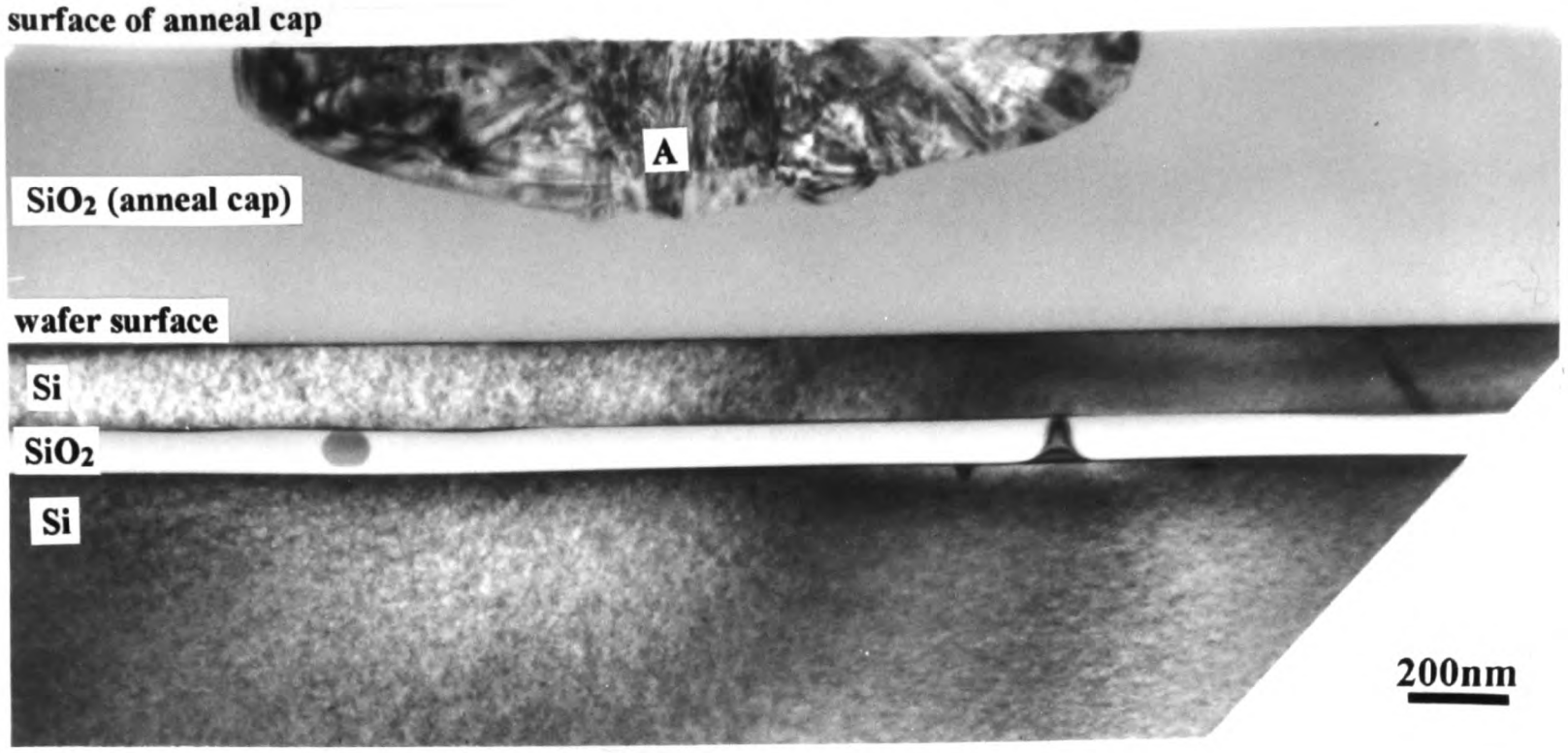

Figure 4.29

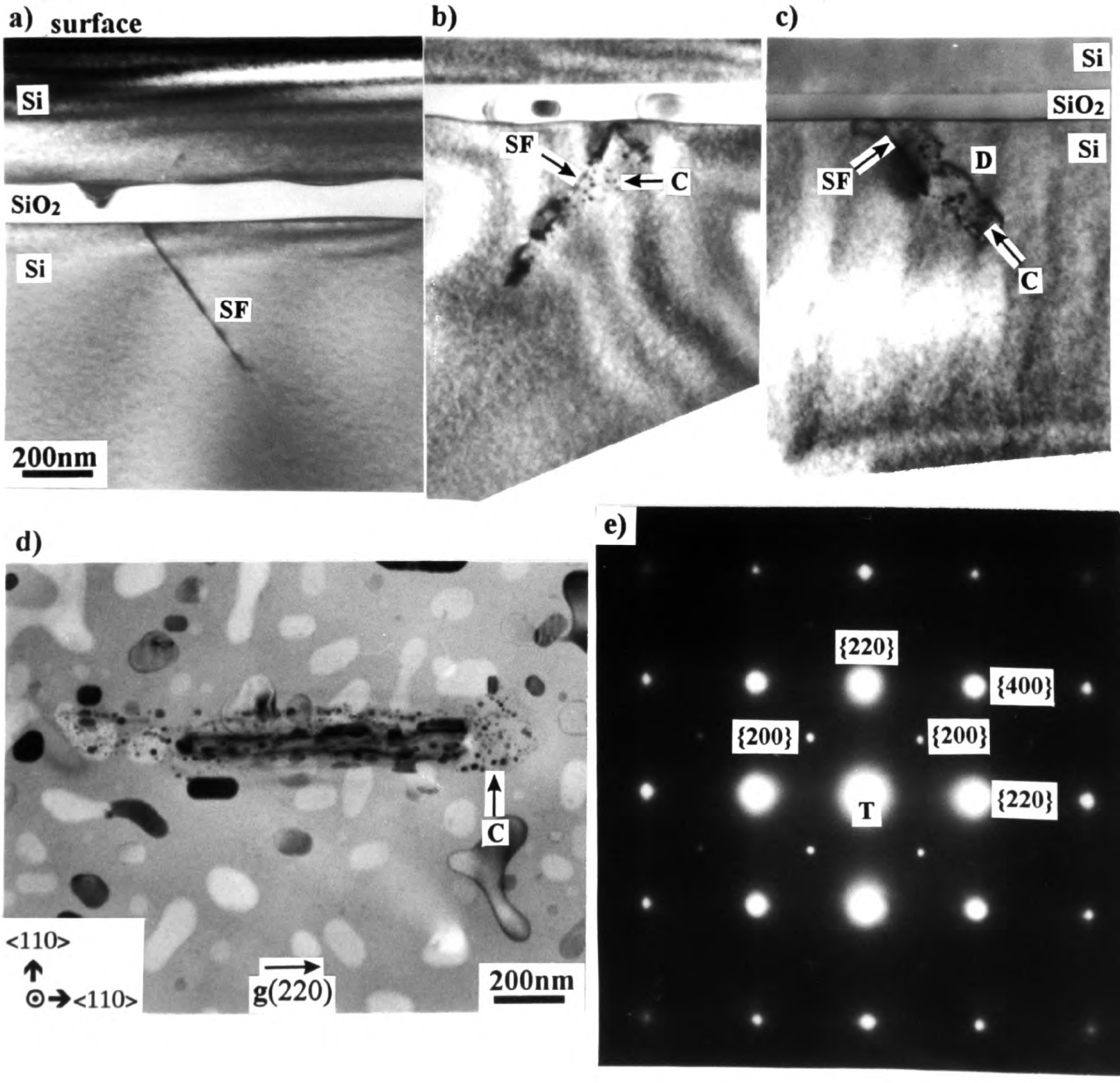

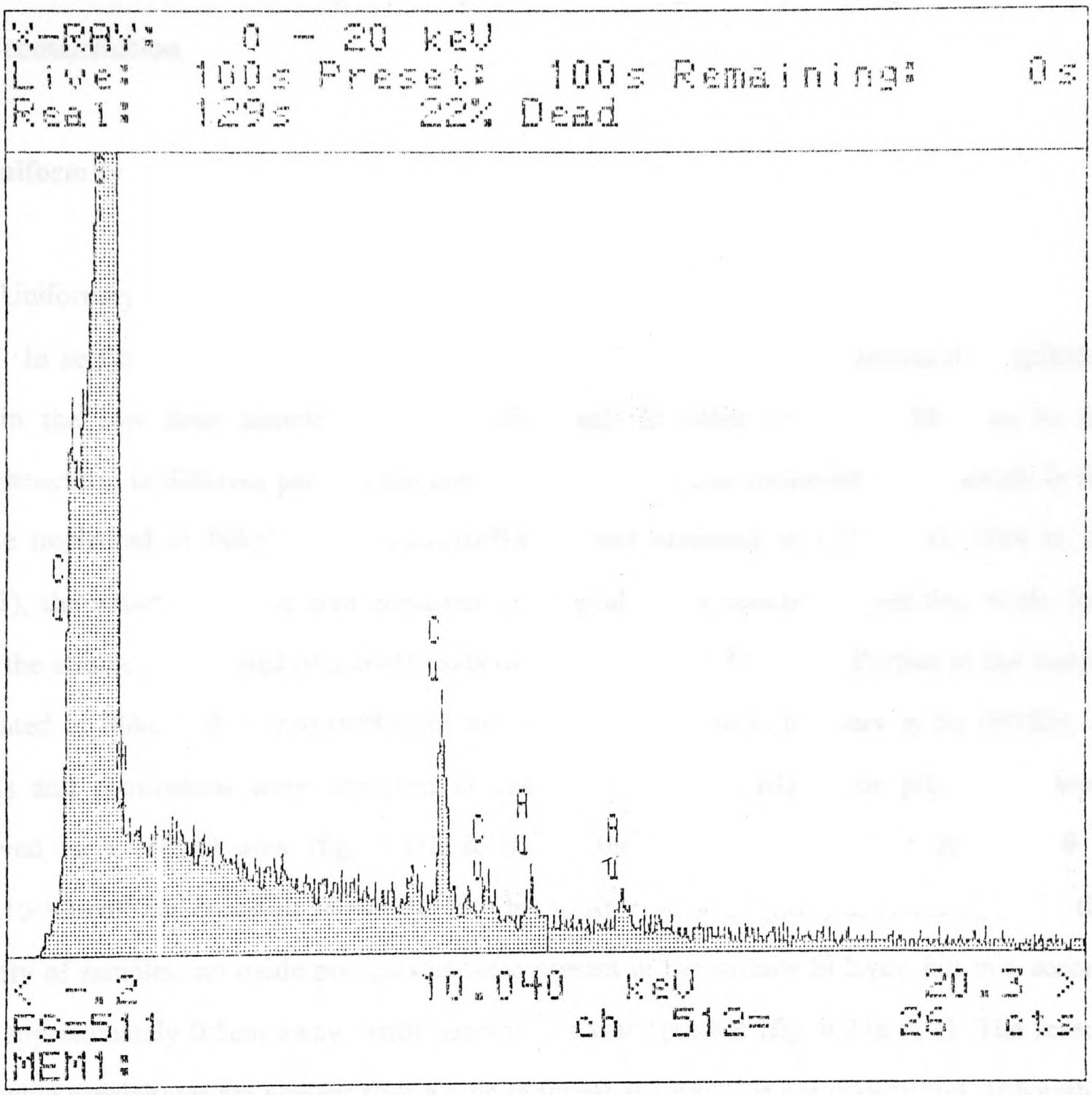

Figure 4.30 EDX spectrum from a region of Si containing a large precipitate colony in a plan-view sample (90keV, $\Phi = 0.5 \times 10^{18} O/cm^2$, $T_i = 680°C$, $I' = 3.1 \mu A/cm^2$, annealed at 1300°C for 6hrs in argon + ½ % oxygen). The sample was mounted on a gold (Au) TEM grid.

from one of the vendors and hence the origin of the copper is thought to be contamination of the wafers prior to purchase. As SF are sometimes observed without the precipitates and dislocations, but the precipitate colonies are only observed connected with a SF, it is considered that the SF act as nucleation sites for the formation of the copper colonies. Hence the presence of SF below the buried oxide layer are a potential advantage if they act as gettering sites for metal contamination.

4.8 Uniformity and Reproducibility

4.8.1 Uniformity across implanted area

In section 4.2 the non-uniform distribution of the oxide structure across the implanted area in the low dose sample H36a was discussed. In other samples differences in the microstructure, in different parts of the implanted area were also observed. For example in the sample implanted at 90keV, Φ = $0.29x10^{18}O/cm^2$ and annealed at 1320°C for 6hrs in N_2 (H123), the structure in one area consisted of an oxide layer containing pinholes, while 1cm away the structure consisted of a continuous oxide layer (fig. 4.31a & b). Further in the sample implanted at 90keV, Φ = $0.4x10^{18}O/cm^2$ and annealed at 1320°C for 6hrs in N_2 (H122), Si islands and protrusions were observed in one area, while no islands or protrusions were observed in a second area (fig. 4.31c & d). In the sample implanted at 200keV, Φ = $0.56x10^{18}O/cm^2$ and annealed at 1300°C for 6hrs in Ar + ½ % O_2 (H93) in one area, as for the majority of samples, no oxide precipitates were present in the surface Si layer, but in a second area, approximately 0.5cm away, oxide precipitates were present (fig. 4.31e & f). The reason why oxide precipitates are present after a 6 hour anneal at 1300°C is not understood, although if the anneal temperature was less than the nominal value or the anneal time was significantly shorter than the nominal time, these could explain their presence.

These differences in structure may be explained by either lateral non-uniformities in the implant or anneal conditions, e.g. in the implanted dose, or uniform implantation and non-uniform lateral redistribution of the oxygen during annealing. It is estimated that during implantation the temperature of the edge of the implanted area is 25°C lower than the

Figure 4.31 Cross-sections micrographs from two different regions from samples implanted,
a) and b) at 90keV, $\Phi = 0.29x10^{18}O/cm^2$, $T_i = 680°C$, $I' = 3.75\mu A/cm^2$ and annealed at 1320°C for 6hrs in nitrogen,
c) and d) at 90keV, $\Phi = 0.4x10^{18}O/cm^2$, $T_i = 680°C$, $I' = 3.75\mu A/cm^2$ and annealed at 1320°C for 6hrs in nitrogen,
e) and f) at 200keV, $\Phi = 0.56x10^{18}O/cm^2$, $T_i = 650°C$, $I' = 5.6\mu A/cm^2$ and annealed at 1300°C for 6hrs in argon + ½ % oxygen (O = oxide precipitates),
showing variations in the microstructure across the implanted area after annealing.

a)
surface
Si
SiO2
Si
200nm
b)
Si
SiO2
Si
c)
surface
Si
SiO2
Si
d)
Si
SiO2
Si
e)
surface
Si
SiO2
Si
200nm
f)
O
O
Si
SiO2
Si

temperature of the centre of the implant (680°C or 700°C)[43]. Further, even if the implant and anneal conditions are uniform the resulting oxygen distribution is the result of many random collision events within the Si and this could lead to regions containing slightly different as-implanted microstructures. Therefore if the post-anneal microstructure is very sensitive to the as-implanted microstructure this may also result in different microstructure in different parts of the implanted area. These explanations may also explain for sample H136, the thinner buried oxide layer and the presence of the Si pinholes in the sample annealed for the RTA plus conventional anneal (H136e), compared to the sample just conventionally annealed (H136b) (table 4.6).

After annealing the majority of the samples in this work, the surface of the implanted area is coloured due to the interference of incident light reflected from the surface and the two buried oxide/Si interfaces[40,41]. In some samples the implanted area after annealing showed variations in the colour across the implanted area, suggesting variations in either the Si or oxide layer thicknesses or in the distribution of Si islands within the oxide layer. These variations in colour and hence structure[40,41] can also be explained in terms of the same mechanisms discussed in the previous paragraph.

Due to beam instabilities and related difficulties associated with the high oxygen beam currents used in this work both small lateral variations in the implanted dose and/or the as-implanted microstructure are a possibility. The lateral variation in structure for a nominal constant dose or the possibility of a lateral variation in dose, makes it difficult to identify the true microstructure for a particular implanted dose, or to estimate critical doses such as ${}^{A}\Phi_{c}$, from the observed microstructure. Further because the RBS measurements of the retained dose and TEM analysis of the microstructure are performed on different parts of the implanted area, this could lead to inconsistencies between the measured retained dose and the dose actually implanted in the area investigated by TEM. For each of the samples described above (H123, H122 & H93) the microstructure first described is from areas closest to the centre of the implanted area and hence has been taken as the appropriate structure for comparing these samples with the other samples in the previous sections in this chapter.

4.8.2 Reproducibility from implant to implant

The potential differences between the retained doses and nominal doses of up to 30% makes it difficult, with the equipment used in this work, to reproduce a particular implanted dose. This is a problem because for some aspects of the annealed structure, i.e. $^{A}\Phi_c$, the dose window and the threading dislocation density are very sensitive to the implanted dose. For example at 70keV a 10% difference between the nominal and actual implanted doses, when the nominal dose is just $>^{A}\Phi_c$ ($0.33x10^{18}O/cm^2$), can make the difference between the optimum structure for subsequent device fabrication and a discontinuous oxide layer, which is undesirable for device fabrication. It is considered that this dosimetry problem is more to do with the particular research implanter used during this work (section 2.2), rather than a fundamental difficulty in controlling oxygen doses at these energies. The accurate control of oxygen doses has already been achieved on the high energy (>125keV) Eaton Nova NV200 dedicated oxygen implanter[42] which suggests that in principle the dose could also be controlled at these lower energies. Hence although the dosimetry problem has made this work more difficult it is not thought to be a problem that would prevent this approach to forming thin-film SIMOX structures from being adopted commercially.

4.9 Summary

The main new work of the present chapter is summarised as follows. The first detailed TEM investigation reported on annealed SIMOX structures;

a) formed at energies of 90keV, 70keV and 50keV and annealing at 1320-1360°C for 6hrs, as a function of the implanted dose for both N_2 and argon + ½ % O_2 anneal ambients,

b) formed by implanting lower than standard doses ($<1.4x10^{18}O/cm^2$) at 200keV and annealing at 1320-1360°C for 6hrs for both N_2 and argon + ½ % O_2 anneal ambients,

c) a comparison of the influence of nitrogen and argon anneal ambients at both high (200keV) and low energies (90keV & 70keV) after implanting doses just greater than the minimum for forming a continuous buried SiO_2 layer after annealing at each energy, and annealing at 1300°C or 1320/60°C for 6hrs,

d) the influence of time-averaged beam current densities, between 2.5μA/cm^2 and 6.25μA/cm^2 on the annealed microstructure (1320-1360°C for 6hrs in nitrogen) for a constant implantation temperature of 680°C, dose $\approx$0.7x10^{18}O/cm^2 and energy 200keV,

e) the influence of graded energy implants at low energies (65keV, 70keV & 75keV) on the annealed (1320-1360°C for 6hrs in nitrogen) microstructure, in particular on the morphology of the Si islands present within the thin (<100nm) buried SiO_2 layer.

f) the use of rapid thermal anneals (1300°C, 1minute), at doses just above the minimum dose to form a continuous buried SiO_2 layer after annealing, at both low (90keV) and high (200keV) energies, to redistribute the oxygen prior to the conventional anneal (1360°C, 6hrs) and hence reduce the density or size of the Si islands within the buried SiO_2 layer.

and;

a) thin-film SIMOX substrates consisting of a thin (<160nm) surface Si layer above a thin (75 to 100nm) buried SiO_2 layer, suitable for the fabrication of "fully depleted" high performance CMOS devices have been successfully fabricated at energies of 90 and 70keV,

b) thin-film SIMOX substrates, consisting of a thin (110nm) buried SiO_2 layer below a standard thickness (400nm) surface Si layer, suitable for fabricating radiation hard circuits with reduced circuit self-heating have successfully been fabricated at energies of 200keV,

c) the optimal doses for forming after annealing both the thin-film SIMOX substrates described in e) and f) with the lowest densities of both the Si islands within the buried oxide layer and the threading dislocations within the surface Si layer have been determined as doses just larger than the minimum dose for forming a continuous buried oxide layer after annealing for any particular energy,

d) the likely mechanisms of the formation of the buried oxide layer during annealing and the origin of threading dislocations present after annealing, including the role of the as-implanted microstructure have been described.

4.10 References

[1] Y Li, Department of Materials, Imperial College, private communication.

[2] C Jaussaud, J Stoemenos, J Margail, A M Papon & M Bruel, Vacuum 42, p341 (1991).

[3] J Burke, The Kinetics of Phase Transformations in Metals (Pergamon, London, 1965).

[4] R C Newman, M J Binns, W P Brown, F M Livingston, S Meroloras, R J Steward, J G Wilkes, Physica 116B, p264 (1983).

[5] J Vanhellemont & C Claeys, J. Appl. Phys. 62, p3690 (1987).

[6] A K Robinson, C D Marsh, U Bussmann, J A Kliner, Y Li, J Vanhellemont, K J Reeson, P L F Hemment & G R Booker, Nucl. Inst. & Meths. B55, p555 (1991).

[7] S Nakashima & K Izumi, J. Mat. Res. 8, p523 (1993).

[8] S Nakashima & K Izumi, Nucl. Inst. & Meths. B55, p847 (1991).

[9] J C Mikkelson, Appl. Phys. Lett. 40, p336 (1986).

[10] G Brebec, R Seguin, J Bevenot & C Martin, Acta Metal 28, p327 (1980).

[11] M Stavola, J R Patel, L C Kimerling & P E Freeland, Appl. Phys. Lett. 42, p73 (1983).

[12] T Y Tan & C Y Kung, J. Appl. Phys. 59, p917 (1986).

[13] J Stoemenos, J Margail, C Jaussaud, M Dupuy & M Bruel, Appl. Phys. Lett. 48, p1470 (1986).

[14] R J Jaccodine, J. Electrochem. Soc. 110, p524 (1963).

[15] E A Irene, E Tierney & J Angilello, J. Electrochem. Soc. 129, p2594 (1982).

[16] H Bender, Phys. Status Solidi A86, p245 (1984).

[17] Y Li, J A Kilner, R J Chater, A Nejim, P L F Hemment, C D Marsh & G R Booker, to be published in Nucl. Inst. & Meths., (1993).

[18] K J Reeson, A K Robinson, P L F Hemment, C D Marsh, K N Christensen, G R Booker, R J Chater, K J Kilner, G Harbeke, E F Steigmeir & G K Celler, Microelectron. Eng. 8, p163 (1988).

[19] A Yoshino, Proc. Electrochem. Soc. 92-13, p321 (1992).

[20] A De Veirman, J Van Landuyt, J Vanhellemont, H E Maes & K Yallup, Vacuum 42, p367 (1991).

[21] S Visitserngtrakul, S J Krause, B F Cordts & P Roitman, Vacuum 42, p353 (1991).

[22] J R Davis, K J Reeson, P L F Hemment & C D Marsh, Elec. Dev. Letts. 8, p291 (1987).

[23] S Serapin, S J Krause, P Roitman & B S Simons, Appl. Phys. Lett. 59, p3003 (1991).

[24] A Hara, T Fukuda, T Miyabo & I Hirai, Appl. Phys. Lett. 54, p626 (1989).

[25] S I Raider, R A Gdula & J R Petrak, Appl. Phys. Lett. 27, p150 (1975).

[26] S Hall, Dept. of Electronic Engineering, University of Liverpool, private communication.

[27] L F Giles, Dept. of Electronic Engineering, University of Surrey, private communication.

[28] L F Giles, A Nejim & P L F Hemment, Mats. Chem.& Phys. 35, p129 (1993).

[29] A Nejim, Dept. of Electronic Engineering, University of Surrey, private communication.

[30] S Krause, J Lee, J Pak, P Roitman & M El-Ghor, Proc. of the Electrochem. Soc. 92-13, p221 (1992).

[31] Y Li, J A Kilner, R J Chater, A Nejim, P L F Hemment, C D Marsh & G R Booker, accepted for publication in Appl. Phys. Lett. (1993).

[32] J Margail, LETI, CEN, Grenoble, France, private communication.

[33] J Silox & P B Hirsch, Phil. Mag. 4, p71 (1959).

[34] J Margail, J M Lamure, A M Papon & J Stoemenos, Proc. of the Electrochem. Soc. 92-13, p207 (1992).

[35] S M Sze, *VLSI Technology* (McGraw-Hill International, Singapore, 1988).

[36] G Das, J. Appl. Phys. 44, p4459 (1973).

[37] E Ness & J K Solberg, J. Appl. Phys. 44, p486 (1973).

[38] J K Solberg, Acta Cryst. A34, p684 (1978).

[39] M D de Coteau, P R Wilshaw & R Falster, Phys. Stat. Sol. A, p403 (1990).

[40] K J Reeson, A J Criddle, P Pearson, R J Chater, K Christensen, J Alderman, G R Booker & J A Kilner, Nucl. Inst. & Meths. B55, p718 (1991).

[41] A J Criddle, P J Pearson, K J Reeson, A K Robinson, P L F Hemment, C D Marsh & G R Booker, Mats. Sci. & Eng. B12, P185 (1992).

[42] J P Ruffel, D H Douglas-Hamilton & K Izumi, Nucl. Inst. & Meths. B21, p229 (1987).

[43] P L F Hemment, Dept. Electronic Engineering, University of Surrey, private communication.

[44] Y Li, J A Kilner, A K Robinson, P L F Hemment & C D Marsh, J. Appl. Phys. 70, p3605 (1991).

Chapter 5

Modelling of the Layer Thicknesses after Annealing

5.1 Buried Oxide Layer

If, after annealing, all the oxygen is present as SiO_2 in the buried SiO_2 layer then the relationship between the dose (Φ) and the thickness of the buried SiO_2 after annealing ($^{A}T_{SiO_2}$) can be given simply by,

$$^{A}T_{SiO_2} = \frac{\Phi Z}{2 \rho N_{avo}} \quad \text{.....Eq. 5.1}$$

where Z is the atomic weight of SiO_2 in grams, ρ the density of SiO_2, N_{avo} Avogadros constant and the factor ½ is because two oxygen ions are incorporated in each SiO_2 molecule. Therefore assuming the density of the buried SiO_2 is the same as thermal SiO_2 (2.2 g/cm^3 [1]) the thickness of the buried SiO_2 layer can be predicted for any dose.

When a buried oxide layer forms, one way of interpreting the process is that the oxide replaces a layer of Si of the same thickness, where some of the Si layer is incorporated in the oxide and the remainder is ejected as Si_i to provide the accommodation volume for strain free precipitation. The thickness (A) of a layer of Si containing the same number of Si atoms as those incorporated in a layer of oxide, if the oxide is formed with a dose Φ, is given by,

$$A = \frac{\varepsilon \Phi}{N} \quad \text{.....Eq. 5.2}$$

where ε is the number of Si atoms incorporated per incident oxygen ion and N is the atomic density of Si. The thickness (B) of a layer of Si containing the same number of Si atoms as those ejected as Si_i in providing the accommodation volume is given by,

$$B = \frac{\beta \Phi}{N} \quad \text{.....Eq. 5.3}$$

where β is the number of Si_i ejected per incident oxygen ion for strain free precipitation. The total thickness of the Si is simply A + B, which is equal to the thickness of the oxide. Hence the thickness of an oxide layer after annealing ($^{A}T_{oxide}$) can also be given by,

$$^{A}T_{oxide} = \frac{\Phi (\beta + \varepsilon)}{N} \quad \text{.....Eq. 5.4}$$

If the oxide layer is stochiometric SiO_2, $\varepsilon = 0.5$ and the thickness of the SiO_2 is given by,

$$^{A}T_{SiO_2} = \frac{\Phi\,(\beta + 0.5)}{N} \quad \text{.....Eq. 5.5}$$

and for strain free formation of SiO_2, $\beta = 0.625$ (section 3.10) and therefore,

$$^{A}T_{SiO_2} = \frac{1.125\,\Phi}{N} \quad \text{.....Eq. 5.6}$$

Eq. 5.1 & Eq. 5.6 are different expressions for the same model and as the value of β was derived from the experimentally measured value of the density of SiO_2, the two equations should give identical answers. Table 5.1 compares the predicted widths of the SiO_2 layer from Eq. 5.1 & Eq. 5.6. The small discrepancy between the predictions of the two equations (<1%) is probably because the actual values of ρ (SiO_2) and β are slightly different from the quoted values. Note that both expressions (Eq. 5.1 & Eq. 5.6) for $^{A}T_{SiO_2}$ are independent of the energy used.

Fig. 5.1 shows Eq. 5.6 plotted as a function of the dose and compares the predictions with the experimental results for all four energies. For high doses the predicted values are in good general agreement with the experimental results. For low doses the thin SiO_2 layers contain Si islands, which is why some of the experimentally measured thicknesses are larger than those predicted by the model. The discrepancies between the model and the experimental points may also arise because a) during annealing, some of the oxygen segregates to the SiO_2 cap, resulting in a thinner than predicted buried SiO_2 layer, b) a Si-rich oxide is formed, i.e. $\varepsilon > 0.5$, resulting in a thicker than predicted buried SiO_2 layer, c) some strain accompanies the formation of the SiO_2, i.e. $\beta < 0.625$, which could result in a thinner than predicted buried SiO_2 layer, d) the density of the oxide formed is different from that of thermal SiO_2, which could result in a thinner or thicker than predicted buried SiO_2 layer, e) the actual dose implanted is different from the quoted values which are plotted in Fig. 5.1, f) of errors in the measurement of $^{A}T_{SiO_2}$ (±10%) or g) of variations in the SiO_2 layer thickness across the implanted area.

For samples that contain no Si islands Eqs. 5.1 and 5.6 can also be used in conjunction with the measured layer thickness $^{A}T_{SiO_2}$ from the TEM results to estimate the implanted dose present after the annealing. This is an alternative technique to Rutherford backscattering spectroscopy (RBS) for calculating the retained dose. Hence from the TEM results it is possible without performing RBS measurements to estimate the retained dose and therefore determine if

Dose ($x10^{18}/cm^2$)	${}^{A}T_{SiO_2} = \frac{\Phi Z}{2 \rho N_{avo}}$ (nm)	${}^{A}T_{SiO_2} = \frac{1.125 \Phi}{N}$ (nm)
0.2	45.3	45.0
0.3	67.9	67.5
0.4	90.6	90.0
0.5	113	112.5
0.6	136	135
0.7	158	157.5
0.8	181	180

Table 5.1 Comparison of the predicted buried oxide layer thickness (${}^{A}T_{SiO_2}$) from the two models described in the text.

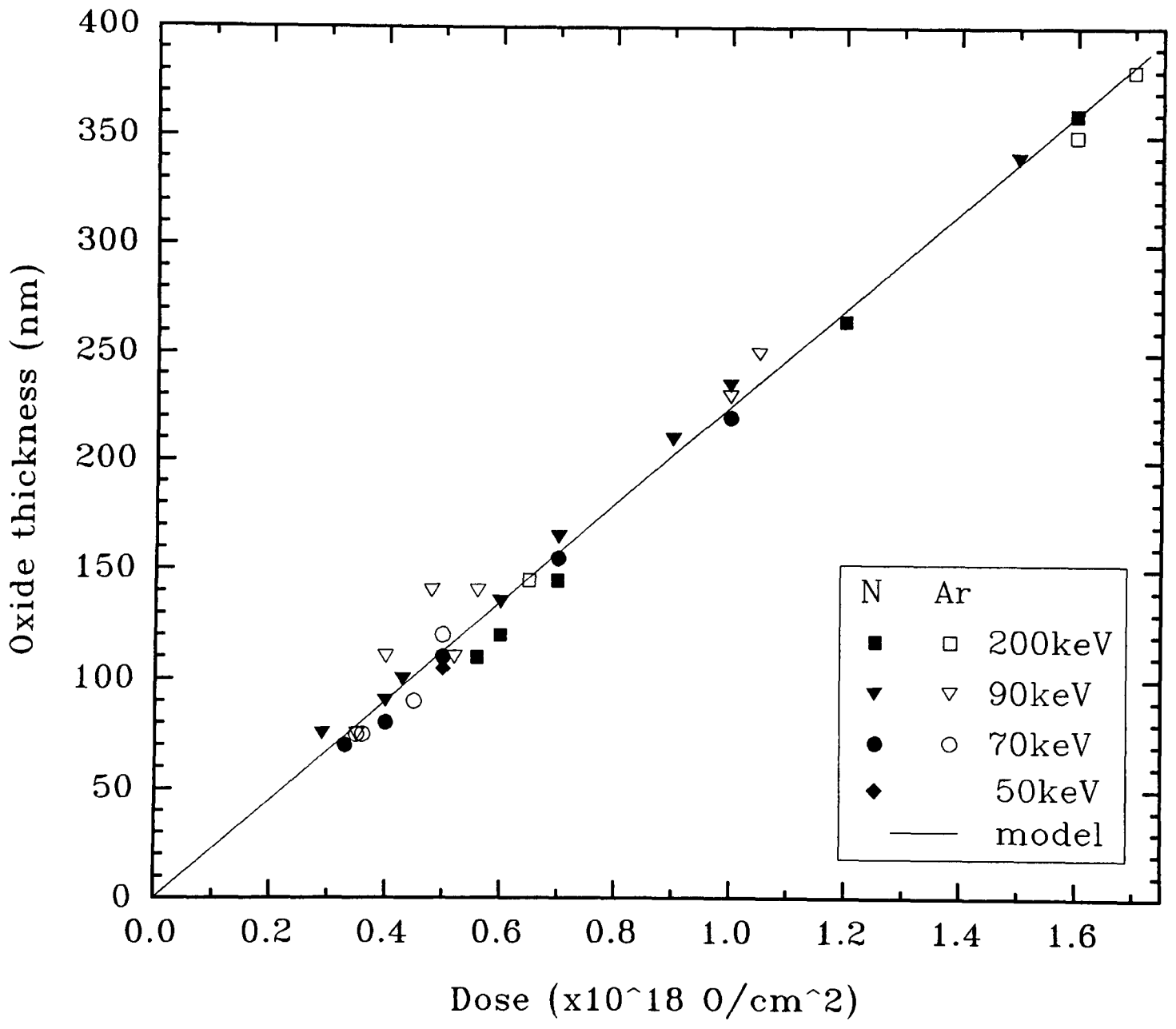

Figure 5.1 Comparison of the experimental values of the buried oxide layer thickness and the predicted values from Eq. 5.6 in the text.

any nominally implanted oxygen is not present after annealing, either due to errors in the implanted dose or oxygen lost from the Si during processing.

5.2 Surface Silicon Layer

During implantation oxide precipitates forms throughout all or most of the depth of the oxygen distribution and, as discussed previously, due to the volume difference between the Si and SiO_2 the wafer surface grows epitaxially (section 3.10.2). The formation of the buried oxide and surface Si layer is shown schematically in Fig. 5.2. The oxide layer will first form at a depth close to the peak of the oxygen concentration ($\hat{R}_p$). For doses of interest, i.e. $>{}^{A}\Phi_c$ and $<{}^{I}\Phi_c$, it is considered that the buried SiO_2 layer will first form at the depth $\hat{R}_p$. If during annealing all the oxygen is gettered to the growing buried SiO_2 layer and the distance between $\hat{R}_p$ and the mean depth of the oxygen distribution after implantation (G) is less than half the thickness of the SiO_2 layer after annealing, the SiO_2 layer that results after the anneal will be approximately centred on the mean depth of the oxygen distribution after implantation (G). Hence after annealing the thickness of the surface Si layer (${}^{A}T_{Si}$) is given approximately by,

$$ {}^{A}T_{Si} = G - \tfrac{1}{2}\,({}^{A}T_{SiO_2}) \qquad \text{Eq. 5.7} $$

The depth of G can be measured by integrating the as-implanted SIMS profiles but a more useful model would be one that enabled ${}^{A}T_{Si}$ to be predicted prior to implantation.

The computer program TRIM90[2] for oxygen into Si predicts values for the mean projected range ($\bar{R}_p$) (table 2.3), but it does not take into account the formation of the SiO_2 phase and therefore also does not take into account the growth of the surface during implantation. Hence the value of $\bar{R}_p$ predicted by TRIM90 is not equivalent to the depth G. If the surface grows a net amount S, taking account of loss by sputtering, during implantation the centre of the oxygen distribution after implantation will occur at a depth which is a distance equal to approximately half the distance S from the original depth of $\bar{R}_p$ (fig. 5.2), and therefore the relationship between the centre of the oxygen distribution after implantation (G) and the mean projected range ($\bar{R}_p$) from TRIM90 is given by,

$$ G = \bar{R}_p + \tfrac{1}{2}\,S \qquad \text{Eq. 5.8} $$

Substituting into Eq.5.7 gives,

$$^{A}T_{Si} = \bar{R}_p + \tfrac{1}{2} S - \tfrac{1}{2} (\,^{A}T_{SiO_2}) \quad \text{.....Eq. 5.9}$$

Substituting from Eq. 3.27 for S and Eq. 5.4 for $^{A}T_{SiO_2}$ gives,

$$^{A}T_{Si} = \bar{R}_p + \frac{\Phi(\beta - Y)}{2N} - \frac{\Phi(\varepsilon + \beta)}{2N} \quad \text{.....Eq. 5.10}$$

$$^{A}T_{Si} = \bar{R}_p - \frac{\Phi}{2N}(Y + \varepsilon) \quad \text{.....Eq. 5.11}$$

where Y is the sputtering yield. The value of $\bar{R}_p$ increases with increasing energy (table 2.3) and Y decreases with increasing energy (table 2.4). Hence for a fixed dose the thickness of the surface Si layer increases with increasing energy.

During implantation once a continuous SiO_2 layer forms at $\hat{R}_p$, marker layer[3,4] and isotope tracer experiments[5] have shown that further oxidation takes place at the upper interface. Hence for doses larger than the minimum dose to form a continuous SiO_2 layer ($^{I}\Phi_c$) the relationship between G and $\bar{R}_p$ given by Eq. 5.7 no longer holds. With increments of dose, above $^{I}\Phi_c$, the depth of the centre of the oxygen distribution (G) occurs at a depth further from the original position of $\bar{R}_p$ by a distance (H) and therefore the relationship between the centre of the oxygen distribution after implantation (G) and the mean projected range ($\bar{R}_p$) is given approximately by,

$$G = \bar{R}_p + \tfrac{1}{2} S - H \quad \text{.....Eq. 5.12}$$

where H is half the thickness of SiO_2 formed by the increments of dose above $^{I}\Phi_c$. Therefore using Eq. 5.4,

$$H = \frac{(\Phi - {}^{I}\Phi_c)(\beta + \varepsilon)}{2N} \quad \text{..... Eq. 5.13}$$

Substituting Eq. 5.13 for H and Eq. 3.27 for S into Eq. 5.12 gives,

$$G = \bar{R}_p + \frac{\Phi(\beta - Y)}{2N} - \frac{(\Phi - {}^{I}\Phi_c)(\beta + \varepsilon)}{2N} \quad \text{.....Eq. 5.14}$$

and substituting Eq. 5.14 for G into Eq. 5.7 gives,

$$^{A}T_{Si} = \bar{R}_p + \frac{\Phi(\beta - Y)}{2N} - \frac{(\Phi - {}^{I}\Phi_c)(\beta + \varepsilon)}{2N} - \frac{^{A}T_{SiO_2}}{2} \quad \text{.....Eq. 5.15}$$

Substituting from Eq. 5.6 for $^{A}T_{SiO_2}$ and rearranging gives,

$$^{A}T_{Si} = \bar{R}_p - \frac{\Phi(Y + \beta + 2\varepsilon)}{2N} + \frac{{}^{I}\Phi_c(\beta + \varepsilon)}{2N} \quad \text{.....Eq. 5.16}$$

Values for $\bar{R}_p$ can be obtained from TRIM90 (table 2.3), values for Y, the sputtering yield, from PROFILE CODE (table 2.4) and assuming that the strain free formation of SiO_2 occurs, then

$\varepsilon = 0.5$ and $\beta = 0.625$ (section 3.10). The values of ${}^{I}\Phi_c$ can be taken from the already performed TEM results or SIMS results. It can also be calculated using the semi-empirical equation (Eq. 5.17) given by Li *et al*[6],

$${}^{I}\Phi_c = 2.5\ {}^{SiO_2}N_O\ \Delta R_p \quad \text{.....Eq. 5.17}$$

where ${}^{SiO_2}N_O$ is the atomic density of oxygen in SiO_2 and ΔR_p the straggle of the implanted oxygen (the predictions of Eq. 5.17 are shown in table 3.7).

Fig. 5.3 shows a comparison between the predictions for ${}^{A}T_{Si}$ of Eq. 5.11 for $\Phi \leq {}^{I}\Phi_c$, and Eq. 5.16 for $\Phi > {}^{I}\Phi_c$, and the experimental results from the samples annealed in N_2. The samples annealed in Ar + ½ % O_2 are not compared with the model because of the problem of the surface Si layer in some samples being oxidised through the capping layer during the Ar + ½ % O_2 annealing. The predicted and experimental values in Fig. 5.3 show a good general agreement. The small systematic (vertical) discrepancy between the experimental and predicted thicknesses for the 200keV implants could be explained if the value predicted for $\bar{R}_p$ by TRIM90 was <5% smaller than the true value. Considering the limitations of the TRIM90 program (section 2.7) this is a reasonable explanation. For each energy the two straight lines of the model, joining at the dose of ${}^{I}\Phi_c$, result from the assumption that for doses $<{}^{I}\Phi_c$ half the oxidation takes place at depths <G and half at depths >G, and for doses $>{}^{I}\Phi_c$ all the oxidation takes place at depths <G. In reality for as the dose increases the change in the depth of the oxidation is more likely to be a gradual transition with increasing dose and hence the plot of the real surface Si layer thickness as a function of dose is expected to be a smooth curve.

When ${}^{A}T_{Si} = S$, the thickness increase due to the epitaxial growth of the surface during implantation, the original wafer surface has been consumed by the buried SiO_2 (when ${}^{A}T_{Si} = S$ this is equivalent to when half the thickness of the buried SiO_2 plus the shift in the centre of the oxygen distribution due to growth of the surface equals $\bar{R}_p$). By putting ${}^{A}T_{Si} = S$ in Eq. 5.16 and rearranging, the dose for which the original surface (os) is consumed by SiO_2 ($\Phi_{OS=0}$) is given by,

$$\Phi_{OS=0} = \frac{2\,N\bar{R}_p + {}^{I}\Phi_c(\beta + \varepsilon)}{3\,\beta + 2\,\varepsilon - Y} \quad \text{.....Eq. 5.18}$$

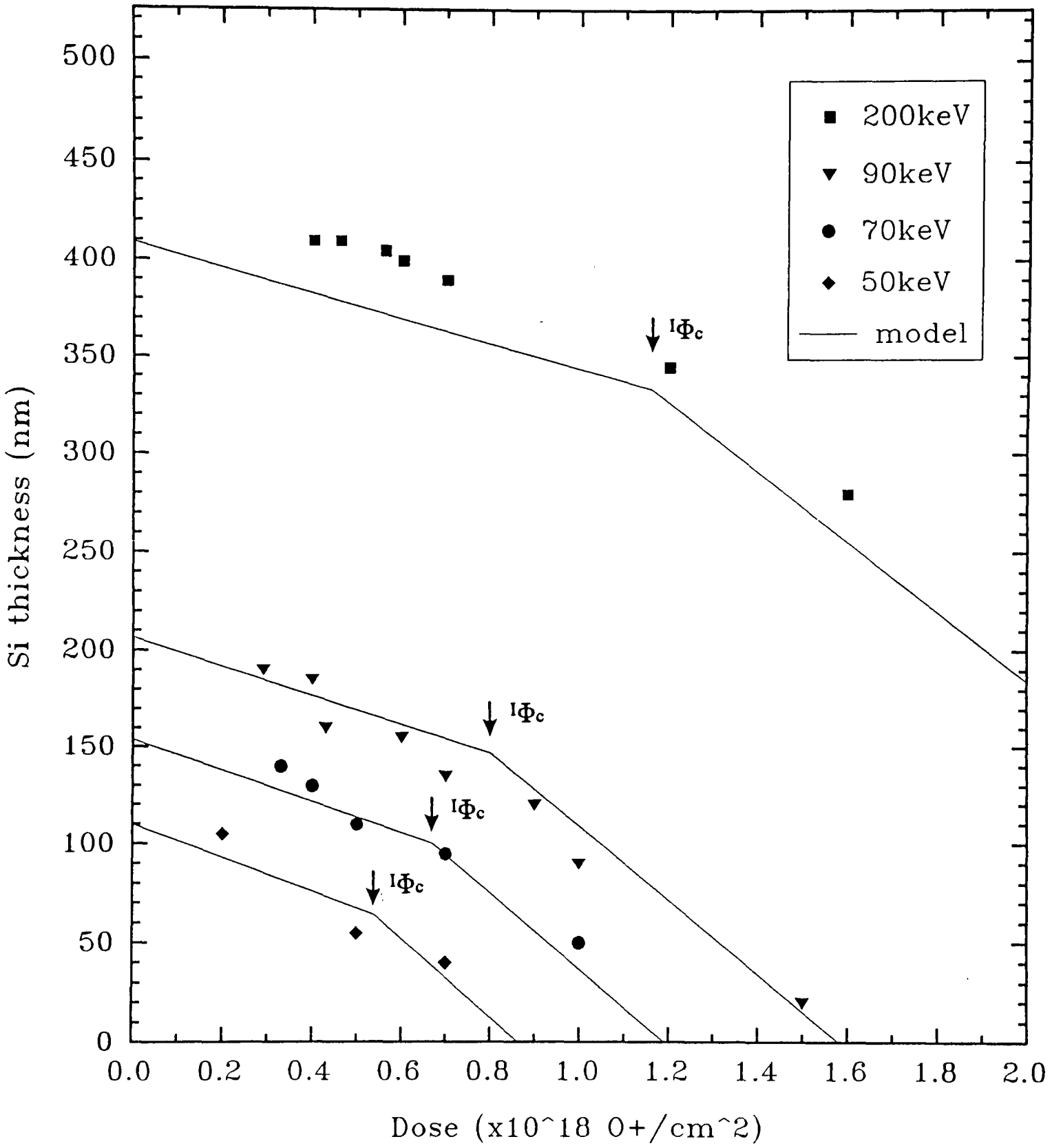

Figure 5.3 Comparison of the experimental values of the surface silicon layer thickness for the samples annealed in nitrogen at 1320°C or 1360°C for 6 hours and the predicted values from the model described in the text. The minimum doses for forming a continuous oxide layer after implantation ($^{I}\Phi_c$) at each energy are labelled.

(if Eq. 5.11 is used the values of the doses predicted are $>{}^{I}\Phi_c$ which indicates that Eq. 5.16 is the correct equation to use). The values of $\Phi_{OS=0}$ for the energies used in this work are shown in Table 5.2. By using Eq. 5.16, or Eq. 3.27, the values of ${}^{A}T_{Si}$ at these doses can also be calculated (table 5.2).

When ${}^{A}T_{Si} = 0$ all the surface Si layer is consumed by the SiO_2 and the structure now consists of a surface, rather than a buried, SiO_2 layer. By putting ${}^{A}T_{Si} = 0$ in Eq. 5.16 and rearranging, the dose for which the surface Si layer is consumed ($\Phi_{Si=0}$) is given by,

$$\Phi_{Si=0} = \frac{2\,N\,\bar{R}_p + {}^{I}\Phi_c(\beta + \varepsilon)}{\beta + 2\,\varepsilon + Y} \quad \text{.....Eq. 5.19}$$

The values of $\Phi_{Si=0}$ for the energies used in this work are shown in Table 5.2. By using Eq. 5.6 the thickness of the surface SiO_2 layer (${}^{A}T_{SiO_2}$) for these doses can also be calculated (table 5.2).

A semi-empirical equation for ${}^{A}T_{Si}$, in collaboration with the author of this thesis, is also given by Li *et al*[6]. The values for ${}^{A}T_{Si}$ from the present model and the experimental results in this work are compared to the values from the equation by Li *et al*[6] in Table 5.3. Both this model and the equation of Li *et al*[6] are in good general agreement with the experimental results accept for high doses (e.g. $1.5\text{x}10^{18}\text{O/cm}^2$ at 90keV, $1.6\text{x}10^{18}\text{O/cm}^2$ and $1.8\text{x}10^{18}\text{O/cm}^2$ at 200keV) where the model in this work, because it takes account of the change in the depth of the oxidation for doses$>{}^{I}\Phi_c$, predicts thicknesses closer to the experimental values. At the same time as this work and the derivation of the equation of Li *et al*[6], a computer program called IRIS was developed elsewhere[7,8,9] to calculate the surface Si and buried oxide layer thicknesses. This program calculates the structure after each increment of dose taking into account the formation of the oxide phase and the physical processes such as surface growth, sputtering, diffusion and segregation taking place. The predictions for the surface Si and buried oxide layers from the simple models in this work are compared to the predictions of IRIS for 200keV and 90keV in Fig. 5.4. At both energies the thickness of the buried oxide layers are in very good agreement. For the thickness of the surface Si layers the two models are in general agreement (fig. 5.4). For the doses of interest, i.e. just $\geq {}^{A}\Phi_c$, they are in good agreement. The largest discrepancies between the two models occur for the doses around ${}^{I}\Phi_c$ because with increasing

Energy (keV)	$\Phi_{OS=0}$ (x$10^{18}O^+/cm^2$)	$^AT_{Si}$ (nm)	$\Phi_{Si=0}$ (x$10^{18}O^+/cm^2$)	$^AT_{SiO_2}$ (nm)
50	0.67	37	0.86	194
70	0.89	58	1.19	268
90	1.13	85	1.58	356
200	1.98	188	3.04	684

Table 5.2 Predictions using the model in this work of the doses ($\Phi_{OS=0}$) at which the original wafer surface is consumed by the buried SiO_2 and the thickness of the epitaxially grown surface Si layers for these doses ($^AT_{Si}$), and the doses ($\Phi_{Si=0}$) for which all the surface Si layer is consumed by the SiO_2 layer, i.e. the structure becomes a surface SiO_2 layer, and the thickness of these SiO_2 layers ($^AT_{SiO_2}$).

Energy (keV)	Dose (x$10^{18}O^+/cm^2$)	Thickness of surface Si layer ($^AT_{Si}$) nm			
		Experiment	Calculated		
			This model	Li *et al*[6]	IRIS[7,8,9]
50	0.2	100	93	85	*
	0.5	75	68	59	*
	0.7	40	33	35	*
70	0.3	130	130	131	*
	0.7	95	95	87	*
	1.0	55	37	54	*
90	0.4	180	177	167	170
	0.7	135	151	137	140
	1.0	90	109	107	105
	1.5	20	16	57	15
200	0.4	410	383	385	410
	0.7	390	364	361	375
	1.2	345	327	321	330
	1.6	280	256	289	260
	1.7	225	245	281	250

Table 5.3 Comparison of the experimental values of the thickness of the surface Si layer ($^AT_{Si}$) in this work with the calculated values, using the model in this work, the equation of Li *et al*[6] and the computer program model IRIS[7,8,9]. * value not calculated.

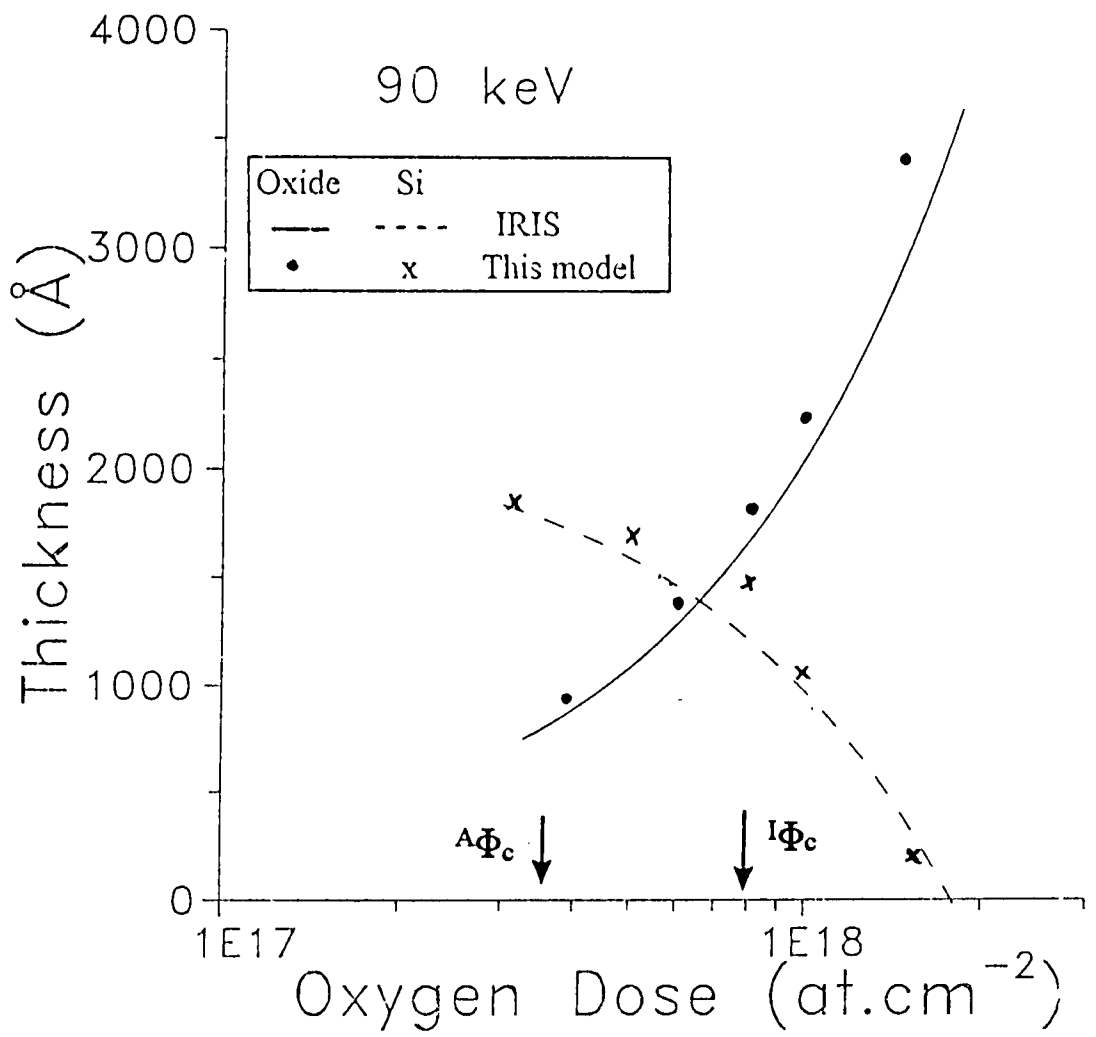

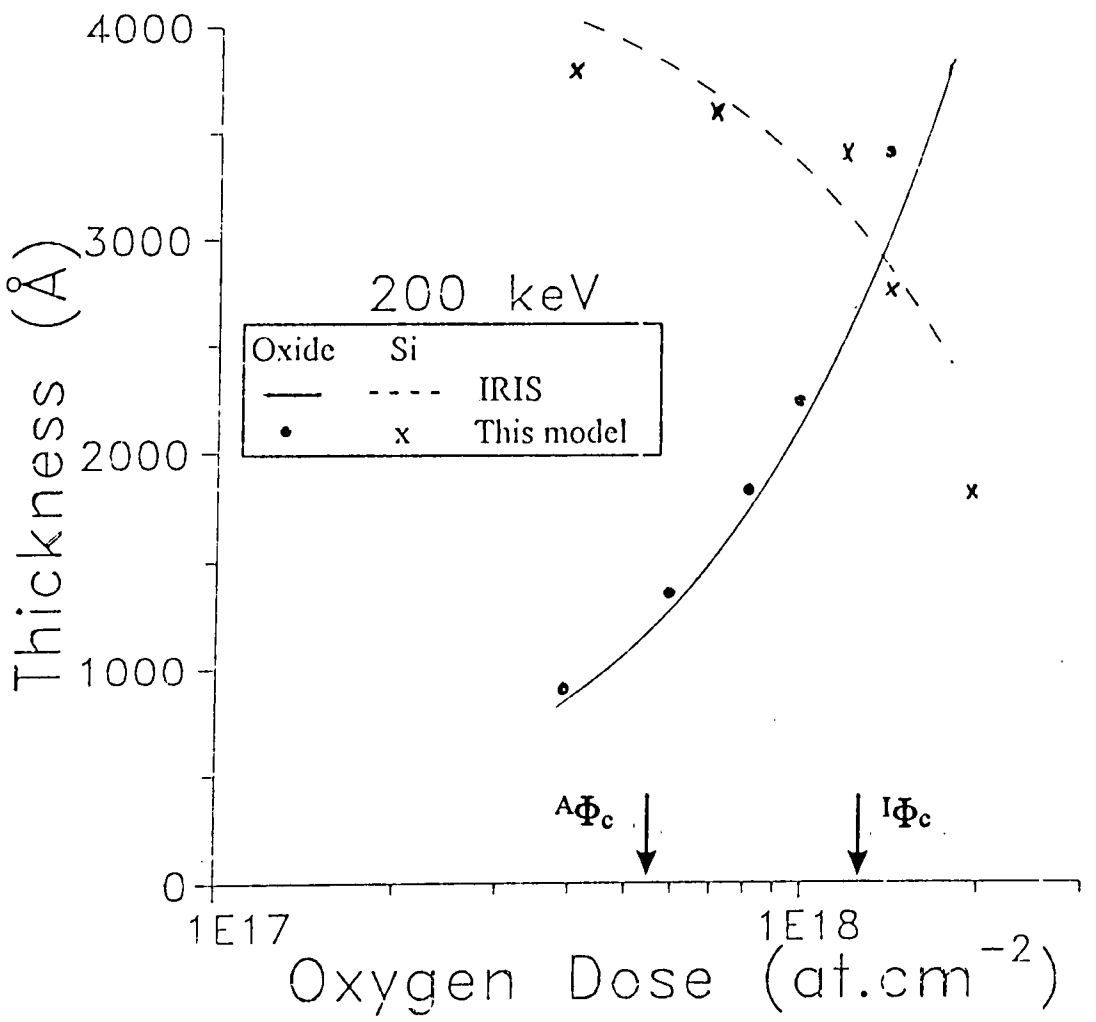

Figure 5.4 Comparison of the surface silicon and buried oxide layer thicknesses after annealing for the models in this work and the computer program model IRIS[7,8,9] ($^{I}\Phi_c$ and $^{A}\Phi_c$ are the minimum doses determined experimentally to form a continuous buried oxide layer after implantation and after annealing, respectively).

dose the model in this thesis assumes an abrupt change in the depth of the oxidation at ${}^{I}\Phi_{c}$ rather than the more realistic smooth change. The values of the surface Si layer thickness from IRIS, taken from the graphs in Fig. 5.4, are compared with the experimental thickness values in Table 5.3. At both energies, for the majority of the dose range (table 5.3) IRIS predicts values which are marginally closer to the experimental values than the values calculated from the model in this work. Although the computer program IRIS gives predictions slightly closer to the experimental surface Si layer thickness, the equations in this work enable the layer thickness to be estimated very quickly without the need to run a computer program.

5.3 References

[1] S M Sze, *Physics of Semiconductor Devices* (Wiley, New York, 1985).

[2] J F Ziegler, J P Biersack & U Littmark, *The Stopping and Ranges of Ions in Solids* vol 1, ed. J F Ziegler (Pergamon, New York, 1985).

[3] K J Reeson, Nucl. Inst. & Meths. B19/20, p269 (1987).

[4] P L F Hemment, K J Reeson, J A Kilner, R J Chater, C D Marsh, G R Booker, J R Davis & G K Celler, Nucl. Inst. & Meths. B21, p129 (1987).

[5] R J Chater, J A Kilner, P L F Hemment, K J Reeson & R F Peart, Proc. Electrochem. Soc. 86-4, p652 (1986).

[6] Y Li, J A Kilner, A K Robinson, P L F Hemment & C D Marsh, J. Appl. Phys. 70, p3605 (1991).

[7] U Bussman & P L F Hemment, Nucl. Inst. & Meths. B47, p22 (1990).

[8] U Bussman & P L F Hemment, Appl. Phys. Lett. 57, p1200 (1990).

[9] U Bussman, A K Robinson & P L F Hemment, Nucl. Inst. & Meths. B55, p852 (1991).

Chapter 6

Conclusions and Suggestions for further work

6.1 Conclusions

6.1.1 As-implanted microstructure

a) similar microstructures and similar changes in the microstructure as a function of increasing dose are observed at the different implant energies of 200keV, 90keV, 70keV and 50keV,

b) for all the doses ($0.1x10^{18}O/cm^2$ to $1.7x10^{18}O/cm^2$) and energies (200keV, 90keV, 70keV and 50keV) investigated, oxide precipitates are present in the surface Si and buried damage/oxide layers. Five different morphologies of oxide precipitates have been observed. The oxide precipitate morphology depends on the local oxygen concentration and the depth below the surface. The local and long range strain and the Si_i and Si_v concentrations are also considered to play important roles in determining the precipitate morphology,

c) for doses of $0.5x10^{18}O/cm^2$ to $1.2x10^{18}O/cm^2$ implanted at 200keV, defects are observed at the wafer surface. In c.s. the depth of the lower edge of this region of defects increases with increasing dose. For doses of $0.5x10^{18}O/cm^2$ to $0.7x10^{18}O/cm^2$ these defects are non-uniformly distributed across the implanted area. The non-uniformly distributed defects at the wafer surface are present in randomly distributed regions which in p.v. are rectangular in shape with edges parallel to <100> directions. With increasing dose, within this range, the fraction of the wafer surface that contains these rectangular regions or overlapping rectangular regions of defects increases. With increasing time-averaged beam current densities between $2.5\mu A/cm^2$ and $6.25\mu A/cm^2$ (for a dose of $\approx 0.7x10^{18}O/cm^2$ and an implantation temperature of 680°C) the fraction of the wafer surface that contains these rectangular regions, or overlapping rectangular regions of defects decreases. This is the first known report of the non-uniform distribution across the implanted area of the defects at the wafer surface and their occurrence in regions with precise rectangular shapes,

d) the spheroidal inclusions close to the surface for doses of $0.56x10^{18}O/cm^2$ to $1.2x10^{18}O/cm^2$ implanted at 200keV implants could be oxide precipitates or voids. Comparison of their microstructure with reports of voids in the literature suggest that they are voids,

e) the "line" defects below the peak of the oxygen distribution for energies of 90keV, 70keV, 50keV and 200keV are thought to be platelets on {100} planes and edge dislocation loops on {110} planes. This is the first report of the presence and the microstructure of these "line" defects,

f) the rod-like defects observed in the surface Si layer are stacking fault pairs, one intrinsic stacking fault and one extrinsic stacking fault. The formation mechanism is thought to be the relief of stress introduced during the cooling of the samples at the end of the implantation due to the smaller thermal expansion coefficient of SiO_2 compared to that of Si,

g) a simple model enables the typical oxygen diffusion lengths during implantation as a function of the implantation conditions to be calculated,

6.1.2 Annealed microstructure

a) thin film SIMOX structures consisting of a thin ($\approx$100nm) surface Si layer above a thin ($\approx$100nm) buried SiO_2 layer can be formed by implanting doses of the order of $\approx 0.35x10^{18}O/cm^2$ at energies of either 90keV, 70keV or 50keV and annealing at 1300-1360°C for 6hrs in N_2 or Ar + ½ % O_2 ambients. The precise thicknesses of the surface Si and buried SiO_2 layers depends on dose and energy (see following conclusions),

b) thin film SIMOX structures consisting of a thin ($\approx$110nm) buried SiO_2 layer below a standard thickness ($\approx$400nm) surface Si layer can be formed by implanting doses of $\approx 0.6x10^{18}O/cm^2$ at 200keV and annealing at 1300-1360°C for 6hrs in N_2 or Ar + ½ % O_2 ambients,

c) the oxygen concentration at the peak of the as-implanted oxygen concentration plays an important role in determining whether the buried SiO_2 layer, after annealing at 1300-1360°C for 6hrs in N_2 or Ar + ½ % O_2 ambients, is continuous or discontinuous. The required

minimum oxygen concentration at the peak of the as-implanted oxygen concentration is $2.2x10^{22}/cm^3$. This is independent of the implantation energy,

d) the minimum thickness of continuous buried oxide layers, after annealing at 1300-1360°C for 6hrs in N_2 or Ar + ½ % O_2 ambients, decreases with decreasing implantation energy. This is because of the decrease in the straggle with decreasing energy,

e) For all the energies (200keV, 90keV, 70keV and 50keV) the thickness of the surface Si layer decreases with increasing dose and for a fixed dose the thickness of the surface Si layer decreases with decreasing energy. The thickness of the buried SiO_2 layer increases linearly with increasing dose and is independent of the implant energy,

f) The thickness of the buried SiO_2 and surface Si layers after annealing can be predicted prior to implantation using simple equations. The predicted values from the simple equations presented in this work are in good agreement with the experimental results. Conversely, to form a certain buried SiO_2 or surface Si layer thickness the required dose and energy can be calculated using the same equations. These equations can be quickly used prior to implantation to calculate these parameters,

g) After annealing at 1300-1360°C for 6hrs in N_2 or Ar + ½ % O_2 ambients the two major defects present are Si islands in the buried SiO_2 layer and threading dislocations in the surface Si layer. The Si islands originate, for doses higher than the minimum dose to form a continuous SiO_2 layer during implantation, from Si isolated from the surface Si layer and substrate during implantation. For doses less than the minimum dose to form a continuous SiO_2 layer during implantation, they originate from Si isolated from the surface Si layer and substrate during annealing. The threading dislocations mostly originate from the defects at the wafer surface after implantation and grow down during annealing,

h) the optimum doses for forming both types of thin-film SIMOX substrates, with both the lowest Si island density within the buried SiO_2 layer and the lowest threading dislocation density within the surface Si layer, and after annealing at 1300-1360°C for 6hrs in N_2 or Ar + ½ % O_2 ambients were just larger than the minimum doses which form a continuous buried SiO_2 layer after annealing for all energies (200keV, 90keV, 70keV and 50keV),

i) annealing in an Ar + ½ % O_2 ambient, compared to an N_2 ambient, results for doses just larger than the minimum doses which form continuous buried SiO_2 layers after annealing and for both high (200keV) and low energy (90keV and 70keV) implants, in a more planar buried SiO_2/surface Si layer interface. The planarity of the SiO_2/substrate interfaces are similar after annealing in either ambient,

j) care has to be taken when annealing in an Ar + O_2 ambient because under some conditions (not determined) the surface Si layer can be oxidised through the anneal cap,

k) with increasing time-averaged beam current densities, between 2.5μA/cm^2 and 6.25μA/cm^2, for a constant implantation temperature of 680°C (dose $\approx$0.7x10^{18}O/cm^2 and energy 200keV) the results suggest that the threading dislocation density decreases with increasing beam current density,

l) low dose graded energy implants at low energies (0.11x10^{18}O/cm^2 at 65keV, 70keV and 75keV) after annealing at 1320°C for 6hrs in N_2 reduce the size of the Si islands within the buried SiO_2 layer, compared to single implants of the same total dose implanted at the mean energy of the graded energy implants (i.e. 0.33x10^{18}O/cm^2 at 70keV). The graded energy implants do not influence the density of the Si islands in the buried SiO_2 layer or the threading dislocation density in the surface Si layer, compared to the single energy implant. For the graded energy implants, the order of the implant energies (i.e. 65keV, 70keV and 75keV compared to 75keV, 70keV and 65keV) does not affect the post-anneal microstructure,

m) a RTA (1300°C for 1minute in N_2) at doses just above the minimum dose to form a continuous buried SiO_2 layer after annealing, for both low (90keV, dose 0.43x10^{18}O/cm^2) and high (200keV, dose 0.6x10^{18}O/cm^2) energies, redistributes the oxygen and results in a structure very different to both the as-implanted and post-annealed (1360°C in N_2 for 6hrs) structures. RTA at 1300°C for 1minute in N_2 prior to a conventional anneal at 1360°C in N_2 for 6hrs, does not reduce the density of the Si islands in the buried oxide layer, the Si pinholes through the buried SiO_2 layer or the threading dislocations in the surface Si layer.

Hence to form a SIMOX substrate with a buried SiO_2 layer of a certain thickness and a surface Si layer of a certain thickness, the desired thickness of buried SiO_2 layer can be formed by selecting the appropriate dose and then the desired thickness of surface Si layer can be formed by implanting that dose at the appropriate energy. The appropriate dose and energy can be calculated for any combination of layer thicknesses using the equations in chapter 5. The results enable, for the implant and anneal conditions used in this work, the likely threading dislocation density within the surface Si layer and Si island density within the buried oxide layer to be estimated for a particular dose and energy.

Thin-film SIMOX substrates consisting of a thin (<160nm) surface Si layer above a thin (75nm to 100nm) buried SiO_2 layer, suitable for the fabrication of "fully depleted" high performance CMOS devices have been successfully fabricated by implanting doses of $\geq 0.35 \times 10^{18} O/cm^2$ and $\geq 0.35 \times 10^{18} O/cm^2$ at energies of 90 and 70keV, respectively. Thin-film SIMOX substrates, consisting of a thin (110nm) buried SiO_2 layer below a standard thickness (400nm) surface Si layer, suitable for fabricating radiation hard circuits with reduced circuit self-heating have been successfully fabricated by implanting doses of $\geq 0.56 \times 10^{18} O/cm^2$ at an energy of 200keV.

6.2 Suggestions for Further Work

Further work is required to extend the characterisation of the microstructure and to reduce further the Si island and the threading dislocation densities. The following are suggestions for further investigations;

a) the outstanding question about the as-implanted microstructure is the composition of the spheroidal inclusions present close to the surface in some of the 200keV implants, i.e. are they oxide precipitates or voids. The spheroidal inclusions could be investigated using through-focal series diffraction contrast TEM and HREM investigations to try and obtain further information on their composition,

b) the effect of varying the time-averaged beam current density between values of between $2.5 \mu A/cm^2$ and $6.25 \mu A/cm^2$ on the threading dislocation density after annealing is not clear,

based on the c.s. TEM and etch pit results. The accuracy of determining the threading dislocation density as a function of the changing beam current density can be improved by performing p.v. TEM analysis,

c) the exchange of oxygen between the buried layer and the anneal cap could be further studied as a function of various experimental parameters, such as dose and energy. This investigation is more suitable for SIMS analysis than TEM,

d) implanting oxygen at a temperature >950°C at which SiO_2 is viscous, may reduce the build up of strain and defects in the surface Si layer and hence reduce the threading dislocation density after annealing. Doses greater than the minimum to form a continuous oxide layer after implanting at >950°C may reduce the number of pieces of Si isolated within the buried SiO_2 layer during implantation and hence reduce the Si island density after annealing,

e) the influence of different ramp rates after implantation and after annealing on the as-implanted microstructure and the densities of the threading dislocations and the Si islands after annealing,

f) a systematic correlation of the electrical properties of the buried SiO_2 layer as a function of the Si island density and size, and the presence of Si protrusions at the Si/buried oxide interfaces to assess the effect of the Si islands and protrusions in the buried SiO_2 layer on the electrical properties.